LEABHARLANN CHOLÁISTE NA TRÍONÓIDE, BAILE ÁTHA CLIATH | TRINITY COLLEGE LIBRARY DUBLIN
Ollscoil Átha Cliath | The University of Dublin

Terms and Conditions of Use of Digitised Theses from Trinity College Library Dublin

Copyright statement

All material supplied by Trinity College Library is protected by copyright (under the Copyright and Related Rights Act, 2000 as amended) and other relevant Intellectual Property Rights. By accessing and using a Digitised Thesis from Trinity College Library you acknowledge that all Intellectual Property Rights in any Works supplied are the sole and exclusive property of the copyright and/or other IPR holder. Specific copyright holders may not be explicitly identified. Use of materials from other sources within a thesis should not be construed as a claim over them.

A non-exclusive, non-transferable licence is hereby granted to those using or reproducing, in whole or in part, the material for valid purposes, providing the copyright owners are acknowledged using the normal conventions. Where specific permission to use material is required, this is identified and such permission must be sought from the copyright holder or agency cited.

Liability statement

By using a Digitised Thesis, I accept that Trinity College Dublin bears no legal responsibility for the accuracy, legality or comprehensiveness of materials contained within the thesis, and that Trinity College Dublin accepts no liability for indirect, consequential, or incidental, damages or losses arising from use of the thesis for whatever reason. Information located in a thesis may be subject to specific use constraints, details of which may not be explicitly described. It is the responsibility of potential and actual users to be aware of such constraints and to abide by them. By making use of material from a digitised thesis, you accept these copyright and disclaimer provisions. Where it is brought to the attention of Trinity College Library that there may be a breach of copyright or other restraint, it is the policy to withdraw or take down access to a thesis while the issue is being resolved.

Access Agreement

By using a Digitised Thesis from Trinity College Library you are bound by the following Terms & Conditions. Please read them carefully.

I have read and I understand the following statement: All material supplied via a Digitised Thesis from Trinity College Library is protected by copyright and other intellectual property rights, and duplication or sale of all or part of any of a thesis is not permitted, except that material may be duplicated by you for your research use or for educational purposes in electronic or print form providing the copyright owners are acknowledged using the normal conventions. You must obtain permission for any other use. Electronic or print copies may not be offered, whether for sale or otherwise to anyone. This copy has been supplied on the understanding that it is copyright material and that no quotation from the thesis may be published without proper acknowledgement.

Trinity College Library Dublin



University of Dublin

THIS THESIS MAY BE READ ONLY

IN THE LIBRARY

Trinity College Library College Street Dublin 2 Ireland

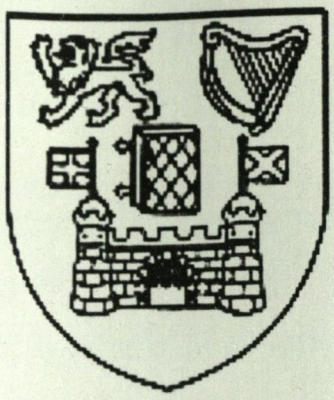

CrO_2: A General Study

Dedicated to my Family

by

Amanda Barry

A thesis submitted to

The University of Dublin

in application for the degree of

Doctor of Philosophy

Department of Physics

University of Dublin

Trinity College

October 1999

TRINITY COLLEGE
22 FEB 2000
LIBRARY DUBLIN
Tesis
5336

Dedicated to my Family

Declaration

This thesis is submitted by the undersigned for examination for the degree of Doctor in Philosophy at the University of Dublin. It has not been submitted as an exercise for a degree at any other university.

This thesis, apart from the advice, assistance and joint effort mentioned in the acknowledgements and in the text, is entirely my own work.

I agree that the library may lend or copy this freely on request.

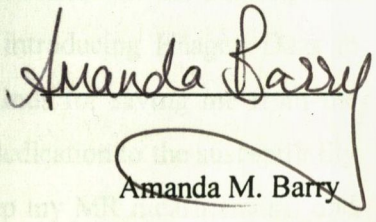

Amanda M. Barry

October 1999

Acknowledgements

My sincerest thanks go to my supervisor Professor J.M.D. Coey for the great interest he has shown in my work and his support and guidance throughout both my undergraduate and post-graduate years at Trinity College Dublin. I would particularly like to express my gratitude for allowing me the opportunity of working in some of the best laboratories in both Europe and the USA.

A big thank you goes to all members of group D, both past and present. In particular, I would like to thank Janko Versluijs for your patience and diplomacy in some of the trickier moments of my thesis writing, Treasa Ní Mhíocháin for turning every Tuesday morning talk that you may have given into something really interesting, Paul Smith for always reminding me that there is no where quite like Ireland, Katie Gallagher for Thanks Giving - hint, hint, Nora Dempsey for.....just being Nora, Laurent Ranno for all his help and encouragement through the trying times, Mazhar Bari for introducing Häagen Dazs to Ireland.....is there anything you can't organinse? Gareth Hinds for saving me from the Hamilton chocolate cake challenge. Cora O'Reilly for your dedication to the susceptibility cause, Rui, Fred 'the Big Guy' Ott - even if you did mess up my MR measurements and Michel Viret for his help with "The Device". Also, thanks to the SPM group/creatures of the night. Thanks also to the more transient members of Group D for keeping the river flowing.

My most profound thanks also go to Steffen Wirth for all his help and particularly his support during the final stages of writing up, it has been a pleasure working with you. I'd also like to thank Steve Watts, Steffen von Molnar and Bertrand Raquet of the MARTECH Laboratory, Tallahasee as well as John Gregg, Will Allen, John Philippe Schillé, Man and Nathalie Viart of the Clarendon Laboratories, Oxford and Claude Fermont of the C.E.A., Paris for welcoming me into their teams.

Many thanks go to the technical and workshop team and the secretaries; Tom Burke, John Kelly, Dave Grouse, James Egan, Joe McCauley, Ken Col Canon and Jemmer, Liz, Elaine, Michelle, Jeannette and Siobhán.

To my partners in crime, excessive beer drinking, Yoda impressions, tears and laughter, weird and wonderful conversation but always very happy memories: James - you are young but you will learn Jedi not quite yet (yeh yeh yeh), Rhian - toilet bowel and furrrruckkkk, Jackie - YAG LASER legs, Laurent-ze-froggie-tramp/wanna-be-comedian and Johnny-Windows 2.1 - THANK YOU.

Many thanks to the girls Sue, Ciara, Fiona and Derval for the extra-curricular activities, the chat and the gossip and to anyone else I may have failed to mention because I have like zero time left to finish this thesis.

To my Mum, my Dad, Debbie, Seán, Robert and my wee wee sis' Siobhán the BIGGEST thanks for ..... just about everything. I most certainly would not have done this without ya's. Lem Shem Nem Sem and Mussa Mana. A big big thank you goes also to Vin and Tom, my grandparents and each and everyone of my more extended family.

Summary

The aims of this work were (i) to prepare chromium dioxide, CrO_2, in thin film and powder form (ii) to study its magnetic, electronic and thermal properties and (iii) to introduce thin films of CrO_2 into a multilayer device structure and study its transport properties.

Thin films and powders of CrO_2 have been prepared by thermally decomposing CrO_3 under high oxygen pressure. Thin films of CrO_2 grown on oriented TiO_2 substrates have the same orientation as the substrate. The films have a distinct needle-like texture with needles up to 50 μm in length. Powders comprising large acicular needles of up to 20 μm in length are produced as a by-product of the thermal decomposition reaction. Commercial powder, containing 0.2 atomic % iron, prepared by a hydrothermal technique comprises fine particles up to 1 μm in length.

The spin polarisation of CrO_2 at 1.6 K is almost 100% at the Fermi level and the low temperature saturation magnetisation of oriented CrO_2 films is close to the value of 133 J/T kg (= $2\mu_B/CrO_2$) predicted for half-metallic ferromagnetic CrO_2. The residual resistivity is metallic lying in the range 0.1 - 10 μΩ m, the difference relating to the granular texture of the films and the quality of the sample. A T^2 - dependence of the resistivity is found in all films above a certain cut-off temperature of approximately 80K. The perpendicular magnetoresistance also shows a transition from a positive-like to a negative-like behaviour on passing through T = 80 K and the field dependence of the Hall effect changes significantly at this temperature. The temperature $T \approx 80$ K is thought to signify a critical temperature below which electron-magnon spin-flip scattering is suppressed giving rise to the various properties observed.

Low temperature neutron diffraction studies on the commercial powder reveal a moment of 2.11(3) μ_B/Cr atom along the c-axis and is interpreted as being an indication of an oxygen moment of $\sim -0.05\mu_B$/O atom and therefore of holes in the O 2p band. This is supported by low temperature Hall data where a sign reversal with field is explained in terms of a two-band model in which highly mobile holes as well as a much larger number of less mobile electrons are present.

The magnetoresistance of oriented thin films of CrO_2 depends strongly on the sample orientation and the direction of the magnetic field with respect to the crystallographic c-axis. A large positive magnetoresistance observed for (110) oriented films at low temperatures is associated with the Lorentz force acting on conduction electrons. A negative magnetoresistance observed for (001) oriented films is most likely a GMR response where in addition to scattering by a spin-dependent potential, there is also scattering at the grain boundaries.

The hysteresis loops of oriented CrO_2 films are also strongly influenced by the substrate orientation. Measurements on a (110) oriented film enabled an estimation of the uniaxial anisotropy constant $K_1 = 6.5 \times 10^4$ J/m^3 at 5 K and 3.7×10^4 J/m^3 at 300 K. The low temperature dependence of the magnetisation for both films and powder is found to follow a Bloch $T^{3/2}$-law for spin-waves. The low temperature specific heat data shows a similar $T^{3/2}$-dependence arising from the magnetic contribution to the specific heat in addition to the lattice and electronic contributions. The Curie temperature of both films and powders of CrO_2 have been found to have an average value of 400 K. Temperature dependent Raman spectroscopy show that the peak linewidths and positions show distinct anomalies at T_c and the resistivity shows a change in slope. The behaviour is attributed to spin fluctuations near and above the Curie temperature.

The temperature dependence of resistivity of pressed powder compacts of commercially produced CrO_2 shows that the resistivity is dominated by the inter-particle contacts. A hysteretic negative magnetoresistance with maxima at the coercive field is observed and is related to the tunneling between contiguous ferromagnetic particles along a critical path with a spin-dependent Coulomb gap. Dilution with insulating Cr_2O_3 powder reduces the conductivity by three orders of magnitude but, enhances the magnetoresistance ratio which reaches 50% at 5 K.

A magnetic tunnel junction (CrO_2/I/Co) has been fabricated using photolithography techniques. A native oxide layer presumed to be Cr_2O_3 provides the insulating layer. The conductance curve, fitted to the Simmons' theory for tunneling, finds a barrier height of 20 Å and width 0.76 eV. The magnetoresistance of the device at 77K measures -1%.

Table of Contents

Declaration.....i

Summary.....ii

Acknowledgements.....iv

Chapter 1. Introduction 1

1. 1. General 1

1. 2. Crystal Structure of CrO_2 3

1. 3. Orbital Structure 5

1. 4. Electronic Structure of CrO_2 7

1. 4. 1. Ionic Model 8

1. 4. 2. Band Model 12

1. 5. Physical properties 18

1. 5. 1. Magnetic Properties 18

1. 5. 2. Transport Properties 20

1. 5. 3. Spectral Properties 23

1. 5. 4. Overview 24

1. 6. This Work 25

Chapter 2: Sample Preparation and Characterisation 29

2. 1. Sample Preparation 29

2. 1. 1. Thermal decomposition of CrO_3 and mixed chromium oxides 29

2. 1. 2. Thermal decomposition of CrO_2Cl_2 33

2. 1. 3. Hydrothermal methods 34

2. 1. 4. Oxidation of $Cr(OH)_3$and CrOOH 36

2. 1. 5. Other methods 38

2. 2. Sample Preparation in this Work 40

2. 3. Sample Characterisation 45

2. 3. 1. Structural Characterisation 45

2. 3. 1. 1. X-Ray Diffraction 45
2. 3. 1. 2. Neutron Diffraction 47
2. 3. 2. Microscopy 49
2. 3. 2. 1. Atomic Force Microscopy 49
2. 3. 2. 2. Optical Microscopy 50
2. 3. 2. 3. Scanning Electron Microscopy 50
2. 4. Results and Discussion 51
2. 4. 1. X-Ray Diffraction 51
2. 4. 2. Neutron Diffraction 54
2. 4. 3. AFM analysis 56
2. 4. 4. Optical Microscopy 57
2. 4. 5. SEM Analysis 58

Chapter 3: Magnetic Properties of CrO_2 62
3. 1. Introduction 62
3. 2. Background 62
3. 2. 1. Domains 64
3. 2. 2. Anisotropy 65
Magnetocrystalline Anisotropy 65
Shape Anisotropy 66
3. 2. 3. Hysteresis Loops 71
3. 2. 4. Spin Waves 73
3. 3. Experimental Methods 75
3. 3. 1. Magnetometry 75
3. 3. 2. Magnetic Neutron Diffraction 77
3. 4. Results 77
3. 4. 1. Magnetic Hysteresis 77
A. Powders 77
B. Films 82
3. 4. 2. Magnetisation versus Temperature 85
A. Powder 85

B. Films 87
3. 4. 3. Neutron Diffraction 90
3. 5. Discussion 91
A. Powders 91
Magnetisation 91
Coercivity and Remanence 93
Curie temperature 94
Temperature dependence of Magnetisation 94
Magnetic Moment 95
B. Films 96
Magnetisation 96
Coercivity and Remanence 97
Temperature Dependence of Magnetisation 98

Chapter 4. Thermal Properties of CrO_2 101
4. 1. Introduction 101
4. 1. 1. Phonons 101
4. 1. 2. Raman Spectroscopy 106
4. 1. 3. Specific Heat Capacity 109
4. 2. Experimental Methods 112
4. 2. 1. Raman Spectroscopy 112
4. 2. 2. Heat Capacity 113
4. 3. Results 114
4. 3. 1. Raman Spectroscopy 114
4 .3. 2. Specific Heat 119
4. 4. Discussion 121
Raman Spectroscopy 121
Specific Heat Capacity 122

Chapter 5: Transport Properties of CrO_2 125
5. 1. Transport Properties 125

5. 1. 1. Background 125
5. 1. 2. Resistivity versus Temperature 128
5. 1. 3. Magnetoresistance 131
A. Ordinary Magnetoresistance 133
B. Anisotropic Magnetoresistance 134
C. Colossal Magnetoresistance 135
D. Giant Magnetoresistance 136
E. Tunnel Magnetoresistance 138
F. Powder Magnetoresistance 141
5. 1. 4. The Hall Effect 141
5. 2. Experimental Procedure 144
5. 2. 1. Sample Preparation 144
5. 2. 2. Electronic Transport Measurements 145
5. 3. Results 147
5. 3. 1. Resistivity versus Temperature 147
A. Films 147
B. Powders 153
5. 3. 2. The Hall Effect 156
5. 3. 3. Magnetoresistance 159
A. Films 159
B. Powders 169
5. 4. Discussion 173
A. Films 173
B. Powders 181

Chapter 6: Device Fabrication and Application 187
6. 1. Introduction 187
6. 2. Spin-Polarised Tunneling and Transport 188
6. 2. 1. Background 188
6. 2. 2. Magnetic Tunnel Junctions 192
6. 2. 3. Andreev Reflection 195

6. 3. Experimental Procedure 198
6. 3. 1. Device Fabrication 199
Stage 1: Sample Preparation 199
Stage 2: Photolithography 199
Stage 3: Wet Etching 201
Stage 4: Deposition of the Insulating Layer 202
Stage 5: Deposition of the Top Ferromagnetic Electrode: Co 202
Stage 6: Contacts 204
6. 3. 2. Transport measurements 206
6. 4. Results and Discussion 206
6. 4. 1. I-V characteristics of a CrO_2/I/Co tunnel junction 206
6. 4. 2. Spin Polarisation by Andreev reflection 211
6.5. Discussion 212

Chapter 7: Conclusions 216
7.1. Conclusions 216
7.2. Suggestions for Future Work 218

Appendix 1 219

Chapter 1

Introduction

"Fear leads to anger, anger leads to hate and hate leads to……suffering."

Yoda-the Jedi master when training Luke Skywalker to use the force in The Empire Strikes Back.

1. 1. General

Chromium dioxide (CrO_2) is one of the technologically most important transition-metal oxides and it owes much of its importance to its use as a particulate recording medium for video and audio applications.[1] It is the only binary transition metal oxide that is ferromagnetic and its ferromagnetism arises from the co-existence of localised and itinerant electrons, a property that can be related to the ratio of its lattice parameters, c/a.[2] The electronic structure of CrO_2 can be compared to that of insulating TiO_2 and metallic RuO_2, both paramagnetic transition metal dioxides.[3, 4] That is, CrO_2 shows the simultaneous presence of metallic-like electrons for one spin orientation (e.g. spin-↑) and insulating-like electrons for the other spin orientation (e.g. spin-↓). This property has earned CrO_2 the title "*Half-Metallic Ferromagnet*" – a term first introduced by de Groot et al. in 1983 to describe Mn-based Heusler Alloys showing a similar energy band structure. A striking consequence of the property of half-metallicity is the presence of fully spin-polarised electrons at the Fermi level (P = 100%). Materials having 100% spin-polarisation are expected to show specific magneto-optical and magneto-transport effects. A large magnetoresistance is expected if half-metallic CrO_2 is incorporated into a tunneling device. This is an exciting prospect from the point of view of device applications where CrO_2 would serve as a source of spin-polarised electrons, applicable to such fascinating ideas as magnetic tunnel junctions, switches and sensors.[5] The main features of a half–metallic ferromagnet are best illustrated by comparing a simple schematic of its density of states shown in figure 1.1 to that of a ferromagnetic metal and a ferromagnetic insulator.

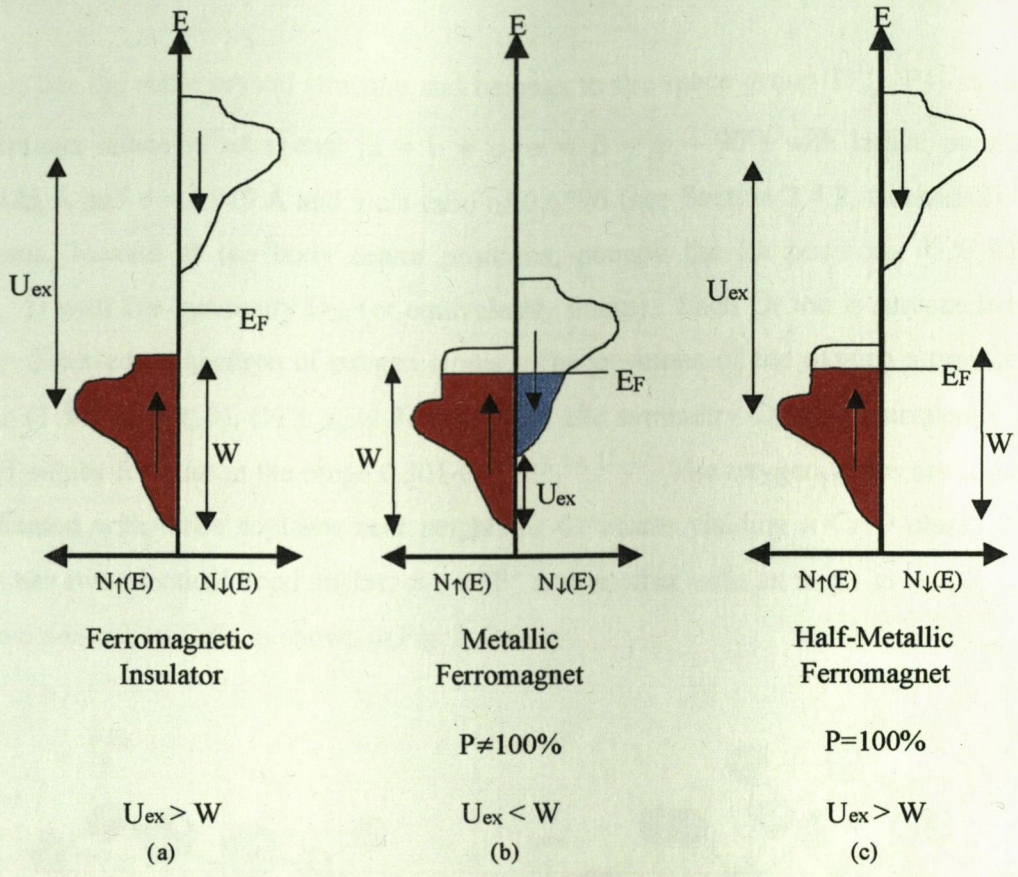

Fig. 1. 1. Density of states of (a) a ferromagnetic insulator showing a full spin-↑ band and a Fermi level that falls into a gap between the spin-↑ and spin-↓ density of states. (b) a metallic ferromagnet showing the presence of two spin orientations at the Fermi level so that P < 100%. This is an example of a weak ferromagnet where the exchange splitting $U_{ex} < W$, the bandwidth (c) A half-metallic ferromagnet where the spin-↑ band is only partially filled and $U_{ex} > W$ so that P = 100%.

In the sections following, the above general statement will be developed by presenting an overview of chromium dioxide's crystal, orbital and electronic structure with reference made later to existing experimental evidence. Lastly, the work to be outlined in this thesis will be described.

1. 2. Crystal Structure of CrO_2

CrO_2 has the rutile crystal structure and belongs to the space group D_{4h}^{14} : $P4_2/mnm$.[6, 7, 8] The Bravais lattice is tetragonal ($a = b \neq c$, $\alpha = \beta = \gamma = 90°$) with lattice parameters $a = 4.425$ Å and $c = 2.919$ Å and a c/a ratio of 0.6596 (see Section 2.4.2, Chapter 2). The Cr atoms, located at the body centre positions, occupy the 2a positions (0, 0, 0) and (½, ½, ½) with site symmetry D_{2h} (or equivalently mmm). Each Cr ion is surrounded by a slightly distorted octahedron of oxygen atoms. The positions of the oxygen atoms are the 4f sites ($1 \pm x$, $1 \pm x$, 0), ($½ \pm x$, $½ \mp x$, ½) with site symmetry C_{2v} (or equivalently mm). Typical values for x lie in the range 0.301-0.303.[9, 10, 11, 12] The oxygen atoms are trigonally co-ordinated with three coplanar near neighbour Cr atoms yielding a Cr_3O cluster. This cluster has two identical bond angles, $\omega \sim 130°$ and another with an angle $\omega' \sim 100°$. The primitive unit cell of CrO_2 is shown in Fig. 1. 2a.

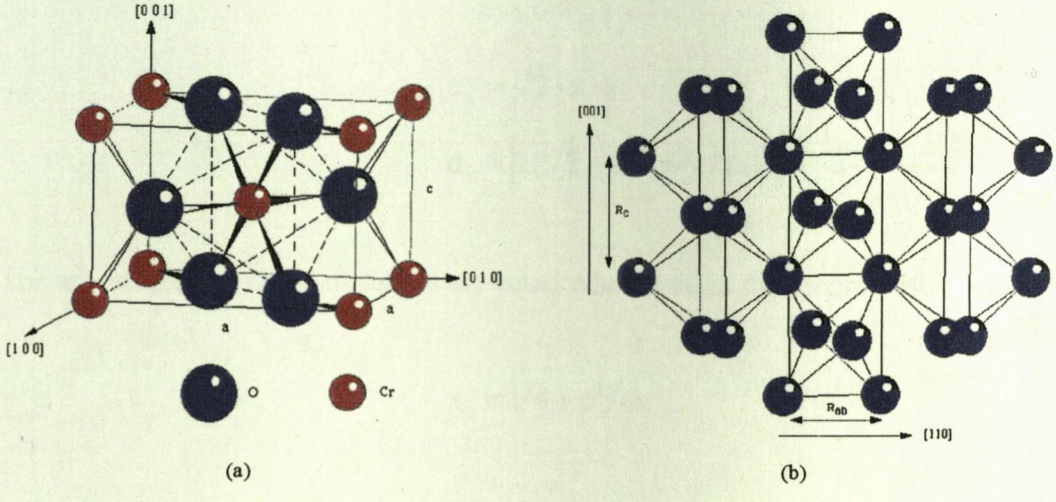

Fig. 1. 2. (a) Rutile structure of CrO_2 showing the Cr^{4+} ion to be surrounded by a distorted octahedron of O^{2-} anions. The hollow bonding illustrates the Cr_3O trigonal cluster, the black bonding, the octahedral site (b) The oxygen octahedra sharing a common edge form ribbons running parallel to the c-axis, adjacent ribbons share a common corner. The octahedra can be transformed into each by a 90° rotation about the c-axis followed by a translation of ½ (a, a, c).

The orientation of the octahedra centred at (0, 0, 0) and (½, ½, ½) differ by a 90° rotation about the c-axis with the oxygen atoms forming a hexagonal close packed sub-lattice with half of the octahedral sites being filled by the Cr atoms. In rutile-like compounds, the octahedra share two edges and one can visualise this arrangement as ribbons of these edge-shared octahedra running parallel to the c-axis and joined at the corners. The filling of only half the octahedral sites means that there is no sharing of octahedral faces. The connectivity of the oxygen octahedra is shown Fig. 1.2b. The octahedra can be transformed into each other by rotating each ribbon by 90° about the c-axis and translating by ± ½ (a, a, c).

By taking the principal axis of the octahedron shown in Figure 1.2a along the [110] direction, it is possible to identify two inequivalent Cr-O distances. The first is the apical distances, d_a, defined between the Cr cation at (½, ½, ½) and the two O anions at (½ ± x, ½ ∓ x, ½). The second is the equatorial distance, d_e, defined between the Cr cation at (½, ½, ½) and the four O anions at (1 ± x, 1 ± x, 0) and (1 ± x, 1 ± x, 1). The apical and equatorial distances can be determined using the equations 1.1 and 1.2 below:

$$d_a = \sqrt{2} \cdot x \cdot a \qquad 1.1$$

$$d_e = \left|2(1/2 - x)^2 + (c/2a)^2\right|^{1/2} \cdot a \qquad 1.2$$

The apical and equatorial distances are equal when x takes the special value, x_c, defined by:

$$x_c = 1/4 + c^2/8a^2 \qquad 1.3$$

and when $x = x_c$ a perfect octahedron is obtained. However, when $x > x_c$ the apical distances are larger than the equatorial distances and when $x < x_c$ the opposite is true. For CrO_2, $x_c = 0.3044$. Consequently, $x < x_c$ and an octahedron characterised by four long equatorial lengths, two short apical lengths and an enhanced c/a ratio is expected. This factor is important since the relative stability of the various energy levels in CrO_2 depends on the c/a axial ratio of the crystal. For example, due to the high valence state of the Cr atom (Cr^{4+}) in CrO_2, a small c/a ratio would result in a repulsive metal-metal interaction

along the c-axis and an unfavourable high energy situation. This is relieved by increasing the c/a ratio. The result is a distortion of the oxygen octahedron away from it ideal geometry so that $d_e > d_a$.

1. 3. Orbital Structure

Before considering the electronic structure of CrO_2, it is instructive at this point to describe the various orbitals involved in the bonding of the Cr and O atoms and their orientation with respect to the crystal lattice. In this way it will be possible to identify more easily the energy bands arising as a result of the orbital overlap. The co-ordinate system in which the p orbitals of the oxygen ions and the d orbitals of the Cr ion are defined is shown in Fig. 1.3. The co-ordinate systems of the Cr and O ions do not coincide and both differ from that of the unit cell.[8]

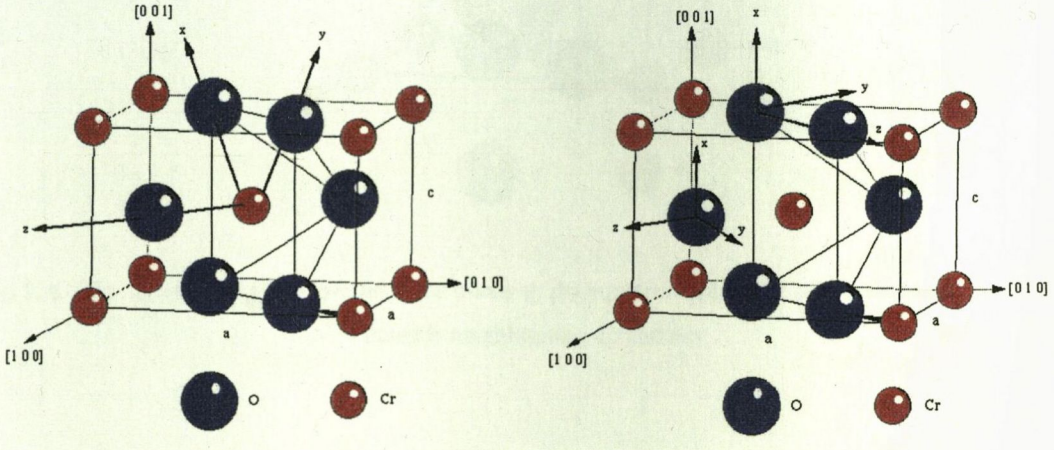

Fig. 1. 3. Local co-ordinate system for (a) the Cr ion and (b) the oxygen anion in CrO_2.

The Cr atom in CrO_2 is a d^2 ion and the d orbitals can be classified into a group of two e_g orbitals of orientation d_z^2, $d_{x^2-y^2}$, and three t_{2g} orbitals of symmetry d_{xy}, d_{yz} and d_{zx}. The e_g orbitals are combined with s and p orbitals to form six hybrid orbitals, $e_g^2sp^3$, appropriate to its octahedral environment. These orbitals point towards the neighbouring oxygen anions, this is shown by the black bonding in Fig. 1.2a.

Of the t_{2g} orbitals, the d_{xy} orbital lies in the equatorial plane of the oxygen octahedron parallel to the c-axis. These orbitals, often denoted $t_{2g}^{\parallel}$, have their lobes oriented between the equatorial oxygen atoms pointing towards neighbouring body centred Cr cations, see Fig. 1.4.

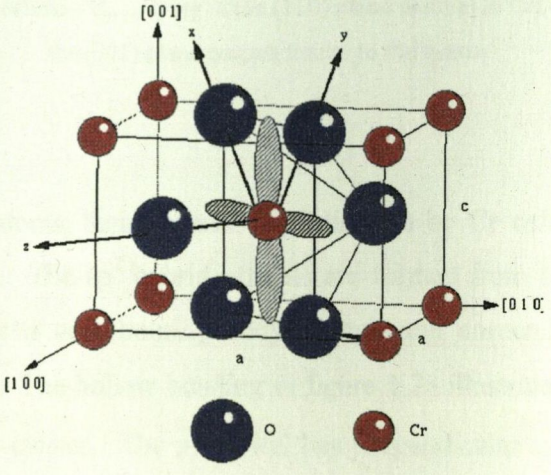

Fig. 1. 4. The t_{2g} orbital-d_{xy} lies parallel to the c-axis in the equatorial plane. It points between oxygen atoms towards neighbouring Cr cations.

The t_{2g} orbitals d_{yz} and d_{zx} are degenerate and are added and subtracted to yield two hybrid orbitals, d_{yz+zx}, d_{yz-zx}. The t_{2g} orbital - d_{yz+zx} lies in the (110) plane parallel to the c-axis. The lobes of these orbitals point towards the octahedral faces in the direction of neighbouring body-centred cations, see Fig. 1.5a. Finally, the t_{2g} orbital - d_{yz-zx} lies in the (001) plane perpendicular to the c-axis and the other two t_{2g} orbitals, Fig. 1.5b. The two degenerate orbitals, d_{yz+zx} and d_{yz-zx} are often denoted $t_{2g}^{\perp}$.

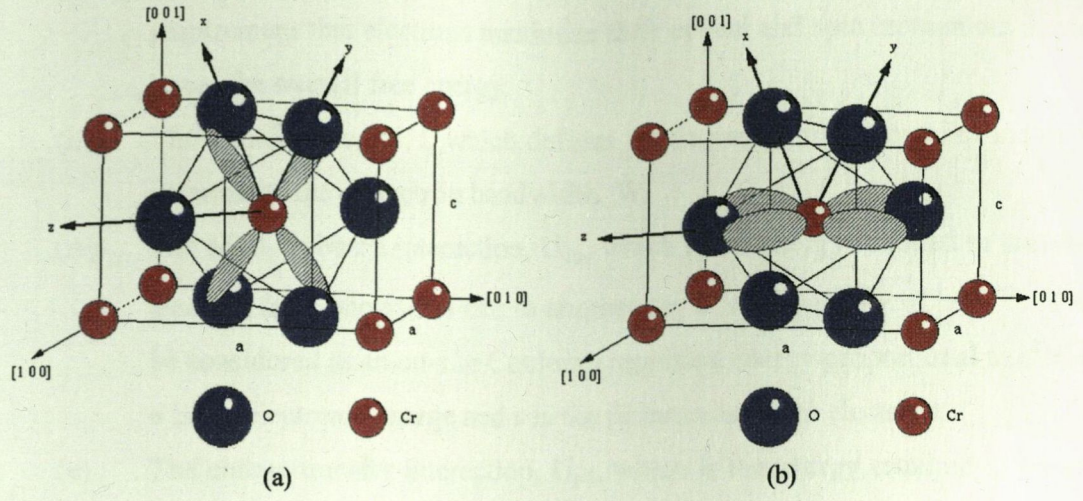

Fig. 1. 5. (a) Hybridised t_{2g} orbital – d_{yz+zx} lying in the (110) plane parallel to the c-axis and (b) d_{yz-zx} lying in the (001) plane perpendicular to the c-axis.

Regarding the oxygen atoms, their trigonal co-ordination by Cr calls for sp^2 hybridisation of the central O^{2-} anion. The sp^2 hybrid orbitals are formed from the oxygen s, p_x and p_z orbitals and point towards neighbouring body-centred and corner located Cr ions in the (110) and $(\bar{1}10)$ planes. The hollow bonding in figure 1.2a illustrates the orientation of the sp^2 orbitals in the Cr_3O cluster. The p_y orbital lies perpendicular to these orbitals and the c-axis in the (001) plane.

1. 4. Electronic Structure of CrO_2

The electronic structure of CrO_2, as for many of the transition-metal-oxides arises as a result of several interactions all of similar magnitude, 1 eV. The principle interactions can be summarised as follows:

(i) The crystal field interaction Δ_{cf}. In CrO_2, the crystal field is an inhomogeneous electrostatic field caused by the surrounding octahedron of negative charge (O^{2-}).

(ii) The on-site Hund's rule exchange interaction, $U_{ex} = 2J_H$. This underlines the requirement that electrons maximise their orbital and spin momentum in order to lower the overall free energy.

(iii) The transfer integral, t, which defines the degree of orbital overlap and therefore determines the d-electron bandwidth, W.

(iv) The Mott-Hubbard interaction, U_{dd}, which is the energy required to transfer a d-electron from one cation site to another i.e. $d^n + d^n \xrightarrow{U_{dd}} d^{n-1} + d^{n+1}$. This can be considered as an on-site Coulomb repulsion energy proportional to e^2/r, where e is the electronic charge and r is the distance between electrons.

(v) The charge-transfer interaction, U_{pd}, which is the energy required to transfer an oxygen p-electron to a neighbouring d ion i.e. $p^6 + d^n \xrightarrow{U_{pd}} p^5 + d^{n-1}$.

By considering the energy interactions (i) and (ii) above it is possible to define the 3d electron energy levels of the Cr ion. The electronic structure is then obtained by considering the overlap of Cr and O orbitals and this involves turning on the interactions (iii), (iv) and (v). The simplest approach to determining the electronic structure of CrO_2 is to consider it as an ionic compound with well defined 3d energy levels and an integral number electrons per ion. The simple ionic model (section 1.4.1) predicts successfully many of the physical properties of CrO_2 such as its ferromagnetic and metallic behaviour. However, to take account of the admixture of different orbitals, which would give rise to properties such as a non-integral value for the magnetic moment and the presence of holes, a band model should be used (section 1.4.2).

1. 4. 1. Ionic Model

In the simple ionic picture, each Cr atom in CrO_2 has a formal valence state of 4+ and two outer 3d electrons. The d-states are split by the cubic crystal field produced by the surrounding octahedron of negative charge by an amount Δ_{cf}, the crystal field energy, into the three low lying t_{2g} states and two higher energy doubly degenerate e_g states defined in

section 1. 3. Moreover, because of the distortion of the oxygen octahedron from ideal octahedral symmetry, there is a further splitting, here denoted $\Delta_{c/a}$, of the t_{2g} orbitals into a two-fold degenerate level ($d_{yz \pm zx}$) and a lower energy d_{xy} level. The on-site Hund's rule exchange interaction then causes a splitting of the spin-up (α) and spin-down (β) states by an amount U_{ex}, the Hund's rule exchange energy giving rise to the one electron energy level diagram shown on the left hand side of figure 1.6.

As a result of the splitting of spin-up and spin-down states, only spin-up states are available to the two d-electrons and a spontaneous magnetic moment is induced. In an ionic crystal containing transition metal elements, the magnetic moment is due only to the spin angular momentum of the outer d-electrons. This is because the net orbital angular momentum of the transition metal is averaged to zero as a result of the quenching action of the crystal field. Hence, the Cr^{4+} ion is expected to carry an integral magnetic moment of 2 μ_B. The filling of the states of lowest energy by the two outer d-electrons of the Cr^{4+} ion gives rise to empty e_g orbitals and partially filled t_{2g} orbitals. The left hand side of Figure 1.6 shows the occupation of the lower lying t_{2g} states according to the arguments described above.

The first qualitative model describing the electronic structure of CrO_2 was proposed by Goodenough in 1971.[13, 14] In this model, the atomic orbitals of the Cr and O ions are combined to yield the molecular orbital scheme illustrated in the centre of figure 1.6. To begin with, the six empty hybrid orbitals, $e_g^2sp^3$, are oriented such that they combine with the filled sp^2 orbitals of the neighbouring oxygen anions to form molecular bonding and antibonding σ states. The orbital overlap extends throughout the crystal giving rise to broad energy bands denoted σ and σ^* in figure 1.6.[13]

The $t_{2g}^{\perp}$ orbitals - $d_{yz \pm zx}$ are properly oriented to yield a π-bond with the p_y orbital of the apical oxygen atom giving rise to the π-bonding and π^*-antibonding states in Fig. 1.6. Due to the difference in energy between the O 2p and Cr 3d states, the bonding orbital is mainly p-type whilst the antibonding orbital is mainly d-like in character. The splitting of the d-states by the exchange interaction U_{ex}, into spin-up and spin-down states is also seen as a splitting of the π^*-band into the spin-up and spin-down states of figure 1.6. The $t_{2g}^{\perp}$ orbital - d_{yz+zx} is oriented such that a π-bond with the p_x orbital of the apical oxygen atom is

possible. However, this interaction is weak since the p_x orbitals of the oxygen atoms are engaged in sp^2 hybridisation with the s and p_z orbitals. The d_{yz+zx} orbital is also oriented in such a way as to yield π-bonding with neighbouring cations along the shared edges of the octahedra. Finally, the orientation of the $t_{2g}^{\parallel}$ orbital - d_{xy} suggests σ-bonding with the neighbouring body-centred cations.

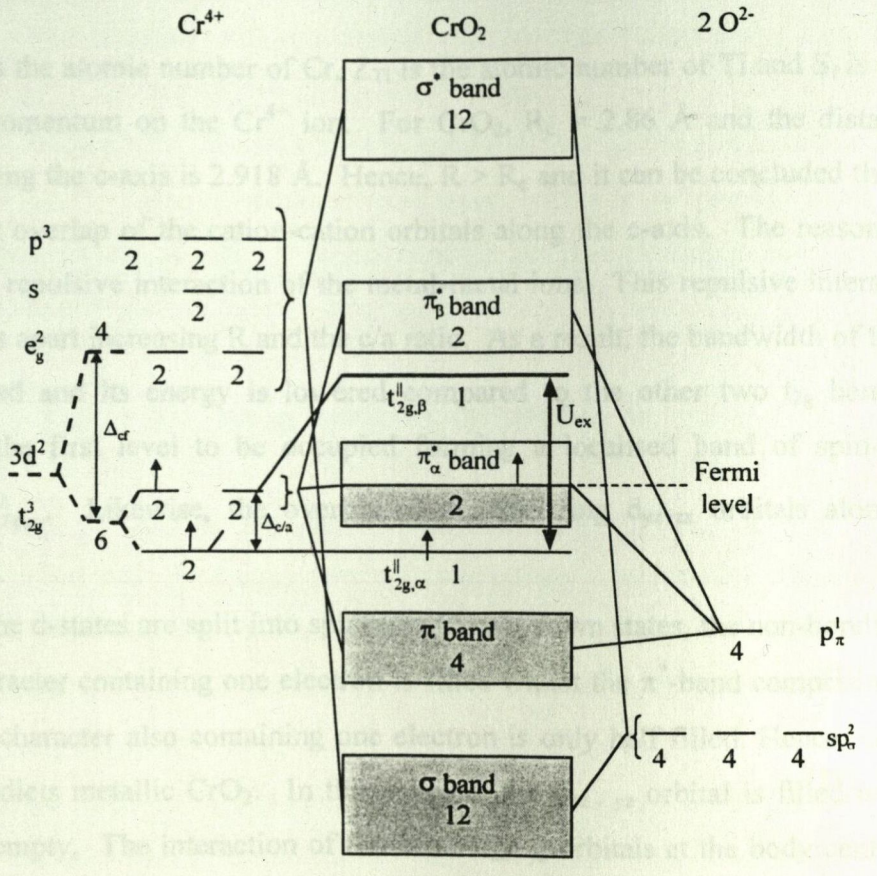

Fig. 1. 6. Molecular orbital scheme for CrO_2 as proposed by Goodenough. The left hand side shows the splitting of the free ion Cr^{4+} d-states by the crystal field (Δ_{cf}) into three low lying t_{2g} states and two higher energy doubly degenerate e_g states. The additional splitting of the t_{2g} states by the crystal field ($\Delta_{c/a}$) into a lower energy t_{2g} level and two higher energy doubly degenerate t_{2g} levels arises from the distortion of the octahedron. The spin up (β) and spin-down (β) states are split by the Hund's rule exchange interaction, J_H. The O^{2-} orbitals, shown on the right, contain sp^2 hybrid orbitals due to a Cr_3O cluster of trigonal symmetry and a p orbital capable of π-bonding with neighbouring Cr t_{2g} orbitals.

The σ- and π-bonding along the c-axis of the d_{xy} and d_{yz+zx} orbitals respectively, depends critically on the distance, R, between Cr cations and this in turn governs the physical properties of CrO_2. A critical distance R_c can be defined as that below which the cation-cation distance is small enough to enable an appreciable overlap of cation orbitals. R_c is given by:[13]

$$R_c = 3 - 0.03(Z-Z_{Ti}) - 0.045S_i(S_i+1)\text{Å} \qquad 1.4$$

where Z is the atomic number of Cr, Z_{Ti} is the atomic number of Ti and S_i is the total spin angular momentum on the Cr^{4+} ion. For CrO_2, R_c = 2.86 Å and the distance between cations along the c-axis is 2.918 Å. Hence, $R > R_c$ and it can be concluded that there is no significant overlap of the cation-cation orbitals along the c-axis. The reason that $R > R_c$ lies in the repulsive interaction of the metal-metal ions. This repulsive interaction pushes the Cr ions apart increasing R and the c/a ratio. As a result, the bandwidth of the d_{xy} orbital is narrowed and its energy is lowered compared to the other two t_{2g} bands so that it becomes the first level to be occupied forming a localised band of spin-up electrons denoted $t^{\parallel}_{2g,\alpha}$. Likewise, the overlap of neighbouring d_{yz+zx} orbitals along the c-axis negligible.

Since the d-states are split into spin-up and spin-down states, the non-bonding t_{2g} orbital of d_{xy} character containing one electron is filled whilst the π^*-band comprising t_{2g} orbitals of $d_{xz \pm yz}$ character also containing one electron is only half filled. Hence, Goodenough's model predicts metallic CrO_2. In this scheme, the $d_{xz\,-\,yz}$ orbital is filled and the $d_{xz\,+yz}$ orbital is empty. The interaction of the filled $d_{xz\,-\,yz}$ orbitals at the body centred positions with neighbouring empty $d_{xz\,+\,yz}$ orbitals of the Cr cations located at the corners of the unit cell occurs via the oxygen anion through an angle of ~ 135°. From Goodenough's second rule, which pertains to the contact of filled and empty orbitals of the same type, this interaction is ferromagnetic.[15] Hence, Goodenough's model predicts ferromagnetic CrO_2.

1. 4. 2. Band Model

The overlap of the Cr 3d orbitals in CrO_2 with neighbouring orbitals gives rise to bands having a width W = 2zt, where z is the number of nearest neighbour cations and t is the transfer integral. Due to the possible mixed character of these bands (e.g. p and d character) an ionic model, in which orbitals are considered to retain their s, p and d character, is no longer adequate in describing the electronic structure. The admixture of the p and d orbitals together with the intra-atomic correlations are taken into account in an averaged way in the calculations of the band structure.

In 1986, Schwarz published the first calculations of the band structure and the density of states for CrO_2.[16] These calculations were based on the local-spin–density approximation (LSDA) and an atomic-sphere approximation for the crystal potential. The results confirmed the phenomenological model proposed by Goodenough (Fig. 1.6) showing that majority (spin–up) electrons were metallic while the minority (spin-down) electrons presented a gap in the energy spectrum into which the Fermi level fell and were consequently semiconducting. CrO_2 was classed a "Half-Metallic Ferromagnet" with fully spin polarised conduction electrons at the Fermi level. The original band structure calculated by Schwarz for the majority spin and minority spin band is shown in Fig. 1.7.

Schwarz explained that the metallicity for the majority spin-states was due to a relatively strong covalent interaction between similar energy O 2p and Cr 3d↑ states whilst for the exchange split spin-down states, the separation in energy between the O 2p and Cr 3d↓ states was large enough to cause a gap to open between the O 2p and Cr 3d↓ states leading to the half-metallic character of CrO_2. In addition, the calculations of the density of states showed that the Fermi level fell close to the top of the gap in the spin-down density of states and close to a local minimum in the spin-up density of states. A sharp peak in the density of states below this minimum was later attributed to the narrow band of localised states of d_{xy} character and the broader band crossing the Fermi level to the delocalised electrons of $d_{yz \pm zx}$ character, underlining the dualistic behaviour of the t_{2g} states.[17] The magnetic moment on the Cr ion was also calculated and found to be 2.03 μ_B showing that the spin-polarisation resided mostly on the Cr atom despite the strong covalency between O 2p and Cr 3d↑ states. A moment of – 0.02 μ_B was calculated for the

oxygen ion ensuring a total integral moment of 2 μ_B /CrO_2, as required in a half-metallic system. That is, half-metallic ferromagnets are strong ferromagnets with no 4s states at the Fermi level and the integral moment arises from there being only d-like electrons of one spin orientation (e.g. d↑) at the Fermi level.

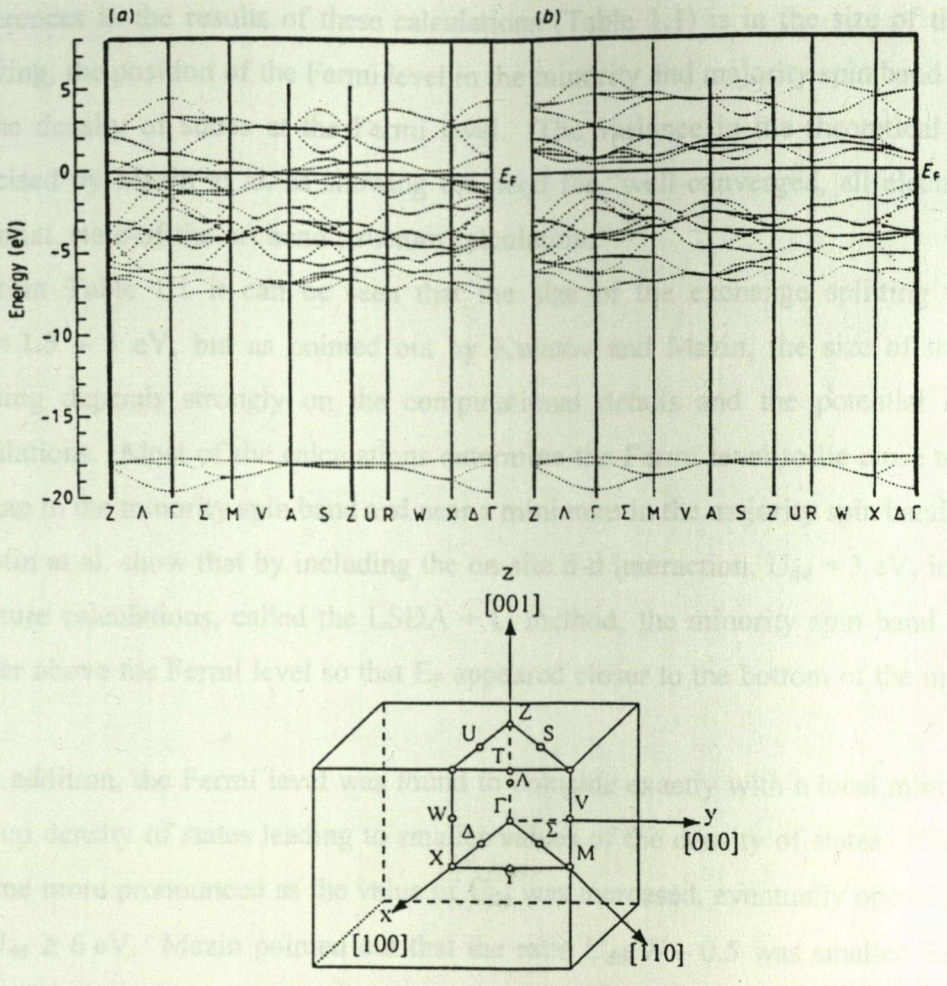

Fig. 1. 7. Original band structure calculation of Schwarz's showing majority and minority spin energy bands in CrO_2. Below is shown the Brillouin zone showing the directional properties associated with the symmetry notation, Γ. Λ, Z etc.

Since that time, several band structure calculations based on various methods have been carried out and, with the exclusion of Nikolaev's results, all show that CrO_2 is a half-metallic ferromagnet.[8, 9, 17, 18, 19, 20, 21, 22] In the calculations of references 10, 15-17 and 19 an atomic sphere approximation was used for the crystal potential, whilst in reference 18 a

muffin-tin approximation was used. The first calculation to use a fully expanded potential representation to take account of the non-spherical part of the crystal potential was performed by Sorantin and Schwarz in a study of the chemical bonding in rutile-like compounds.[8] Lewis was later to use a pseudopotential based method.[21] The main differences in the results of these calculations (Table 1.1) is in the size of the exchange splitting, the position of the Fermi level in the minority and majority spin band and the size of the density of states at the Fermi level. The variance in the theoretical results was criticised by Mazin et al. as showing the need for "well-converged, all electron and full potential, state-of-the-art band structure calculations".[22]

From Table 1.1 it can be seen that the size of the exchange splitting varies from $U_{ex} = 1.5 - 5$ eV, but as pointed out by Kulatov and Mazin, the size of the exchange splitting depends strongly on the computational details and the potential used in the calculations. Most of the calculations determine the Fermi level to lie close to the top of the gap in the minority spin band and near a minimum in the majority spin band. However, Korotin et al. show that by including the on-site d-d interaction, $U_{dd} = 3$ eV, into the band structure calculations, called the LSDA + U method, the minority spin band was shifted further above the Fermi level so that E_F appeared closer to the bottom of the minority spin gap.

In addition, the Fermi level was found to coincide exactly with a local minimum in the spin-up density of states leading to smaller values of the density of states. The minimum became more pronounced as the value of U_{dd} was increased, eventually opening into a gap for $U_{dd} \geq 6$ eV. Mazin pointed out that the ratio $U_{dd}/W \sim 0.5$ was smaller than for most other strongly correlated transition metal oxides and that in this case, it was unclear whether including U_{dd} explicitly into the calculations resulted in a more accurate picture of the electronic structure. He concluded that a full potential LSDA approach was adequate to explain the electronic structure of CrO_2 and the inclusion of additional strong correlation effects was not necessarily an improvement on the situation.

As an example of the differences that can occur in the band structure calculations, the density of states from the calculations of Korotin et al and Mazin et al. are compared in Fig. 1.8. These differences underline the need for state-of-the-art experiments to resolve the still controversial issues regarding the electronic structure of CrO_2.

Table 1. 1. Comparison of the results of the band structure calculations referred to in the text. Here, Δ_{cf} is the crystal field potential estimated from the middle of the t_{2g} band to the middle of the eg band in the calculated DOS. U_{ex} is the exchange splitting estimated from the middle of the $t_{2g}\uparrow$ band to the middle of the $t_{2g}\downarrow$ band. W is the estimated bandwidth of the t_{2g} band. $D(E_F)$ is the density of states at the Fermi level and μ_{Cr} and μ_O are the calculated moments for the chromium and oxygen ions respectively

Reference	Method	Δ_{cf} (eV)	U_{ex} (eV)	W (eV)	$D(E_F)$ (states/eV cell)	μ_{Cr} (μ_B/ion)	μ_O (μ_B/ion)
Schwarz '86	ASW[a] LSDA[b]+ ASA[c] for potential	3.0	1.8	2.5	1.60	2.03	-0.02
Kulatov '90	LMTO[d] LSDA + ASA for potential	2.7	4.0	2.7	2.34	1.945	0.028
Matar '92	ASW LSDA+ ASA for potential	2.7	2.0	3.0	1.60	2.049	-0.034
Sorantin '92	LAPW[e] LSDA + full potential	2.5	1.8	2.2	2.0	-	-
Nikolaev '93	LAPW + muffin-tin potential	-	0	4.0	3.31	1.772	0.077
van Leuken '95	LSW[f] LSDA + ASA for potential	3.0	2.5	2.0	2.0	2.021	-
Lewis '97	PW[g] LSDA + pseudopotential	2.5	1.8	2.5	1.38	2.0	-
Korotin '98	LSDA + U + ASA for potential	2.5	3.0	2.5	0.5	-	-
Mazin '99	LAPW LSDA + full potential	2.5	2.5	5-6	1.9	-	-

a - augmented spherical wave
b - local-spin-density approximation
c - atomic sphere approximation
d - linear muffin-tin orbital
e - linear augmented plane wave
f - localised spherical wave
g - plane wave

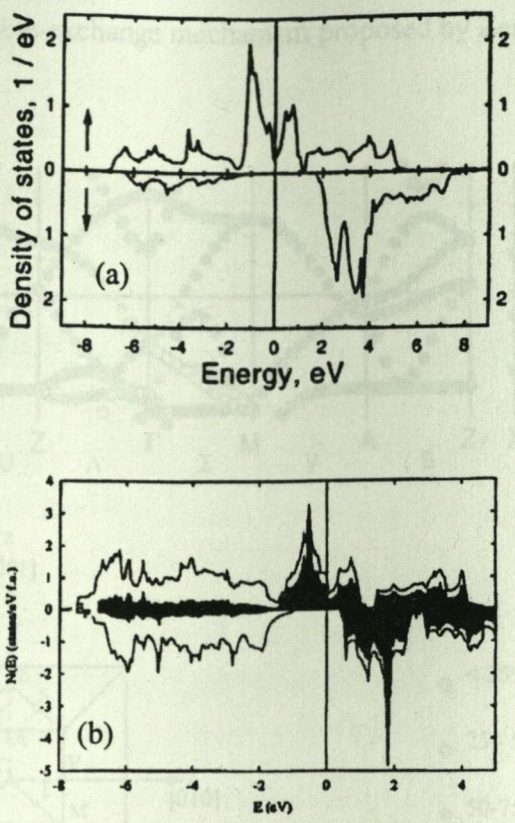

Fig. 1. 8. Total density of states of the majority and minority bands of CrO_2 using (a) the LSDA + U approach of Korotin et al. (b) the full potential LSDA approach of Mazin et al. The shaded area in (b) corresponds to the Cr 3d contribution to the density of states.

Fig. 1.9 shows the band structure for the majority electrons as calculated by Korotin et al. This diagram is of interest since it is the only band picture where the energy levels are decomposed to show both the O 2p and Cr 3d contributions to the energy bands. Of particular importance is the nature of the bands crossing the Fermi level. At approximately 1 eV below the Fermi level, it is possible to identify an almost dispersionless band of almost pure d character. This band corresponds to the localised d_{xy} orbitals occupied by one majority spin electron. On the other hand, d-states with considerably more p-type character correspond to the $d_{yz \pm xz}$ orbitals and form dispersive bands that cross the Fermi level. These electrons move through the core of localised d_{xy} electrons which because of

the Hund's rule coupling polarise them, resulting in a ferromagnetic exchange which can be compared to the double-exchange mechanism proposed by Zener.[23]

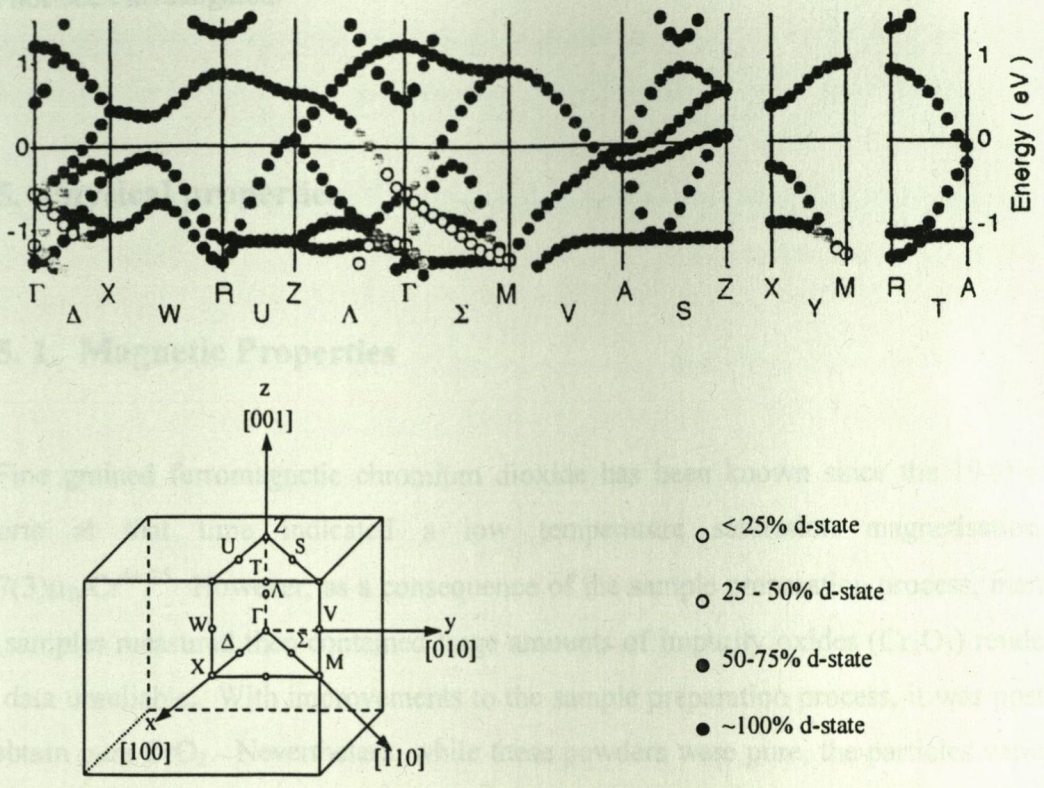

Fig. 1. 9. Band structure of CrO_2 for the majority spin band as calculated by Korotin et al. using the LSDA + U method. The degree of d-like character of the bands is highlighted by the different shaded circles shown in the legend in the bottom right hand corner of this diagram. The corresponding Brillouin zone showing the directional properties associated with the symmetry notation, Γ. Λ, Z etc. is also shown.

At the Γ point, it can be seen that bands of predominantly O 2p character extend up to the Fermi level. These states can act as electron or hole reservoirs causing a non-integral occupation of the d-states. Korotin et al. refer to this as self-doping and it results in Cr becoming mixed valent. Self-doping refers to the interaction U_{pd}, where an electron is transferred from a p orbital to a neighbouring d orbital. U_{pd} is called the charge-transfer energy. An interesting consequence of self-doping is the contribution of the oxygen holes

to the transport and magnetic properties of CrO_2. Schwarz had already shown that the oxygen ion harbours a significant magnetic moment in a direction opposing that of the Cr ion. But the contribution of holes in the p-band to the transport properties until recently had not been investigated.[24]

1. 5. Physical properties

1. 5. 1. Magnetic Properties

Fine grained ferromagnetic chromium dioxide has been known since the 1940's and reports at that time indicated a low temperature saturation magnetisation of $2.07(3)\mu_B/Cr^{4+}$.[25] However, as a consequence of the sample preparation process, many of the samples measured then contained large amounts of impurity oxides (Cr_2O_3) rendering the data unreliable. With improvements to the sample preparation process, it was possible to obtain pure CrO_2. Nevertheless, while these powders were pure, the particles varied in size and distribution and this was reflected in the wide range of values for the saturation magnetisation (1.9 - 2.07 μ_B/Cr^{4+}), Curie temperature (385 – 405 K) and coercivity (0.002 - 0.15 T) reported later.[10, 26, 27, 28, 29] Darnell showed that at low temperature, the saturation magnetisation, Curie temperature and coercivity for powders of less than 1 μm in length, was 1.9 μ_B/Cr^{4+}, 405 K and 0.15 T respectively whilst for powders of approximately 10 μm in length the same values were 2.03 μ_B/Cr^{4+}, 392 K and 0.002 T respectively.

Particles of less than 1 μm in length were generally single-domain particles and due to their regular shape and morphology, were particularly suitable for use in the production of high quality recording tapes.[1, 30, 31, 32, 33] The coercivity of these small particles was found to be controlled by the shape anisotropy (Section 3.1.3, Chapter 3) and by introducing chemical modifiers (e.g. Sb_2O_3 and RuO_2) into the preparation process it was possible to optimise the particle size and shape thus maximising the shape anisotropy and the

coercivity.[10, 27, 34, 35, 36, 37] The drawback was that many of these powders contained traces of the modifiers used. Moreover, the approach to saturation was observed to be slow for these smaller particles and was attributed to a lower surface symmetry.[10] Iron doping was the method later adopted to maximise the coercivity of fine-grained CrO_2 powders.[30] Incorporating Fe into the lattice was found to cause an expansion of the unit cell along the a-direction, while the c-parameter remained unchanged. The result was an increased magnetocrystalline anisotropy and an enhanced coercivity and Curie temperature of up to 0.95 T and 450 K respectively.[30, 38] However, since the iron coupled antiferromagnetically to the Cr^{4+} ions, the saturation magnetisation was generally lower than that of the pure unmodified CrO_2 powders.

Large single crystals revealed a low temperature saturation moment in the range 1.93-1.98 μ_B/CrO_2 and a Curie temperature of 398-400 K.[10, 28, 39] However, for single crystalline films of CrO_2 grown on TiO_2 or sapphire substrates, the moment could only be estimated as lying in the range 2 μ_B/CrO_2 due to the uncertainty in the film thickness.[40] The coercivity of the thin films was found to depend on the sample thickness and the magnetisation reversal was determined as being one of domain-wall motion.[41]

The magnetic field dependence of magnetisation parallel and perpendicular to the single crystal c-axis yielded a value for the uniaxial magnetocrystalline anisotropy of 3×10^4 J/m^3 and an easy-direction of magnetisation lying in the a-c plane at an angle of 30-40° to the c-axis.[10, 39] However, in contrast to these reports, magnetocrystalline anisotropy studies on epitaxial CrO_2 films deposited on single crystal TiO_2 substrates indicated a c-axis anisotropy of 2×10^4 J/m^3 at room temperature.[42] The issue is still not fully resolved as recent powder neutron diffraction studies revealed a magnetic moment of 2.1 μ_B/Cr^{4+} lying at an angle of 20° to the c-axis in the a-c plane.[12]

Above the Curie temperature, studies have shown that the susceptibility of pure unmodified CrO_2 powder follows a typical Curie-Weiss law.[10, 26, 28] In the range 330 - 570 K, Darnell determined a Curie constant $g^2S(S+1) = 8.3$ consistent with $S = 1$ and a spin only moment of $2\mu_B/CrO_2$.[10] Kouvel and Rodbell examined the susceptibility near the critical transition temperature and showed that it varied as $T^{1.63}$ near T_c but quickly tended towards a normal Curie-Weiss behaviour at higher temperatures.[29] The magnetisation as a function of temperature of pure CrO_2 powder was measured by Siratori

and Iida and by Chamberland, but the results were only related to the Curie temperature which was found to be 400 K. Brändle later published the temperature dependent magnetisation for an epitaxial CrO_2 film grown on a sapphire substrate but again no interpretation of the results was given.

1. 5. 2. Transport Properties

One of the first measurements of the electrical conductivity of CrO_2 was carried out by Chapin et al in 1965 on compacted powder samples.[43] While this measurement gave a room temperature resistivity of a magnitude usually associated with metallic conduction, the temperature dependence of the resistivity was ambiguous with respect to the nature of the conductivity. The following year, Rodbell et al. were to measure the resistivity of single crystals of CrO_2 grown on oriented TiO_2 substrates in the temperature range 10 – 500 K.[44] Their results indicated unmistakably the metallic character of CrO_2 with a resistivity that increased with increasing temperature, a residual resistivity of the order 2.5 $\times 10^{-6}$ Ω m and a change in slope of the resistivity at the ferromagnetic-paramagnetic transition temperature which was associated with the intrinsic properties of the metallic ferromagnet.

More recent measurements of the transport properties have been prompted by the need to correlate the observed resistivity behaviour with the half-metallic electronic structure predicted for CrO_2 and the implications of large magneto-transport properties arising as a result of incorporating CrO_2 films into a multilayer device structure.[45] The recent resistivity measurements of single crystalline films show characteristics similar to those of Rodbell but an explanation for the observed behaviour remains pending. Suzuki et al. have suggested that, in keeping with the half-metallicity of CrO_2, the conduction process involves a parallel combination of metallic majority spin electrons and semiconducting minority spin electrons where the Fermi level plays the role of a donor level for the semiconducting minority spin electrons. Lewis on the other hand, modelled the low-temperature resistivity on the Bloch-Grüneisen formula for electron-phonon scattering

while Mazin et al. compared the resistivity behaviour of CrO_2 to that of $SrRuO_3$, a so-called bad-metal.[21, 22] However, for a ferromagnetic metal such as CrO_2, electron-magnon scattering is thought to be the most likely source of scattering at low temperatures (Section 5.4A , Chapter 5).

The correlation of the resistivity to particle size and perfection was referred to as early as 1965 by Darnell and Cloud who found that resistivities were larger for powder compacts comprising of smaller particles with a greater degree of surface degradation.[10] In 1998, this was shown directly when Hwang et al. showed that by heat treating polycrystalline films grown on $SrTiO_3$ substrates, the intergrain barriers could be modified and the resistivity increased to show an insulating behaviour with temperature.[46] The increased sample resistivity was found to coincide with a nearly threefold enhancement of the magnetoresistance ratio (10 to 25% at 5 K) and the source of the magnetoresistance was said to arise from intergrain tunneling. This idea was developed independently by Coey et al. who found that a large negative magnetoresistance (~ 30% at 5 K) could be obtained for pressed powder compacts of CrO_2 which could be further enhanced by diluting CrO_2 powders with powders of Cr_2O_3 (50% at 5 K). The large magnetoresistance effect associated with these pressed powder compacts was coined *powder magnetoresistance* and is discussed in Chapter 5.[47]

One of the earliest reports of the magnetoresistance of pure single crystalline CrO_2 was by Rodbell who claimed (without publication of the results) that the magnetoresistance of an epitaxial CrO_2 film was linear and approximately –1.8% at room temperature in a 3T field applied parallel to the [001] axis and the current direction.[44] Since that time, there have been very few reports regarding the magnetoresistance of CrO_2. The next reference coming from Ranno et al. who reported a linear room temperature magnetoresistance of ~1% at 1.2 T for a polycrystalline CrO_2 film grown on a sapphire substrate.[48] Suzuki et al. later published results of the longitudinal and perpendicular magnetoresistance of CrO_2 films grown on ZrO_2 substrates.[45] Both were found to be negative and linear up to fields of 3T for temperatures above 200 K. The behaviour in both cases was interpreted in terms of the suppression of magnon scattering by the magnetic field. For temperatures below 200 K, both the transverse and longitudinal magnetoresistance showed a large low field response which saturated at higher fields in the case of the longitudinal magnetoresistance.

On the other hand, the transverse magnetoresistance showed a strong positive contribution for fields greater than 3T. The low temperature transverse MR behaviour was accounted for in terms of the electron cyclotron motion and size effects which occur when the carrier mean free path is comparable to the film thickness. The low temperature longitudinal MR was not interpreted. However, whilst these measurements are among the first of their kind and thus important in their own right, the crystallographic quality of these films was not clearly expressed. This may be an important factor since Li et al recently showed that the magnetoresistance depended strongly on the direction of the current and the magnetic field with respect to the c-axis as well as on the temperature.[49] At 5 K, their (100) oriented CrO_2 film showed a non-saturating positive magnetoresistance of 25% in a 4 T field when the current is parallel to the crystallographic c-axis and the field is perpendicular to the c-axis but in the plane of the film. For the same current-field-c-axis configuration at 380 K, a temperature close to the Curie temperature of CrO_2, the magnetoresistance was found to be negative and of the order of 7% at 4 T with no sign of saturating. However, when the field and current were both parallel to the c-axis a smaller positive MR of approximately 2.5% was observed at 5 K and 4 T. At 380 K, the magnetoresistance for this configuration was similar to that observed for the transverse field geometry. The positive MR was associated with the Lorentz force acting on the conduction electrons and the negative MR to the suppression of spin disorder scattering. Hence in order to determine and interpret the MR behaviour of CrO_2 correctly it is necessary to work with well characterised samples for which the orientation and quality are known.

Recent Hall measurements show conflicting results. Brändle et al. determined a carrier concentration of 0.49 electrons/CrO_2 whilst Li et al. show a carrier concentration of 0.3 holes/CrO_2.[40, 49] Li admitted however that a more detailed analysis of the Hall data could reveal both electron and hole contributions.

Specific heat measurements also reveal discrepancies between the various reports.[40, 50] Values of the electronic contribution to the specific heat have been found to lie in the range 2.25 - 7 mJ/K^2 mole corresponding to a large distribution of values for the density of states i.e. 1.9 - 6.0 states/eve cell.

1. 5. 3. Spectral Properties

The electronic structure, first predicted by Goodenough, was later consolidated by measurements of the optical conductivity and thermoreflectance carried out by Dissanayake in 1978 and 1981 respectively.[51, 52] In these experiments, peaks in the optical conductivity occurring at 0.85 eV, 1.9 eV and 3 eV were assigned to transitions from (1) the Cr spin-up band to the Cr spin-down band, (2) the oxygen π-band and the π-band of Cr spin-up electrons and (3) the oxygen π-band and the π-band of the Cr spin-down electrons respectively. These were thus the first energy scales introduced into the energy band scheme for CrO_2. More recent measurements of the diagonal optical conductivity by Brändle et al found peaks at similar energies.[40] In this report however, they attribute the peak at 0.8 eV to a $d\uparrow$-$d\uparrow$ transition, the peak at 1.8 eV to a spin-flip transition between the majority spin-up and minority spin-down states and the peak at 3 eV to transitions between the O 2p band and the Cr 3d band. Calculations of the off-diagonal conductivity by Uspenskii et al. agreed with these experiments.[53] Tsujioka et al have also studied the electronic structure by photoemission spectroscopy.[50] These measurements revealed a much larger splitting of the Cr 3d states of 5 eV. Tsujioka claims that the recent LSDA band structure calculations underestimate the magnitude of the splitting by neglecting the Hubbard splitting of the d-band and that their results are more consistent with the LSDA + U calculations of Korotin et al.[17] In this case, the large splitting is due to the combined exchange and on-site correlation effects. Furthermore, comparison of the density of states at the Fermi level calculated from the spectral intensity to the density of states calculated from the electronic specific heat show that there exists a substantial mass renormalization due to electron correlation implying that the LSDA + U band description is a better starting point to understand the electronic structure of CrO_2. However, the large splitting reported by Tsujioka is obviously in contrast to the other experimental and theoretical reports and is therefore questionable.

The most attractive feature of CrO_2 is the likelihood of it having a 100% fully spin-polarised conduction band at the Fermi level. Spin resolved photoemission experiments carried out by Kämper et al in 1987 showed that CrO_2 did show a spin polarisation of nearly 100%.[54] However, the optical measurements only probed electrons at 2 eV below

the Fermi level and showed that there was a vanishing density of states at the Fermi level. Furthermore, spin-polarised vacuum tunneling experiments carried out by Wiesendanger et al. measured a spin polarisation of only 20%.[55] These results opposed strongly the predictions of the band structure calculations. Consequently, the question of the spin polarisation of CrO_2 remained until now unresolved and the subject of much controversy.

Furthermore, the large magneto-optical effects, such as a large Kerr and Faraday rotation, expected for half-metallic ferromagnetic materials were not observed.[40, 56] In the energy range which is interesting for applications in optical storage (1.5 - 3 eV) Brändle measured a Kerr rotation of much less than 0.1°. At 3.7 eV a maximum Kerr rotation of 0.154° was measured. Uspenskii et al. later calculated values for the Kerr rotation which were twice as large as the experimental data in the energy range 1.5-2.5 eV. He attributed the discrepancy between theory and experiment to the sensitivity of the measurements to the film texture and microstructure. Both these factors were not included in the calculations.

1. 5. 4. Overview

Despite the widespread use of chromium dioxide as a particulate recording medium, there is little data relating to the magnetic properties of pure single crystalline films of CrO_2, and the data pertaining to powder measurements vary largely from one author to the next. The discrepancy between experiments calls for detailed magnetisation measurements of well-characterised samples in order to determine such basic magnetic properties as coercivity, Curie temperature and saturation magnetisation.

Similarly, experimental evidence regarding the transport and thermal properties of CrO_2 which may lend support to the existing theories are also severely lacking and the data that do exist again varies from one report to the next. Consequently, there is a strong need for a thorough and detailed study of the magnetotransport and thermal properties in order to ascertain the true physics of this material.

1. 6. This Work

When this research was started in 1996, very little was known about CrO_2 and the impetus for studying this material came from the original band structure calculation of Schwarz who showed that CrO_2 was a half-metallic ferromagnet and the potential application of these materials to devices operating on the basis of spin-dependent phenomena. The lack of experimental data supporting the theory has lead to a detailed study of the fundamental properties of CrO_2.

In the work presented here, CrO_2 is being studied as part of a European Community funded project called OXSEN - Oxide Spin Electronic Network. The aim of OXSEN is to explore in particular the physical properties of highly correlated 3d-band ferromagnetic oxides, mixed valence manganites, chromium dioxide and conducting ferrites with a view to applying these materials to new electronic devices. These devices will operate on the basis of the electron spin (i.e. spin-dependent transport phenomena) as opposed to the electron charge as in conventional electronics. Particular interest in chromium dioxide arose from the expectation of having a fully spin-polarised conduction band at the Fermi level (see section 1. 1 and 1.4) and it serving as a source of spin polarised electrons. Chromium dioxide also has a Curie temperature of 400 K, a value well above room temperature and higher than most of the other oxides being studied as part of the OXSEN project. These factors combined make chromium dioxide a suitable choice for use in the fabrication of spin electronic devices. Involved in the OXSEN project are 7 laboratories from 5 other European countries. Collaborations also include the MARTECH group, FSU, Tallahasee, USA; UCSD, La Jolla, California, USA, the Texas Centre for Superconductivity, UH, Texas, USA and the Naval Research Laboratory, Washington DC, USA.

In Chapter 2, the various methods for preparing CrO_2 are outlined with particular attention being paid to the method involving the thermal decomposition of a precursor which is the preparative technique most frequently used in the production of oriented thin films and powder samples of CrO_2. Their subsequent structural characterisation using diffraction and microscopy techniques is discussed. Chapters 3 and 4 describe the basic magnetic and thermal properties of CrO_2 films and powders. In chapter 5 the transport

properties are investigated and a model based on the suppression of electron-magnon scattering is proposed to explain the resistivity behaviour of half-metallic ferromagnetic CrO_2. Detailed Hall measurements and magnetoresistance data are presented for the first time. Chapter 6 is concerned with the fabrication of a magnetic tunnel junction using photolithographic techniques and its transport properties. In this chapter, experiments based on measuring directly the spin polarisation of CrO_2 using a superconducting tip in contact with the CrO_2 film surface will also be presented. These measurements are the first of their kind and the results show directly the half-metallic nature of CrO_2. Chapter 7 will conclude the work presented in this thesis and discuss the future of CrO_2 in research.

References

[1] G. Bate, J. Mag. and Mag. Mat., **100**, 413-424 (1991)

[2] D. I. Khomskii and G. A. Sawatsky, Sol. St. Commun., **102**, 87-99 (1997)

[3] K. M. Glassford, J. R. Chelikowsky, Phys. Rev. B, **46**, 1284-1298 (1992)

[4] K. M. Glassford and J. R. Chelikowsky, Phys. Rev. B, **47**, 1732-1741 (1993)

[5] J. M. D. Coey, M. Viret and S. von Molnar, Adv. Phys., **48**, 167-293 (1999)

[6] Journal of Crystallographic Powder Diffraction Files (JCPDF); number 09-332, neutron diffracton and x-ray diffraction of films and powders presented in chapter 2.

[7] International Table of Crystallography, Vol. 3

[8] P. I. Sorantin and K. Schwarz, Inorg. Chem., **31**, 567-576 (1992)

[9] S. Matar, G. Demazeau, J. Sticht, V. Eyert and J. Kübler, J. Phys. I France, **2**, 315-328 (1992)

[10] F. J. Darnell and W. H. Cloud, Colloque International du CNRS, **4**, 1164-1166 (1965)

[11] B. J. Thamer, J. Am. Chem. Soc., **79**, 547-550 (1957)

[12] J. K. Burdett, G. J. Miller, J. W. Richardson, Jr. and J. V. Smith, J. Am. Chem. Soc., **110**, 8064-8071 (1988)

[13] J. B. Goodenough, Prog. Sol. St. Chem., **5**, 235-360 (1971)

[14] J. B. Goodenough, , Phys. Rev., **117**, 1442-1451 (1960)

[15] R. Skomski and J. M. D. Coey, Permanent Magnetism, IoP (1999)

[16] K. Schwarz, J. Phys. F: Met. Phys., **16**, L211-L215 (1986)

[17] M. A. Korotin, V. I. Anisimov, D. I. Khomskii and G. A. Sawatsky, Phys. Rev. Lett., **80**, 4305-4308 (1998)

[18] E. Kulatov and I. I. Mazin, J. Phys.: Condens. Matter, **2**, 343-350 (1990)

[19] A. V. Nikolaev and B. V. Andreev, Phys. Sol. St., **35**, 603-605 (1993)

[20] H. van Leuken and R. A. de Groot, Phys. Rev. B, **51**, 7176-7177(1995)

[21] S. P. Lewis, P. B. Allen and T. Sasaki, Phys. Rev. B, **55**, 10253-10260 (1997)

[22] I. I. Mazin, D. J. Singh and C. Ambrosch-Draxl, Phys. Rev. B, **59**, 411-418 (1999)

[23] C. Zener, Phys. Rev., **82**, 403 (1951)

[24] S. Watts, S. Wirth, S. von Molnar, A. Barry and J. M. D. Coey, Phys. Rev. B (in press)

[25] P. C. Guillaued, A. Michel, J. Bénard and M. Fallot, Compt. Rend., **219**, 58 (1944)

[26] K. Siratori and S. Iida, J. Phys. Soc. Jap., **15**, 210-211 (1960)

[27] T. J. Swoboda, P. Arthur Jr., N. L. Cox, J. N. Ingraham, A. L. Oppegard and M. S. Sadler, J. Appl. Phys., **32**, 374S-375S

[28] B. L. Chamberland, Mat. Res. Bull., **2**, 827-835 (1967)

[29] J. S. Kouvel and D. S. Rodbell, Phys. Rev. Lett., **18**, 215-218 (1967) and J. Appl. Phys., **38**, 979-981 (1967)

[30] M. W. Müller, E. Schwab and R. J. Veitch, IEEE Trans. Mag., **26**, 1897-1899 (1990)

[31] K. Götz, J. Mag. And Mag. Mat., **120**, 19-24 (1990)

[32] M. P. Sharrock, IEEE Trans. Mag., 25, 4374-4389 (1989)

[33] H. Auweter, R. Feser, M. W. Müller, N. Müller, E. Schwab and R. J. Veitch, IEEE Trans. Mag. **26**, 66-68 (1990)

[34] U. Kullmann, E. Köster and B. Meyer, IEEE Trans. Mag., **20**, 742-744 (1984)

[35] D. M. Hiller, J. Appl. Phys., **49**, 1821 (1978)

[36] H. Y. Chen, IEEE Trans. Mag., **20**, 24 (1984)

[37] T. Crandall, IEEE Trans. Mag., **23**, 36 (1987)

[38] H. Auweter, IEEE Trans. Mag., 1990.

[39] W. H. Cloud, D. S. Schreiber and K. R. Babcock, J. Appl. Phys., **33**, 1193-1194 (1962)

[40] H. Brändle, D. Weller, S. S. P. Parkin, J. C. Scott, P. Fumagalli, W. Reim, R. J. Gambino and R. Ruf, Phys. Rev. B, **46**, 13889-13895 (1992)

[41] D. S. Rodbell, R. C. deVries,, W. R. Barber and R. W. deBlois, J. Phys. Soc. Jpn.,**38**, 4542-4543 (1967)

[42] D. S. Rodbell, J. Phys. Soc. Jpn., **21**, 1224-1225 (1966)

[43] D. S. Chapin, J. A. Kafalas and J. M. Honig, J. Am. Chem. Soc., **69**, 1402-1409 (1965)

[44] D. S. Rodbell, J. Phys. Soc. Jpn., **21**, 2430 (1966)

[45] K. Suzuki and P. M. Tedrow, Phys. Rev. B, **58**, 11597-11602 (1998)

[46] H. Y. Hwang and S. –W. Cheong, Science, **278**, 1607-1609 (1997)

[47] J. M. D. Coey, A. E. Berkowitz, Ll. Balcells, F. F. Putris and A. Barry, Phys. Rev. Lett., **80**, 3815-3818 (1998)

[48] L. Ranno, A. Barry, J. M. D. Coey, J. Appl. Phys., **81**, 5774-5776 (1997)

[49] X. W. Li, A. Gupta, T. R. McGuire, P. R. Duncombe and G. Xiao, J. Appl.Phys., **85**, 5585-5587 (1999)

[50] T. Tsujioka, T. Mizokawa, J. Okamoto, A. Fujimori, M. Nohara, H. Takagi, K. Yamaura and M. Takano, Phys. Rev. B, **56**, 509-512 (1997)

[51] M. A. K. L. Dissanayake and L. L. Chase, Phys. Rev. B, **18**, 6872-6879 (1978)

[52] M. A. K. L. Dissanayake and L. L. Chase, Phys. Rev. B., **23**, 6254 - 6258 (1981)

[53] Y. A. Uspenskii, E. T. Kulatov, S. V. Halihov, Phys. Rev. B, 54 474-482 (1996)

[54] K. P. Kämper, W. Schmitt, G. Güntherodt, R. J. Gambino and R. Ruf, **59**, 2788-2791 (1987)

[55] R. Wiesendanger, H. -J. Güntherodt, G. Güntherodt, R. J. Gambino and R. Ruf, Phys. Rev. Lett., **65**, 247-250 (1990); AIP Conference Proceedings, **241**, 504-510 (1991)

[56] A. M. Stoffel, J. Appl. Phys., **40**, 1238-1239 (1969)

Chapter 2

Sample Preparation and Characterisation

"F = what?"

Johnny Coleman when discussing the effects of alcohol on the brain one sunny afternoon in the summer of '96.

2. 1. Sample Preparation

Chromium dioxide, CrO_2, can be prepared by several methods. The most common methods involve thermally decomposing a precursor in a closed reactor vessel at a particular temperature and pressure. Films can then be prepared by exposing a suitable substrate to either the melt or the vapour of the decomposing precursor. A general review by Chamberland describes the thermal decomposition of the most frequently used precursors and are categorised into four classes:[1]

(1) Thermal decomposition of CrO_3 and mixed chromium oxides

(2) Thermal decomposition of CrO_2Cl_2

(3) Hydrothermal methods

(4) Oxidation of CrO(OH) and $Cr(OH)_3$

In this section the methods listed above will be discussed as well as some of the more recent techniques such as laser-induced and plasma-assisted deposition, electrochemical deposition and the deposition of CrO_2 by a technique which utilises the thermodynamic sink of CrO_2.

2. 1. 1. Thermal decomposition of CrO_3 and mixed chromium oxides

The thermal decomposition of CrO_3 is the simplest and most frequently used method for preparing thin film, powder and single crystalline samples of CrO_2. There are many variations to the method. The simplest method involves the decomposition of CrO_3 in a

closed reactor vessel under high pressure. CrO_3 decomposes on heating by releasing oxygen:

$$CrO_3 \rightarrow CrO_2 + 1/2O_2 \uparrow \qquad 2.1$$

This release of oxygen is often enough to provide the high pressure required to drive the reaction to completion providing that the oxygen pressure is maintained during decomposition.[2] Several authors have reported the thermal decomposition of CrO_3 to its stable oxidation state, Cr_2O_3, via several intermediate phases.[3, 4, 5] At low pressure and temperature these intermediate phases were isolated and the following reaction sequence determined:[3, 4]

$$CrO_3 \rightarrow Cr_3O_8 \rightarrow Cr_2O_5 \rightarrow CrO_2 \rightarrow Cr_2O_3 \qquad 2.2$$

By varying the oxygen pressure in the reactor vessel - either by increasing the amount of CrO_3 in the sample space or by externally supplying an oxygen pressure - it was observed that the transitions from CrO_3 to Cr_3O_8 and Cr_3O_8 to Cr_2O_5 depended only on temperature whilst the transition from CrO_2 to Cr_2O_3 depended on both temperature and pressure. This is illustrated in the pressure-temperature diagram in Fig. 2. 1, which shows that at atmospheric pressure CrO_3 starts decomposing at 220°C, Cr_3O_8 at 280°C, Cr_2O_5 at 370°C and CrO_2 at 450°C.

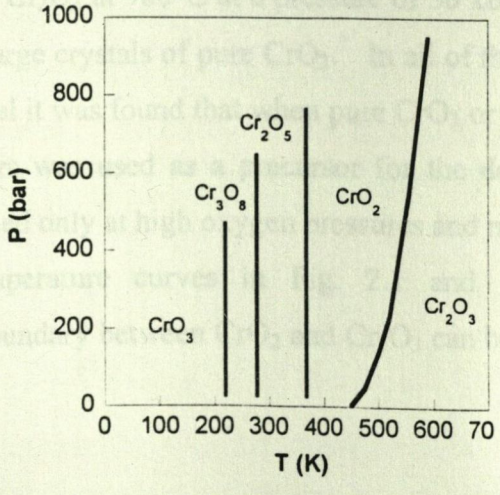

Fig. 2. 1. Pressure-temperature diagram for the chromium oxide system showing the stability regions for intermediate phases during the decomposition of CrO_3 to Cr_2O_3 at low pressure.[3]

While the pressure-temperature diagram of figure 2.1, would suggest it possible to obtain CrO_2 at 400°C and 1 bar of oxygen, in general, pure CrO_2 can only be obtained at higher oxygen pressures using this method.

Mixtures of CrO_3 + CrO_2 and CrO_3 + Cr_2O_3 have also been used as precursors for the decomposition reaction:

$$CrO_3 + CrO_2 \xrightarrow{\Delta, P(O_2)} 2CrO_2 + 1/2\,O_2 \qquad 2.3$$

$$CrO_3 + Cr_2O_3 \xrightarrow{\Delta, P(O_2)} 3CrO_2 \qquad 2.4$$

In these experiments it was found that pure CrO_2 could only be obtained at very high pressures. In an experiment by Wilhelmi, pure CrO_2 was prepared from 80 % CrO_3 + 20% CrO_2 or equimolar mixtures of CrO_3 + CrO_2 under 2000 bars of oxygen at 250°C.[6] In this experiment it was found that for pressures in excess of 1000 bars Cr_6O_{15} and Cr_5O_{12} were formed as by-products of the decomposition reaction in the temperature regions 210-230°C and 230-240°C respectively. At pressures below 1000 bar the reaction followed the sequence set out in equation 2.2 in accordance with the low pressure-low temperature diagram shown in Fig. 2.2.[6] The dashed lines in figure 2.2 are estimates of the phase boundaries between the various intermediate oxides at pressures below 200 bar. Again it should be mentioned that whilst the diagram suggests the presence of CrO_2 at low temperature and pressure, pure CrO_2 is only obtained at higher pressures. Another experiment by Porta et al., treated an equimolar mixture of CrO_3 and Cr_2O_3 at 900°C at a pressure of 36 kbar of oxygen which resulted in the formation of large crystals of pure CrO_2.[7] In all of the experiments carried out in a closed reactor vessel it was found that when pure CrO_3 or mixtures of CrO_3 with other lower oxide members was used as a precursor for the decomposition reaction, pure CrO_2 could be obtained only at high oxygen pressures and moderate temperatures.

The pressure-temperature curves in Fig. 2.1 and Fig. 2.2. representing the equilibrium phase boundary between CrO_2 and Cr_2O_3 can be described by the following formula:[8]

$$\log P(O_2) = C - 2\frac{\Delta H}{RT} \qquad 2.5$$

where $P(O_2)$ is the oxygen pressure, C is a constant, ΔH = 111.3 kJ/mole is the heat of decomposition for the reaction $CrO_2 \rightarrow Cr_2O_3 + 1/2O_2$, R is the gas constant and T is the absolute temperature.[3]

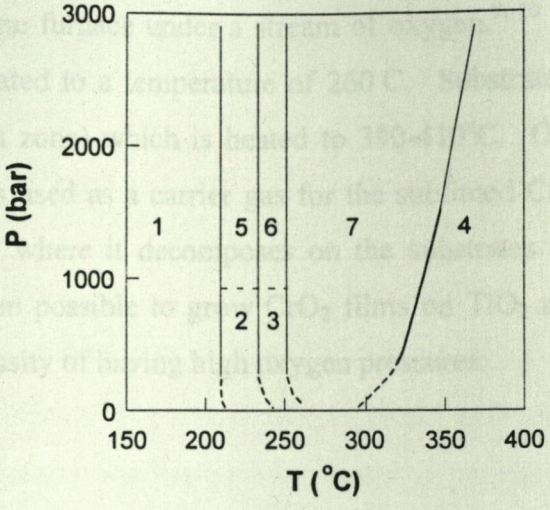

Fig. 2. 2. Pressure-temperature diagram for the chromium oxide system at elevated oxygen pressures.[6]
1=CrO_3/Cr_2O_3, 2=Cr_3O_8, 3=Cr_2O_5, 4=Cr_2O_3, 5=Cr_6O_{15}, 6=Cr_5O_{12}, 7=CrO_2

In addition to temperature and pressure, the reaction time may also be a critical factor in the isolation of a particular intermediate phase.[3, 6] In particular, CrO_2 starts to decompose after some interval of time known as the induction period when heated in air to its decomposition temperature. The induction period decreases with increasing decomposition temperature. The initial stage of decomposition of CrO_2 is governed by a linear law:

$$\Delta W = k \cdot t \qquad 2.6$$

where ΔW is the weight loss (%), k the rate constant and t the time in minutes. The rate constant, k, is expressed by the Arrhenius equation:

$$k = A \exp(-\frac{E_a}{RT}) \qquad 2.7$$

and A is a constant, E_a is the activation energy and is equal to 258.2 kJ and 201.7 kJ for the decompostion of Cr_2O_5 and CrO_2 to Cr_2O_3 in air respectively, R is the gas constant and T is the absolute temperature.[3]

A recent development in this method for producing CrO_2 involves decomposing CrO_3 in a two zone furnace under a stream of oxygen.[9, 10] CrO_3 is placed in the first zone which is heated to a temperature of 260 C. Substrates are placed in the second zone (the reaction zone) which is heated to 390-410°C. Oxygen flowing at a rate of 100 cm^3/minute is used as a carrier gas for the sublimed CrO_3 which is transported to the reaction zone where it decomposes on the substrates to form CrO_2. Using this method it has been possible to grow CrO_2 films on TiO_2 and Al_2O_3 substrates whilst avoiding the necessity of having high oxygen pressures.

2. 1. 2. Thermal decomposition of CrO_2Cl_2

The thermal decomposition of CrO_2Cl_2 also yields magnetic CrO_2 providing the temperature is below 400 °C at low pressures.[11, 12] The reaction is usually carried out between 360°C and 400°C in oxidising or inert atmospheres e.g. O_2, N_2 or Cl_2. A typical reaction is given by:

$$CrO_2Cl_2 \xrightarrow{O_2,\Delta} CrO_2 + Cl_2 \qquad 2.8$$

Early experiments revealed that pure CrO_2 could not be obtained by this reaction and the product formed often contained a second phase which was non-magnetic. However, pure CrO_2 was obtained when CrO_2Cl_2 was thermally decomposed in an evacuated silica tube onto oriented Al_2O_3 substrates at 380°C.[12] The substrate was found to enhance nucleation and growth of CrO_2, and the resulting films were magnetic and highly textured. The solid residue from the silica tube was analysed and identified as Cr_2O_5. Decomposition of CrO_2Cl_2 onto TiO_2 discs in a H-shaped Pyrex system under

12-25 bars of oxygen also yielded pure CrO_2.[1] In this experiment, the oxygen pressure was generated by the decomposition of CrO_3 in one leg of the apparatus prior to the decomposition of the CrO_2Cl_2 at 370 °C.

As well as the thermal decomposition of CrO_2Cl_2, the photochemical decomposition of CrO_2Cl_2 has been studied as a means of producing CrO_2.[13, 14] In the work carried out by Halonbrenner et al., CrO_2Cl_2 was shown to photolytically* decompose under UV lamp excitation at wavelengths below 420 nm. The decomposition took place by the sequential elimination of the two Cl atoms due to the absorption of one or two photons of energy hυ:[13]

$$CrO_2Cl_2 \xrightarrow{h\upsilon} CrO_2Cl + Cl \rightarrow CrO_2 + Cl + Cl \qquad 2.9$$

Arnone et al. used an Ar-ion laser focused to a 5 μm diameter spot and operating at wavelengths between 488-515 nm to induce the photochemical deposition of chromium oxide.[14] At low laser power the deposition was by photolysis of the absorbed CrO_2Cl_2 molecules. Higher laser powers initiated photochemical deposition and drove it with a combined photolytic/pyrolytic reaction.

2. 1. 3. Hydrothermal methods

The thermal decomposition of CrO_3 in the presence of water was first reported by Thamer et al. in 1957.[15] CrO_3 reacts in water to form aqueous chromic acid, H_2CrO_4 which decomposes on heating according to the following relation:

$$H_2CrO_4 \xrightarrow{\Delta} CrO_2 + + H_2O + 1/2\,O_2 \qquad 2.10$$

* A photolytic reaction refers to a chemical reaction or decomposition produced by exposure to light or UV radiation. A pyrolytic reaction refers to a chemical reaction or decomposition produced due to the action of heat.

It was observed that in a closed container chromic acid solutions evolved oxygen at an appreciable rate at 300°C and 325°C and at pressures between 50 and 200 bars. Under these conditions it was possible to obtain pure black crystals of CrO_2. Swoboda et al. also reported on the decomposition of CrO_3 in the presence of equimolar amounts of water at temperatures between 400-525°C and pressures between 500-3000 bars.[16] CrO_2 was found to be stable up to 525°C but at this temperature pressures as high as 3000 bar were required to prevent the dioxide from decomposing further to Cr_2O_3. The hydrothermal reaction of CrO_3 mixed with Cr_2O_3 at 900 °C and at pressures in excess of 30 kbar also formed large crystals (3-10 μm) of CrO_2:[17]

$$CrO_3 + Cr_2O_3 \xrightarrow{\Delta, P(O_2), H_2O} 3CrO_2 + H_2O \qquad 2.11$$

The oxidation of Cr_2O_3 with excess CrO_3 under hydrothermal conditions is now the procedure adotped for producing commercially CrO_2 for magnetic recording tapes. In a paper by Chen et al, the reaction sequence for commercially producing CrO_2 is described as a two step process.[18] The first step in the reaction sequence, carried out a temperature of 350°C and a pressure of 440 bar, is the same as that set out in equation 2.11. The second step in the reaction sequence is the decomposition of the excess CrO_3 in the presence of water:

$$CrO_3 \xrightarrow{350^\circ C, 440 bar, H_2O} CrO_2 + 1/2O_2 \qquad 2.12$$

The decomposition of the excess CrO_3 provided the oxygen pressure required to stabilize the formation of the CrO_2 crystals. The result was the production of high purity, single domain acicular CrO_2 crystals of uniform distribution. Chemical modifiers such as Sb_2O_3 and Fe_2O_3 are often used to enhance the acicular shape of these particles.[18, 19] Antimony was found to increase crystal nucleation and promote acicular particle growth. Fe_2O_3 was also found to promote acicular growth, however, Fe^{3+} ions were also found to substitute Cr^{4+} in the rutile lattice causing an increase of the magnetocrystalline anisotropy and the Curie temperature. Ir was also used as a dopant for improving the crystal quality and the magnetic properties of CrO_2 particles. However, due to the high cost of Ir, Sb_2O_3 and Fe_2O_3 are the preferred dopants.

The decomposition of dilute solutions of KCr_3O_8 at 250 °C and 3000 bar also yield pure CrO_2.[1] KCr_3O_8 is prepared by the reaction of KCr_2O_7 and CrO_3.[20] KCr_3O_8 then decomposes on heating as follows:

$$2MCr_3O_8 \xrightarrow{\Delta, P(O_2), H_2O} 5CrO_2 + MCrO_4 + O_2 \qquad 2.13$$

where M is any of the alkali earth metals.

2. 1. 4. Oxidation of $Cr(OH)_3$and CrOOH

The oxidation of $Cr(OH)_3$ and CrOOH in a closed reactor vessel under high oxygen pressure was studied by Shibasaki et al.[21] When dry $Cr(OH)_3$ was used, CrO_2 crystallised at a temperature of 380°C in an oxygen atmosphere of 80 bar and at 600°C and 1500 bar of oxygen. The crystals formed under the latter conditions were found to be equiaxed and at high temperature and pressure tended to be of the order of 40 μm in size compared to 1-3 μm at the lower temperature and pressure. Below 350°C the reaction proceeded with water being evaporated from the $Cr(OH)_3$ producing rhombohedral-type CrOOH:

$$Cr(OH)_3 \xrightarrow{\Delta} CrOOH + H_2O \qquad 2.14$$

CrOOH was found to be stable against oxidation under hydrothermal conditions below 350°C and H_2CrO_4, which readily decomposes to CrO_2 under an oxygen pressure was not formed at these temperatures. Above 350°C, CrO_2 was formed by the combined oxidation and dehydration of CrOOH:

$$4CrOOH + O_2 \xrightarrow{\Delta} 4CrO_2 + 2H_2O \qquad 2.15$$

Figure 2.3 shows the pressure-temperature diagram for this reaction.

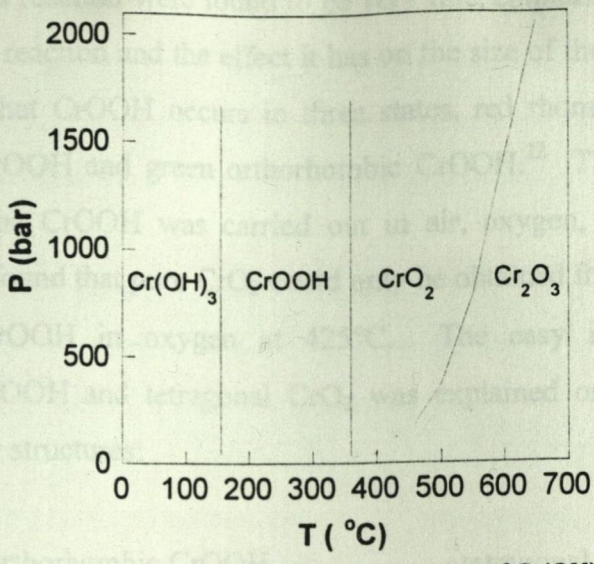

Fig. 2. 3. Phase diagram for the decomposition of $Cr(OH)_3$ to CrO_2.[21]

Wet $Cr(OH)_3$ was also found to be a good starting material. In this case, the $Cr(OH)_3$ reacted with water to give a chromic acid solution:

$$4Cr(OH)_3 + nH_2O + 3O_2 \rightarrow 4H_2CrO_4 + (2+n)H_2O \qquad 2.16$$

It was thought that water acted as a catalyst for this oxidation process i.e. Cr^{3+} to Cr^{6+}. When the chromic acid solution was heated, a two step process took place. First the water evaporated from the solution of chromic acid and then the chromic acid thermally decomposed to produce CrO_2 in manner like that set out in equation 2.10, in which Cr is reduced from 6+ to 4+. In this case, crystals of CrO_2, 60 x 40 x 40 μm^3 in dimension, were found to crystallise at 450°C and at an oxygen pressure of 1700 bar. The reason for such large crystal growth was not explained. It was found that the rate of crystal growth varied if the rate of the reaction of equation 2.16 was controlled by the change in oxygen pressure at low temperature. It was concluded that the presence of water and an oxygen pressure both accelerated this reaction and affected the size and shape of the CrO_2 crystals.

When rhombohedral CrOOH was used as the starting material, CrO_2 was obtained in the same temperature and oxygen pressure ranges as for dry $Cr(OH)_3$. The reaction that took place was the same as that set out in equation 2.15. However, the crystals which

resulted from this reaction were found to be very fine, emphasising the role of water as a catalyst for the reaction and the effect it has on the size of the crystals. Alario Franco et al., reported that CrOOH occurs in three states, red rhombohedral CrOOH, green boehmite-like CrOOH and green orthorhombic CrOOH.[22] The decomposition of the orthorhombic type CrOOH was carried out in air, oxygen, nitrogen, hydrogen and vacuum. It was found that pure CrO_2 could only be obtained from the decomposition of orthorhombic CrOOH in oxygen at 425°C. The easy interconversion between orthorhombic CrOOH and tetragonal CrO_2 was explained on the basis of the close similarity of their structures:

orthorhombic CrOOH	tetragonal CrO_2
a = 4.861 Å	a = 4.421 Å
b = 4.292 Å	
c = 2.960 Å	c = 2.918 Å
$\rho = 4500$ kg m^{-3}	$\rho = 4922$ kg m^{-3}

2. 1. 5. Other methods

Other than the methods described above, which generally involve the thermal decomposition of some precursor under various temperature and pressure conditions, several other techniques can be used to prepare CrO_2 samples.

A recent paper by Chen et al. describes an elegant method of producing CrO_2/Co multilayers on Cu (100) by a technique that utilises the thermodynamic sink of CrO_2.[23] This method involves depositing 4 layers of Co onto Cu (100) and exposing the Co to oxygen such that the oxidation reaction: $Co + O \rightarrow CoO$ occurred at the surface of the film. Approximately half a layer of Cr was then deposited on this structure. The Gibbs free energy[†] for the oxidation reaction $Cr + 2O \rightarrow CrO_2$ is energetically more favourable than for the reaction $Co + O \rightarrow CoO$. Thus, the deposited Cr reduces to

[†] The Gibbs free energy, G, refers to the amount of energy required to cause change in a particular system. It is defined by G = H – TS where H is the enthalpy, i.e. the amount of energy of the system stored as heat, T is the temperature of the system and S is the entropy or the degree of disorder in a system.

CoO to form CrO_2. That CrO_2 was formed was confirmed by measuring the magnetic hysteresis loops of the structure using the magneto-optical Kerr effect. As more Cr layers are deposited, eventually Cr_2O_3 is formed due to the limited amount of oxygen available for the oxidation of the Cr layer. For this reason, it is only possible to make thin layers of CrO_2 using this technique.

Laser-induced and plasma-induced deposition techniques based on photolytic and pyrolytic reactions of gaseous precursors such as CrO_2Cl_2 (see section 2.1.2) and $Cr(CO)_6$ provide additional routes for preparing CrO_2. The laser-induced photolytic decomposition of $Cr(CO)_6$ has been studied by several authors the most complete of these studies being given by Perkins et al.[24, 25, 26] In this case, a nitrogen laser operating at 337 nm was used to decompose $Cr(CO)_6$ in an oxygen carrier gas onto water cooled Si substrates. The decomposition of $Cr(CO)_6$ is by the sequential removal of (CO) groups:

$$Cr(CO)_6 \xrightarrow{O_2} CrO_2 + 6CO \qquad 2.17$$

Cr_2O_3 films were deposited using an oxygen pressure of 1.3×10^{-6} bar and 1.3×10^{-5} bar of $Cr(CO)_6$. CrO_2 could be deposited in significantly higher oxygen pressures of 2×10^{-5} bar and 1.3×10^{-6} bar of $Cr(CO)_6$.

The plasma-induced deposition of $Cr(CO)_6$ onto Si substrates held at a temperature of 242°C was carried out using a 13.56 MHz rf plasma operating at 10W.[25, 26] The oxygen pressure for preparing CrO_2 films was greater than 2×10^{-5} bar and the $Cr(CO)_6$ pressure was 1.3×10^{-5} bar. Again, Cr_2O_3 films could be prepared by reducing the oxygen pressure.

The films prepared by laser-induced and plasma-assisted methods were in general analysed using Auger spectroscopy and the magneto-optical Kerr effect and, where CrO_2 growth was expected, were found to be ferromagnetic. However, the exact degree of crystallisation of the CrO_2 films was never clearly stated.

Fousse et al. describe the electrochemical behaviour of CrO_2 in a neutral solution of NaH_2PO_4 at 25 °C using cyclic voltammetry. In this experiment platinum and chromium coated steel electrodes were used and samples were prepared from pressed CrO_2 powder on a soft platinum substrate. The cyclic voltammograms showed two

regions in which oxygen evolved. It was claimed that this corresponded to a two step process which they summarised as follows:

$$CrO_2 \rightarrow Cr_2O_3 \qquad 2.18$$

$$Cr_2O_3 \rightarrow CrO_2 \rightarrow CrO_3 \qquad 2.19$$

The first step involved the irreversible reduction of CrO_2 to Cr_2O_3. The second step involved the reversible oxido-reduction of the as formed Cr_2O_3. Evidence for the formation of CrO_2 was not presented. Furthermore, these results are in conflict with those of Beverskog et al. who calculated the Pourbaix diagrams (potential-pH diagrams) for chromium in the range 25-300°C.[27] In this well documented paper it was concluded that Cr_2O_3 was the only stable chromium oxide in aqueous solution in this temperature range. This is consistent with the generally accepted idea that Cr^{4+} is not stable in aqueous solution.

2. 2. Sample Preparation in this Work

As can be seen from the sections described above, there are many various roots for preparing CrO_2. The most reliable methods for producing pure CrO_2 samples involve the thermal decompostion of a precursor under high oxygen pressure. Of these precursors, CrO_3 is the most favourable as it decomposes by releasing oxygen to produce CrO_2 in a closed container. This is a simple, effective, low cost technique with excellent results for producing pure CrO_2 samples. CrO_2Cl_2 on the other hand decomposes by releasing harmful Cl_2 gas, whilst the decomposition of precursors such as $Cr(OH)_3$ and CrOOH run the risk of forming CrO_2 which may be contaminated with OH ions. Hydrothermal techniques, whilst extremely successful in producing pure CrO_2 on a commercial scale may also run the risk of producing (OH) contaminated CrO_2 samples.

The production of CrO_2/Co multilayers by utilising the heat sink of CrO_2 is very attractive from the point of view of multilayer device applications. However as

mentioned, the thickness of the CrO_2 is limited by the amount of oxygen available in the CoO layer. Furthermore, for measuring the transport properties of CrO_2, Co is not a good choice of substrate since it is metallic. Laser- and plasma-induced techniques for producing CrO_2 require cumbersome and expensive experimental set-ups. Furthermore, the films produced by these methods are of much poorer quality compared to those produced by thermal decomposition of a precursor. Electrochemical deposition is a quick and easy method of film deposition. Unfortunately, attempts to produce CrO_2 films using this method have failed with Cr_2O_3 forming the only stable chromium oxide in aqueous solution.

In this study, the procedure of thermally decomposing CrO_3 in a closed reactor vessel was adopted to successfully grow well-oriented films of CrO_2. The starting material, CrO_3, was slowly heated at a rate of 0.5°C/minute up to a temperature of 420-425°C. The material was left to decompose at this temperature over a period of 60 minutes. Films of CrO_2 were grown by exposing oriented TiO_2 (or Al_2O_3) substrates to the CrO_3 melt (the melting temperature, T_m, of CrO_3 is 196°C). As mentioned in section 2.1.1, to produce pure CrO_2 it is vital that the high oxygen pressure is maintained during the decomposition of CrO_3 to CrO_2. This was achieved by placing an aluminium gasket around the sample reaction space in the reactor vessel. On closing the reactor vessel the aluminium ring was compressed to form a tight seal, Fig. 2. 4. In this way, it was possible to attain oxygen pressures of up to 800 bar for a sample space of volume 10^{-8} m^3.

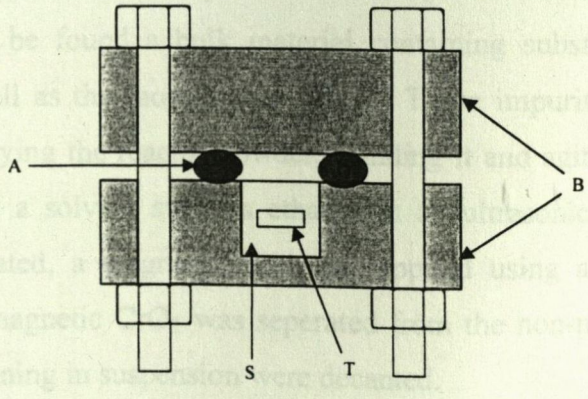

Fig. 2. 4. (B) High – pressure bomb. (S) starting material CrO_3, (T) substrate, (A) Al ring seal

After decomposition, the resulting film was removed from the reactor vessel by digging away the matrix CrO_2 that had formed around the substrate in the reactor vessel. Films of CrO_2 were found to grow most successfully on rutile (TiO_2) which has the same crystal structure and similar lattice parameters (a = 4.593 Å, c = 2.959 Å) as CrO_2. Films grown on TiO_2 substrates with their c-axis in-plane (e.g. (100) and (110) oriented films) are black in colour, highly reflecting and show a high degree of purity and texture. Films grown on TiO_2 substrates having their c-axis out-of-plane i.e. (001) oriented films are grey in colour, non-reflecting but also show a high degree of purity and texture. Under these conditions, CrO_2 grows in needle-like grains, the grain-axis lying along the c-direction. As a result, films with their c-axis in-plane contain needles of CrO_2 in the plane of the film making them quite smooth and therefore reflecting. On the other hand, films with the needle-axis lying out-of-plane are similar in effect to the New York skyline (see section 2.4). As a result, a (001) oriented film is not as smooth and hence not as reflecting.

The powder produced as a by-product of the decomposition reaction (in addition to the film) usually contains small amounts of impurities. These have been identified as the intermediate phases of the decomposition reaction of equation 2.2. The fact that not all the CrO_3 decomposes to CrO_2 can be explained as follows. During the melting of CrO_3 the oxygen which is released moves to the surface as large bubbles. As the decomposition reaction proceeds, the melt becomes increasingly viscous due to the formation of the solid intermediate phases Cr_3O_8 and Cr_2O_5. As a result of this increased viscosity, the diffusion of oxygen through the decomposing material becomes slower. The result is the formation of a pure film of CrO_2 at the surface of the substrate, underneath which may be found a bulk material containing substantial amounts of Cr_3O_8 and Cr_2O_5 as well as the more stable Cr_2O_3. These impurities were removed from the powders by drying the reactor powder, grinding it and agitating a mixture of the reactor powder and a solvent such as ethanol in an ultrasonic bath. When the mixture was fully agitated, a magnetic field was applied using a small permanent magnet. In this way, magnetic CrO_2 was seperated from the non-magnetic impurites and the impurities remaining in suspension were decanted.

In order to get some indication of the required decomposition temperature, thermopiezic analysis (TPA) was used to monitor the decomposition of CrO_3.[28] TPA curves were measured using typically 10 mg of CrO_3 powder. TPA gives quantitative results about the decomposition temperature and the oxygen released during

decomposition for pressures below 2 bar, as shown in Fig. 2.3. CrO_3 is found to start decomposing at 250°C in vacuum. At 375°C CrO_2 is formed and remains stable up to 435°C. However it should be noted that at this low pressure, there may already exist traces of Cr_2O_3 (stable oxidation state of chromium) and remnant traces of Cr_2O_5. If the heating is stopped here the pressure continues to rise emphasising the role of kinetics in this temperature range and the fact that slow heating rates (e.g. 0.5°C/min) are required to avoid decomposing CrO_2 further once it has formed. Above 500°C the reduction is complete and pure Cr_2O_3 is obtained. These measurements enabled selection of the narrow band of temperatures in which to work in order to prepare CrO_2.

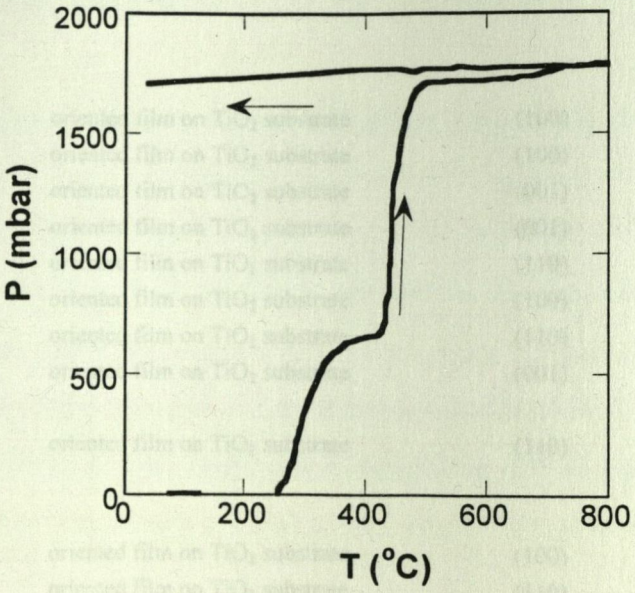

Fig. 2. 5. TPA curve monitoring the decomposition of CrO_3 to CrO_2

Table 2. 1. List of samples used in the work presented in this thesis. Shown is the sample label, type, orientation and indication of what the various samples were used for.

Sample Label	Type	Orientation	Use
F3	oriented film on TiO_2 substrate	(100)	Low-T R(T)
F11	oriented film on TiO_2 substrate	(100)	M(T)
F15	oriented film on TiO_2 substrate	(001)	Low-T R(T)
F17	oriented film on TiO_2 substrate	(110)	Low-T R(T)
F31	oriented film on TiO_2 substrate	(100)	AFM
F40	oriented film on TiO_2 substrate	(001)	AFM
F49	oriented film on TiO_2 substrate	(110)	AFM
			MR(H)
			Hall
F50	oriented film on TiO_2 substrate	(110)	XRD
			Raman
F51	oriented film on TiO_2 substrate	(001)	XRD
			AFM
			Optical
			Raman
F52	oriented film on TiO_2 substrate	(100)	XRD
F54	oriented film on TiO_2 substrate	(100)	Optical
F55	oriented film on TiO_2 substrate	(001)	MR(H)
F56	oriented film on TiO_2 substrate	(001)	High-T R(T)
F61	oriented film on TiO_2 substrate	(110)	High-T R(T)
F62	oriented film on TiO_2 substrate	(100)	High-T R(T)
F71	oriented film on TiO_2 substrate	(110)	Andreev Reflection
F85	oriented film on TiO_2 substrate	(001)	Rocking curve
			M(H)
F86	oriented film on TiO_2 substrate	(110)	Rocking curve
			M(T)
			M(H)
F87	oriented film on TiO_2 substrate	(100)	Rocking curve
F90	oriented film on TiO_2 substrate	(110)	Magnetic Tunnel junction
B9	unfiltered reactor powder		SEM
B49	filtered reactor powder		XRD
B58	filtered reactor powder		M(T)
			M(H)
B85	unfiltered reactor powder		$\chi_{ac}(T)$
B87	filtered reactor powder		$\chi_{ac}(T)$
B88	filtered reactor powder		XRD
			M(T)
B1503	commercial powder		SEM
			$\chi_{ac}(T)$
B1507	commercial powder		M(T)
			c(T)
Bnew	commercial powder		Neutrons
			R(T)
			M(H)
			MR(H)
			R(T)

2. 3. Sample Characterisation

Below is given a brief description of the various techniques used to characterise the structure, composition and morphology of samples prepared by the thermal decomposition of CrO_3.

2. 3. 1. Structural Characterisation

2. 3. 1. 1. X-Ray Diffraction

For the structural characterisation and phase identification of oriented films and powders of CrO_2, x-ray diffraction patterns were measured using a Siemens 500 Diffractometer equipped with a copper anode (K_α radiation λ=1.5418 Å) operating in the θ-2θ geometry, Fig. 2.4. In this configuration, the sample is rotated through an angle θ while the detector is rotated through an angle 2θ about an axis in the plane of the sample. The diffractometer is controlled by a MicroVAX system which provides data analysis facilities as well as on-line access to the JCPDS catalogue, enabling phase identification, lattice parameter refinement and analysis of peak shape.

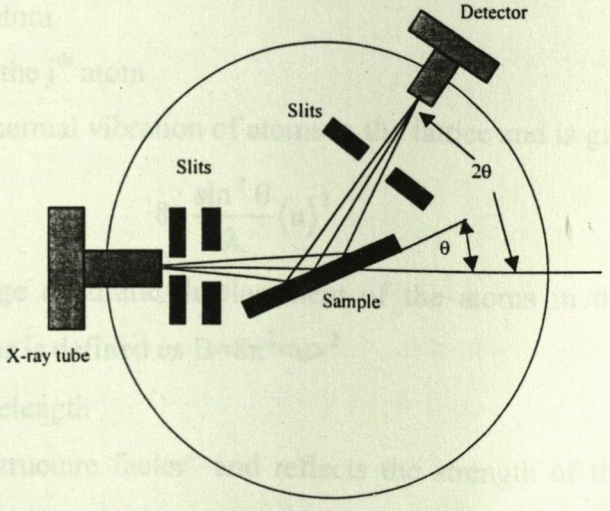

Fig. 2. 6. Schematic diagram of the θ-2θ geometry for X-ray diffraction

The θ-2θ geometry is most often employed to characterise polycrystalline powder samples. However, it also proves very useful in the analysis of well-oriented films.

A diffraction pattern is observed when the path difference between waves diffracted from a set of crystal planes defined by Miller indices (hkl), and separated by a distance d, is an integral number of X-ray wavelengths, nλ. This leads to the Bragg condition:

$$n\lambda = 2d\sin\theta \qquad 2.20$$

The diffracted beam intensity is proportional to the square of the "*structure factor*" F(hkl). F(hkl) represents the relationship between the amplitude of the wave diffracted by all the atoms in the cell to the amplitude of a wave diffracted by an electron.

$$F(hkl) = \sum_j f_j \exp(-2\pi i(\vec{k}\cdot\vec{r}_j) - W_j) \qquad 2.21$$

and

$$I(hkl) \propto |F(hkl)|^2 \qquad 2.22$$

where:

- j represents the jth atom
- r_j is the position of the jth atom
- W_j represents the thermal vibration of atoms in the lattice and is given by:

$$8\pi\frac{\sin^2\theta}{\lambda}\langle u\rangle^2$$

- $\langle u\rangle^2$ is the average quadratic displacement of the atoms in the unit cell and the Debye-Waller factor is defined as $B=8\pi^2\langle u\rangle^2$
- λ is the X-ray wavelength
- f_j is the "atomic structure factor" and reflects the strength of the interaction of the radiation with the atom.

Oriented films measured using the θ-2θ geometry show diffraction peaks corresponding to crystal planes coplanar with the sample plane. However, whilst X-ray diffraction patterns of films measured in this mode provide a good indication as to the degree of crystallographic texture normal to the sample plane, they gives no information about the in-plane texture of the film or whether the film is truly epitaxial. For this reason, rocking curves and X-ray diffraction patterns at grazing incidence were measured. When measuring rocking curves, one rotates or *rocks* the sample through a very small angular range, $\theta_B \pm \varepsilon$, bringing the lattice planes in and out of the Bragg condition. The detector is kept fixed at the position $2\theta_B$. In this way it is possible to measure the extent in which the in-plane texture deviates from epitaxy, as shown in Fig. 2. 7.

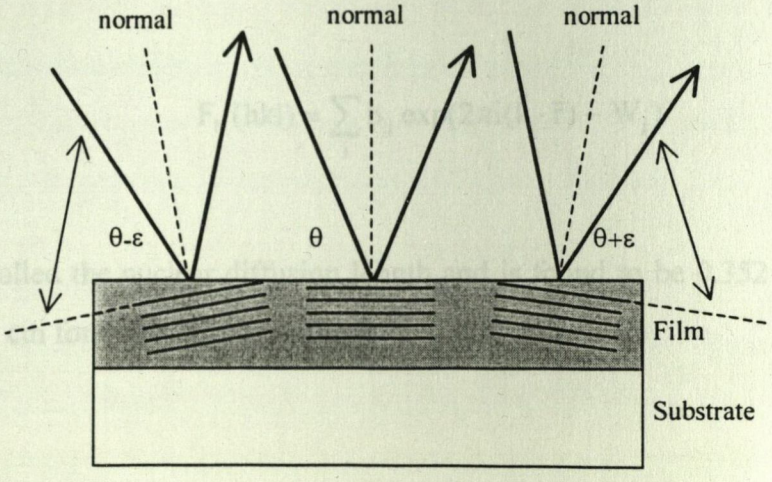

Fig. 2. 7. Rocking curve technique: measures deviation from epitaxy

2. 3. 1. 2. Neutron Diffraction

Due to the wave nature of neutrons they can be diffracted by crystalline materials provided that their wavelength λ_n is comparable to the inter-atomic spacing in crystals. The wavelength of the neutrons is given by the de Broglie equation, $\lambda_n = h/p$ where h is Planck's constant and p is the momentum of the neutron given by $p = (3M_nkT)^{1/2}$, if the neutrons are in thermal equilibrium, and M_n is the mass of the neutron. A beam of neutrons interacts with a material in two ways:

(i) incoming neutrons are scattered by the nuclei of the host atoms → *nuclear diffraction*

(ii) incoming neutrons are scattered by atoms having a permanent electronic dipole moment → *magnetic diffraction*

(i) Nuclear Diffraction

When a beam of neutrons is diffracted from a plane defined by Miller indices (hkl), the diffracted beam has an intensity proportional to the square of the *nuclear* structure factor $F_N(hkl)$. $F_N(hkl)$ is defined as the ratio of the amplitude of the wave diffracted by all the atoms in the unit cell to that diffracted by a nucleus. It is given by:

$$F_N(hkl) = \sum_j b_j \exp(2\pi i(\vec{k} \cdot \vec{r}) - W_j) \qquad 2.23$$

where b_j is called the nuclear diffusion length and is found to be 0.352×10^{-12} cm and 0.577×10^{-12} cm for Cr and O respectively.[29]

(ii) Magnetic Diffraction

Although neutrons are electrically neutral particles, they possess a nuclear spin and hence a dipole moment. Magnetic diffraction results from the dipole-dipole interaction of the magnetic moment of the neutron with the electronic moment of the magnetic atoms in the lattice. The diffracted intensity due to this interaction is proportional to the square of the *magnetic* structure factor $F_M(hkl)$ and is written:

$$F_M(hkl) = \sum_j p_j \exp(2\pi i(\vec{k} \cdot \vec{r}) - W_j) \qquad 2.24$$

where p_j is the amplitude of the wave scattered by the jth magnetic atom and is given by:

$$p_j = \left(\frac{e^2\gamma}{2mc^2}\right) g\bar{J}f_M \qquad 2.25$$

with

- e the charge of the electron
- γ the magnetic moment of the neutron
- m mass of an electron
- g Landé g-factor and (g=1.913 for neutrons)
- $\bar{J}$ total angular momentum
- f_M magnetic form factor

At $\theta = 0$ the magnetic scattering amplitude, p, for Cr is of the order of 1×10^{-12} cm. This value decreases rapidly as the angle, θ, is increased.[29]

Neutron diffraction spectra were analysed using the Rietveld method. The Rietveld algorithm fits the observed diffraction pattern using as variables:

- the instrumental parameters (beam profile, instrumental resolution)
- the experimental parameters (scale factor, zero point of detector, background polynomial coefficients)
- the sample parameters (cell parameters, atomic positions, Debye-Waller factor, magnitude and direction of the magnetic moments of the magnetic atoms etc.)

The Rietveld method for refining neutron diffraction spectra uses a least-squares minimisation technique (see Appendix 1) and is carried out with the aid of the programme FULLPROF.

2. 3. 2. Microscopy

2. 3. 2. 1. Atomic Force Microscopy

Atomic force microscopy was used to determine the surface morphology of oriented films of CrO_2. A table-top Burleigh Instruments AFM operating at room temperature

was used. AFM images are acquired by monitoring the deflection of a sharp tip, attached to a cantilever, as it is scanned over the surface of the film. As the tip and sample interact, forces act on the tip causing the cantilever to deflect. The position of the cantilever is monitored by a 4-cell detector which measures the intensity of laser light reflected from the tip of the cantilever. The output of the detector is connected to a feedback controller which regulates the force between the tip and the sample, which is mounted on top of a piezo crystal, by moving the sample up or down. In this way an image of the surface topography is acquired.

2. 3. 2. 2. Optical Microscopy

The granular texture of the oriented films could easily be observed using an optical microscope. An Olympus BH-2 microscope with magnifications 50, 100, 500 and 1000 times was used. A polarisation filter enhanced the contrast and provided a clear image of the sample.

2. 3. 2. 3. Scanning Electron Microscopy

Films and powders of CrO_2 were analysed using Scanning Electron Microscopy (SEM). In this technique electrons generated by a tungsten filament are accelerated through a voltage of typically 20 kV. The electrons are then focussed into a narrow beam by magnetic lenses forming a fine probe at the specimen's surface. Interaction of these primary electrons with the material produce secondary electrons, back-scattered electrons and X-rays. Secondary electrons can be used to provide an image of the morphology of the sample. Back-scattered electrons give information regarding the sample composition and hence can be used to identify the different phases present in the material. Finally, the energy spectrum of X-rays produced is characteristic of the chemical composition of the sample.

2. 4. Results and Discussion

2. 4. 1. X-Ray Diffraction

Figure 2.8 shows a typical X-ray diffraction pattern of a randomly oriented polycrystalline CrO_2 sample measured in the range 20-90°. The peaks were indexed for a crystal with a tetragonal Bravais lattice and a space group $P4_2/mnm$. For this particular reactor powder the average grain size is of the order of 75 nm within micron sized particles. The grain size was calculated using the Scherrer formula:

$$d = \frac{0.94\lambda}{B\cos\theta} \qquad 2.26$$

where λ is the wavelength of the X-rays used, B the full width at half maximum and θ the angle of reflection. However, the Scherrer formula underestimates the grain size because apart from particle size broadening effects there also exists instrumental line broadening and strain broadening.

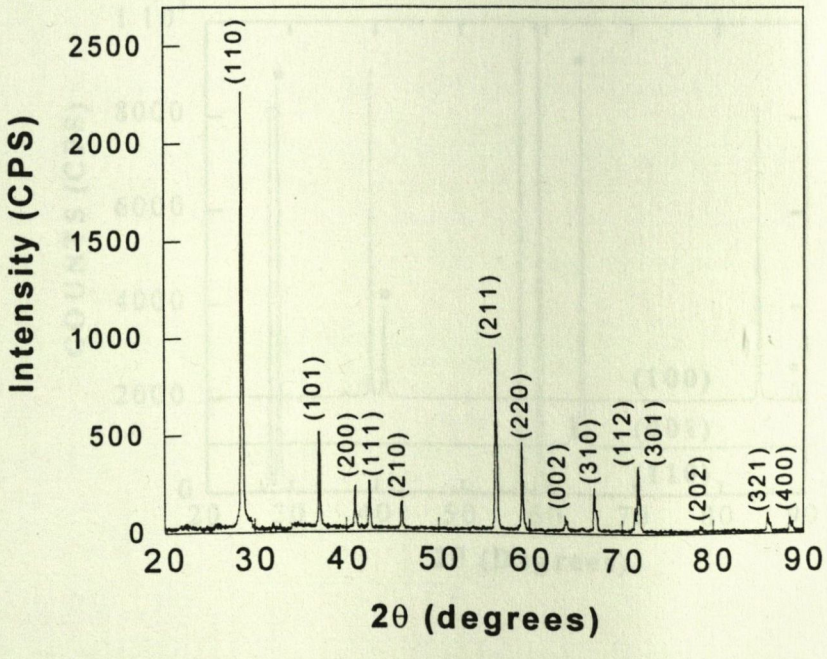

Fig. 2. 8. Powder X-ray diffraction pattern for tetragonal CrO_2 (B58).

Figure 2.9. shows X-ray diffraction patterns for films of CrO_2 grown on TiO_2 substrates. From these patterns it is clear that when the correct preparation conditions are used the films grown on TiO_2 substrates are highly textured and free from impurities. The absence of impurities is evident from the non-appearance of diffraction peaks that would otherwise correspond to other phases. The texture induced by the substrate is apparent from the absence of some of the X-ray lines normally observed for powders. Rutile-TiO_2 was found to be the best substrate to use from this point of view, due to the close lattice matching with CrO_2. The black circles in Fig. 2.9 mark the diffraction peaks for CrO_2. For CrO_2 films grown on a (110) oriented TiO_2 substrate there are two intense peaks at $2\theta = 28.4°$ and 59.2° corresponding to the (110) and (220) reflections. The diffraction pattern for the (001) oriented CrO_2 film features just one peak at $2\theta = 64.1°$ and corresponds to the (002) reflection. The (100) oriented film also shows two diffraction peaks, the first at $2\theta = 41.3°$ and the second at $2\theta = 88.6°$and corresponds to the (200) and (400) reflections respectively. The absence of odd (hkl) reflections for the (100) and (001) reflections arises as a consequence of the symmetry of CrO_2 which requires that h+k+l=2n, forbidding certain reflections. In general it was found that (001) oriented films grew with better coverage and texture at the slightly higher temperature of 425°C whilst the (100) and (110) were found to grow well at 420°C.

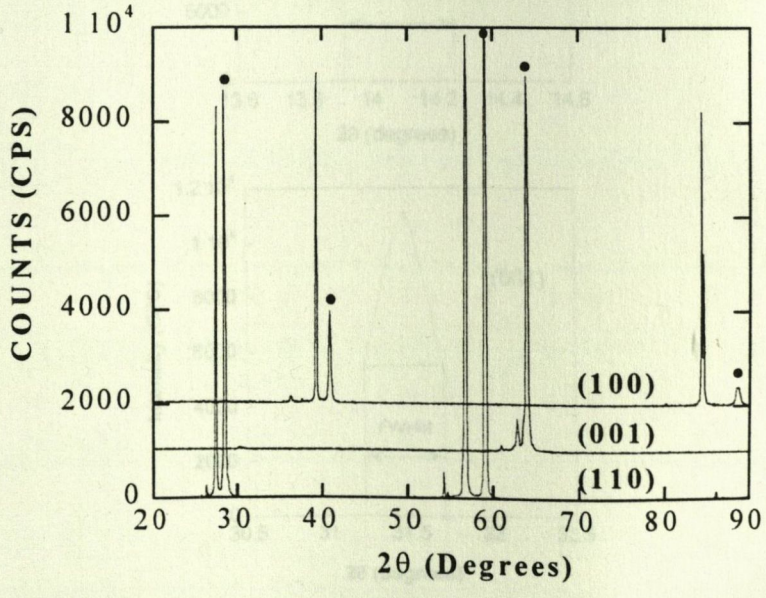

Fig. 2. 9. X-ray diffraction patterns of F50-(110), F51-(001) and F52-(100) oriented CrO_2 films on TiO_2 substrates. The black spot marks the CrO_2 diffraction peak.

Fig. 2. 10 shows the rocking curves for all three oriented films about their main diffraction peaks. In all cases the full width at half max (FWHM) is of the order of 0.35°. Well oriented, epitaxial films are characterised generally as having a rocking curve with a FWHM within the range of 0.1-0.5°.[30] Hence it is evident that the thermal decomposition of CrO_3 onto oriented TiO_2 substrates produces well oriented, epitaxial films of CrO_2.

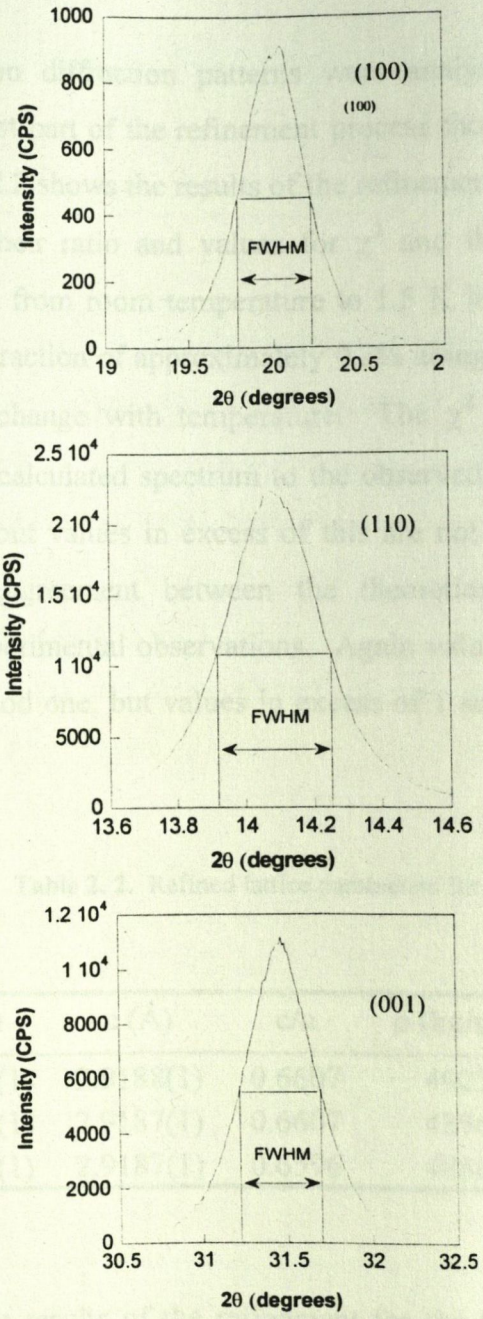

Fig. 2. 10. Rocking curves for CrO_2 F87-(100), F86-(110) and F85-(001)

Before magnetic filtration, the reactor powder was often found to show several diffraction peaks corresponding to the phases Cr_2O_5 and Cr_2O_3 in addition to the CrO_2 diffraction peaks. After filtration these peaks were found to disappear and a pure diffraction pattern such as that shown in Fig. 2.9 could be obtained.

2. 4. 2. Neutron Diffraction

The powder neutron diffraction patterns were analysed using the FULLPROF programme. In the first part of the refinement process the crystallographic parameters were obtained. Table 2.2 shows the results of the refinement for the lattice parameters a and c together with their ratio and values for χ^2 and the Bragg-R factor. As the temperature is reduced from room temperature to 1.5 K it can be seen that the lattice undergoes a small contraction of approximately 0.2% along the a (= b) axis. The c-axis shows no significant change with temperature. The χ^2 factor is a measure of the goodness of fit of the calculated spectrum to the observed spectrum. Theoretically χ^2 should converge to 1 but values in excess of this are not uncommon. The Bragg R-factor expresses the agreement between the theoretical model used during the refinement and the experimental observations. Again values close to 1 are expected if the model used is a good one, but values in excess of 1 such as those in Table 2.2 are acceptable.

Table 2. 2. Refined lattice parameters for CrO_2

T (K)	a (Å)	c (Å)	c/a	ρ (kg/m^3)	χ^2	Bragg-R
1.5 K	4.4177(1)	2.9188(1)	0.6607	4925	6.68	5.36
50 K	4.4176(1)	2.9187(1)	0.6607	4896	5.41	4.22
300 K	4.4251(1)	2.9187(1)	0.6596	4880	8.35	5.03

Table 2.3 shows the results of the refinement for the O atomic positions. The Cr atomic positions are kept fixed at the sites (0, 0, 0) (see Figure 1.2, Section 1.2 for a

diagram of the crystal structure of CrO_2). The change with temperature is slight, with an increase in x at 50 K.

Table 2. 3. Atomic positions for Cr and O

T (K)	Atom	x	z
1.5 K	Cr	0.0000(0)	0.0000(0)
	O	0.3019(2)	0.0000(0)
50 K	Cr	0.0000(0)	0.0000(0)
	O	0.3023(2)	0.0000(0)
300 K	Cr	0.000(0)	0.0000(0)
	O	0.3021(2)	0.0000(0)

Values for the apical distance d_a and the equatorial distance d_e are calculated using Equations 1.1 and 1.2, the values of the refined lattice parameters a and c and the atomic position parameter x. These values are listed in Table 2. 4. The distance d_a defines the distance between the metal atom at the equivalent site position (1/2, 1/2, 1/2) and the two anions at $(1/2 \pm x, 1/2 \mp x, 1/2)$ and d_e defines the distance between the metal atom and the four anions at $(1 \pm x, 1 \pm x, 0)$ and $(1 \pm x, 1 \pm, 1)$. Whilst these parameters vary only slightly with temperature there is a small elongation of the apical Cr-O distance as the temperature is raised. The equatorial distance shows no continuous increase with temperature. At 1.5 K the ratio d_a/d_e shows that the oxygen octahedron is distorted from the ideal structure by approximately 1.5%. For a certain value of $x = x_c$ (equation 1. 3) the two distances d_a and d_e become equal and ideal octahedral coordination is obtained. This value is also listed in table 2.4.

Table 2. 4. Octahedron distances Cr - O

T (K)	x_c	x	d_a (Å)	d_e (Å)	d_a/d_e
1.5 K	0.3046	0.3019	1.886	1.914	0.985
50 K	0.3046	0.3023	1.889	1.912	0.988
300 K	0.3044	0.3021	1.891	1.914	0.988

2. 4. 3. AFM analysis

The surface morphology and roughness of CrO_2 films was analysed using an AFM. Images of a (110), (100) and (001) oriented film are shown in Fig. 2. 11. From these images it can be seen that the (110) and the (100) films comprise of long needles lying in the plane of the film. The needles appear to be as much as 50 μm in length and up to 3 μm in diameter. The (001) oriented film reveals a distribution of circular shapes corresponding to the cross section of needles lying out of the plane of the film. This film is much rougher, as can be seen from the increased contrast in the image. The needles in this case are up to 2 μm in length and 5 μm in diameter.

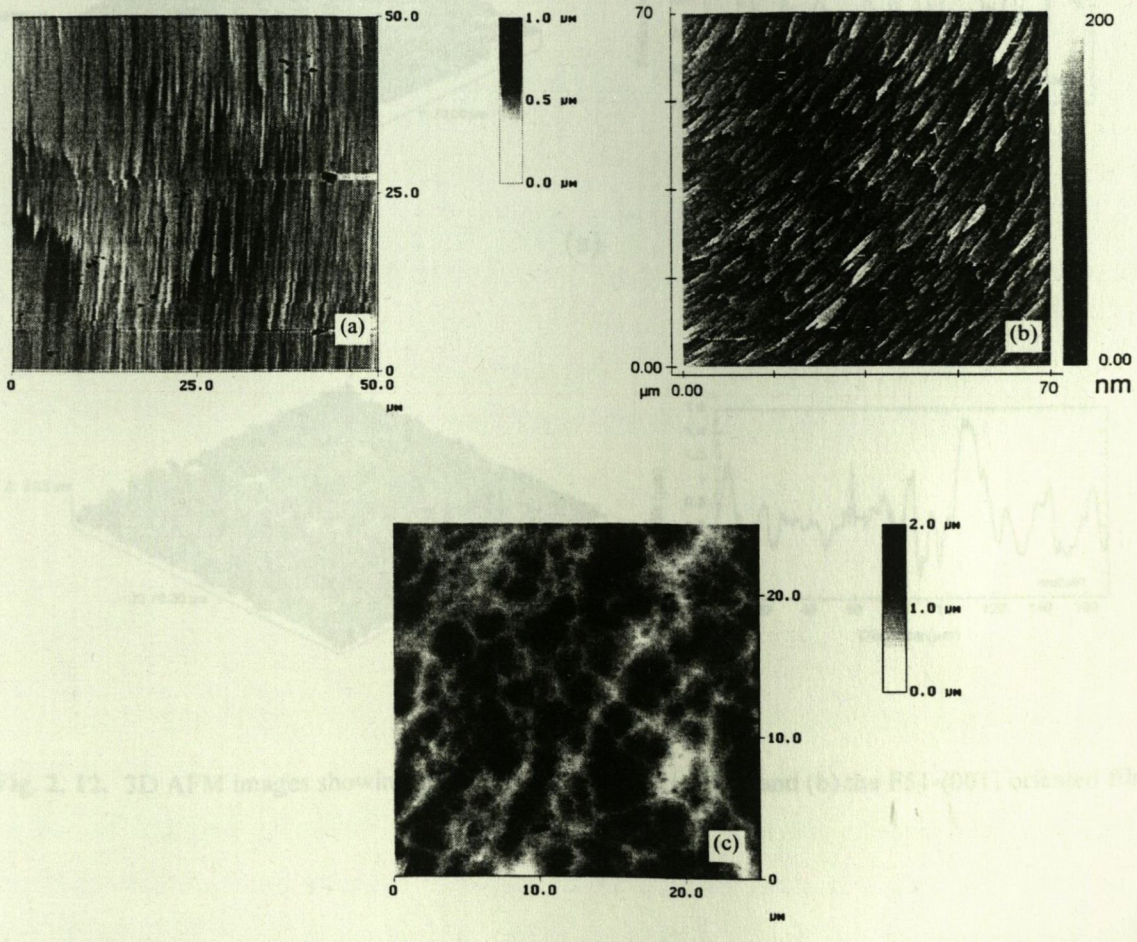

Fig. 2. 11. AFM images of (a) a F49-(110), (b) a F31-(100) and (b) a F51-(001) oriented CrO_2film.

The roughness of the films is best observed in the 3D AFM image which shows the film relief aspect. The right hand side of figure 2.12 shows the 3D image of the (100) and the (001) films, the left hand side shows the cross-sectional profile. The (100) (and similarily the (110) oriented film) oriented films generally have a thicknesses of the order of 1 μm. Hence the roughness, as determined by the cross-sectional profiles is approximately 10%. The (001) films show a much larger surface roughness of approximately 50%. The increased roughness of the (001) film is thought to be due to chemical attack by the molten CrO_3.[5]

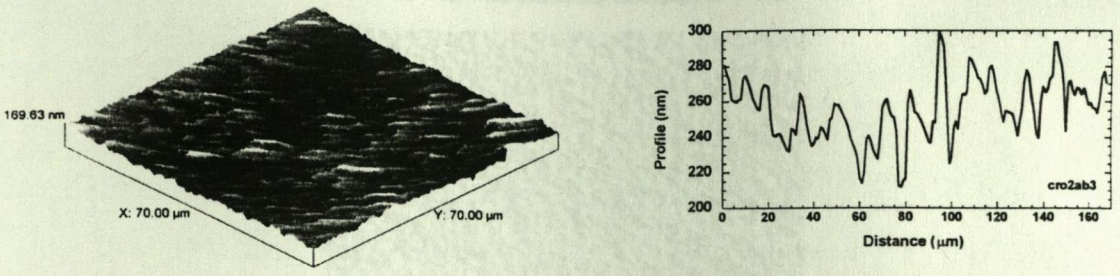

(a)

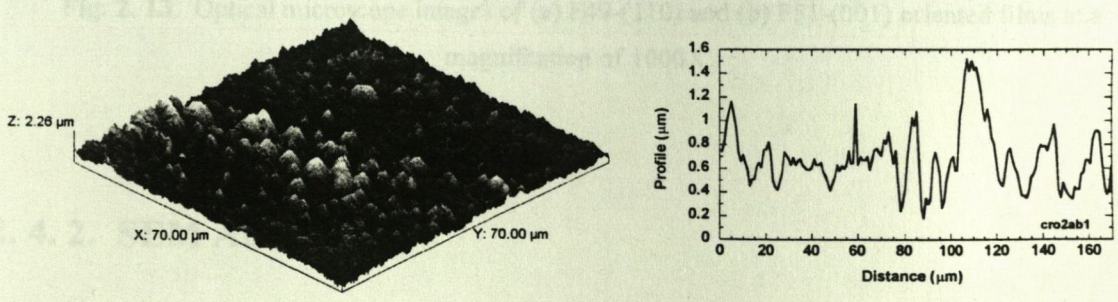

(b)

Fig. 2. 12. 3D AFM images showing relief aspect (a) the F31-(100) and (b) the F51-(001) oriented film.

2. 4. 4. Optical Microscopy

It is also possible to observe the grain structure of the CrO_2 films and the relief aspect using an optical microscope, as shown in Fig. 2.13. Images were photographed at a magnification of 1000X. From these photos the grains are clearly seen as needle-

like structures lying in and out of the plane. In particular, the rough nature of the (001) film is observed as sharp peaks protruding from the plane.

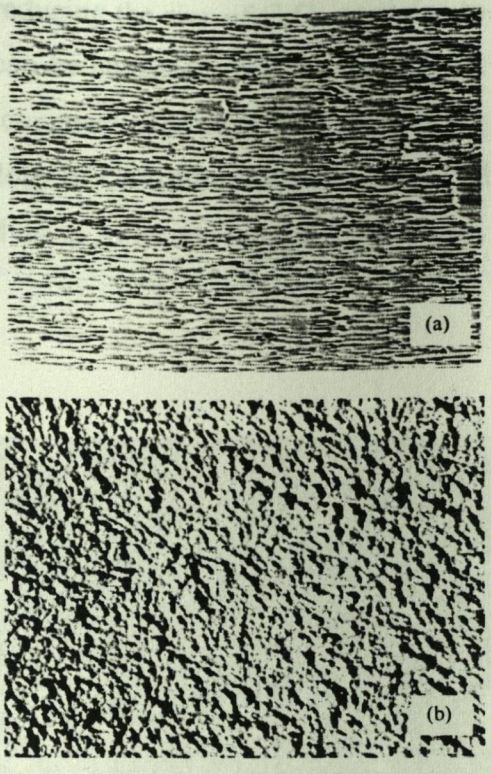

Fig. 2. 13. Optical microscope images of (a) F49-(110) and (b) F51-(001) oriented films at a magnifcation of 1000X.

2. 4. 2. SEM Analysis

Using energy dispersive X-rays spectroscopy (EDXs) in the SEM it was possible to determine the chemical composition of the samples. In general, the films were found to be free of impurity elements. The reactor powder, on the other hand, was on occasion found to contain small traces of impurity elements such as Zn and Cu. This was due to the diffusion of these elements from the brass reactor vessel during the decomposition process. The image of the powder produced by the backscattered electrons showed that the reactor powder comprised of very large particles up to 20 μm in length and 1 μm in diameter. Commercially produced powder was also analysed in the SEM. This powder was observed to be much finer and more homogeneous than the reactor powder, with

particles up to 1 μm in length and 0.2 μm in diameter. Iron (0.2 atomic %) was also found to exist in the commercial powder. This is not surprising, however, since elements such as Fe and Sb are often used as additives in commercially produced CrO_2 powder as a means of reducing the size of CrO_2 particles to single domain dimensions, so that the coercivity can be enhanced (see Section 2.1.3). The SEM images for the reactor powder and the commercial powder are shown in Fig. 2.14.

The surface morphology of CrO_2 films was also observed using the SEM. However, this was better observed using AFM and optical microscopy.

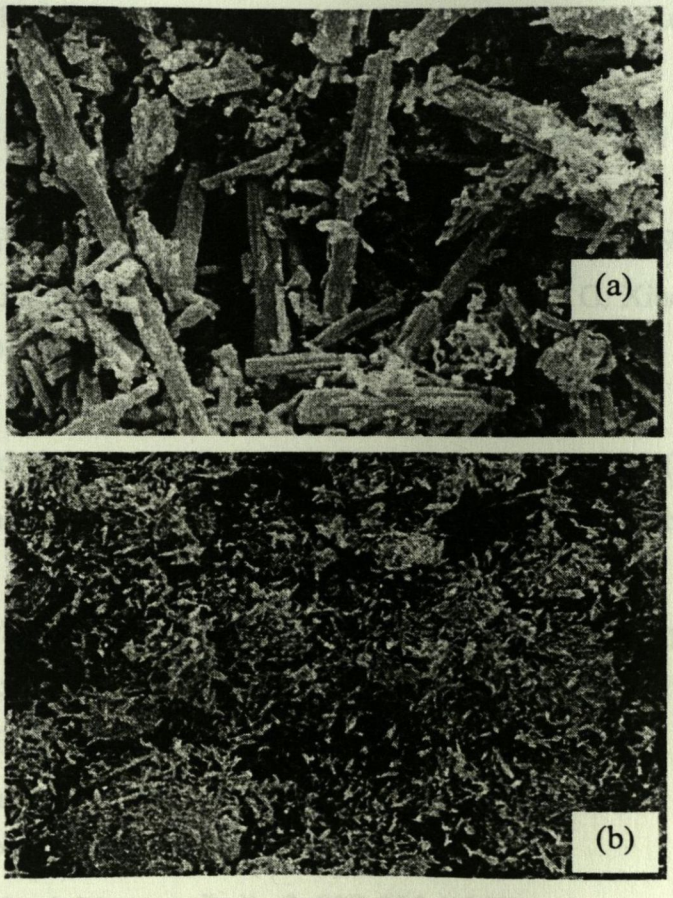

Fig. 2. 14. SEM image of (a) the unfiltered reactor powder (B9) and (b) the commercial powder (B1503).

References

[1] B. L. Chamberland, CRC Critical Reviews in Solid State and Materials Sciences, **7**, 1-29 (1977)

[2] L. Ranno, A. Barry and J. M. D. Coey, J. Appl. Phys., **81**, 5774-5776 (1997)

[3] B. Kubota, J. Am. Ceram. Soc., **44**, 239-248 (1961)

[4] R. S. Schwartz, I. Fankuchen and R. Ward, J. Am. Chem. Soc., **74**, 1676-1677 (1952)

[5] R.C. De Vries, Mat. Res. Bull., **1**, 83-89 (1966)

[6] K. Wilhelmi, Acta Chem. Scand., **22**, 2565-2573 (1968)

[7] P. Porta, M. Marezio, J. P. Remeika and P. D. Dernier, Mat. Res. Bull., **7**, 157-162 (1972)

[8] Y. Shibasaki, F. Kanamaru, M. Koizumi, K. Ado and S. Kume, J. Am. Chem Soc., **56**, 248-249(1973)

[9] K. Suzuki and P. M. Tedrow, Sol. St. Commun., **107**, 583-585 (1998)

[10] X. W. Li, A. Gupta, T. R. McGuire, P. R. Duncombe and G. Xiao, J. Appl. Phys., **85**, 5585-5587 (1999)

[11] A. Michel and J. Bénard, Bull. Soc. Chim. Fr., **10**, 315 (1945)

[12] L. Ben-Dor and Y. Shimony, J. Crystal Growth, **24/25**, 175-178 (1974)

[13] R. Halonbrenner, J. R. Huber, U. Wild and H. H. Gunthard, J. Phys. Chem., **72**, 3929 (1968)

[14] C. Arnone, M. Rothschild, J. G. Black and D. J. Ehrlich, Appl. Phys. Lett., 48, 10181-20 (1986); F. K. Perkin et al., Thin Solid Films, **198**, 317-329 (1991)

[15] B. J. Thamer, R. M. Douglas and e. Staritzky, J. Am. Chem. Soc., **79**, 547-550 (1957)

[16] T. J. Swoboda, J. P. Arthur, N. L. Cox, J. N. Ingraham, A. L. Oppegard and M. S. Sadler, J. Appl. Phys., **32**, 374S-375S (1961)

[17] B. L. Chamberland, Mat. res. Bull., **2**, 827-835 (1967)

[18] H. Y. Chen, D. M. Hiller, J. E. Hudson, C. J. A. Westenbroek and E. I. du Pont de nemours, IEEE trans. Mag., **20**, 24-26 (1984)

[19] T. G. Crandall, H. -Y. Chen, G. R. Cole, R. S. Lawton and C. J. A. Westenbroek and E. I. du Pont de nemours and Co., IEEE Trans. Mag., **23**, 36-38 (1987)

[20] L. Suchow, I. Fankuchen, and R. Ward, J. Am. Chem. Soc., **74**, 1678-1679 91952)

[21] Y. Shibasaki et al., Mat. Res. Bull., **5**, 1051-1058 (1970)

[22] M. A. Alario Franco, K. S. W. Sing, J. Therm. Anal., **4**, 47-52 (1972)

[23] Q. Chen, A. Wall and M. Onellion, J. Magn. and Magn. Mat., **139**, 171-174 (1995)

[24] M. J. Almond and M. Hahne, J. Chem. Soc. Dalton Trans., **9**, 2255-2260 (1988)

[25] P. A. Dowben, Y. G. Kim, S. B. Tosh, G. O. Ramseyer, C. Hwang and M. Onellion, J. Appl. Phys., **67**, 5658-5660 (1990)

[26] F. K. Perkins, C. Hwang, M. Onellion, Y. -G. Kim, and P. A. Dowben, Thin Solid Films, **198**, 317-329 (1991)

[27] B. Beverskog and I. Puigdomenech, Corrosion Science, **39**, 43-57 (1997)

[28] D. H. Ryan and J. M. D. Coey, J. Physics E, **19**, 693 (1986)

[29] G. E. Bacon, Neutron Diffraction, 2nd Edition, Clarendon Press (1962)

[30] B. E. Warren, X-Ray Diffraction, Dover Publications, Inc. (1990)

Chapter 3

Magnetic Properties of CrO_2

"This may require more skill than I actually possess."
Mike Coey when simultaneously overtaking a juggernaut and looking over one shoulder to talk to passengers in the rear on a road under construction in Jena, March 1997.

3. 1. Introduction

In this chapter, some of the magnetic properties of CrO_2 shall be elucidated. These include a determination of the magnetic moment per Cr ion and the Curie temperature, both of which can be related to recent band structure calculations. The temperature variation of the magnetisation will be presented with a view to relating the behaviour to existing theories. These measurements will also lend support to the transport measurements to be presented in Chapter 5. The variation of the magnetisation with magnetic field of both CrO_2 powders and oriented films will also be presented. In particular, these measurements will highlight the effect of substrate orientation on the magnetisation processes of oriented films.

3. 2. Background

CrO_2 is a ferromagnetic material and its ferromagnetism arises as a result of the interaction of the Cr^{4+} cations, see Section 1.4, Chapter 1. A ferromagnetic material is one in which there is a spontaneous parallel alignment of atomic magnetic moments below some critical temperature (the Curie temperature). The source of the alignment can be thought of as being equivalent to a magnetic field (the Weiss molecular field) produced by the surrounding moments which acts on neighbouring moments causing them to align parallel to each other. This field is of the order of 1000 T and cannot arise from a classical mechanism, since, the current required to produce a field of this magnitude is $\sim 10^9$ A/m, a current large enough to melt the sample. The physical

origins of the Weiss field were explained by Heisenberg in terms of a quantum mechanical exchange interaction. The exchange interaction is essentially an electrostatic effect and is based on the idea that the total wavefunction (spatial × spin) of a quantum state must be antisymmetric. Hence, the exchange interaction between neighbouring ions is determined by the Pauli exclusion principle and the Coulomb repulsion between electronic charge. The exchange Hamiltonian of a given atom i with its neighbours can be written as:

$$H = -2\sum_{j} J_{ij}\bar{S}_i \cdot \bar{S}_j \qquad 3.1$$

where the summation is over the nearest neighbour atoms at site j of atom i, J_{ij} is the exchange integral and is related to the overlap of the wavefunctions of the atoms at sites i and j and $\bar{S}_{i,j}$ are the spin momenta at the atomic sites i and j. When $J > 0$, the magnetic ordering is ferromagnetic and when $J < 0$ the magnetic ordering may be antiferromagnetic. Magnetic order in a ferromagnetic system is destroyed at a critical temperature known as the Curie temperature, T_c, and in the molecular field theory it is given by:

$$T_c = \frac{2zJS(S+1)}{3k_B} \qquad 3.2$$

where $z = 8$ is the number of interacting Cr neighbours, J is the exchange constant, S the total spin momentum on each Cr ion and k_B is the Boltzmann constant. In CrO_2, the Curie temperature is of the order of 400 K so that $J/k_B = 37.5$ K.

Ferromagnetism can be described by either a localised or an itinerant model.[1, 2] The first model pertains to the idea that atomic moments are localised at atomic sites. The interaction of atomic moments is then a result of the exchange interaction described above. The itinerant model concerns electrons at atomic sites which are close enough for there to be an appreciable overlap of atomic orbitals. As a result, electrons may be free to move through the crystal in energy bands which are modified by the periodic potential of the lattice. Whether a material is ferromagnetic or not within the itinerant

model depends on whether the potential energy (associated with the exchange energy between electrons) is greater than the kinetic energy (associated with the delocalisation of electrons). The criterion for ferromagnetism within the itinerant model framework was proposed by Stoner and is written as: $I \times n(E_F) > 1$ where the Stoner parameter I is determined by the Coulomb exchange interaction ($I \approx 1$ eV) and $n(E_F)$ is the density of states at the Fermi level.[3] Both these models are relevant to the magnetic properties of CrO_2 since one of the $3d^2$ electrons is expected to be localised in a t_{2g} orbital of xy character and the other delocalised in a degenerate orbital of yz ± zx character (see Section 1.4, Chapter 1).[4]

3. 2. 1. Domains

It is common for a sample of ferromagnetic material to have zero magnetisation on a macroscopic scale. This is the case when the sample has never been exposed to a magnetic field or has been thermally demagnetised by heating above its Curie temperature. This behaviour is accomplished by having magnetic domains (localised regions of magnetisation) which are oriented in such a way as to reduce the overall magnetisation to zero. Within each domain, the magnetic moments are aligned parallel to each other and the magnetisation of the domain is called the spontaneous magnetisation. The spontaneous magnetisation at zero temperature is the saturation magnetisation, M_o. The reason for the formation of a domain structure is that the magnetostatic energy, E_m, associated with the magnetised sample is minimised.

$$E_m = -\left(\frac{\mu_o}{2}\right)\int \bar{M} \cdot \bar{H} dV \qquad 3.3$$

The reduction in the magnetostatic energy is balanced by the energy required to form a domain, this coming from the magnetocrystalline anisotropy, exchange energy and magnetoelastic energy. Each domain is separated from a neighbouring domain by a domain wall. This can be a Bloch wall or a Néel wall depending on whether the spins rotate through 180° out of the sample plane (e.g. bulk materials) or in the plane of the sample (e.g. thin films) respectively. The width of the Bloch walls, δ, is given by:

$$\delta = \pi\sqrt{\frac{A}{K_1}} \qquad 3.4$$

where $A = 2JS^2/a$ is the exchange stiffness, J is the exchange integral, S the spin on each ion and $a = 3.449$ Å is the inter-atomic distance between neighbouring Cr ions. Using $J/k_B = 37.5$ K, we find $A = 3.0$ pJ/m. K_1 is the magnetocrystalline anisotropy constant and has a room temperature value of 3.7×10^4 J/m^3 (see Section 3.3.1B). Both A and K_1 are intrinsic properties of the material. The exchange energy acts to increase the wall width while the anisotropy tends to decrease the wall width. From the values for A and K_1 given above, we deduce a wall width $\delta = 28.3$ nm. The energy associated with the domain wall, γ_{wall}, is given by:

$$\gamma_{wall} = \sqrt{AK_1} \qquad 3.5$$

and using the same values for A and K_1 as above, $\gamma_{wall} = 3.3 \times 10^{-4}$ J/m^2.

3. 2. 2. Anisotropy

Magnetocrystalline Anisotropy

In ferromagnetic materials there may exist several types of anisotropy, the most common of which is the *magnetocrystalline anisotropy*. It is an intrinsic property which gives rise to the preferential orientation of magnetic moments along a particular crystallographic direction and arises from the spin-orbit interaction. Electron orbits are linked to the crystallographic structure, and by their interaction with the electron spins, the orbits force the spins to lie preferentially along well-defined crystallographic axes. This results in there being directions of 'easy' magnetisation (those in which it is energetically favourable for spins to lie) and 'hard' magnetisation (those at 90° to the easy directions). The magnetocrystalline anisotropy energy for a uniaxial crystal, where the easy magnetisation direction is along the c-axis, is given by:

$$E_a = K_1 \sin^2\theta + K_2 \sin^4\theta + \ldots. \qquad 3.6$$

where K_1 and K_2 are the anisotropy constants in J/m^3, θ is the angle between the magnetisation and the easy axis. In general, it is sufficient to define the anisotropy energy using just the first term. It is often useful to define an anisotropy field, $H_a = 2K_1/\mu_o M_s$ where M_s is the spontaneous magnetisation defined above.

CrO_2 is said to have a uniaxial anisotropy with magnetic moments that lie along the c-axis. The room temperature uniaxial magnetocrystalline anisotropy constant has been measured previously to lie in the range $2.0 - 3.3 \times 10^4$ J/m^3 with a corresponding anisotropy field 0.06-0.10T.[5, 6, 7, 8, 9] A low temperature uniaxial magnetocrystalline anisotropy constant of 4.9×10^4 J/m^3 has been measured by Rodbell et al.[6] However, there have been reports claiming that the magnetisation lies in the a-c plane at an angle of 20-40° to the c-axis.[8, 10] However, since $J >> K_1\Omega$, where Ω is the volume occupied per Cr atom, it is reasonable to expect a single magnetic axis within each domain; a four-fold easy axes configuration has never been observed.

Shape Anisotropy

Another source of anisotropy arises from the shape of magnetic samples. The shape anisotropy originates from the magnetostatic properties of the sample. When the magnetisation of a ferromagnetic body is saturated in a magnetic field, magnetic 'poles' appear on its surfaces. The effect is produced by the normal component of magnetisation being discontinuous at the surface. The H-field inside the sample is then a superposition of the applied field and the field arising from the distribution of magnetic poles, $\mu_o \vec{M} \cdot \hat{n}$, at the surface which is in a direction that opposes the applied field, Fig. 3.1. This opposing field is known as the demagnetising field and can be written as:

$$H_d = -N_d M \qquad 3.7$$

where N_d is called the demagnetising factor (since it reduces the field inside the sample) and is determined from the shape of the sample and M is the magnetisation. The demagnetisation field depends therefore on only two factors, the magnetisation in the material and the shape of the specimen.

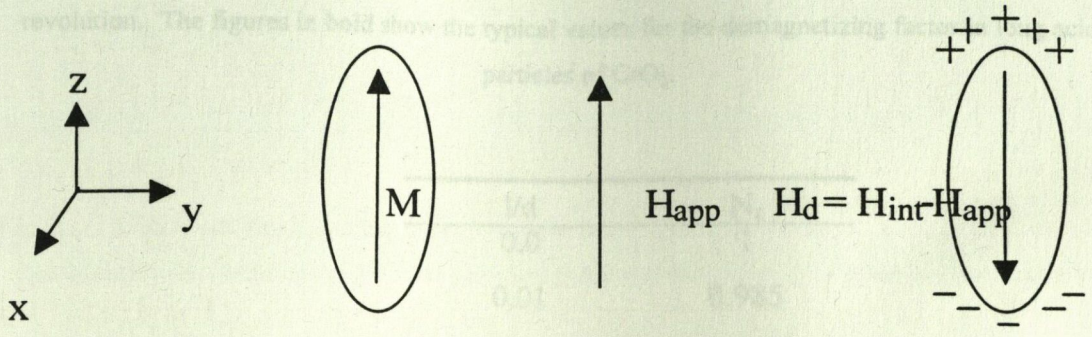

Fig. 3. 1. The magnetic field inside a bulk magnetic material due to the distribution of magnetic poles at the surface opposes the applied magnetic field.

The sum of the demagnetising factors for an ellipsoid measured in three mutually orthogonal directions is equal to 1, i.e.

$$N_x + N_y + N_z = 1 \qquad 3.8$$

Hence it can be concluded that for a sphere, $N_x = N_y = N_z = 1/3$. For an ellipsoid of infinite length, N_z is zero and $N_x = N_y = 0.5$ whilst a thin flat disc has $N_z \approx 1$ and consequently $N_x = N_y = 0$. The demagnetising factor, N_z, for an ellipsoid of arbitrary revolution as a function of the length to diameter ratio l/d is listed in Table 3.1 below. The general expression for the energy associated with the self-demagnetising field of a general uniformly magnetised ellipsoid is given by:

$$E_m = \mu_o V(N_x M_x^2 + N_y M_y^2 + N_z M_z^2)/2 \qquad 3.9$$

where the magnetisation has been decomposed into vector components x, y and z. This is similar to equation 3.3 where H has been replaced the demagnetising field of equation 3.7.

Table 3. 1. Demagnetising factor, N_z, as a function of the length to diameter ratio of an ellipsoid of revolution. The figures in bold show the typical values for the demagnetizing factor in long acicular particles of CrO_2.

l/d	N_z
0.0	1
0.01	0.985
0.1	0.861
1	0.333
3	0.109
5	**0.0557**
10	**0.0199**
20	**0.00676**
50	**0.00143**
100	0.00042

It can be shown that below a critical size of magnetic particle it is energetically unfavourable to form a domain wall. Stoner and Wohlfarth developed a model for the hysteresis behaviour of an assembly of non-interacting single domain particles with uniaxial anisotropy, assuming coherent rotation of the magnetisation, Fig. 3.2.[2] The anisotropy can arise from magnetocrystalline or shape anisotropy energy which can both be written in a manner similar to equation 3.6.

$$E_{an} = - K\sin^2\theta \qquad 3.10$$

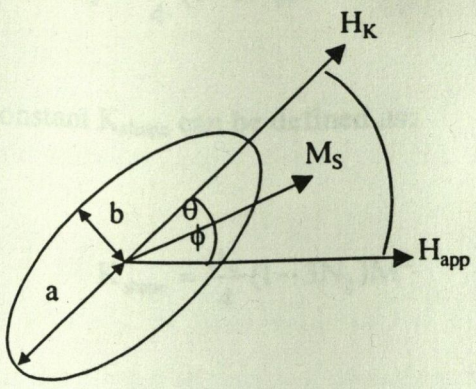

Fig. 3. 2. Ellipsoidal single-domain particle with a shape anisotropy field H_K. The particle has a higher demagnetisation factor along the short axis than along the long axis. This leads to shape anisotropy.

For single-domain particles, the anisotropy energy arising from the shape can be obtained by taking account of the magnetostatic energy associated with the particle. If we assume that the magnetisation lies in the zy plane and denote $N_z = N_{||}$ and $N_y = N_x = 1\text{-}N_{||}/2$, then from equation 3.9:

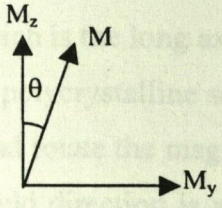

$$E_m = \frac{\mu_o}{2}(N_{||}M_z^2 + \frac{(1-N_{||})}{2}M_y^2)$$

$$= \frac{\mu_o}{2}(N_{||}\cos^2\theta + \frac{(1-N_{||})}{2}\sin^2\theta)M^2$$

$$= \frac{\mu o}{2}(N_{||} - \frac{3N_{||}}{2}\sin^2\theta + \frac{1}{2}\sin^2\theta)M^2$$

and θ defines the angle between the magnetisation M and the z-direction. The first term in the last equation can be ignored since this is a constant leading to:

$$E_m = \frac{\mu_o}{4}(1-3N_{\|})M^2 \sin^2\theta$$

Hence, a shape anisotropy constant K_{shape} can be defined as:

$$K_{shape} = \frac{\mu_o}{4}(1-3N_{\|})M^2 \qquad 3.11$$

For reactor grown CrO_2 powder, the magnetisation, σ, at room temperature is typically 80 J/T kg (see section 3.3). The density of CrO_2 is 4925 kg/m^3 hence $M = 3.95 \times 10^5$ J/Tm^3. Hence, for particles having an aspect ratio l/d ~ 20 and $N_{\|} \sim 0.00676$, $K_{shape} \approx 4.9 \times 10^4$ J/m^3. At low temperatures, the saturation magnetisation is of the order of 110 J/T kg and K_{shape} is then 1×10^5 J/m^3. This is compared to the magnetocrystalline anisotropy which is of the order of 3×10^4 J/m^3.[6]

The easy axis associated with the shape of the particle does not necessarily have to lie in the same direction as the magnetocrystalline anisotropy axis. In this case there is a competition between then anisotropies which try to align the magnetisation parallel to their related easy axes. In CrO_2 powder, the problem is simplified however by assuming that the easy axes are the same for both magnetocrystalline and shape anisotropies lying along the c-axis which is the long axis of the particle.

To saturate the magnetisation in a polycrystalline sample, a sufficiently large field is needed to overcome the anisotropy and rotate the magnetic moments from the easy axis into the field direction. When the field direction is perpendicular to the easy axis the magnitude of the field required to rotate the moments is $H_K = 2K/\mu_o M_s$ where H_K is the anisotropy field. In this model K is the anisotropy constant associated with either the shape or the magnetocrystalline anisotropy energy. In the Stoner-Wohlfarth model for single-domain particles, which assumes coherent rotation, it is possible to estimate the coercivity by equating H_K and H_c. However, it is a known fact (Brown's Paradox) that this method tends to overestimate the coercivity by a factor of 2-10.[11] This is because it does not take account of incoherent magnetisation reversal due to nucleation sites arising from sample defects and inhomogeneities.

3. 2. 3. Hysteresis Loops

A magnetic hysteresis loop is the most common way to represent the magnetic properties of a ferromagnetic material. It is a plot of the magnetisation, M, as a function of the magnetic field, H. The hysteresis loop enables the determination of the spontaneous magnetisation, M_s, the coercivity, H_c and the remanent magnetisation M_R. A simple schematic diagram of a typical hysteresis loop of a ferromagnet is given in Fig.3.3. Hysteresis loops may be plotted in terms of the externally applied field H_{app} or the internal field H_{int}.

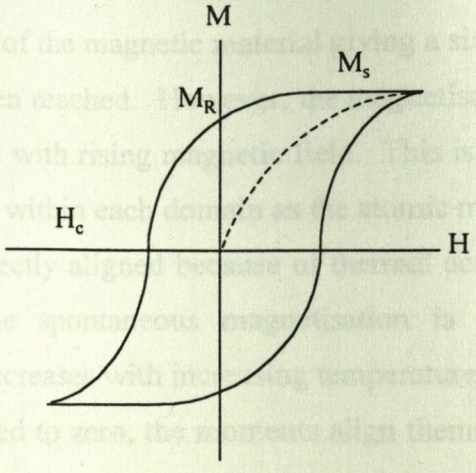

Fig. 3. 3. Typical hysteresis loop of a ferromagnetic material showing the saturation magnetisation, M_s, the remnant magnetisation, M_R, and the coercivity, H_c. The dashed line shows the virgin magnetisation curve.

The spontaneous magnetisation is the magnetisation within each domain. At low temperature, the spontaneous magnetisation can be replaced by the saturation magnetisation which is the upper limit of magnetisation when all the magnetic moments are aligned with the field within a single domain. The saturation magnetisation is dependent only on the magnitude of the atomic magnetic moments and the number of atoms per unit volume. The remanent magnetisation is the magnetisation in zero field after saturation has been reached. The coercivity is the magnetic field that must be applied to reduce the magnetisation of the sample to zero. Remanence and coercivity depend on sample shape and microstructure.

The origin of the hysteresis loop can be explained in general terms as follows. When a small magnetic field is applied to an initially unmagnetised magnetic material, there occurs a reversible rotation of the magnetisation within the domains and a reversible movement of the domain walls. As the field is increased, there is an irreversible enlargement of domains which have their moments favourably aligned in the direction of the applied field. These domains grow at the expense of less favourably aligned domains by irreversible domain wall motion. As the field is further increased, the unfavourably oriented domains rotate so that their axes of magnetisation lie in a direction close to that of the magnetic field. Finally, there is a coherent rotation of magnetic moments, now aligned along a preferred magnetic crystallographic easy axis lying close the field direction, into the field direction. At this point, all the domain walls have been driven out of the magnetic material giving a single domain material and technical saturation has been reached. However, the magnetisation may be observed to continue to increase slowly with rising magnetic field. This is due to an increase in the spontaneous magnetisation within each domain as the atomic moments within the single domain which are not perfectly aligned because of thermal activation, are brought into complete alignment. The spontaneous magnetisation is equal to the saturation magnetisation at 0 K but decreases with increasing temperature.

When the field is reduced to zero, the moments align themselves to the easy axis in each grain and the magnetisation decreases to the remanent magnetisation value. The size of the remanent magnetisation depends on the distribution of easy axes and the microstructure of the particles or films. The magnetisation can be reduced to zero by applying a sufficiently large negative magnetic field known as the coercive field and the resistance of a magnetic material to demagnetisation is the coercivity. The coercivity of a material is closely related to the influences which fix domain walls in position making them difficult to move under the influence of an applied field. There may exist several underlying mechanisms to the coercivity. For example, the presence of defects can act to "pin" the domain walls whilst magnetocrystalline and shape anisotropy give rise to preferred directions of magnetisation resulting in the need for larger fields to rotate the magnetic moments in the direction of the applied field. On the other hand, magnetisation reversal at nucleation sites arising from sample inhomogeneities can also give rise to non-uniform rotation of the magnetisation which effectively lowers the coercivity.

3. 2. 4. Spin Waves

At T = 0 K in a ferromagnetic crystal, all the spins are aligned parallel to each other and the spontaneous magnetisation within a domain is equal to M_o, Fig. 3.4a. However, as the temperature is raised from zero, thermal energy causes misalignment of the directions of the magnetic moments within the domains giving rise to an excited state. An example of an excited state is shown in Fig. 3.4b where a spin has been reversed so that it is aligned antiparallel to the other spins in a chain of spins. The energy required to completely reverse one spin relative to the other spins is of the order of the exchange energy ($2zJS^2 \sim 600K$) and is large compared to the energy required to turn spins successively through a small angle θ. The latter situation is thus a low-lying excited state because neighbouring spins are very nearly parallel to each other and hence, very little exchange energy is lost. This propagation of spins from a spin-up state to a spin-down state over many lattice spacings is known as a spin-wave and is depicted schematically in Fig. 3.4c.

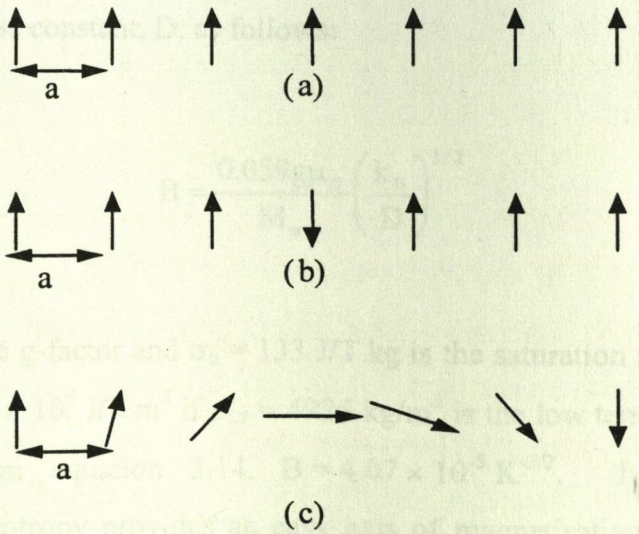

Fig. 3. 4. A linear ferromagnetic chain (a) in the ground state at T=0 K, (b) in an high energy excited state with one spin antiparallel, (c) a low energy excited state where moments are turned successively through an angle θ relative to its neighbours

The energy of a ferromagnetic spin wave of wavevector $\bar{k}$ is $E_k = Dk^2$ in the limit of small $\bar{k}$, and D is the spin wave stiffness constant which is defined as:[11]

$$D = \frac{zJSa^2}{d} \qquad 3.12$$

For CrO_2, z = 8, J = 37.5 K (or 3.25 meV), a = 3.449 Å, S=1 is the spin on the Cr ion and d = 3 (d is the lattice dimension) so that D is determined to be 1.65×10^{-40} J/m^2 or equivalently 103 meV Å^2. The spin-wave stiffness constant is a measure of the strength of the interactions that stabilise the magnetically ordered state. Spin waves cause the magnetisation to decrease from its saturation magnetisation value as the temperature is raised from 0 K. Bloch showed that the magnetisation varied with temperature according to:[12]

$$M(T) = M_s\left[1 - BT^{3/2}\right] \qquad 3.13$$

where M_s is the saturation magnetisation and B is the Bloch constant and can be related to the spin wave stiffness constant, D, as follows:

$$B = \frac{0.059g\mu_B}{M_o}\left(\frac{k_B}{D}\right)^{3/2} \qquad 3.14$$

where g =2 is the Landé g-factor and σ_o = 133 J/T kg is the saturation magnetisation of CrO_2 so that $M_o = 6.55 \times 10^5$ J/T m^3 if $\rho_{LT} = 4925$ kg/m^3 is the low temperature density of CrO_2. Hence, from equation 3.14, $B = 4.07 \times 10^{-5}$ K$^{-3/2}$. In real crystals, magnetocrystalline anisotropy provides an easy axis of magnetisation and the lowest energy excited state corresponds to deviations from this preferred direction. As a result, the spin wave frequency tends towards a finite value in the long-wavelength limit and the energy of the spin wave is given by $E_K = Dk^2 + \Delta$, where $\Delta \approx K_1\Omega$ is the anisotropy energy where Ω is the volume per Cr ion. Δ is interpreted as a gap in the spin wave spectrum and it manifests itself in the magnetisation versus temperature curves which are described by the equation:[13]

$$M_s(T) = M_o\left[1 - BT^{3/2}\exp(-\Delta/k_B T)\right] \qquad 3.15$$

In CrO_2 the anisotropy is small, and any deviation from the usual Bloch $T^{3/2}$ law is also expected to be small. For example, at low temperature the magnetocrystalline anisotropy for CrO_2 has been measured to be $K_1 \approx 6.5 \times 10^4$ J/m^3 and this is equivalent to a temperature $T \approx 0.3$ K. On the other hand, the needle shape anisotropy at low temperature is typically 9×10^4 J/m^3 (see section 3. 1. 3) and is equivalent to a temperature of $T \approx 0.4$ K while the film shape anisotropy gives rise to an anisotropy energy of the order of 2×10^5 J/m^3 which is equivalent to a temperature $T \approx 1$ K. Hence, in all cases, any deviations from the usual $T^{3/2}$ behaviour due to anisotropy occur at temperatures which are lower than the measuring temperature ($T > 4$ K).

3. 3. Experimental Methods

3. 3. 1. Magnetometry

To study the magnetic properties of films and powders of CrO_2, magnetisation curves as a function of temperature (0-300 K) and field (up to 6 T) were measured. Powder samples were measured using either axial extraction or vibrating sample magnetometers equipped with a superconducting coil whilst films were measured using a SQUID magnetometer. Axial extraction measurements were carried out at the Laboratoire Louis Néel, Grenoble France. SQUID measurements were carried out at MARTECH, FSU, Tallahasee, USA and l'Orme des Merisiers, France.

The magnetisation of a powder sample is measured via two pick-up coils between which the sample is vibrated or extracted. The displacement of the sample gives rise to a change in magnetic flux ϕ across the pick-up coils which induces an electromotive force ε. The total variation in the flux due to the displacement of the sample is obtained by integrating over ε with respect to time and this is proportional to the magnetisation.

The absolute value of magnetisation is obtained by comparing the signal obtained to a previously measured calibration sample such as nickel. A simple schematic diagram of the experimental set-up is shown in Fig. 3.5.

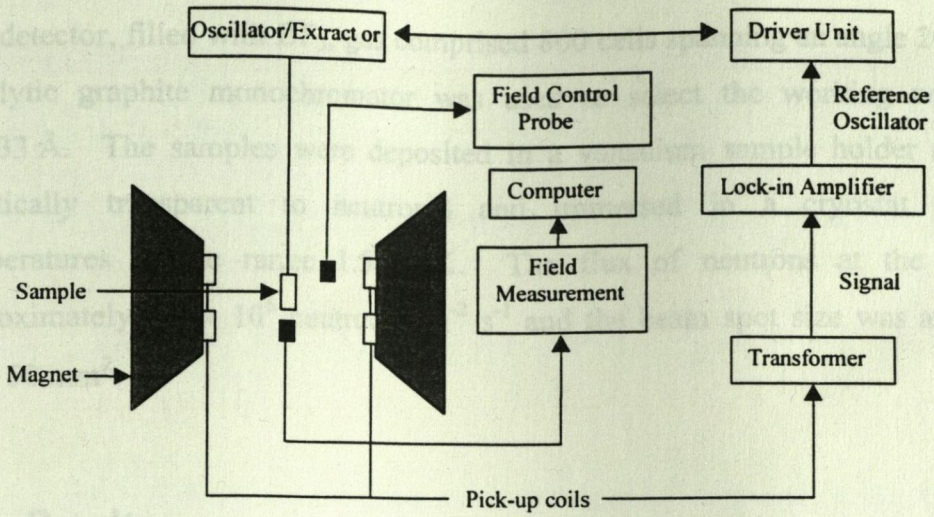

Fig. 3. 5. Schematic diagram of a vibrating-sample/axial extraction magnetometer

For SQUID measurements (where the SQUID consists of a superconducting ring with a small insulating layer called a 'weak-link'), the flux passing through the ring is quantized once the ring has become superconducting i.e. $\phi_o = h/2e$. The weak-link enables the trapped flux to change by discrete amounts. Changes in the pick-up voltage occur as the flux is incremented in amounts ϕ_o. In this way it is possible to measure the very small changes in flux ($\sim 10^{-14}$ T) such as is produced by thin film samples.

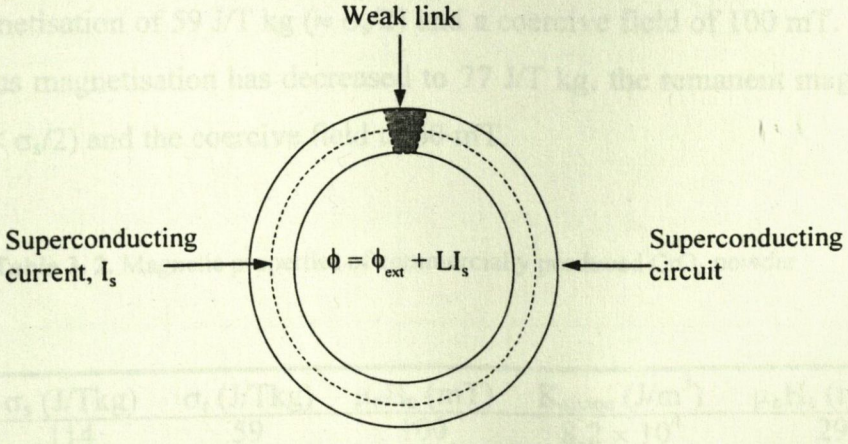

Fig. 3. 6. Basic schematic diagram of the SQUID configuration

3. 3. 2. Magnetic Neutron Diffraction

Powder neutron diffraction spectra were carried out at the LLB, Paris. A double axis DN5 diffractometer equipped with a linear multidetector was used to collect the data. The detector, filled with BF_3, gas comprised 800 cells spanning an angle 2θ of 160°. A pyrolytic graphite monochromator was used to select the working wavelength of 2.3433 Å. The samples were deposited in a vanadium sample holder (vanadium is practically transparent to neutrons) and immersed in a cryostat operating at temperatures in the range 1.5-300K. The flux of neutrons at the sample was approximately 1.5×10^6 neutrons cm^{-2} s^{-1} and the beam spot size was approximately 10×50 mm^2.

3. 4. Results

3. 4. 1. Magnetic Hysteresis

A. *Powders*

The hysteresis loops for the commercial powder at 5 K and 300 K are shown in Fig. 3.7 and the resulting magnetic properties are summarised in Table 3.2 below. At 5 K, the commercial powder shows a saturation magnetisation of 114 J/T kg, a remanent magnetisation of 59 J/T kg ($\approx \sigma_s/2$) and a coercive field of 100 mT. At 300 K the spontaneous magnetisation has decreased to 77 J/T kg, the remanent magnetisation to 29 J/T kg ($< \sigma_s/2$) and the coercive field to 60 mT.

Table 3. 2. Magnetic properties of commercially produced CrO_2 powder

T (K)	σ_s (J/Tkg)	σ_r (J/Tkg)	$\mu_0 H_c$ (mT)	K_{shape} (J/m^3)	$\mu_0 H_c$ (mT)^{SW}
5K	114	59	100	8.2×10^4	292
300K	77	29	60	3.8×10^4	198

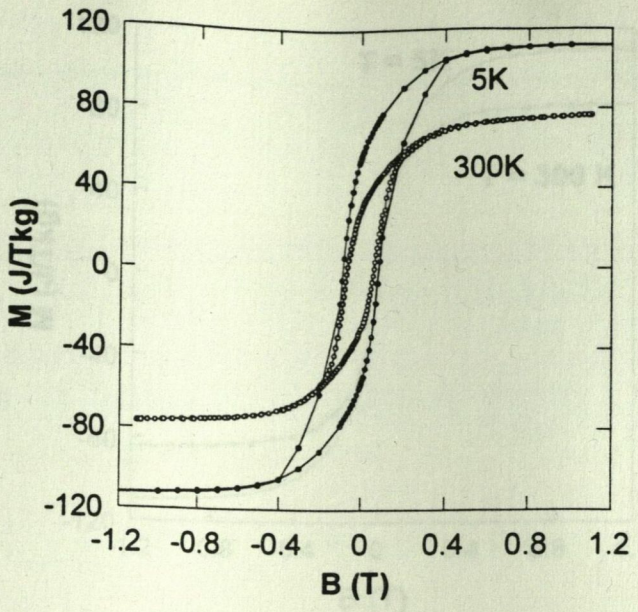

Fig. 3. 7. The hysteresis loop for a commercial powder (B-new) at 5 K and 300 K

Also shown in Table 3.2 is the coercivity $H_c = 2K_{shape}/\mu_o M_s$ calculated using the Stoner-Wohlfarth model. The shape anisotropy has been determined at 5 K and 300 K using equation 3.11. The aspect ratio of the commercial powder measured here is l/d ~ 5 hence, $N_{\|} = 0.0557$. The coercivity determined by this method is significantly larger than the measured values. Hence the commercial powder does not show ideal Stoner-Wohlfarth behaviour.

The magnetisation curves for a magnetically filtered reactor powder at 5 K and 300 K are shown in Fig. 3.8 and the values for the saturation magnetisation, remanence and coercivity are listed in Table 3.3.

Table 3. 3. Magnetic properties of magnetically filtered CrO_2 reactor powder (B58)

T (K)	σ_s (J/Tkg)	σ_r (J/Tkg)	$\mu_o H_c$ (mT)	K_{shape} (J/m^3)
5K	110	7.5	5	9×10^4
300K	82	4.3	3	4.9×10^4

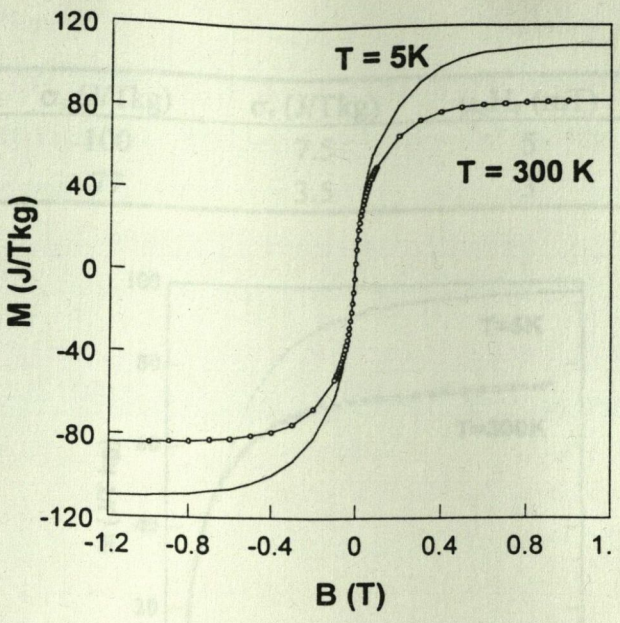

Fig. 3. 8. Hysteresis loop of a magnetically filtered reactor powder (B58) at 5 K and 300 K.

At low temperatures, the saturation magnetisation still falls short of the theoretical value of 133 J/T kg corresponding to 2 μ_B/CrO_2, possibly due to the fact that filtering the powder did not remove all the impurities. The shape anisotropy energy is also calculated for this powder assuming an aspect ratio l/d ~ 20 so that $N_{\|} \sim 0.00676$. However, unlike the commercial powders, which have dimensions of approximately $0.5 \times 0.1 \times 0.1\ \mu m^3$ and can be considered as single-domain particles, the reactor powders comprise particles up to 20 μm in length. Consequently, the particles contain many domains which leads to the much lower coercivity observed.

The magnetisation of an unfiltered powder was also measured at 5 K and 300 K. The results are shown in Fig. 3.9 and summarised in Table 3.4 below. For this sample, the saturation magnetisation is further reduced due to the presence of significant amounts of non-magnetic Cr_2O_3. The percentage of Cr_2O_3 in the sample was estimated from the x-ray diffraction pattern to be ~ 25%. This correlates with the reduction in the magnetisation by 33 J/T kg for this sample. The shape anisotropy has also been calculated for this powder assuming l/d ~20 and $N_{\|} \sim 0.00676$. As for the filtered powder, low coercivities are observed, despite the relatively large shape anisotropy , due to the particles being multidomain.

Table 3. 4. Magnetic properties of magnetically unfiltered CrO_2 reactor powder (B58)

T (K)	σ_s (J/Tkg)	σ_r (J/Tkg)	$\mu_o H_c$ (mT)	K_{shape} (J/m^3)
5K	100	7.5	5	7.4×10^4
300K	77	3.5	3	4.4×10^4

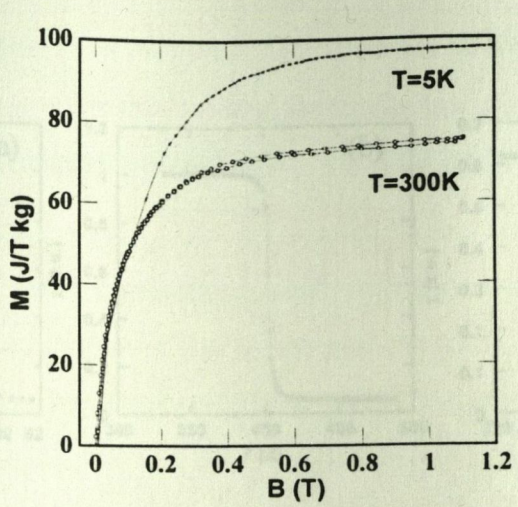

Fig. 3. 9. Hysteresis loop of an unfiltered reactor powder (B9) at 5 K and 300 K.

To determine the Curie temperature, T_c, of the magnetically filtered reactor powder and the commercial powder, the variation of the magnetisation with temperature in the range 5-400 K was measured at 0.05 T and 0.01 T respectively. The results are plotted in Fig. 3.10. Both powders exhibit a sharp decrease to zero magnetisation at 400(5) K.

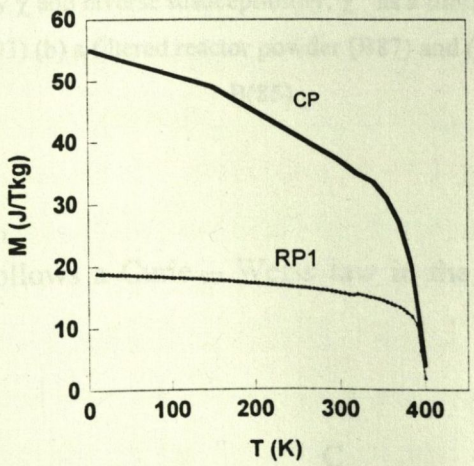

Fig. 3. 10. Magnetisation curve as a function of the temperature at a field of 0.01 T for a magnetically filtered reactor powder, RP1 (B58) and a field of 0.05 T for the commercial powder, CP (Bnew).

The Curie temperature of each powder was also determined using high temperature ac-susceptibility where a field of 1 mT oscillating at a frequency of 1 kHz was applied. T_c for each sample was determined by plotting the inverse susceptibility as a function of the temperature, see Fig. 3.11. The commercial powder showed a T_c = 400(2) K, the filtered powder showed a T_c = 395(5) K and the unfiltered reactor powder showed a T_c = 397(5) K.

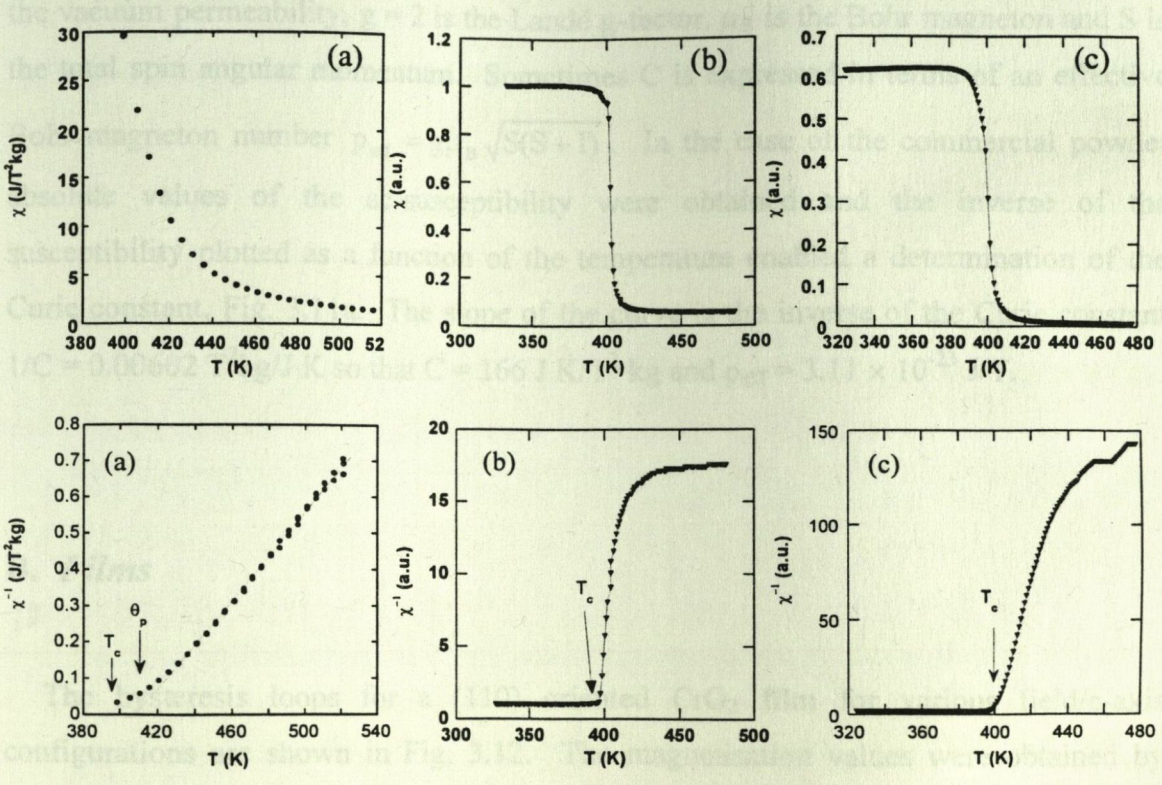

Fig. 3. 11. Susceptibility χ and inverse susuceptibility, χ^{-1} as a function of temperature for (a) the commercial powder (B1503) (b) a filtered reactor powder (B87) and (c) the unfiltered reactor powder B(85).

The susceptibility follows a Curie – Weiss law in the paramagnetic region i.e. at temperatures $T > T_c$:

$$\chi = \frac{C}{T - T_c} \qquad 3.16$$

where C is the Curie constant, defined as:

$$C = \frac{N\mu_o g^2 \mu_B^2 S(S+1)}{3k_B} \qquad 3.17$$

and $N = 3.5 \times 10^{28}$ Cr atoms/m^3 is the number of magnetic atoms per unit volume, μ_o is the vacuum permeability, $g = 2$ is the Landé g-factor, μ_B is the Bohr magneton and S is the total spin angular momentum. Sometimes C is expressed in terms of an effective Bohr magneton number $p_{eff} = g\mu_B\sqrt{S(S+1)}$. In the case of the commercial powder absolute values of the ac-susceptibility were obtained and the inverse of the susceptibility plotted as a function of the temperature enabled a determination of the Curie constant, Fig. 3.11a. The slope of the curve is the inverse of the Curie constant $1/C = 0.00602\ T^2kg/J\ K$ so that $C = 166\ J\ K/T^2\ kg$ and $p_{eff} = 3.11 \times 10^{-23}$ J/T.

B. *Films*

The hysteresis loops for a (110) oriented CrO_2 film for various field/c-axis configurations are shown in Fig. 3.12. The magnetisation values were obtained by taking an average sample thickness of 0.80(4) μm. This gave rise to values for the saturation magnetisation of 130(6) J/Tkg for all field/c-axis configurations which is in good agreement with the theoretical value of 133 J/Tkg.

The hysteresis loops vary depending on the direction of the magnetic field with respect to the film plane and the c-axis and can be associated with the various anisotropies that are present. When the field is in the plane of the film and parallel to the c-axis, there is very little hysteresis ($H_c \sim 1.7$ mT) and the magnetisation is easily saturated. The c-axis corresponds to both the needle axis and the easy axis of magnetisation. In this configuration, neither the needle shape nor the film shape play a role. Instead the hysteresis can be attributed entirely to the domain wall motion associated with the magnetocrystalline anisotropy. Rodbell et al. found the same result when the coercivity of an oriented CrO_2 film of thickness 0.8 μm was measured.[14]

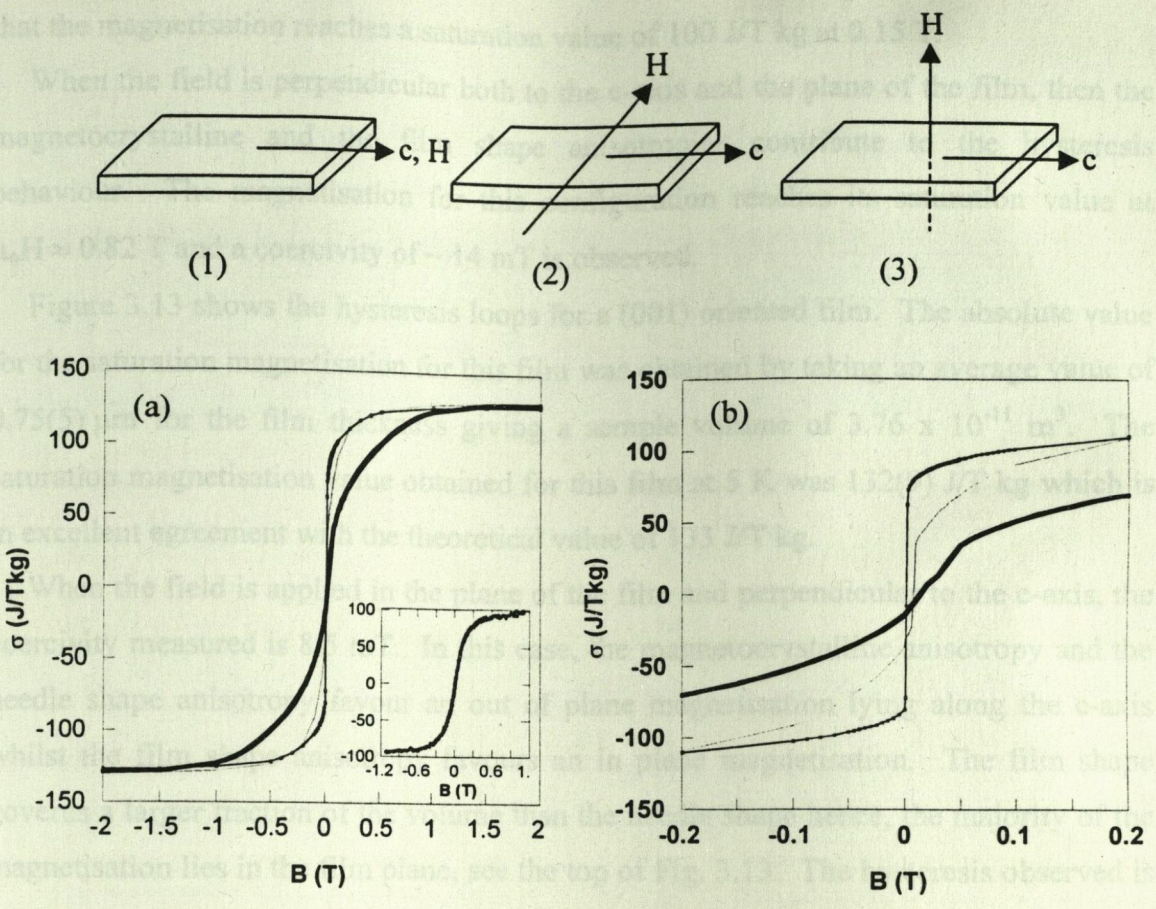

Fig. 3. 12. Hysteresis loops for a (110) oriented film (F86) at 5 K for the various field-c-axis configurations. The line containing the crosses corresponds to configuration (1), the thin solid line corresponds to configuration 2 and the thick solid line corresponds to configuration 3. Shown in (b) is an expanded view of the data from (a) for the field range – 0.2 - 0.2 T. The inset to (a) shows the hysteresis loop obtained at room temperature for the measuring configuration (2).

When the field is perpendicular to the c-axis but in the plane of the film the magnetocrystalline anisotropy must be overcome in order to align the magnetic moments with the magnetic field. The magnetisation in this case is observed to reach saturation at approximately 0.2 T and a small coercivity $H_c \sim 9$ mT is observed. The large slope in the hysteresis loop around zero field is most likely due to the misalignment of the sample in the external field i.e. the applied field may not have been at exactly 90° to the c-axis. That this is the case is supported by the fact that no such behaviour is observed for the room temperature curve (shown in the inset of Fig. 3.12a)

obtained for the same field/c-axis configuration. The room temperature curve shows that the magnetisation reaches a saturation value of 100 J/T kg at 0.15 T.

When the field is perpendicular both to the c-axis and the plane of the film, then the magnetocrystalline and the film shape anisotropies contribute to the hysteresis behaviour. The magnetisation for this configuration reaches its saturation value at $\mu_0 H \approx 0.82$ T and a coercivity of ~ 14 mT is observed.

Figure 3.13 shows the hysteresis loops for a (001) oriented film. The absolute value for the saturation magnetisation for this film was obtained by taking an average value of 0.75(5) μm for the film thickness giving a sample volume of 3.76×10^{-11} m^3. The saturation magnetisation value obtained for this film at 5 K was 132(9) J/T kg which is in excellent agreement with the theoretical value of 133 J/T kg.

When the field is applied in the plane of the film and perpendicular to the c-axis, the coercivity measured is 8.5 mT. In this case, the magnetocrystalline anisotropy and the needle shape anisotropy favour an out of plane magnetisation lying along the c-axis whilst the film shape anisotropy favours an in plane magnetisation. The film shape governs a larger fraction of the volume than the needle shape hence, the majority of the magnetisation lies in the film plane, see the top of Fig. 3.13. The hysteresis observed is largely a result of the growth of in-plane domains. Consequently, the magnetisation curve increases smoothly and rapidly up to the saturation point. The hysteresis associated with this field configuration is larger than that normally associated with domain wall motion and may be a result of pinning by the grain boundaries as well as the contribution from the out-of-plane magnetisation arising from the weaker magnetocrystalline and needle shape anisotropy.

When the field is applied out of the film plane and parallel to the c-axis two features are observed. The first is a smaller hysteresis of 4 mT and the second is a clear change of slope at H ~ 6 mT. In this configuration, the magnetic field must work to rotate the magnetisation out of the film plane. However, due to the rough texture of the (001) oriented films (Section 2. 4. 3, Chapter 2) there may already exist a component which lies out of the film plane. It is this part of the magnetisation that gives rise to the hysteresis loop observed at low fields. Once the out of plane component of magnetisation has been aligned the in plane component of magnetisation is aligned with the field. The magnetisation reaches saturation at an applied field of ~ 0.8 T. This

value corresponds to the demagnetisation field associated with the in plane film anisotropy i.e. $H_d = N_d M_o$ where $N_d = 1$.

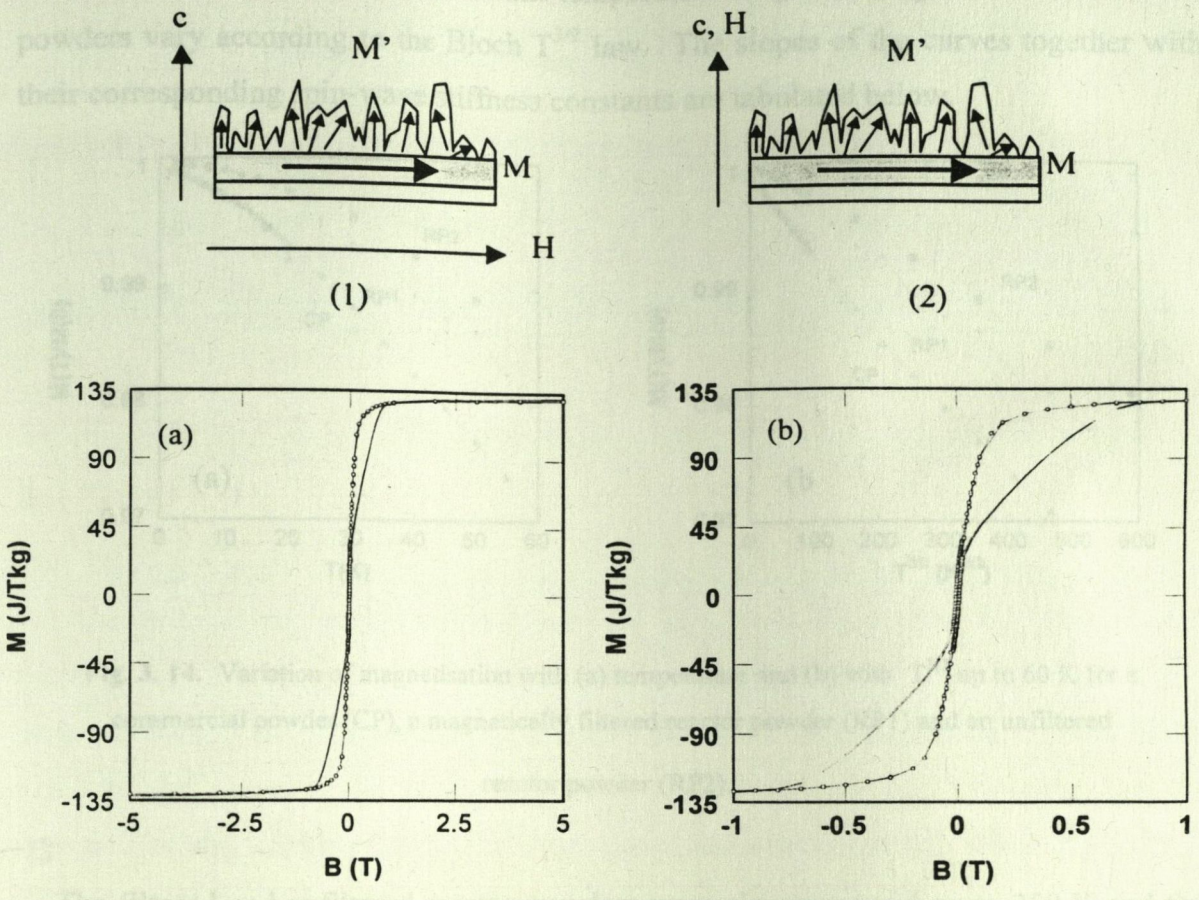

Fig. 3. 13. Top diagrams show the field/c-axis measuring configurations. M corresponds to the bulk in-plane magnetisation and M' corresponds to the out-of-plane component of magnetisation arising as a result of the rough texture of these films. Below are shown the hysteresis curves of the (001) oriented film (F85) at 5 K. The solid line with the open circles corresponds to the measuring configuration (1) and the thin black line corresponds to configuration (2). Diagram (a) shows the hysteresis loops up to 2 T, (b) shows an expansion of the loops for fields up to 1 T.

3. 4. 2. Magnetisation versus Temperature

A. *Powder*

The temperature dependence of magnetisation for a commercial powder (CP), a magnetically filtered reactor powder (RP1) and an unfiltered reactor powder (RP2) in

the temperature range 0-60 K is shown in Fig. 3.14. All the powders show the same general behaviour, but differ slightly in the rate at which the magnetisation decreases with temperature. It is clear that in this temperature range, the magnetisation for all the powders vary according to the Bloch $T^{3/2}$ law. The slopes of the curves together with their corresponding spin-wave stiffness constants are tabulated below.

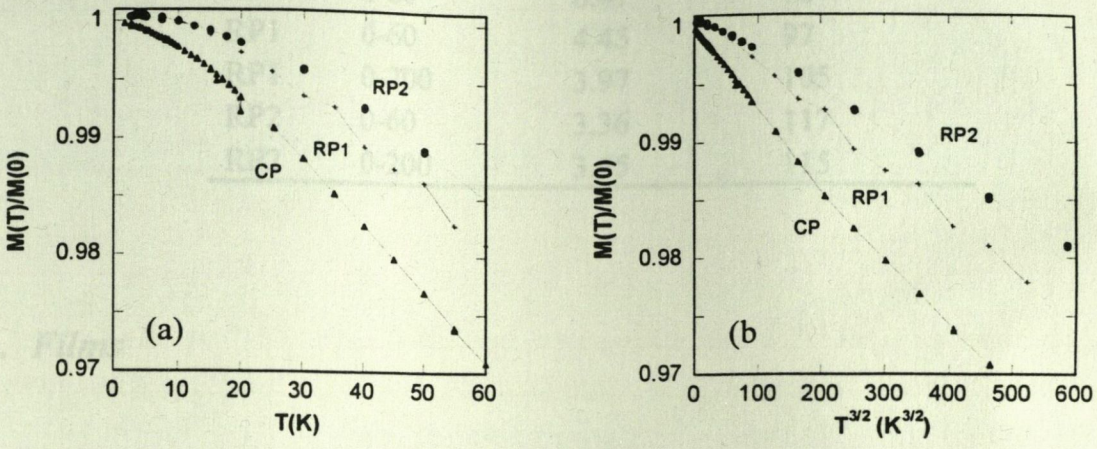

Fig. 3. 14. Variation of magnetisation with (a) temperature and (b) with $T^{3/2}$ up to 60 K for a commercial powder (CP), a magnetically filtered reactor powder (RP1) and an unfiltered reactor powder (RP2).

The filtered and unfiltered reactor powders were also measured up to 300 K and the magnetisation was observed to follow a $T^{3/2}$ dependence up to 200 K, Fig. 3.15. The results of the linear fits to this data are shown in Table 3.5 below.

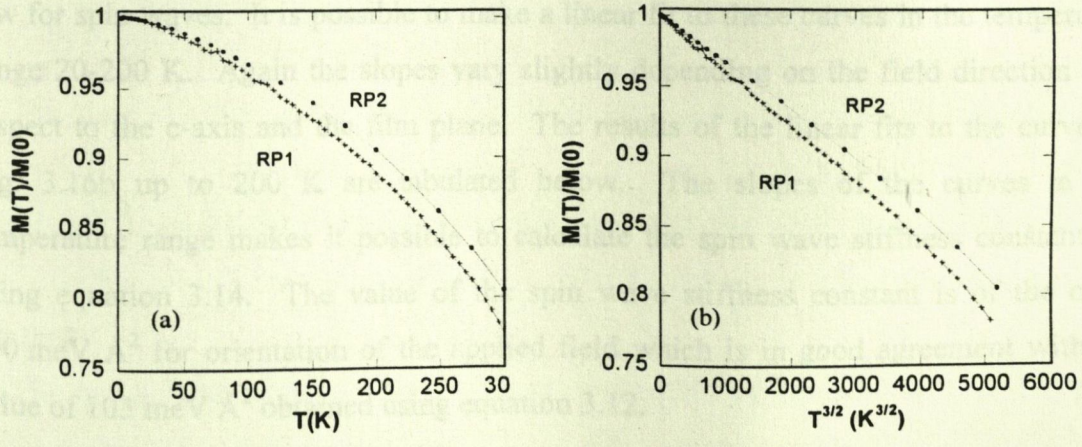

Fig. 3. 15. Variation of magnetisation with (a) temperature and (b) with $T^{3/2}$ for the filtered (RP1) and unfiltered (RP2) reactor powder up to 300 K.

Table 3. 5. Bloch constants and corresponding spin wave stiffness constants for the commercial powder (CP), filtered (RP1) and unfiltered (RP2) reactor powders

Sample	Temperature Range (K)	B ($\times 10^{-5}$ $K^{-3/2}$)	D (meV Å)
CP	0-60	6.47	76
RP1	0-60	4.45	97
RP1	0-200	3.97	105
RP2	0-60	3.36	117
RP2	0-200	3.45	115

B. *Films*

The normalised magnetisation curves for a (110) oriented film are plotted as a function of temperature in Fig. 3.16a for a magnetic field applied parallel and perpendicular to the c-axis and in the plane of the film and perpendicular to both the c-axis and the plane of the film. The M(T) curves vary slightly depending on the direction of the applied field. The most rapid decrease occurring when the field is applied parallel to the c-axis and in the plane of the film and the slowest decrease in magnetisation occurring when the field is applied perpendicular to both the c-axis and the film plane.

Figure 3.16b shows the variation of the magnetisation according to the Bloch $T^{3/2}$ law for spin waves. It is possible to make a linear fit to these curves in the temperature range 20-200 K. Again the slopes vary slightly depending on the field direction with respect to the c-axis and the film plane. The results of the linear fits to the curves in Fig. 3.16b up to 200 K are tabulated below. The slopes of the curves in this temperature range makes it possible to calculate the spin wave stiffness constant, D, using equation 3.14. The value of the spin wave stiffness constant is of the order 100 meV $Å^2$ for orientation of the applied field which is in good agreement with the value of 103 meV $Å^2$ obtained using equation 3.12.

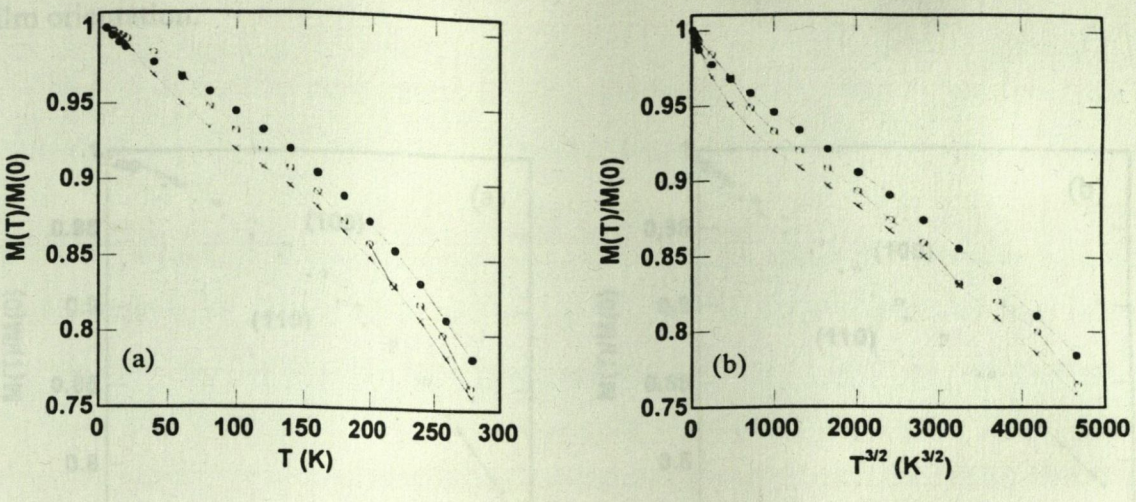

Fig. 3. 16. Variation of the magnetisation with (a) temperature and (b) $T^{3/2}$ for a (110) oriented film (F86) when H || plane and c-axis (solid circles), H || plane and ⊥ c-axis (empty circles), H ⊥ plane and c-axis (crosses).

Table 3. 6. Results of the linear fits to the normalised magnetisation curves plotted as a function of $T^{3/2}$ in the temperature range 20-200 K

Field Orientation	Temperature Range (K)	B ($\times 10^{-5}$ $K^{-3/2}$)	D (meV Å^2)
H || plane of film and c-axis	20-200	4.08	103
H || plane of film and ⊥ c-axis	20-200	4.52	97
H ⊥ plane of film and c-axis	20-200	4.13	102

The magnetisation curves for a (001) film were also measured in the temperature range 5-300 K with the field applied parallel and perpendicular to the c-axis. However, the signals obtained for these curves were quite noisy and it was impossible to extract any conclusive information regarding the Bloch constant or the spin-wave stiffness constant.

The normalised magnetisation curves as a function of temperature and $T^{3/2}$ for a (100) and a (110) oriented film from 5-300 K are compared in Fig. 3.17. The slopes of the curves for the (100) and (110) film were found to be 4.4×10^{-5} $K^{-3/2}$ and 4.1×10^{-5} $K^{-3/2}$ respectively, corresponding to spin-wave stiffness constants of 98 meV Å^2 and 102

meV Å^2. This shows that the spin wave stiffness constant does not depend greatly on film orientation.

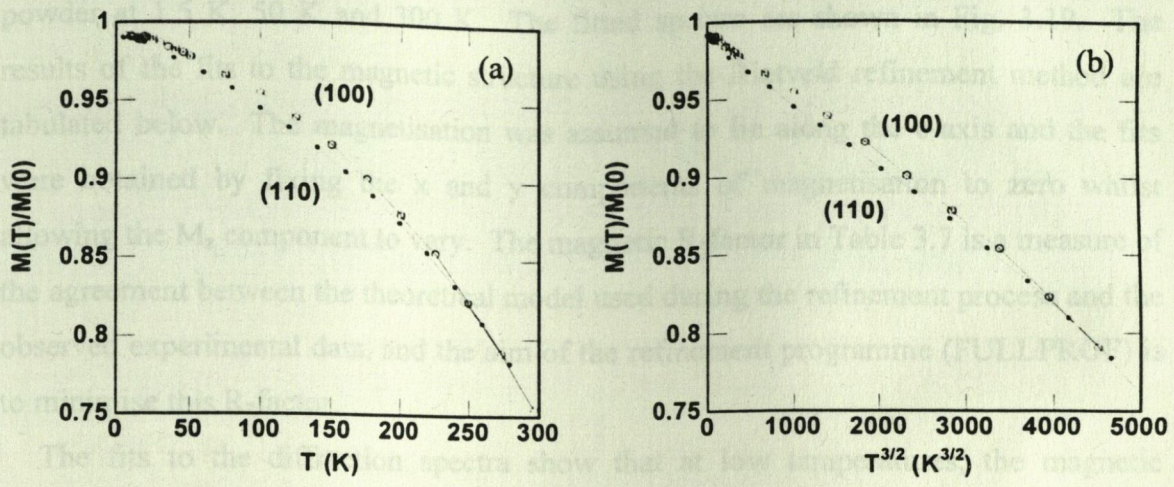

Fig. 3. 17. Solid circles and hollow circles show the variation of the magnetisation with (a) the temperature and (b) $T^{3/2}$ for a (100)-F11 and a (110)-F86 oriented film in the range 5-300 K with an applied field of 2 T.

The Curie temperature has been determined for the (110) oriented CrO_2 film to be 400 K. This was done by extrapolating the low temperature magnetisation curve to higher temperatures using a mean field approximation with S = 1.

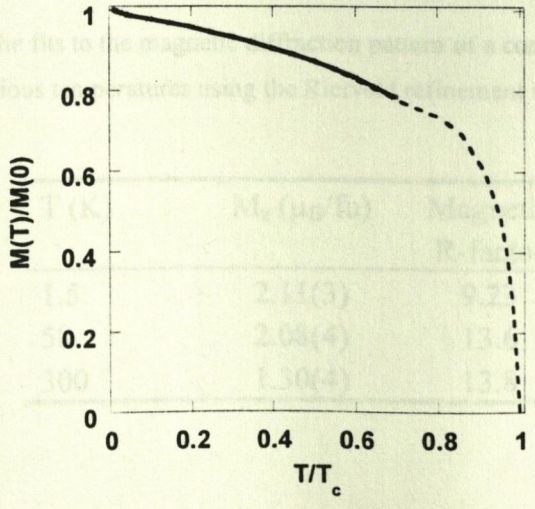

Fig. 3. 18. Temperature dependence of magnetisation for the (110) oriented CrO_2 film (F86). The dashed line shows the mean-field theory prediction for S = 1.

3. 4. 3. Neutron Diffraction

Neutron diffraction experiments were carried out on commercially produced CrO_2 powder at 1.5 K, 50 K and 300 K. The fitted spectra are shown in Fig. 3.19. The results of the fits to the magnetic structure using the Rietveld refinement method are tabulated below. The magnetisation was assumed to lie along the c-axis and the fits were obtained by fixing the x and y components of magnetisation to zero whilst allowing the M_z component to vary. The magnetic R-factor in Table 3.7 is a measure of the agreement between the theoretical model used during the refinement process and the observed experimental data, and the aim of the refinement programme (FULLPROF) is to minimise this R-factor.

The fits to the diffraction spectra show that at low temperatures, the magnetic moment on the Cr ion is a little larger than the expected moment of 2 μ_B/Cr^{4+} ion. The magnitude of the moment measured here is in good agreement with those reported by other authors who also found moments greater than 2 μ_B/Cr^{4+} ion at low temperatures.[10, 15] The larger values of the magnetic moment are expected to be an indication of a magnetic moment of opposite spin of the order of 0.05 μ_B on the oxygen anions with which the Cr^{4+} ions are hybridised. This idea is supported by the fact that magnetic X-ray dichroism experiments measured at the K-edge of oxygen show the presence of a moment on the oxygen anion of the order of -0.03 μ_B/O^{2-} ion.

Table 3. 7. Results of the fits to the magnetic diffraction pattern of a commercially produced powder at various temperatures using the Rietveld refinement method

T (K)	M_z (μ_B/fu)	Magnetic R-factor
1.5	2.11(3)	9.23
50	2.08(4)	13.6
300	1.30(4)	13.8

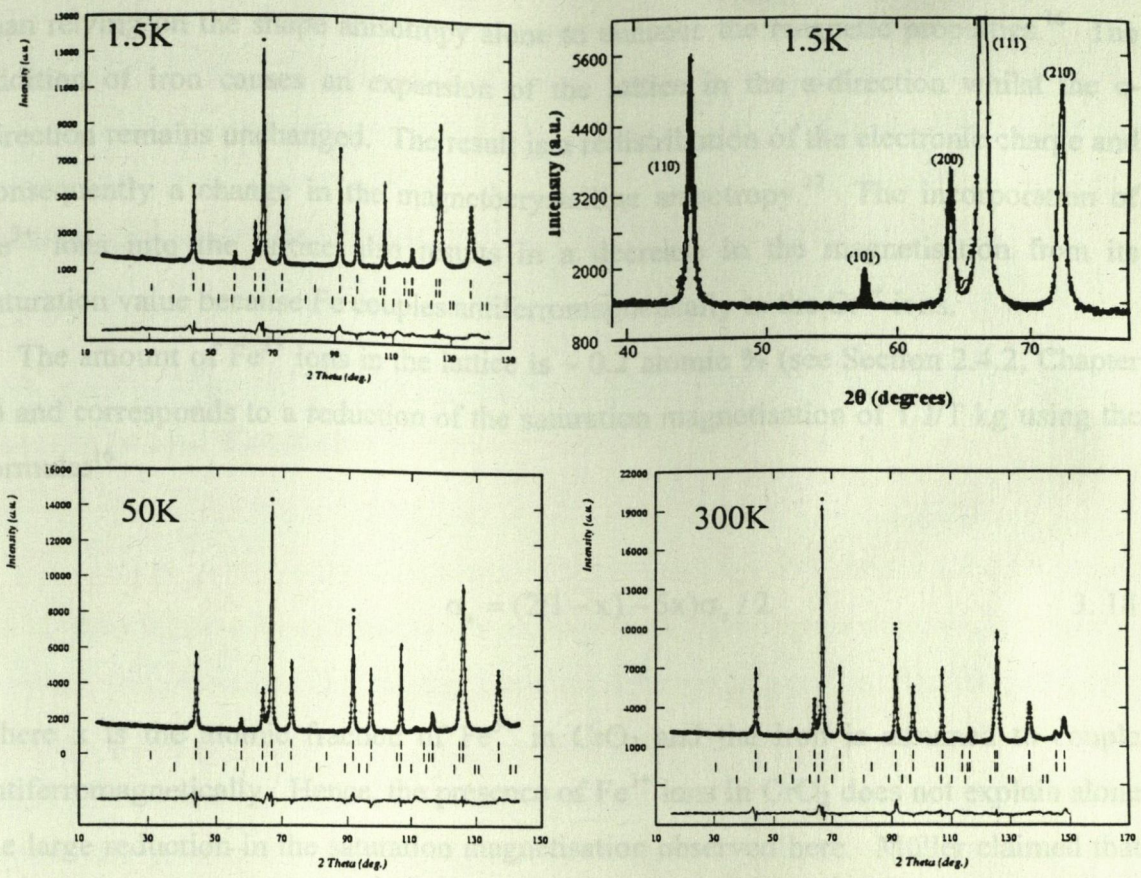

Fig. 3. 19. Neutron diffraction spectra of commercial powder (Bnew) at 1.5 K, 50 K and 300 K. The magnetic contribution to the Bragg peaks at 1.5 K are shaded.

3. 5. Discussion

A. Powders

Magnetisation

Low temperature bulk magnetisation measurements show that the saturation magnetisation of the commercial powder is 114 J/T kg. This is 15% smaller than the value of 133 J/T kg expected for half-metallic CrO_2 in which there are only two d-electrons at the Fermi level. In the commercial powder used here, Fe^{3+} is present as an

additive, and serves to increase the magnetocrystalline anisotropy of the material rather than relying on the shape anisotropy alone to enhance the magnetic properties.[16] The addition of iron causes an expansion of the lattice in the a-direction whilst the c-direction remains unchanged. The result is a redistribution of the electronic charge and consequently a change in the magnetocrystalline anisotropy.[17] The incorporation of Fe^{3+} ions into the lattice also results in a decrease in the magnetisation from its saturation value because Fe couples antiferromagnetically to the Cr^{4+} ions.

The amount of Fe^{3+} ions in the lattice is ~ 0.2 atomic % (see Section 2.4.2, Chapter 2) and corresponds to a reduction of the saturation magnetisation of 1 J/T kg using the formula:[16]

$$\sigma_s = (2(1-x)-5x)\sigma_s / 2 \qquad 3.18$$

where x is the atomic fraction of Fe^{3+} in CrO_2 and the iron is assumed to couple antiferromagnetically. Hence, the presence of Fe^{3+} ions in CrO_2 does not explain alone the large reduction in the saturation magnetisation observed here. Müller claimed that the measured magnetisation value is always lower than those calculated by equation 3.16 due to the formation of a non-magnetic stabilisation layer during the final stages of the hydrothermal production process.[16] This stabilisation layer was recently identified, using high resolution electron microscopy, as orthorhombic (or equivalently β) CrOOH (see Section 2.1.4) and layers typically 2.5-3 nm in thickness were found to exist in particles of length 300 nm and width 35 nm. The result was a reduction of the saturation magnetisation of up to 20% for the commercial powder and explains the large 15% reduction in the saturation magnetisation observed here.[18]

Bulk magnetisation measurements of pure reactor powder show a low temperature saturation magnetisation of 110 J/T kg, a value which is also smaller than the predicted value of 133 J/T kg by 17%. Since the reactor powders were prepared using an anhydrous method (see Section 2.2, Chapter 2), the presence of a β-CrOOH surface layer at this stage of sample production is not possible. Furthermore, the particle size is much larger than for the commercial powder. However, it is possible that the filtration process resulted in the formation of a β-CrOOH surface layer as solvents such as ethanol and acetone were used. It is also likely that not all the Cr_2O_3 was removed during filtration. Yet, whilst the presence of β-CrOOH and Cr_2O_3 would explain the

large reduction in saturation magnetisation neither were detected in the powder x-ray diffraction patterns. This may be because they were poorly crystallised.

The bulk saturation magnetisation of the unfiltered reactor powder shows a value for the saturation magnetisation of 100 J/ T kg. Powder x-ray diffraction revealed the presence of ~ 25% non-magnetic Cr_2O_3 in this sample. This correlates well with the reduction in moment of 33 J/T kg.

Coercivity and Remanence

The absence of any appreciable amount of coercivity for both the pure and unfiltered reactor powders can be ascribed to the fact that these particles are large (~ 20 μm) and therefore multi-domain. On the other hand, the commercial powder comprises of single domain particles (length ~ 0.3-1.0 μm), giving rise to the much larger coercivities observed for these powders. It should be noted however, that even the single domain commercial powders do not show an ideal Stoner-Wohlfarth behaviour for which coercivities three times larger than those observed are calculated. As mentioned in section 3.1.3, the Stoner-Wohlfarth model for coherent rotation overestimates the coercivity by a factor of 2-10. This is because it does not take account of the nucleation of reverse domains due to sample defects and inhomogeneities. This is known as Brown's Paradox.

The critical single-domain radius has been calculated for the commercial powder having a room temperature saturation magnetisation of 77 J/T kg to be 67 nm using the formula:[11]

$$R_{sd} = \frac{36\sqrt{AK_1}}{\mu_o M_s^2} \qquad 3.19$$

where the exchange stiffness is typically A = 3.0 pJ/m and $K_1 = 3.7 \times 10^4$ J/m^3 is the room temperature anisotropy constant. The interaction of single-domain particles result in a reduction of the magnetostatic energy and consequently an increase in the critical single-domain radius. Hence, the particles of dimension 0.3-1 μm in the commercial

powder are single domain but with lower coercivities than predicted using the Stoner Wohlfarth model.

However, the remanence observed for the commercial powders at 5 K does coincide with that predicted by the Stoner-Wohlfarth model for which $M_R \approx \sigma_s/2$. The filtered and unfiltered reactor powders on the other hand show much smaller remanent magnetisation owing to the particle microstructure. That is, it is easier to nucleate reverse domains in larger particles

Curie temperature

The Curie temperature has been determined for the commercial powder and the filtered and unfiltered reactor powder using high temperature susceptibility measurements. In all cases $T_c \approx 400$ K and this correlates well with high temperature magnetisation data obtained for the commercial and filtered reactor powder. Furthermore, the Curie temperature of 400 K is in good agreement with previously reported values.[12, 19, 20] Absolute values for the susceptibility, obtained for the commercial powder give a Curie constant $C = 166$ J/T^2 K kg and a resulting effective Bohr magneton $p_{eff} = 3.35\mu_B$. This exceeds the theoretical value $p_{eff} = 2.83\mu_B$ for $S = 1$ by 15%. An enhanced Curie-Weiss susceptibility has been recognised recently as a key signature of short range ferromagnetic correlations owing to magnetic clustering in the paramagnetic regime as has been evidenced for the manganites in the paramagnetic regime.[21] However, the discrepancy observed here is more likely due to the fact that a powder sample having a large volume porosity was measured as opposed to a solid sample with negligible demagnetising effects.[22]

Temperature dependence of Magnetisation

The low-temperature dependence of the magnetisation for the commercial powder and the filtered and unfiltered reactor powders show the $T^{3/2}$ Bloch law expected for ferromagnets. In particular, the data obtained for the filtered and unfiltered reactor can

be fitted up to $T \sim T_c/2$ using equation 3.13. The spin wave stiffness constant, D, for both the filtered and unfiltered reactor powder is of the same order of magnitude as the value of 103 meV $Å^2$ calculated using equation 3.12. The commercial powder on the other hand shows a more rapid decrease in the magnetisation with increasing temperature and consequently a smaller spin wave stiffness constant of 76 meV $Å^2$. This is understood by taking account of the surface layer of the CrO_2 particles whose magnetisation falls off more quickly than that of the bulk CrO_2. Therefore, the relative change of the magnetisation with temperature is expected to be larger for the commercial powder than for the reactor powder. Consequently, a smaller spin wave stiffness constant is determined. The same argument may also be used for the slightly larger change in the magnetisation of the filtered reactor powder with temperature compared to the unfiltered powder.

Magnetic Moment

Neutron diffraction experiments, carried out on the same commercial CrO_2 powder as used in the bulk magnetisation measurements, show directly a low temperature moment of 2.11(3) μ_B/Cr^{4+} in agreement with a previous measurement by Burdett et al.[10] The presence of Fe^{3+} in the sample is not expected to contribute much to the moment measured as it is present in very small quantities ($\leq$ 0.2%). CrO_2 is a half-metallic ferromagnet and is expected to show an integral moment of 2 μ_B/CrO_2. Hence, it is concluded that the oxygen atom possesses a negative moment of $\sim$ -0.05 μ_B/O^{2-} in order to achieve this value. This correlates with the value of –0.03 μ_B/O^{2-} recently measured by K. Attenkofer and G. Schütz using X-ray circular dichroism at the K-edge of oxygen as well as certain band structure calculations (see Section 1.4, Chapter 1).[23] The existence of an oxygen moment implies the presence of holes in the O 2p band, as stated by Korotin et al.[4] As we shall see in chapter 5, the presence of holes may lead to unusual transport properties that can be explained using a two band model in which electrons and holes contribute to the transport properties.

An unfortunate aspect of the neutron diffraction experiments presented here is that the direction of the moment was not allowed to vary during the refinement process i.e.

the moment was assumed to lie along the c-axis. However, this is a reasonable assumption to make for this powder since the demagnetising field associated with these small acicular particles ensures that the magnetisation lies parallel to the c-axis. As mentioned, there have been reports indicating that the moment lies in the a-c plane at an angle of 20-40° to the c-axis. It is possible that including a transverse moment in the spectral refinements may result in a larger moment in which case, the opposing moment on the oxygen and consequently the number of holes in the O 2p band may be larger. Refinements including a transverse moment are in progress. It should be pointed out however, that since the exchange energy $J = 37.5\ K >> K_1 = 0.2\ K$ a c-axis anisotropy is more likely than an off c-axis anisotropy. An off c-axis anisotropy would suggest a four-fold easy axis anisotropy since the crystal is tetragonal. There is no evidence for this. Furthermore, complete directional information about the magnetic moment in a tetragonal system is not obtainable from a powder diffraction experiment. For these reasons, assuming a c-axis magnetisation during refinement is acceptable and gives a good estimate for the moment on the Cr ion. Neutron diffraction experiments were not carried out on reactor produced CrO_2 powders, since the amount of powder produced in the reactor vessel is too little.

B. Films

Magnetisation

The magnetisation of the (110) and the (001) oriented films show a bulk magnetisation of 130(3) J/T kg and 132(3) J/T kg which is in good agreement with the expected magnetisation of 133 J/T kg. These values were obtained by taking an average thickness of 0.80(2) μm and 0.75(2) μm for the (110) and (001) film respectively.

Coercivity and Remanence

The shape of the magnetic hysteresis loops of oriented CrO_2 films was found to depend largely on the substrate orientation and the applied field to c-axis configuration. For the (110) oriented film, a small coercivity of nearly 2 mT is observed when the external field is applied parallel to the c-axis and in the plane of the film and is attributed to the domain wall motion associated with the magnetocrystalline anisotropy.

When the field is applied perpendicular to the c-axis of the (110) oriented film, a coercivity of ~ 9 mT is observed and the magnetisation reaches saturation at $\mu_o H_s \sim 0.2$ T. The anisotropy energy, K_1, can be determined by equating H_s to the anisotropy energy i.e. $H_s \sim 2K_1/M_s$. In this case, K_1 is determined to be 6.4×10^4 J/m^3 which is significantly larger than the low temperature value $K_1 = 4.9 \times 10^4$ J/m^3 deduced by Rodbell et al. using ferromagnetic resonance techniques.[6] It should be noted that these films have a clear needle-like texture (see Section 2.4.3, Chapter 2) which can induce an additional anisotropy so that the anisotropy measured is in fact a superposition of the magnetocrystalline anisotropy and the induced anisotropy arising from the needle-like texture of the films leading to larger values of the anisotropy energy. The coercivity of 9 mT in this case is larger than that normally associated with domain wall motion. However, pinning by grain boundaries arising also as a result of the needle-like texture of these films is possible and may account for the larger coercivity. In addition, it is suspected that the sample may not have been aligned properly with the applied field (this is suggested by the sharp change in the magnetisation about zero field) so that the coercivity measured may not be exactly 9 mT. The room temperature magnetisation of this film reaches saturation at 0.15 T with a value of 100 J/T kg, as evidenced by room temperature magnetisation measurements carried out for the field in the film plane and perpendicular to the c-axis. In this case, the anisotropy constant is determined to be $K_1 = 3.7 \times 10^4$ J/m^3.

When the field is applied perpendicular to the plane of the (110) plane, the magnetisation is observed to reach saturation at an applied field $\mu_o H \sim 0.8$ T. This is exactly as expected because of the demagnetising field, H_d, associated with the film shape. The demagnetisation factor $N_\perp = 1$ is determined using equation 3.7. A coercivity of 14 mT is observed in this case and is again attributed to domain wall

motion and pinning by the grain boundaries associated with the films needle-like texture.

The hysteresis loops observed for the (001) oriented films are explained in terms of the competing effects of needle-shape anisotropy and magnetocrystalline anisotropy both of which favour an out-of-plane magnetisation and a film shape anisotropy which favours an in-plane magnetisation. The small coercivities observed when the applied field is both parallel and perpendicular to the c-axis is due to domain wall motion of the in-plane magnetisation, irreversible rotation of the out-of-plane component of magnetisation (M') and pinning by the grain boundaries.

Temperature Dependence of Magnetisation

The temperature dependence of magnetisation for a (110) oriented film and a (100) oriented film show similar behaviour and can be fitted up to a temperature $T = T_c/2$ using the Bloch $T^{3/2}$ law defined in equation 3.13. The spin wave stiffness constant, D, for each sample was found to be similar for both samples and correlated well with the theoretical value of 103 meV $Å^2$ deduced using equation 3.12.

The magnetisation as a function of temperature was also measured in the case of the (110) oriented film for an external field applied parallel and perpendicular to the c-axis and in the plane of the film and perpendicular to the c-axis and the film plane. The resulting curves showed similar behaviour and fits up to 200 K using equation 3.13 showed that the slope of these curves (= Bloch constant) varied only slightly with field/c-axis orientation. The Curie temperature for the (110) oriented film was deduced to be 400 K using a mean field extrapolation for S = 1.

As a summary, a table, listing the magnetic properties of the films and powders measured, is shown below.

Table 3. 8. Magnetic properties measured for oriented CrO_2 films, F85-(001) and F86-(110) and the commercial powder and filtered and unfiltered reactor powders. (Note: the exchange stiffness, A, was determined using the experimentally determined values of the spin-wave stiffness constant, $D = 2AV/N_{at}S$) where V is the volume of the unit cell and N_{at} is the number of Cr ions in the unit cell

Sample	F-86 (110)	F-85 (001)	CP	RP1	RP2
T_c	400	-	400(5)	398(5)	397(5)
J (meV)	3.25	3.25	3.25	3.22	3.21
K_1 $(J/m^3)_{5K}$	6.5×10^4	-	-	-	-
K_1 $(J/m^3)_{300K}$	3.7×10^4		-	-	-
K_{shape} $(J/m^3)_{5K}$	-	-	8.2×10^4	9×10^4	7.4×10^4
K_{shape} $(J/m^3)_{300K}$	-	-	3.8×10^4	4.9×10^4	4.4×10^4
M_o $(J/T\ kg)_{5K}$	130(3)	132(3)	114	110	100
M_o $(\mu_B/fu)_{5K}$	1.96(5)	1.99(5)	1.72	1.66	1.5
M_o $(\mu_B/Cr^{4+})_{5K}$	-	-	2.11	-	-
M_s $(J/Tkg)_{300K}$	100	-	77	82	80
D (meV Å^2)	101	-	76	101	116
A (pJ/m)	2.83	-	2.13	2.83	3.25

References

[1] J. Crangle, *Solid State Magnetism*, Hodder and Sunderland Ltd. (1991)

[2] A. Ahoroni, *Introduction to the Theory of Ferromagnetism*, Clarendon Press, Oxford (1996)

[3] L. Levy, *Magnétisme et Supraconductivité* (1994)

[4] M. A. Korotin, V. I. Anisimov, D. I. Khomskii and G. A. Sawatsky, Phys. Rev. Lett., **80**, 4305-4308 (1998)

[5] T. J. Swoboda, P. Arthur Jr., N. L. Cox, J. N. Ingraham and M. S. Sadler, J. Appl. Phys., **32**, 374S-375S (1961)

[6] D. S. Rodbell, J. Phys. Soc. Jpn., **21**, 1224-1225 (1966)

[7] R. A. McCurrie, *Ferromagnetic Materials: Structure and Properties*, Academic Press (1994)

[8] W. H. Cloud, D. S. Schreiber and K. R. Babock, J. Appl. Phys., **33**, 1193-1194 (1962)

[9] F. J. Darnell and W. H. Cloud, Colloque International du C.N.R.S., **4**, 1164-1166 (1965)

[10] J. K. Burdett, G. J. Miller, J. W. Richardson, Jr. and J. V. Smith, J. Am. Chem. Soc., **110**, 8064-8071 (1988)

[11] R. Skomski and J. M. D. Coey, *Permanent Magnetism*, IoP Publishing Ltd. (1999)

[12] D. Jiles, *Introduction to Magnetism and Magnetic Materials*, Chapman and Hall (1991)

[13] K. Niira, Phys. Rev., 117(1), 129-133 (1960); A. R. Mackintosh Phys. Rev. Lett, **4**, 140-142 (1963);

[14] D. S. Rodbell, R. C. de Vries, W. D. Barber and R. W. de Blois, J. Phys. Soc. Jpn., **38**, 4552-4553 (1967)

[15] K. Siratori and S, Iida, J. Phys. Soc. Jap., **15**, 210-211 (1960)

[16] M. W. Müller, E. Schwab and R. J. Veitch, IEEE Transactions on Magnetics, **26**, 1897-1899 (1990)

[17] H. Y. Chen and D. M. Hiller, J. E. Hudson, C. J. A. Westenbroek and E. I. Du Pont de Nemours, IEEE Trans. Mag., **20**, 24-26 (1984)

[18] M. Essig, M. W. Müller and E. Schwab, IEEE Trans. mag., **26**, 69-71 (1990)

[19] H. Brändle, D. Weller, S. S. Parkin, J. C. Scott, P. Fumagalli, W. Reim, R. J. Gambino, R. Ruf, G. Güntherodt, Phys. Rev. B, **46**, 13889-13895 (1992)

[20] J. B. Goodenough, *Magnetism and the Chemical Bond*, John Wiley and Sons, Inc (1976)

[21] J. M. de Theresa, Nature, **386**, 256 (1997)

[22] Rhian-Mari Thomas, Ph. D. Thesis (1999)

[23] K. Attenkofer and G. Schütz, J. Phys. IV France, **7**, C2459-C2460(1997)

Chapter 4

Thermal Properties of CrO_2

4. 1. Introduction

As part of the characterisation of the physical properties of CrO_2 it is useful to study and measure its thermal properties. Measurement of the specific heat, for example, makes it possible to determine the density of states at the Fermi level, a quantity that reveals much about the electronic structure of CrO_2 and validates band calculations. Quantised lattice vibrations, *phonons*, are central to the understanding of the thermal properties of solids and measuring the phonon spectra of CrO_2 enables us to quantify the atomic motions whilst providing an indication of the importance of phonons to the overall physical properties observed. Thus, these measurements, whilst fundamental to the overall understanding of CrO_2, can also lend support to the theories proposed to explain other properties such as the electronic transport.

4. 1. 1. Phonons

A crystal is depicted as a regular arrangement of stationary atoms. However, according to Heisenberg's uncertainty priniciple, it is not possible to know simultaneously and exactly the position and the momentum of a particle i.e. $\Delta x \Delta p \approx \hbar$. Thus in a real crystal at the absolute zero of temperature, atoms are not fixed at lattice sites but vibrate around their equilibrium position, R_e. The energy the atoms possess as a result of this zero point motion is known as the zero point energy. As the temperature increases, the atoms acquire more thermal energy and the amplitude of the oscillations increases. The potential energy associated with the vibrating atom/molecule can be represented, in its simplest form, by:

$$V(q) = \tfrac{1}{2}Kq^2 \qquad 4.1$$

where K is the force constant in Hooke's law ($F = -Kq$) for the displacement $q = R-R_e$ of an atom from its equilibrium position. The graph of this function is a parabola and is referred to as the harmonic potential. However, in a real crystal, the energy required to bring two atoms closer together (i.e. to compress a bond) is greater than the energy required to stretch a bond. Consequently, anharmonic functions, such as the Morse function: $V(q) = D(1-\exp(-aq)^2)^2$, describe more effectively the interatomic potential.

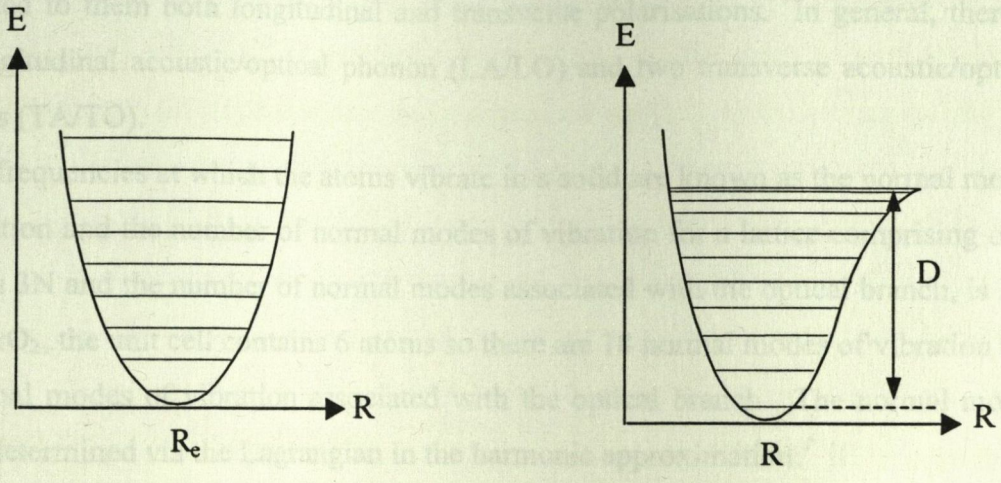

Fig. 4. 1. (a) Harmonic potential and (b) anharmonic potential showing the discrete vibrational energy levels in a solid. D is the dissociation energy and refers to the energy required to break the bonds in a crystal.

According to classical mechanics, an harmonic oscillator may vibrate with any amplitude. Quantum mechanics, however, shows that atoms in a solid can only exist in discrete energy states:

$$E_i = (n + \tfrac{1}{2})\hbar\,\omega_i, n = 1, 2, 3..... \qquad 4.2$$

In the case of the harmonic potential, the energy levels are equidistant whilst for the anharmonic potential the distance between levels decreases as the energy increases.

The repetitive and systematic displacement of atoms from their equilibrium positions gives rise to lattice vibrational waves whilst the discrete nature of the atomic vibrations in a crystal allows them to be classified as a type of particle. The particle or quantised aspect of the lattice vibration is called the *phonon.*

Phonons can be either 'acoustic' or 'optical' depending on whether the atoms in the lattice and their centre of mass vibrate together or whether the atoms vibrate against each other with their centre of mass fixed. If there are two types of atom of opposite charge, the latter motion can be excited by electric fields as, for example, light waves. Hence, optical phonon. Acoustic phonons are low energy vibrations whilst optical phonons are higher energy lattice vibrations. The acoustic and optical phonons have associated to them both longitudinal and transverse polarisations. In general, there is one longitudinal acoustic/optical phonon (LA/LO) and two transverse acoustic/optical phonons (TA/TO).

The frequencies at which the atoms vibrate in a solid are known as the normal modes of vibration and the number of normal modes of vibration for a lattice comprising of N atoms is 3N and the number of normal modes associated with the optical branch, is 3N-3. In CrO_2, the unit cell contains 6 atoms so there are 18 normal modes of vibration and 15 normal modes of vibration associated with the optical branch. The normal modes can be determined via the Lagrangian in the harmonic approximation:[♪]

$$L(q_i, \dot{q}_i, t) = \sum_i \frac{\dot{q}_i^2}{2\mu_i} - \frac{1}{2}\sum_{i,j} K_{ij} q_i q_j \qquad 4.3$$

and the Lagrange equations i.e.

$$\frac{d}{dt}\left(\frac{dL}{d\dot{q}_i}\right) - \frac{dL}{dq_i} = 0 \qquad 4.4$$

[♪] The harmonic approximation assumes that the vibrations of atoms about their equilibrium position, R_e, is small so that the interatomic potential (V(R)) can be expanded using a Taylor series expansion for which $(dV/dR)_{Re} = 0$.

Substituting equation 4.3 into equation 4.4 it is possible to obtain a system of coupled equations of the type:

$$\ddot{q}_i + \sum_j \mu_i K_{ij} q_j = 0 \qquad 4.5$$

where q_i is the displacement of the ith atom from its equilibrium position, μ_i is the reduced mass and $K_{ij} = \partial^2 V / \partial q_i \partial q_j$ is the force constant. The solutions to equation 4.5, in $\exp(i\omega_i t)$, yield the normal modes of vibration of frequency ω_i. The solutions are therefore an assembly of independent harmonic oscillators defined by frequencies ω_i and normal coordinates Q_i.[1] In the elastic continuum limit, the velocity, v, of the lattice vibrations through the crystal is proportional to the frequency of the vibrations and $\omega = vk$ that is, the velocity is independent of frequency where k is the wave-vector. However, the periodicity of the lattice causes the medium to be dispersive so that the velocity of propagation of the lattice wave is in fact a function of the frequency. A phonon dispersion relation describes the dependence of frequency ω on the wave-vector, k. A typical phonon dispersion relation showing the dispersion of acoustical and optical branches is shown below.

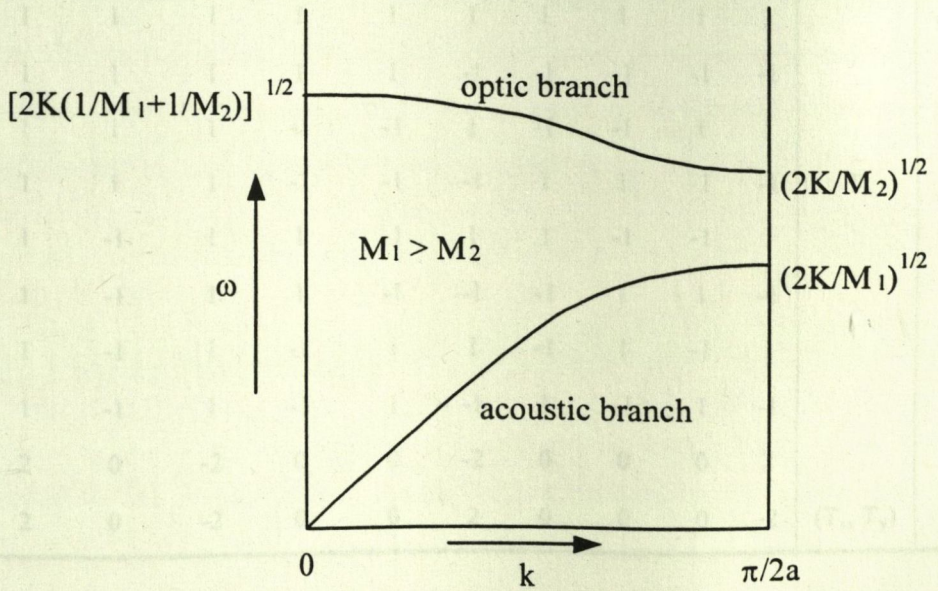

Fig. 4. 2. Phonon dispersion relation showing the acoustic and optical branches for the simplest case of a linear diatomic lattice.

The motion of the atoms in a crystal depend also on the symmetry of the crystal which is defined by a particular point group. A point group comprises of a set of symmetry operations which when applied to the crystal leaves it unchanged. The point group of CrO_2 is 4/mmm or D_{4h}. The frequency of the normal modes of vibration can be represented by one of the irreducible representations of this point group which are listed in the corresponding character table, see Table 4.1 below. The theoretical treatment of the classification of solids into their point groups and the labelling of the normal modes by an irreducible representation of the point group is discussed in many text books on spectroscopy and Group Theory and shall not be discussed further here.[1, 2]

Table 4. 1. Character Table for the point group D_{4h}: 4/mmm. The first row shows the point group and the symmetry elements belonging to this point group. The first column shows the labels of the irreducible representations. Columns 2-10 list the characters of the irreducible representations. (The characters of an irreducible representation express the directional properties associated with a particular symmetry element). Columns 11 and 12 show which irreducible representation describe the infra-red and Raman active modes of vibration.

D_{4h}	E	$2C_4(z)$	C_2''	$2C_2$	$2C_2'$	σ_h	$2\sigma_v$	$2\sigma_d$	$2S_4$	i	IR	Raman
A_{1g}	1	1	1	1	1	1	1	1	1	1		$\alpha_{xx}+\alpha_{yy}$, α_{zz}
A_{1u}	1	1	1	1	1	-1	-1	-1	-1	-1		
A_{2g}	1	1	1	-1	-1	1	-1	-1	1	1		
A_{2u}	1	1	1	-1	-1	-1	1	1	-1	-1	T_z	
B_{1g}	1	-1	1	1	-1	1	1	-1	-1	1		$\alpha_{xx}-\alpha_{yy}$
B_{1u}	1	-1	1	1	-1	-1	-1	1	1	-1		
B_{2g}	1	-1	1	-1	1	1	-1	1	-1	1		α_{xy}
B_{2u}	1	-1	1	-1	1	-1	1	-1	1	-1		
E_g	2	0	-2	0	0	-2	0	0	0	2		$(\alpha_{yz}, \alpha_{xz})$
E_u	2	0	-2	0	0	2	0	0	0	-2	(T_x, T_y)	

where:

- E is the identity
- C_4 is a four-fold rotation axis about the z-axis
- C_2'' is a two-fold rotation axis about the z-axis
- C_2 and C_2' are two-fold rotation axes perpendicular to the four-fold rotation axis
- σ_h is a horizontal mirror plane perpendicular to the four-fold rotation axis
- σ_v is a vertical mirror plane containing the four-fold rotation axis
- σ_d is a diagonal mirror plane containing the four-fold rotation axis
- S_4 is a four-fold screw axis
- i is an inversion centre

To observe an optical phonon spectrum both infra-red and Raman spectroscopy can be employed. Infra-red spectroscopy is concerned with the transition between vibrational states due to the absorption of light from an IR source of energy $\Delta E = h\upsilon$ and a vibration is IR-active if the dipole moment is changed during vibration. On the other hand, Raman spectroscopy is concerned with the measurement of the light scattered from a sample when irradiated with laser beams in the UV-visible region. In this case, the energy absorbed is greater than energy required to induce a transition between vibrational states. A vibration is Raman-active if the polarizability is changed during vibration. In the next section the principles of Raman spectroscopy will be discussed in advance of the results to be presented in section 4.3.

4. 1. 2. Raman Spectroscopy

To observe the Raman effect, a sample is irradiated by an intense laser beam, of frequency ν_o, and the light scattered from the sample is observed perpendicular (or antiparallel) to the direction of incident light, Fig. 4.3.

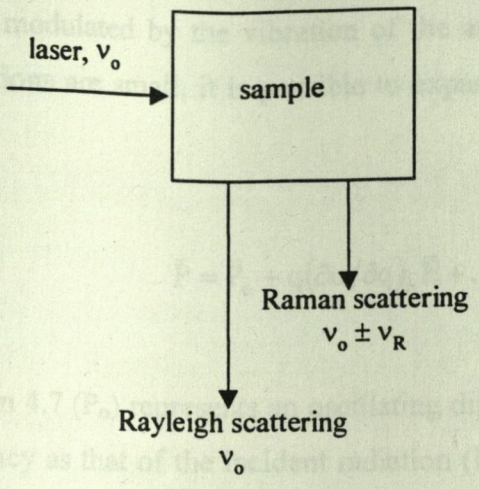

Fig. 4. 3. Laser light incident on a sample is scattered and observed in the direction perpendicular to the incident beam. The scattered light comprises of two components called Rayleigh scattering and Raman scattering.

The scattered light consists of two components. The first is an elastic scattering process called Rayleigh scattering, it has a strong intensity and has the same frequency (ν_o) as the incident radiation. The second is called Raman scattering, it is weaker in intensity and has frequencies $\nu_o \pm \nu_R$ where ν_R is a vibrational frequency of the molecule. The $\nu_o + \nu_R$ and $\nu_o - \nu_R$ lines are called the Stokes and anti-Stokes lines respectively. Thus, Raman spectroscopy involves measuring the vibrational frequency as a shift (ν_R) from the incident beam frequency (ν_o) i.e. vibrational energy $h\nu_R$ is transferred to the lattice in an inelastic scattering process. Raman spectra are measured in the UV-visible region (10^4-10^6 cm^{-1}).

When a solid is exposed to an electric field, electrons and nuclei are forced to move in opposite directions and an electric dipole moment ($\vec{P}$) is induced which is proportional to the electric field strength ($\vec{E}$):

$$\vec{P} = \alpha\vec{E} \qquad 4.6$$

and α is referred to as the polarisability tensor of the material (α_{xx}, α_{xy},....,α_{zz}). In a solid comprising of atoms vibrating about their equilibrium positions, the induced dipole moment is itself modulated by the vibration of the atoms. Providing that the amplitude of the oscillations are small, it is possible to expand P in terms of a Taylor series:

$$\vec{P} = \vec{P}_o + q(\partial\alpha/\partial q)_o \vec{E} + \ldots\ldots\ldots \qquad 4.7$$

The first term in Equation 4.7 (P_o) represents an oscillating dipole moment that radiates light of the same frequency as that of the incident radiation (Rayleigh scattering). The second term represents the modulation of this oscillating dipole moment due to its displacement (q) from equilibrium (Raman scattering). Hence, a lattice vibration can only be observed in the Raman spectrum if there is a modulation of the molecular polarisability by the vibration i.e. $(\partial\alpha/\partial q)_o \neq 0$ and a transition between vibrational states $\langle v'|$ and $|v\rangle$ will only take place if $\langle v'|\vec{P}|v\rangle \neq 0$. Consequently, the components of the polarisability must have the same symmetry as the vibrations. These constraints gives rise to the selection rules for Raman spectra ($\Delta v = \pm 1$).

In any spectrum, a phonon line has a finite width Γ and arises due to several effects. The first effect is referred to as the *natural* line width. This width is attributed to an atom or molecule having a finite lifetime (τ) in a discrete state. This is accompanied by an uncertainty in the energy (wavenumber) of that state, according to Heisenberg's uncertainty principle, $\Delta E \cdot \tau \approx \hbar$. A natural line width of approximately 10^{-8} cm^{-1} is often observed. Another common source of broadening is due to the motion of the radiating atoms in a direction parallel to the direction of propagation of radiation in the sample under study. In this case, molecules absorb at wavenumbers $\tilde{\upsilon} = \tilde{\upsilon}_c(1 \pm \upsilon_{\parallel}/c)$. This results in what is known as *Doppler* broadening and is generally of the order of 10^{-3} cm^{-1}. The last effect is known as *pressure* broadening and arises as a result of the interaction of the atoms in a solid and manifests itself in the anharmonic terms which come from expanding the interatomic potential to higher order terms. In this case, the interactions between the atoms causes a mixing of the energy levels (vibrational levels) so that they can no longer be distinguished. In solids, due to the close compaction of atoms, this is the most likely source of line broadening and can be up to several

wavenumbers either side of the main peak in size. When the anharmonicity is important, it is possible to observe transitions between vibrational states where $\Delta v = 2, 3, \ldots\ldots$

Additional broadening may also arise from the measuring instruments. For example, a detector has a finite resolution, ΔR, and when $\Delta R < \Delta\tilde{\upsilon}$, the distance between spectral lines, the peaks cannot be separated resulting in a superposition of peaks which to the observer looks like one broad peak.

When the wavelength of the exciting laser beam is such that it intercepts the manifold of electronic states, Resonance Raman scattering occurs. In this situation, there are transitions between electronic states as well as vibrational states. The result is a strong enhancement of the intensity of the observed Raman bands. The intensity of a phonon line observed at a frequency ν_o-ν_R is given by:[2]

$$I(\nu) = c \cdot I_o \cdot (\nu_o - \nu_{if})^4 \cdot \sum_{\rho\sigma} \left| (\alpha_{\rho\sigma})_{if} \right|^2 \qquad 4.8$$

Here, i and f denote the initial and final states respectively, of the electronic ground state, I_o is the intensity of the incident beam of frequency ν_o, $(\alpha_{\rho\sigma})_{if}$ is the change in the polarisability caused by the transition between vibrational states via the electronic state and ρ and σ are the x, y and z components of the polarisability tensor. Hence, as the frequency of the incident beam increases, so too does the intensity. However the strong enhancement of the Raman lines occurs when ν_o approaches the frequency required to induce an electronic transition. At this point $(\alpha_{\rho\sigma})_{if}$ becomes very large resulting in a large increase in the Raman line intensity.

4. 1. 3. Specific Heat Capacity

The specific heat (C) of a substance is defined as the quantity of heat (dQ) required to raise the temperature of a unit mass of the substance by a unit degree of temperature (dT):

$$C = \frac{dQ}{dT} \qquad 4.9$$

and is governed by the manner in which the internal energy (E) of the substance is distributed among its constituents. C is temperature dependent (C(T)). For example, in a solid, the atoms vibrate about their equilibrium positions and these lattice vibrations can translate heat through the solid. In the quantum formulation, these lattice vibrations are called phonons and have been discussed in section 4.1.1. At low temperature, the phonons contributing to the specific heat C(T) are long wavelength acoustic phonons. Alternatively, there may be free electrons wandering through the lattice, as in metals. Thermal excitation of these electrons gives rise to an electronic contribution to the heat capacity.

The lattice contribution to the specific heat at low temperature is determined using the Debye model to be:[4]

$$C_L(T) = \beta T^3 \qquad 4.10$$

where $\beta = 1944/\theta_D$ is a measure of the Debye temperature, θ_D which defines an upper limit to the frequency that the lattice vibrations can have. θ_D is itself temperature dependent and the Debye T^3-law generally only holds in real solids at temperatures $T < \theta_D/50$ and $T > \theta_D/2$. At these temperatures the Debye temperature is considered constant. The temperature dependence of θ_D arises from the deviation of the distribution of phonon frequencies, $g(\upsilon)$, from the υ^2-dependence predicted by the Debye model. This is because the Debye model does not adequately take into account the discrete arrangement of atoms in the crystal. The electronic contribution to the specific heat is given by:

$$C_e(T) = \gamma T \qquad 4.11$$

where γ is determined using the expression:

$$\gamma = \frac{2}{3}\pi^2 k_B^2 D(E_F) \qquad 4.12$$

and is therefore a measure of the density of states for both spins at the Fermi level, $D(E_F)$. At room temperature, the electronic contribution to the heat capacity of a metal is significantly smaller than the lattice contribution. However, at low temperatures the situation is quite different since most of the atoms in the lattice are in their vibrational ground states and the energy (heat) required to reach the next vibrational energy level is greater than k_BT. Consequently, the contribution to the specific heat due to the thermal excitation of electrons about the Fermi level becomes dominant at low temperatures. This is also understood by comparing equations 4.10 and 411 where it is seen that C_e decreases linearly with decreasing temperature whereas C_L is proportional to T^3 at low temperature.

In magnetic materials there will also be a magnetic contribution to the specific heat arising from the transfer of heat due to spin waves:

$$C_M(T) = \alpha T^{3/2} \qquad 4.13$$

where $\alpha = cN_Ak_B(k_B/JS)^{3/2}$ is of the order of 2 mJ/mole $K^{5/2}$ when c = 0.059 for a face centred cubic lattice, $N_A = 6.022 \times 10^{23}$ atoms/mole is the Avogadro's number, J/k_B = 37.5 K is the exchange constant and S = 1 is the total spin on the Cr ion. The $T^{3/2}$ behaviour of the specific heat at low temperatures is similar to the variation of the spontaneous magnetisation at low temperatures (section 3.1.3, Chapter 3). Furthermore, the magnetic specific heat due to magnons may also be observed to show an exponential behaviour similar to that for the magnetisation:

$$C_M(T) = \alpha T^{3/2}\exp(-\Delta/k_BT) \qquad 4.14$$

where Δ is related to the magnetocrystalline anisotropy of the material under study.[3] A review of the specific heat in solids is given in most text books on Solid State Physics.[4]

4. 2. Experimental Methods

4. 2. 1. Raman Spectroscopy

Polarised Raman spectroscopy was carried out at the Texas Centre for Superconductivity, University of Houston, Texas, USA. These measurements were performed using a S3000 Jobin-Yvon Triple Spectrometer equipped with a microscope and a liquid nitrogen cooled charge-coupled device (CCD) detector. The samples (a (110) and a (001) oriented CrO_2 film) were mounted in a Microstat He cryostat. In this cryostat it was possible to vary the temperature between 5K and 450K. The spectra were measured using either an Ar^+ laser operating at a wavelength of 514.5 nm (2.4 eV) or a He-Ne laser operating at a wavelength of 632.8 nm (1.96 eV). An objective lens of ×50 magnification was used to both focus the laser beam to a spot size of ~ 5 μm in diameter on the samples surface and to collect the scattered light. The laser power was kept low i.e. between 0.1-0.5 mW at the focus spot, to avoid local heating of the sample.

Measurements on the CrO_2 films and a TiO_2 sample were carried out at 300K using the 632.8 nm laser excitation for four scattering configurations namely: y' (x' x') $\bar{y}$', y' (z z) $\bar{y}$', y' (x' z) $\bar{y}$' and z (x' y') $\bar{z}$. The nomenclature used to describe the various scattering configurations is in keeping with that of S. P. S. Porto et al.[5] For example for a scattering configuration a (b c) d, a and d are the directions of the incoming and out going laser light and b and c are the directions of polarisation of the incident and scattered laser light. An example is shown in Fig. 4.4. In the measurements made here x', y'. and z refer to crystallographic directions [1 $\bar{1}$ 0], [1 1 0] and [0 0 1] respectively. Measurements were also carried out on the (110) CrO_2 film in the temperature range 5K to 420K using the 514.5 nm laser excitation. For these measurements the incident polarisation was along the x' axis and the spectra obtained were a superposition of the y' (x' x') $\bar{y}$' and the y' (x' z) $\bar{y}$' scattering configurations.

The relative intensities of the various observed Raman phonon lines were obtained by fitting the peaks to a Lorentzian function and normalising the peak area to that of the A_{1g} line in the x' x' spectrum with the same laser excitation and at the same temperature.

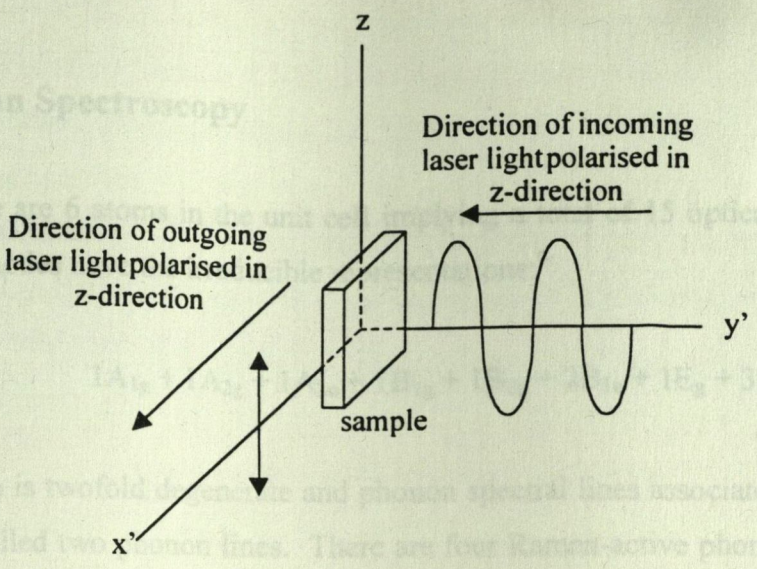

Fig. 4. 4. Schematic of a typical scattering configuration, y' (z z) x' where direction of incoming laser light is along y' axis and outgoing along x' axis. In both cases, the laser light polarised along the z-axis.

4. 2. 2. Heat Capacity

Low temperature specific heat capacity experiments were carried out at the Institut de Physique et Chimie de Strasbourg, France by adiabatic calorimetry. A commercial powder was measured in the temperature range 2-40 K. The sample was prepared by pressing the powder into a pellet having dimensions 5 × 1 mm^2 using a Buehler hydraulic bench top press and a die of diameter 5 mm. The sample was wrapped in Al foil and placed in contact with a Cr/Ti coated sapphire heater in a vacuum of 10^{-6} mbar and immersed in an He bath. The temperature of the sample is raised slightly by allowing a controlled amount of current to flow through the heater. The current is equated to the amount of heat ΔQ applied to the sample. The temperature of the sample is measured using a Ge thermometer before and after heating so that the change in temperature, ΔT, of the sample can be determined. The heat capacity is then extracted using the relation: $C(T) = \Delta Q/\Delta T$.

4. 3. Results

4. 3. 1. Raman Spectroscopy

In CrO_2 there are 6 atoms in the unit cell implying a total of 15 optical vibrational modes. These modes have the irreducible representations:[6]

$$1A_{1g} + 1A_{2g} + 1A_{2u} + 1B_{1g} + 1B_{2g} + 2B_{1u} + 1E_g + 3E_u$$

Each E vibration is twofold degenerate and phonon spectral lines associated with these vibrations are called two phonon lines. There are four Raman-active phonon modes of A_{1g}, B_{1g}, B_{2g} and E_g symmetry.[5, 7] The atomic motions corresponding to these vibrational modes are shown in Fig. 4.5. In the Raman modes, the Cr ion remains at rest and the oxygen atoms vibrate about their equilibrium positions. There are also four infra-red modes and these are given by the irreducible representations of symmetry A_{2u} and E_u.

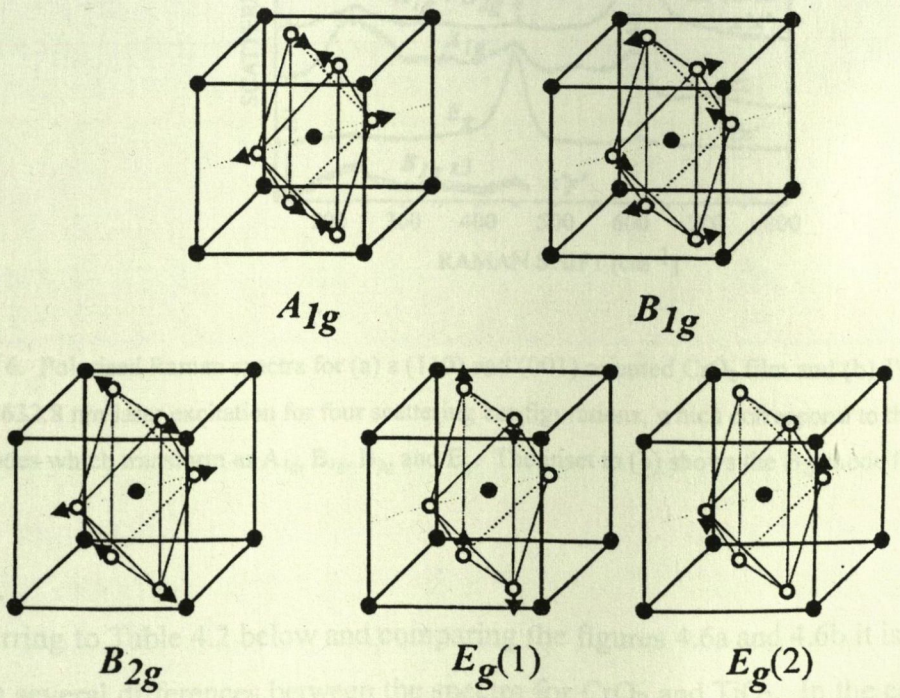

Fig. 4. 5. Raman vibrational modes of CrO_2 labelled according to their irreducible representations A_{1g}, B_{1g}, B_{2g} and E_g.

Figure 4.6a shows the polarised Raman spectra as obtained for a (110) and (001) oriented CrO_2 film at 300 K using the 632.8 nm laser excitation for the four scattering configurations outlined in section 4.3.2.[8] The four different scattering configurations and the corresponding vibrational modes are given in Table 4.2 below. Also listed in Table 4.2 are the positions, the widths and the relative intensities of the peaks of the Raman phonon lines observed at 300 K using this laser excitation. Similar spectra were obtained for the isostructural compound TiO_2 (on which CrO_2 is grown) using the same laser excitation wavelength, Fig. 4.6b.

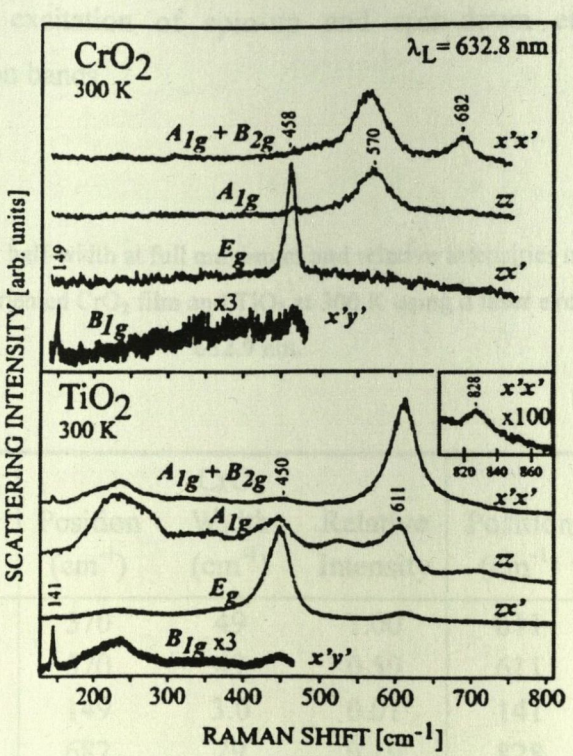

Fig. 4. 6. Polarised Raman spectra for (a) a (110) and (001) oriented CrO_2 film and (b) TiO_2 at 300 K using a 632.8 nm laser excitation for four scattering configurations, which correspond to the vibrational modes which transform as A_{1g}, B_{1g}, B_{2g} and E_g. The inset to (b) shows the B_{2g} mode for TiO_2.

By referring to Table 4.2 below and comparing the figures 4.6a and 4.6b it is possible to observe several differences between the spectra for CrO_2 and TiO_2. In the case of CrO_2 only the one phonon lines are pronounced in contrast to TiO_2 where the intensity of the two phonon line (E_g) is comparable to the one phonon lines. Also, the A_{1g} and B_{2g} lines in CrO_2 are of comparable intensity whilst for TiO_2 the intensity of the B_{2g} line is much

smaller than the intensity of the A_{1g} line. Lastly, similar intensities are observed for the A_{1g} mode in CrO_2 for the y' (x'x') $\bar{y}$' and the y' (z z) $\bar{y}$' scattering configurations whilst TiO_2 exhibits a weaker intensity for the y' (z z) $\bar{y}$' scattering configuration. It is assumed that the differences in the Raman spectra for CrO_2 and TiO_2 are due mainly to the different intermediate electronic states. TiO_2 is a transparent material and has an insulating gap of ~ 3eV.[9, 10] The laser excitation energy of 1.96 eV used in the measurements above is therefore well below the insulating gap for TiO_2. In contrast, there is no gap in the spin-up states for CrO_2 and the gap in the spin-down states is of the order of 1 eV. Consequently, a laser energy of 1.96 eV (as well as the 2.41 eV laser energy) results in an excitation of spin-up and spin-down electrons into their corresponding conduction bands.

Table 4. 2. Wave number, half-width at full maximum and relative intensities of the Raman phonon lines of a (110) and (001) oriented CrO_2 film and TiO_2 at 300 K using a laser excitation of wavelength 632.9 nm.

Scattering configuration	Raman Mode	CrO_2 Position (cm^{-1})	CrO_2 Width (cm^{-1})	CrO_2 Relative Intensity	TiO_2 Position (cm^{-1})	TiO_2 Width (cm^{-1})	TiO_2 Relative Intensity
y' (x'x') $\bar{y}$'	A_{1g}	570	49	1.00	611	44	1.00
y' (z z) $\bar{y}$'		570	49	0.59	611	44	0.33
z (x'y') $\bar{z}$	B_{1g}	149	3.0	0.01	141	3.7	0.006
y' (x'x') $\bar{y}$'	B_{2g}	682	29	0.19	828	14.1	0.002
y' (z x') $\bar{y}$'	E_g	458	11.5	0.22	450	36	0.81

Figure 4.7 shows the temperature variation of the polarised Raman spectra for CrO_2 in the range 5 K and 420 K for the y' (x' x') $\bar{y}$' and y' (z x') $\bar{y}$' scattering configurations using the 514.5 nm laser excitation.[8] The resulting spectra are a superposition of the peaks arising due to the A_{1g}, B_{2g} and E_g vibrational modes. From this diagram it can be seen that as the temperature is increased, the intensities of the peaks gradually decrease whilst the peak position shifts to lower wave numbers and the line width broadens. However, there is no redistribution of the peak intensities with increasing temperature. Neither is there a redistribution of intensities near the Curie

temperature, $T_c \approx 400$ K. This suggests that the electronic structure near 2.4 eV (514.5 nm) is not strongly affected by the magnetic ordering and that the Hund's rule exchange splitting is still present up to 420 K. It is concluded that, the electronic structure above the Curie temperature is similar to that in the ferromagnetic state below T_c.

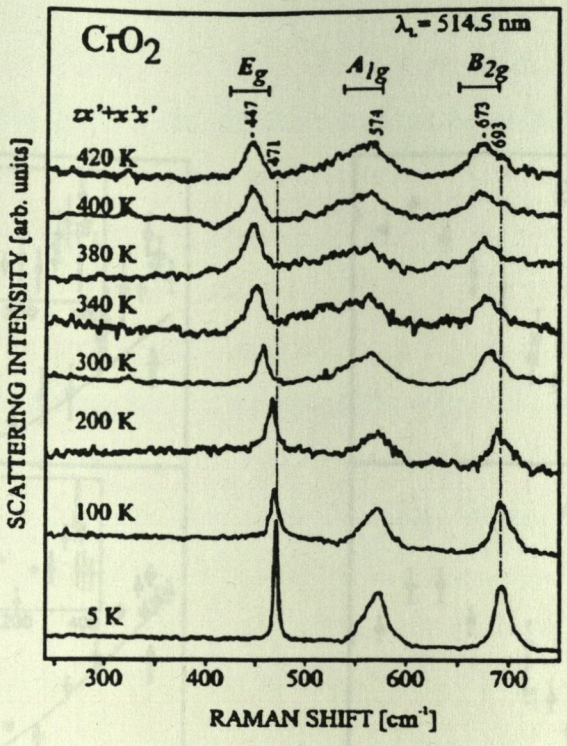

Fig. 4. 7. Polarised Raman spectra for CrO_2 in the y' (x'x') $\bar{y}$' and y' (x' z) $\bar{y}$' scattering configurations and in the temperature range 5-420 K using the 514.5 nm laser excitation.

As mentioned earlier, the photon energies used in these experiments lie within the range of direct interband electronic transitions resulting in spectra arising from transitions between both electronic and vibrational states. Consequently, a significant enhancement of the intensities of the phonon lines is expected due to the modulation of the combined electronic densities of states by particular atomic vibrations (Section 4.1.2). In these measurements, an enhancement of the relative intensity of the B_{2g} phonon line from 0.19 to 0.57 is observed at 300 K when the laser excitation of wavelength of 632.8 nm is replaced by the 514.5 nm laser excitation. The intensity increases further to 0.89 as the temperature is decreased to 5 K for this laser excitation.

The temperature dependence of the peak line widths, $\Gamma(T)$, for the A_{1g} B_{2g} and E_g phonon lines are shown in Fig. 4.8a.[8] The peak line-width is smallest for the E_g phonon line, measuring 4.5 cm^{-1} at 5 K. The A_{1g} and B_{2g} line-widths are significantly larger, measuring 24 cm^{-1} and 16 cm^{-1} respectively at 5 K. The line-width broadening is thought to arise mainly from phonon-phonon scattering (pressure braodening). Consequently, the A_{1g} and B_{2g} phonons are expected to scatter more strongly than the E_g phonon.

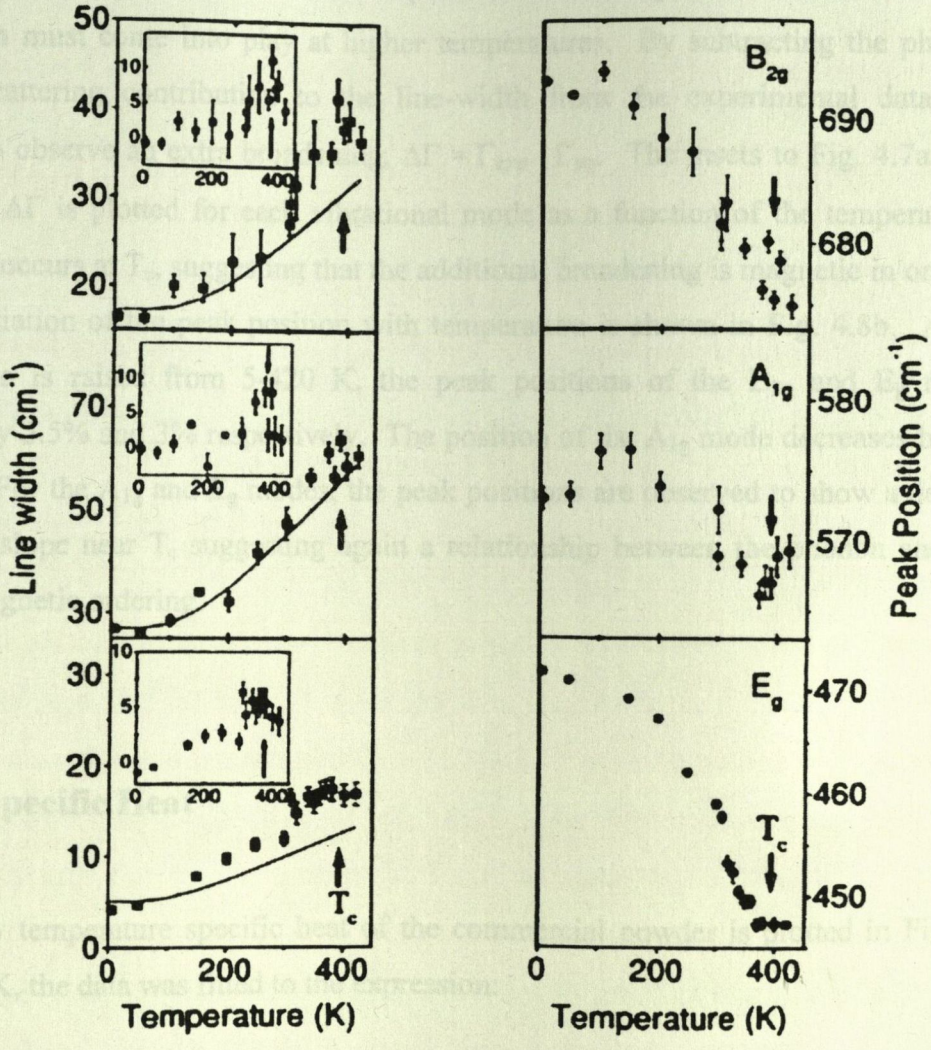

Fig. 4. 8. Variation with temperature of (a) the peak line width and (b) the peak position of the A_{1g}, B_{2g} and E_g vibrational modes. The solid lines in (a) represent the function $\Gamma_{pp}(T)$ described by equation 4. The insets show the additional broadening, $\Delta\Gamma = \Gamma_{exp} - \Gamma_{pp}$, assigned to magnetic scattering.

The temperature dependence of the line-width due to phonon-phonon scattering can be described by:[1]

$$\Gamma_{pp}(T) = \Gamma_o = \left[1 + \frac{2}{\exp(\hbar\Omega / k_B T) - 1}\right] \qquad 4.15$$

where Γ_o is the line-width at T=0 K and Ω is the phonon frequency. However, this model only fits the data at low temperature indicating that another scattering mechanism must come into play at higher temperatures. By subtracting the phonon-phonon scattering contribution to the line-width from the experimental data it is possible to observe an extra broadening, $\Delta\Gamma = \Gamma_{exp} - \Gamma_{pp}$. The insets to Fig. 4.7a show that when $\Delta\Gamma$ is plotted for each vibrational mode as a function of the temperature a maximum occurs at T_c, suggesting that the additional broadening is magnetic in origin.

The variation of the peak position with temperature is shown in Fig. 4.8b. As the temperature is raised from 5-420 K, the peak positions of the B_{2g} and E_g modes decrease by 5.5% and 3% respectively. The position of the A_{1g} mode decreases by less than 1%. For the A_{1g} and E_g modes, the peak positions are observed to show a definite change in slope near T_c suggesting again a relationship between the phonon energies and the magnetic ordering.

4 .3. 2. Specific Heat

The low temperature specific heat of the commercial powder is plotted in Fig. 4.7 Below 15 K, the data was fitted to the expression:

$$C = \gamma T + \beta T^3 + \alpha T^{3/2} \qquad 4.16$$

The solid line in Fig. 4.8 shows the fit to the data when C/T is plotted against the temperature squared. The first term in equation 4.16 corresponds to the electronic heat

coefficient, $\gamma = 5.1(9)$ mJ/mole K^2. This corresponds to a density of states at the Fermi level $D(E_F) = 2.2$ states/eV/spin per CrO_2 formula unit.[11]

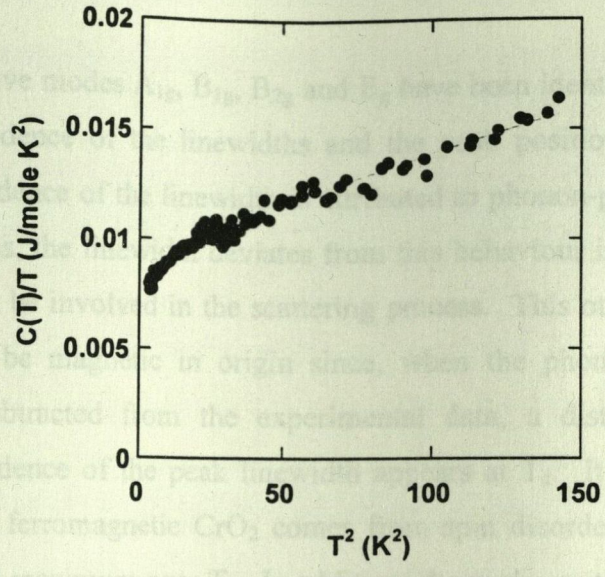

Fig. 4. 9. Specific heat capacity of a pressed commercial powder (B1507) as a function of T^2. The solid line corresponds to the fit to equation 4.16.

The second term in equation 4.16 refers to the phonon contribution to the specific heat. β is determined from the fit to the curve in Fig. 4.8 to be 0.028 mJ/mole K^4 and corresponds to a Debye temperature $\theta_D = (1944/\beta)^{1/3} \approx 410$ K which is in fairly good agreement with Tsujioka's value of 480 K.[15] The third term corresponds to the magnetic contribution to the specific heat due to spin-waves. The value $\alpha \approx 1.9$ mJ/mole $K^{5/2}$. This corresponds to a spin-wave stiffness constant $D \approx 98$ meV Å^2.[15] As for the magnetisation versus temperature data for both powders and films, Section 3.3, Chapter 3, there does not appear to be any gap in the spin wave spectrum (equation 4.14) at these temperatures.

4. 4. Discussion

Raman Spectroscopy

The Raman-active modes A_{1g}, B_{1g}, B_{2g} and E_g have been identified for CrO_2 and the temperature dependence of the linewidths and the peak positions studied. The low temperature dependence of the linewidth is attributed to phonon-phonon scattering. At higher temperatures, the linewidth deviates from this behaviour indicating that another channel could also be involved in the scattering process. This other scattering process is most likely to be magnetic in origin since, when the phonon-phonon scattering contribution is subtracted from the experimental data, a distinct anomaly in the temperature dependence of the peak linewidth appears at T_c. It is suggested that the extra scattering in ferromagnetic CrO_2 comes from spin disorder scattering as this is expected to show a maximum near T_c. In addition, the peak positions are found to shift to lower wave-numbers with increasing temperature with a minimum occurring at T_c, again suggesting a relationship between the phonon energies and the magnetic ordering. Since, the exchange interaction between Cr ions depends on the Cr-O bond lengths and bond angles, it can be understood that the frequency of the oxygen phonon modes depends on the spin alignment of the Cr ions below T_c. This has been found to be the case for the infra-red active vibrations of LCMO for which it has been established that the lattice contraction is not solely responsible for phonon hardening below T_c.[12] Instead it was proposed that the phonon hardening (i.e. phonons moving to higher wavenumbers) stemmed from a decrease of the free carrier screening due to a broadening of the conduction band as the temperature is decreased. Recent Raman spectroscopy measurements on $SrRuO_3$, another bad metal (see Section 5.4A, Chapter 5) showed similar results regarding the behaviour of the peak position (and $\Gamma(T)$) about T_c. In this case, the hardening of the phonon lines was, similarly, explained to arise from an increase of the free carrier concentration upon cooling due to the delocalisation of some electronic states.[13] Likewise, the hardening of the phonon lines in CrO_2 with decreasing temperature may be attributed to an increase in the carrier concentration of the itinerant electrons. However, recent optical conductivity measurements on thin

films of CrO_2 indicate that carrier concentration N_{eff} does not change with temperature.[14]

Specific Heat Capacity

The electronic heat coefficient is measured here to be 5.1(2) mJ/mole K^2 and corresponds to a density of states of 2.2 states/eV/spin/CrO_2. Other authors have measured values of the electronic heat coefficient lying in the range 2.5-7 mJ/ mole K^2 with corresponding densities of states ranging between 1.0 – 3.0 states/eV/spin/CrO_2.[11, 15] Band structure calculations on the other hand have determined values for γ in the range 1.1-3.0 mJ/mole K^2 corresponding to densities of states in the range 0.5 – 1.3 states /eV/spin/CrO_2.[16, 17] With regards to the band calculations, it was pointed out by Mazin et al., that the exchange splitting is highly sensitive to the computational parameters used therefore leading to an extraordinary sensitivity of the calculated density of states to the exchange correlation potential. For example, in some calculations, the Fermi level, is found to fall exactly at a minimum of the calculated density of states. In this case, $D(E_F) \approx 0.5$ states/eV/spin/CrO_2 formula unit whereas, in other cases the Fermi level was found to lie 30 meV below this minimum giving rise to a density of states $D(E_F) \approx 1.1$ states/eV/spin/fu.[16] With regards to the experimental data, it should be noted that at very low temperatures there is a sharp downturn in the C/T versus T^2 curve of Fig. 4.9, whereby it meets the origin with a large slope. Fitting the heat capacity data is very to sensitive to this downturn. Even Tsujioka's value for γ is said to be an underestimate given the sharp change of C/T near T = 0 K. This may explain some of the discrepancy between the various values obtained for the electronic specific heat. Nevertheless, the question as to what the true value of γ is, remains open.

In CrO_2, there are two electrons in the outer d-shell and as mentioned in Section 1.4, Chapter 1, one of these electrons is localised and the other delocalised. It is therefore expected that only one spin-up electron, namely the delocalised electron, should contribute to the electronic specific heat capacity at low temperatures. Given that there are two states available to the delocalised electron in the t_{2g} band which (assuming a rectangular band) has a width $W \sim 2.5$eV, then, the density of states is estimated to be

$D(\varepsilon_F)$ = 2 states/2.5 eV = 0.8 states/eV/spin/CrO_2, see Section 1.4, Chapter 1. The corresponding electronic specific heat coefficient is 2.1 mJ/mole K^2. Thus, an effective mass $m^*=m_e(\gamma_{obs}/\gamma_{theory}) \sim 2.5m_e$ is deduced when γ_{obs} = 5.1 mJ/mole K^2 and γ_{theory} = 2.1 mJ/mole K^2. A large effective mass between 2-4m_e has been inferred from band structure calculations and optical conductivity measurements.[16, 17, 18]

The value of the prefactor α = 1.9 mJ/mole $K^{5/2}$ pertaining to the magnon contribution to the specific heat capacity is in good agreement with the value of α = 1.4 mJ/mole $K^{5/2}$ determined by Tsujioka.[15] Furthermore, α=1.9 mJ/mole $K^{5/2}$ corresponds to a spin-wave stiffness constant D = 98 meV Å^2 which is in fairly good agreement with the value of D obtained from the magnetisation versus temperature data, Section 3.3, Chapter 3.

References

[1] B. Schrader, *Infrared and Raman Spectroscopy - Methods and applications*, VCH (1999)

[2] J. R. Ferraro and K. Nakamoto, *Introductory Raman Spectroscopy*, Academic Press Inc. (1994)

[3] A. R. Mackintosh, Phys. Lett., **4**, 140-142 (1963

[4] E. S. R. Gopal, *Specific Heat at Low Temperatures*, Plenum Press (1966)

[5] S. P. S. Porto, P. A. Fleury and T. C. Damen, Phys. Rev., **154**, 522 (1967)

[6] J. G. Traylor, H. G. Smith, R. M. Nicklow and M. K. Wilkinson, Phys. Rev. B, **3**, 3457-3472 (1971)

[7] P. S. Narayanan, Proc. Indian. Acad. Sci., **32A**, 279 (1950)

[8] M. N. Milko, A. P. Litvinchuk, H. –G. Lee, C. W. Chu, A. Barry and J. M. D. Coey, Phys. Rev. B, **60**, 33-36 (1999)

[9] The value of the insulating gap in TiO_2 was measured using UV absorption spectroscopy courtesy of OPTRONICS, Trinity College Dublin.

[10] P. I. Sorantin and K. Schwarz, Inorg. Chem., **31**, 567-576 (1992)

[11] A. Barry, L. Ranno, K. Ounadjela and J. M. D. Coey, J. Appl. Phys., **83**, 7166-7168 (1998)

[12] K. H. Kim, J. Y. Gu, H. S. Choi, G. W. Park and T. W. Noh, Phys. Rev. Lett., **77**, 1877 (1996)

[13] M. N. Iliev, A. P. Litvinchuk, H. –G. Lee, C. L. Chen, M. L. Dezaneti, C. W. Chu, V. G. Ivanov, M. V. Abrashev and V. N. Popov, Phys. Rev. B, **59**, 364-368

[14] E. J. Singley, D. N. Basov, C. P. Weber, A. Barry, J. M. D. Coey, Phys. Rev. B, **60**, 4126-4130 (1999)

[15] T. Tsujioka, T. Mizokawa, J. Okamoto, A. Fujimori, M. Nohara, H. Takagi, K. Yamaura, M. Takano, Phys. Rev. B, **56**, 509-512 (1997) and references therein

[16] S. P. Lewis, P. B. Allen and T. Sasaki, Phys. Rev. B, **55**, 10253-10260 (1997)

[17] I. I. Mazin, D. J. Singh and C. Ambrosch-Draxl, Phys. Rev. B, **59**, 411-418 (1998)

[18] E. J. Singley, D. N. Basov, C. P. Weber, A. Barry and J. M. D. Coey, Phys. Rev. B, **60**, 4126-4130 (1999)

Chapter 5

Transport Properties of CrO_2

"Don't miss the journey in favour of the destination".

The phrase that clenched the big job in the city, Rhian-Mari Thomas spring 1999.

5. 1. Transport Properties

5. 1. 1. Background

The probability that an electron will occupy a state of energy ε at a temperature T is given by the Fermi distribution function:[1]

$$f(\varepsilon,T)=\frac{1}{\exp[(\varepsilon-\mu)/k_BT]+1} \qquad 5.1$$

μ is the chemical potential. At T = 0K, all states up to the Fermi energy are filled and those above are empty. On raising the temperature, thermal excitation affects only those states that are within a few k_BT of the Fermi surface and only electrons from these states can suffer collisions, the rest have no empty states available into which they can be scattered. The same is true when an external electric or magnetic field is applied. Most states which were initially filled remain so after the application of a field and therefore play no part in the transport process. However, electrons near the Fermi surface are rearranged in such a way that a few empty states become filled and a few on the opposite side become unfilled. The result is the transport of electric charge and a redistribution of electrons away from the equilibrium distribution function described by equation 5.1. The scattering of these electrons round the Fermi surface destroys the transport process and restores the system to equilibrium.

In general, the motion of electrons (or holes) under the action of some applied field is given by the Boltzmann equation. This involves studying a quantity $f_n(\bar{r},\bar{k},t)$, which is the non-equilibrium distribution function and represents the number of electrons in band n, with wave vector $\bar{k}$ at some point $\bar{r}$ in space and t in time. At time t-dt and in the absence of collisions, the electron at $\bar{r}$, $\bar{k}$ at time t must have been at $\bar{r}-\bar{v}(\bar{k})dt, \bar{k}-\bar{F}/\hbar\, dt$ where:

$$\dot{r} = v(\bar{k}) \qquad 5.2a$$

$$\hbar\dot{k} = -e(\bar{E}+\bar{v}\times\bar{B}) = F(\bar{r},\bar{k}) \qquad 5.2b$$

$\bar{v}$ is the velocity of an electron, $\bar{E}$ is the electric field and $\bar{H}$ is the magnetic field. Equations 5.2 are the semiclassical equations of motion which determine how the trajectory of an electron evolves in time between collisions under the action of an external field. The evolution of the distribution function can be obtained by expanding $f_n(\bar{r},\bar{k},t)$ with respect to time so that:

$$\frac{df_n}{dt}(\bar{r},\bar{k},t) = \frac{\partial f_n^{\circ}}{\partial t}(\bar{k},t) + \bar{v}\frac{\partial f}{\partial \bar{r}} + \frac{\bar{F}}{\hbar}\frac{\partial f}{\partial \bar{k}} + \frac{\partial f_n}{\partial t} \qquad 5.3$$

The first term on the right hand side of equation 5.3 is zero since this is the equilibrium value for the distribution function and does not change with time. In the absence of collisions, equation 5.3 is set to zero and the co-ordinates of each electron evolves according to the equations 5.2, in other words:

$$\frac{\partial f}{\partial t} = -\left(\bar{v}\frac{\partial f}{\partial \bar{r}} + \frac{\bar{F}}{\hbar}\frac{\partial f}{\partial \bar{k}}\right) \qquad 5.4$$

However, charge carriers will undergo scattering from impurities, lattice waves etc which tend to restore the thermal equilibrium of the system so that when the external fields are

turned off f_n reduces to the Fermi distribution function of equation 5.1. The process of scattering depends on the number of carriers in state $\bar{k}$, ($f_{\bar{k}}$) and the number of vacancies available in the final state $\bar{k}'$, ($1-f_{\bar{k}'}$), as well as the reverse process from $\bar{k}'$ to $\bar{k}$. For each value of $\bar{k}$ and $\bar{k}'$ there is a transition probability, $W_{\bar{k}',\bar{k}}$, associated with each transition of an electron with wave vector, $\bar{k}$ to a state with wave vector $\bar{k}'$. The rate of change of the distribution function due to scattering is then:

$$\left(\frac{\partial f}{\partial t}\right)_{\text{collisions}} = \int\{f_{k'}(1-f_k) - f_k(1-f_{k'})\}W_{k'k}\,dk' \qquad 5.5$$

The Boltzmann equation states that any point, and for any value of $\bar{k}$, the net rate of change of the distribution function is zero so that we obtain:

$$\left(\frac{\partial f}{\partial t}\right)_{\text{diffusion}} + \left(\frac{\partial f}{\partial t}\right)_{\text{drift}} + \left(\frac{\partial f}{\partial t}\right)_{\text{collisions}} = 0 \qquad 5.6$$

and

$$\left(\frac{\partial f}{\partial t}\right)_{\text{diffusion}} = -\bar{v}\left(\frac{\partial f}{\partial \bar{r}}\right) \qquad 5.7a$$

$$\left(\frac{\partial f}{\partial t}\right)_{\text{drift}} = -\frac{\bar{F}}{\hbar}\left(\frac{\partial f}{\partial \bar{k}}\right) \qquad 5.7b$$

The Boltzmann equation is the starting point for all the transport equations in solids. By introducing the concept of collisions we can also introduce the concept of a "relaxation time, τ" which denotes the lifetime of an electron between collision. If we assume that the steady state distribution does not depart very far from equilibrium then the rate of change of the distribution function due to the scattering processes can be described by the Relaxation Time Approximation:

$$\left(\frac{\partial f}{\partial t}\right)_{\text{collisions}} = -\frac{\left[f_n(\vec{r},\vec{k}) - f_n^{\circ}(\vec{r},\vec{k})\right]}{\tau_n(\vec{r},\vec{k})} \qquad 5.8$$

Inserting this into equation 5.6 we see that: the Boltzmann equation simplifies to a linear partial differential equation[2] from which the various conductivities can be deduced. It should be noted that in a ferromagnetic material, two types of electrons are involved, those with spin-up and those with spin-down and there is a distribution function as well as a relaxation time for each spin orientation.[3,4]

The scattering of electrons gives rise to resistance and may be due to many processes. The various scattering processes associated with a particular resistivity behaviour will be discussed in brief below.

5. 1. 2. Resistivity versus Temperature

Under isothermal conditions a metal will obey Ohm's law:

$$\vec{J} = \sigma \cdot \vec{E} \qquad 5.9$$

where $\vec{J}$ is the current density, $\vec{E}$ the electric field and σ the electrical conductivity of the metal. An expression for the electrical conductivity, σ, is given in the free electron model by:

$$\sigma = \frac{ne^2\tau}{m} \qquad 5.10$$

where n refers to the electron density, e the charge of an electron, τ the time between collisions and m the mass of the electron. For most metals, however, agreement between

equation 5.10 and experiment would require that electrons behave as particles with an *effective* mass, m^* different from the conventional electronic mass. A more explicit expression for the conductivity is given by:[2]

$$\sigma = \frac{1}{4\pi^3}\frac{e^2\tau}{\hbar}\frac{1}{3}\int \lambda dS_F \qquad 5.11$$

λ is the mean free path given by $\lambda = v\tau$ and dS_F is any elementary area on the Fermi surface such that the number of electrons contributing to the current is contained within a volume $dS_F dk$. The reciprocal of the conductivity is referred to as the resistivity, $\rho = 1/\sigma$.

An ideal metal typically shows a temperature dependent resistivity like that shown in Fig. 5.1. In general, the resistivity can be written as a sum of two terms, a temperature independent term referred to as the residual resistivity ρ_o, and a temperature dependent term $\rho'(T)$:

$$\rho(T) = \rho_o + \rho'(T) \qquad 5.12$$

Equation 5.12 is known as Matthiesen's Rule. The residual resistivity is characteristic of the particular metal being measured and arises as a result of scattering from impurities and defects. A metal usually has a residual resistivity in the range 10^{-10}-10^{-6} Ω m. The electrical resistivity of most metals is dominated at low temperature by collisions of the conduction electrons with impurity atoms and defects. At high temperature, the electrical resistivity is usually dominated by collisions of the conduction electrons with lattice phonons. Scattering by lattice phonons does however occur at both low and high temperatures and their contribution to the electrical resistivity (ρ_L (T)) is calculated as being proportional to T^5, or T^3 for d-band metals, and T respectively.

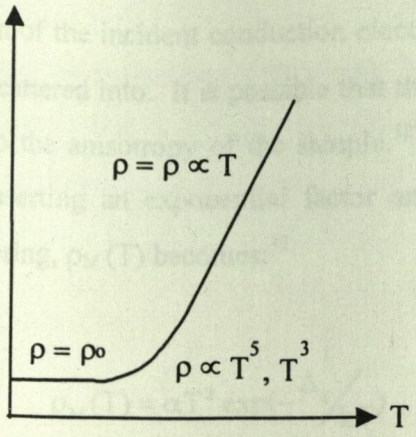

Fig. 5. 1 Schematic temperature dependence of the electrical resistivity for an ideal metal illustrating Matthiesen's Rule.

In a ferromagnetic transition metal oxide, such as CrO_2, the conduction electrons occur in highly correlated d-bands and majority electrons i.e. electrons having only one spin orientation, dominate the conduction processes. In this case, there may be several other scattering processes contributing to the overall resistivity behaviour. For example, at low temperature it is common to observe a T^2-dependence of resistivity such that the resistivity may be written as:

$$\rho(T) = \rho_o + \alpha T^2 \qquad 5.13$$

where α is a coefficient of the T^2-dependence. There exist several origins for this dependence e.g. electron-electron scattering,[5, 6] scattering by impurities[7] and more commonly for ferromagnetic materials, scattering by spin waves or *magnons*.[8] If the scattering is due to electron-electron interactions, then the ratio α/γ^2, where γ is the low-temperature electronic specific heat coefficient (see Chapter 4), is found to be a constant[9] and equal to about 0.9×10^{-6} $\mu\Omega$ cm.(mole K^2/mJ)^2. The scattering of conduction electrons

by spin waves results in a flipping of the conduction electrons' spin. Therefore, for electron-magnon scattering to occur it is necessary that there exists a finite density of ↑ or ↓ states (depending on the spin of the incident conduction electron) at the Fermi level for the conduction electron to be scattered into. It is possible that there may exist a gap, Δ_g, in the spin wave spectrum due to the anisotropy of the sample.[12, 10, 11] In this case the T^2 dependence is modified by inserting an exponential factor and the contribution to the resistivity due to magnon scattering, $\rho_M(T)$ becomes:[12]

$$\rho_M(T) = \alpha T^2 \exp(-\Delta_g / kT) \qquad 5.14$$

Kubo and Ohata[13] extended the standard perturbation calculation of Mannari[8] to consider two magnon processes leading to a $T^{9/2}$ dependence of resistivity.

5. 1. 3. Magnetoresistance

The term 'magnetoresistance' refers simply to the change in resistance of a sample when subjected to a magnetic field and is generally defined in the following way:

$$MR(\%) = \frac{R(0) - R(H)}{R(0)} \qquad 5.15$$

The effect can be either positive or negative in sign and its magnitude and behaviour depend not only on the field strength but also on the field direction with respect to the current. The magnetoresistance also depends on the type of material/structure being measured. Magnetoresistance can be an intrinsic property of a material or else it may depend on the microstructure of the sample, in which case it is an extrinsic property. Among the various types of intrinsic magnetoresistance observed in metals are the

"ordinary" magnetoresistance (OMR),[2, 14] anisotropic magnetoresistance (AMR) and colossal magnetoresistance (CMR),[15] whereas giant magnetoresistance (GMR), tunneling magnetoresistance (TMR) and powder magnetoresistance (PMR) are extrinsic properties. The origins of the various types of magnetoresistance shall be discussed briefly below whilst Fig. 5.2 summarises a classification of the different MR effects based on the intrinsic and extrinsic magnetic properties of materials/structures.[16]

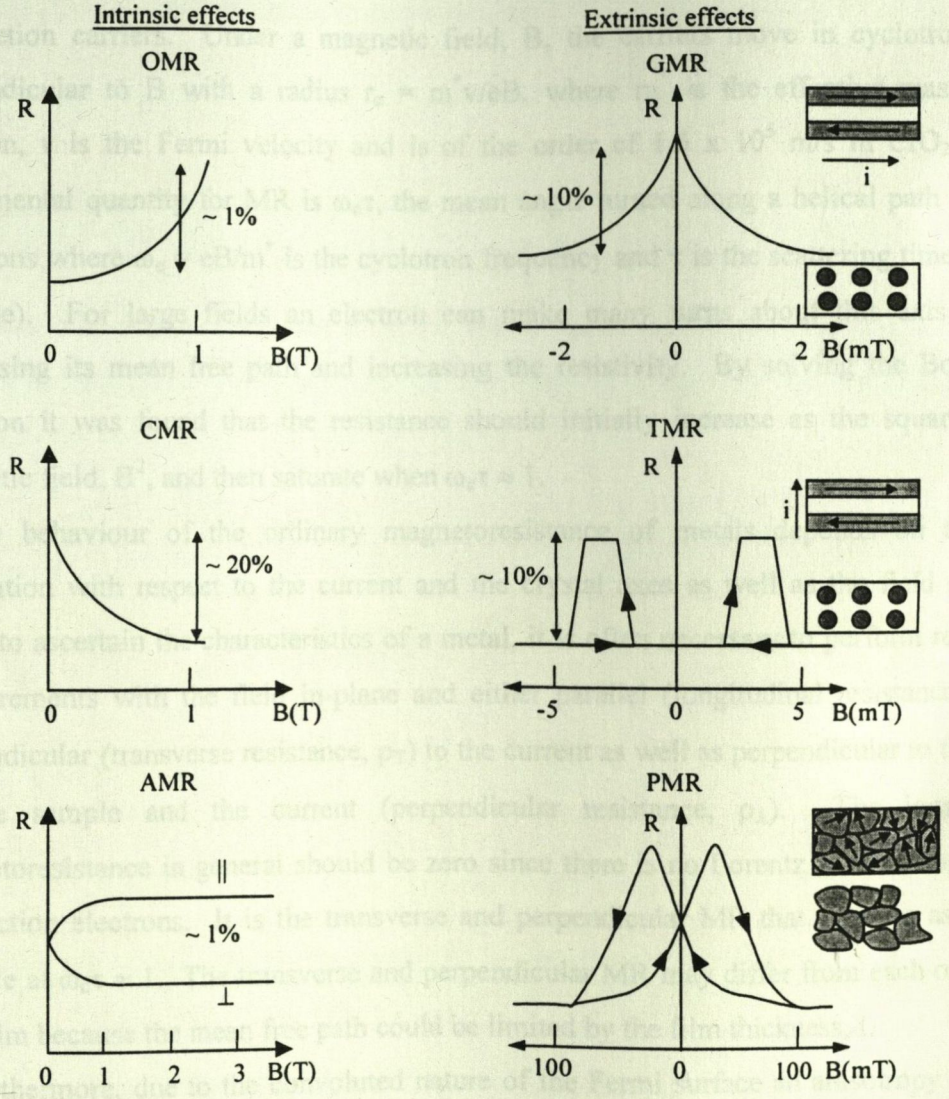

Fig. 5. 2. Classification of the magnetoresistance behaviour arising from the intrinsic and extrinsic properties of materials.

A. *Ordinary Magnetoresistance*

Within the simple Drude model of electrical transport[14], the conduction of an electron gas should be unimpaired by the presence of a magnetic field ($J = \sigma \cdot E$). However, in practice the resistance of an ordinary non-magnetic metal is seen to increase in a magnetic field. This is the ordinary magnetoresistance effect.

The ordinary MR effect arises as a result of the Lorentz force ($\vec{F} = -e\vec{v} \times \vec{B}$) acting on conduction carriers. Under a magnetic field, B, the carriers move in cyclotron orbits perpendicular to B with a radius $r_c = m^* v/eB$, where m^* is the effective mass of the electron, v is the Fermi velocity and is of the order of 1.5×10^5 m/s in CrO_2.[17] The fundamental quantity for MR is $\omega_c\tau$, the mean angle turned along a helical path between collisions where $\omega_c = eB/m^*$ is the cyclotron frequency and τ is the scattering time (carrier lifetime). For large fields an electron can make many turns about this axis thereby decreasing its mean free path and increasing the resistivity. By solving the Boltzmann equation it was found that the resistance should initially increase as the square of the magnetic field, B^2, and then saturate when $\omega_c\tau \approx 1$.

The behaviour of the ordinary magnetoresistance of metals depends on the field orientation with respect to the current and the crystal axes as well as the field strength. Thus, to ascertain the characteristics of a metal, it is often necessary to perform resistance measurements with the field in-plane and either parallel (longitudinal resistance, $\rho_{\parallel}$) or perpendicular (transverse resistance, ρ_T) to the current as well as perpendicular to the plane of the sample and the current (perpendicular resistance, $\rho_{\perp}$). The longitudinal magnetoresistance in general should be zero since there is no Lorentz force acting on the conduction electrons. It is the transverse and perpendicular MR that increase as B^2 and saturate at $\omega_c\tau \approx 1$. The transverse and perpendicular MR may differ from each other in a thin film because the mean free path could be limited by the film thickness, t.

Furthermore, due to the convoluted nature of the Fermi surface an anisotropy between the transverse and perpendicular magnetoresistances can arise in real metals. For example, the magnetoresistance may be seen to saturate at some field for one field-current configuration whilst in the other it may continue to rise as B^2 without saturation. A

magnetoresistance that saturates is generally an indication of closed orbits, in which electrons are prevented from acquiring energy from an applied electric field. A non-saturating MR is evidence for open orbits through which an electron can travel indefinitely if it is not scattered. The shape of the Fermi surface differs with respect to the crystallographic axes and for this reason different MR effects are observed for the various field-current-crystal axes configurations. Moreover, a non-saturating MR is also indicative of a compensated material, that is, a material comprising of two types of charge carriers e.g. electrons and holes occurring in equal numbers.[18]

B. *Anisotropic Magnetoresistance*

Anisotropic magnetoresistance is an intrinsic property related to the orbital moment of the atomic charge distribution and changes sign with the relative orientation of the current and magnetisation. This is illustrated in Fig. 5.3.

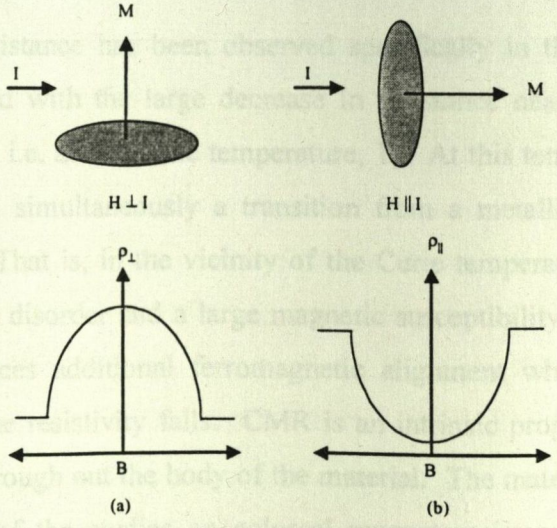

Fig. 5. 3. (a) When the magnetic field is applied perpendicular to the direction of the current, the conducting electrons see a smaller charge distribution from which they are scattered and the resistance decreases with increasing field. (b) The conduction electron travelling in the direction of magnetisation of the sample experience a larger scattering cross-section and the magnetoresistance increases with increasing field.

In the unaligned state, magnetic moments are randomly aligned and the charge distribution surrounding an atom presents an average scattering cross-section from which conduction electrons are scattered isotropically. As a result, the longitudinal and transverse resistivities are the same. However, when a magnetic field is applied, the moments are aligned along the field direction so that the resistance now depends on the direction of the current with respect to the magnetisation. When the current is perpendicular to the magnetisation, the scattering cross-section presented to the conduction electrons is small and the resistance is low and decreases with field. When the current is parallel to the direction of magnetisation the scattering cross-section is much larger leading to a large longitudinal magnetoresistance that increases with field. The result is an anisotropy between the longitudinal and transverse magnetoresistances known as "anisotropic" magnetoresistance (AMR) for which $\rho_{\|} < 0$ and $\rho_T > 0$.

C. *Colossal Magnetoresistance*

Colossal magnetoresistance has been observed specifically in the 3d-transition metal oxides and is associated with the large decrease in resistance near the paramagnetic to ferromagnetic transition i.e. at the Curie temperature, T_c. At this temperature, the material is observed to undergo simultaneously a transition from a metallic to an insulating or semiconducting state. That is, in the vicinity of the Curie temperature of a ferromagnet, there is substantial spin disorder and a large magnetic susceptibility. An applied field of the order of 1 T induces additional ferromagnetic alignment which in turn promotes electron hopping and the resistivity falls. CMR is an intrinsic property because the spin alignment is induced through out the body of the material. The materials which have been at the centre of most of the studies on colossal magnetoresistance are the manganese perovskites, $Ln^{3+}_{1-x}A^{2+}_{x}MnO_3$, where Ln = Y, La, Pr, Nd, Sm and Gd and R = Ca, BA, Sr and Pb. When hole doped at a concentration 20-40% holes/Mn ion, for instance by Ca or Sr, the material is seen to display a transition from a high-temperature paramagnetic-insulator to a low-temperature ferromagnetic-metal.[15] The basic interaction responsible for

CMR is the double exchange interaction between neighbouring heterovalent Mn ions.[19] However, the double exchange mechanism provides only a starting point and is insufficient to explain all the aspects of CMR observed in the manganites. To this, electron-phonon coupling interactions have been added to account for the CMR.[20, 21] The origin of the electron-phonon coupling in the manganites is the large Jahn-Teller effect which occurs for d^4 ions in an octahedral environment.[22] However, whilst progress has been made in understanding qualitatively and quantitatively CMR, there remains no definitive agreed explanation of all the observed effects.

D. *Giant Magnetoresistance*

Giant magnetoresistance, GMR, is associated with alignment of randomly oriented ferromagnetic entities or antiferromagnetically coupled layers in a magnetic field for which the resistance decreases for all field directions. It arises as a result of spin-dependent scattering of conduction electrons in a ferromagnet which may be controlled by changing the magnetic configuration. GMR has been observed in heterogeneous ferromagnetic materials such as thin film multilayers of magnetic and normal metals[23] as well as in granular alloy systems.[24]

The existence of GMR can be understood qualitatively on the basis of a two fluid model for the conduction process.[25] In this model, electrons can be split into two classes, those with their spins parallel to the direction of local magnetisation and those with spins antiparallel. If the scattering of conduction electrons is different for the two spin species, e.g. stronger in the case of antiparallel alignment and weaker for parallel alignment of the conduction electron spin and the magnetisation, then spin-↑ and spin-↓ electrons will exhibit different transport properties. An electron with its spin parallel to the local magnetisation will have a long mean free path while electrons with spins antiparallel to the local magnetisation will have a short mean free path. As a result, spin-↑ electrons in a region of ↑-magnetisation will be weakly scattered leading to a low resistance state whilst spin-↓ electrons will be effectively scattered leading to a high resistance state. Figure 5.4

shows how spin-↑ and spin-↓ electrons are scattered in a multilayer material separated by a non-magnetic spacer layer when the layers are oriented (a) antiparallel and (b) parallel to each other.

The main origins of the spin-dependent scattering lie in (i) the spin-dependent scattering potential experienced by conduction electrons at the interfaces between magnetic and non-magnetic regions and (ii) the spin-dependent density of states of the d-bands. The scattering potential is written in the form $V\text{-}2J\bar{s}.\bar{S}'$ where V is the spin-independent scattering potential and J is the exchange interaction between the spin, $\bar{s}$, of the conduction electron and the localised spin, S,' at the interface/surface of the magnetic scattering centre. Since $s = \pm 1/2$ there exists a different scattering potential for spin-up and spin-down electrons[26]. In addition, spin-up and spin-down conduction electrons are asymmetrically scattered by the spin-dependent density of states of the d-bands since $N_{+}^{(d)} \neq N_{-}^{(d)}$ in a ferromagnet.

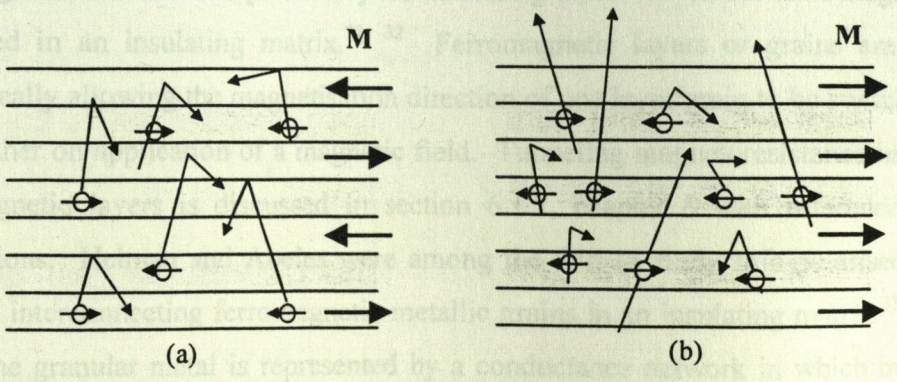

Fig. 5. 4. Schematic of the conduction in a magnetic multilayer for (a) antiparallel and (b) parallel alignment of magnetic layers. (a) shows that there is equal scattering of spin-up and spin down electrons. (b) When a magnetic field is applied, the moments in the magnetic layers are aligned and only electrons with spins parallel to the magnetisation of the layers can traverse the multilayer. Hence we go from a high resistance state to a low resistance state on turning on the magnetic field.

GMR is also observed in granular materials where it is assumed that there are no magnetic interactions between neighbouring magnetic regions.[24] In zero field the magnetic

moments are randomly oriented and both spin-up and spin-down electrons are scattered equally. When a field is applied the moments are aligned providing a low resistance path for half of the conduction electrons i.e. for those electrons with moments parallel to the magnetisation. With this in mind it can be understood that if a fully spin-polarised current was used, then when conduction electrons are aligned antiparallel to the direction of local magnetisation, all the current is effectively blocked whilst in the aligned configuration, all the current can pass leading to larger magnetoresistance effects. For a more detailed review of GMR in magnetic mulitlayers and granular solids see references.[27, 28]

E. *Tunnel Magnetoresistance*

Tunnel magnetoresistance refers to the tunneling of a spin-polarised current between ferromagnetic electrodes separated by an insulating layer[29, 30] or between magnetic grains imbedded in an insulating matrix.[31, 32] Ferromagnetic layers or grains are decoupled magnetically allowing the magnetisation direction of one layer/grain to be switched relative to the other on application of a magnetic field. Tunneling magnetoresistance in uncoupled ferromagnetic layers is discussed in section 6.1.2, chapter 6 with reference to device applications. Helman and Abeles were among the first to study spin-polarised tunneling between interconnecting ferromagnetic metallic grains in an insulating matrix.[33, 34] In this study, the granular metal is represented by a conductance network in which metal grains are interconnected by weak links having resistivities given by:

$$\rho = \rho_{\infty} \exp(\Delta / k_B T)^{1/2} \qquad 5.16$$

where ρ_{∞} is the resistivity at T = 300K and Δ is proportional to the charging energy $E_c = e^2/2C$, and C is the capacitance of the ferromagnetic grains. The charging energy E_c is associated with the energy involved in transferring an electron from one grain to another. This phenomenon is known as Coulomb Blocade.[35] The effect is illustrated in Fig. 5.5

whereby an electron tunneling from one grain to a neighbouring grain results in the transfer of a net negative charge so that a net positive charge builds up on neighbouring grains.. The capacitance of a small metallic particle is $C = 4\pi\varepsilon_o\varepsilon_r r$ where ε_o is the permittivity in vacuum, ε_r is the relative permittivity and r is the average radius of the grains which are assumed to be approximately spherical.[36] The potential change due to one extra electron is $\Delta V = e/C$, which leads to the expression for E_c.

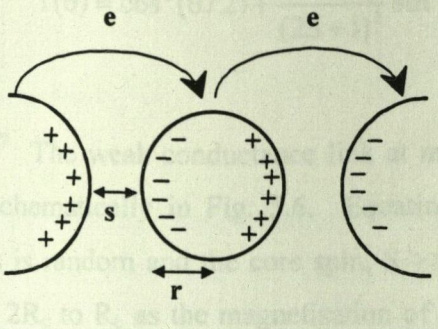

Fig. 5. 5. Electron tunneling resulting in Coulomb Blocade and a capacitance C. The energy required to generate a pair of positively and negatively charged grains is the charging energy, E_c.

The distance between the grains, s, corresponds to the tunnel barrier thickness and tunneling will occur via paths which make the conductivity largest. At high temperatures, the dominant contribution to the conductivity is due to tunneling between small grains with thin tunnel barriers whereas at low temperatures, the dominant contribution is due to larger grains separated by thicker barriers.[33]

When tunneling occurs between ferromagnetic small metallic grains, an extra energy term, E_m, relating to the difference in exchange energies of an electron situated on two different grains must be incorporated. Tunneling now depends on whether the tunneling electrons have moments parallel or antiparallel to that of the grain magnetisation and the current through the weak link is controlled by the relative orientation θ_{ij} of the grains' magnetisation. The resistance is:[32]

$$R_c = R_{ij} / f(\theta_{ij}) \qquad 5.17$$

where R_{ij} is the resistance between neighbouring grains i and j and depends on the barrier height, junction area and junction thickness and $f(\theta_{ij})$ is the probability that an electron will transfer into an adjacent particle and is written as:

$$f(\theta) = \cos^2(\theta/2) + \frac{2S}{(2S+1)^2}\sin^2(\theta/2) \qquad 5.18$$

where S is the core spin.[37] The weak conductance link at magnetic saturation and at the coercive field is shown schematically in Fig. 5.6. Equation 5.18 averages to ½ if the orientation of the particles is random and the core spin, $S >> 1$. Hence, the resistance of the weak link varies from $2R_c$ to R_c as the magnetisation of the particles is aligned and a magnetoresistance of 100% is predicted in this case.

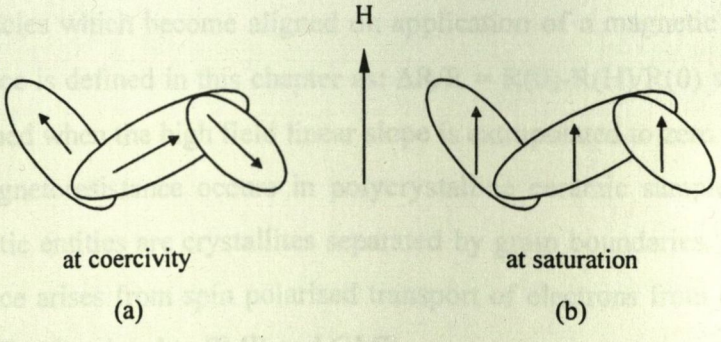

Fig. 5. 6. A weak conduction link in a path of high conductivity. The arrows indicate the direction of magnetisation at (a) the coercive field and (b) at magnetic saturation.

Helman and Abeles also deduced a classical expression for the magnetoresistance of ferromagnetically coupled grains in an insulating matrix given by:[33, 38]

$$\frac{\Delta\rho}{\rho} = -\frac{JP}{4k_B T}\left[m^2(H,T) - m^2(0,T)\right] \qquad 5.19$$

where J is the intergrain exchange constant, P is the polarisation and m is the magnetisation normalised to the saturation value. Hence, the higher the value of P the larger the magnetoresistance expected.

F. *Powder Magnetoresistance*

Powder magnetoresistance (PMR) is essentially the same phenomenon as tunneling magnetoresistance. In this case, however, the ferromagnetic entities are now powder particles assembled so that whilst there is a weak contact between particles allowing spin-polarised transport to take place there is no exchange coupling. Negative magnetoresistance arises due to tunneling of spin-polarised electrons between magnetically misaligned particles which become aligned on application of a magnetic field.[16] Powder magnetoresistance is defined in this chapter as: $\Delta R/R = R(0)-R(H)/R(0)$ where R(0) is the resistance obtained when the high field linear slope is extrapolated to zero field.

Granular magnetoresistance occurs in polycrystalline ceramic samples or thin films. The ferromagnetic entities are crystallites separated by grain boundaries. Again, negative magnetoresistance arises from spin polarised transport of electrons from one crystallite to the next. The effect is related to PMR and GMR.

5. 1. 4. The Hall Effect

When a metal is placed in a magnetic field, $\bar{H}$, and a current density, $\bar{J}$, is passed through it, then an electric field, $\bar{E}_H$ perpendicular to both field and current is set up,

Fig. 5.7. This electric field is proportional to the cross product of the field and the current density and is given by:

$$\vec{E}_H = R_H \vec{B} \times \vec{J} \qquad 5.20$$

$\vec{E}_H$ is known as the Hall voltage and R_H is the Hall coefficient.

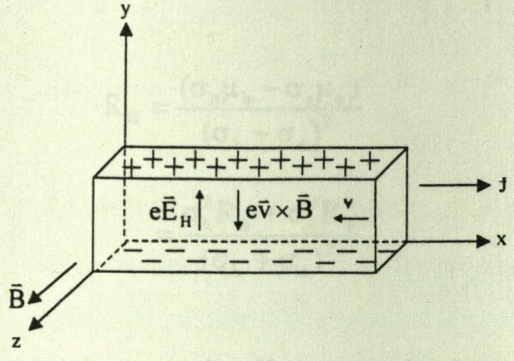

Fig. 5. 7. Hall effect geometry. The Lorentz force $-e\vec{v} \times \vec{B}$ acting on the electrons is just balanced by the force $-e\vec{E}_H$ due to the Hall effect.

The origin of the Hall effect is the Lorentz force, $-e\vec{v} \times \vec{B}$, which acts on the conduction electrons in a magnetic field. Electrons travelling in the -x-direction are deflected downwards by the Lorentz force with the result that negative charge builds up on the lower surface of the metal. To compensate this, positive charge builds up on the upper surface creating a Hall voltage, $\vec{E}_H$ in the –y direction. As a consequence of the Hall voltage, current continues to flow in the x-direction, as it must for a metal rod with electrical connections at both ends. Under steady state conditions in the free electron model, $E_y = v_x B = J_x B/(-ne)$ so that the Hall coefficient is then written as:

$$R_H = -1/ne \qquad 5.21$$

where n is the carrier concentration and e the electronic charge. Therefore R_H is not only a measure of the carrier concentration but also of the type of carrier (electron or hole) since the sign of R_H depends on the carrier type. This effect is often referred to as the "normal" Hall effect. R_H can also be written in terms of the mobility μ and the conductivity σ as $R_H = \mu/\sigma$ and his measured in $m^3\ C^{-1}$.

When both electrons and holes are present in significant numbers, as can sometimes happen in a semiconductor or a metal, then the Hall coefficient is given by:[39]

$$R_H = \frac{(\sigma_h\mu_h - \sigma_e\mu_e)}{(\sigma_h + \sigma_e)^2} \qquad 5.22$$

$$= \frac{\sigma_h^2 R_h + \sigma_e^2 R_e}{(\sigma_h + \sigma_e)^2}$$

where σ_h is the hole conductivity, σ_e is the electron conductivity, μ_h the hole mobility and μ_e the electron mobility. R_h and R_e are the Hall coefficients for the holes and the electrons respectively and are defined by equation 5.21 where the electron concentration is replaced by the hole concentration, p in the case of holes. The Hall resistance within this two band model is then written as:[40]

$$\rho_H = B\frac{\sigma_h^2 R_h + \sigma_e^2 R_e + \sigma_h^2\sigma_e^2 R_h R_e (R_h + R_e)B^2}{(\sigma_h + \sigma_e)^2 + \sigma_h^2\sigma_e^2 (R_h + R_e)^2 B^2} \qquad 5.23$$

In addition to the "normal" Hall effect there exists another effect known as the "anomalous" or "extraordinary" Hall effect. In the case of magnetic materials, the motion of conduction electrons is subject to external and internal magnetic fields and the Hall resistivity is given by:

$$\rho_H = R_H B + R_s M \qquad 5.24$$

where $B = \mu_o(H+(1-N)M)$ where N is the demagnetisation factor and M the magnetisation. The last term in equation 5.24 is the anomalous Hall resistivity which is magnetisation dependent and R_s is the anomalous Hall coefficient. The effect has two origins: one is due to the internal field produced by the magnetisation and the other is due to the spin-orbit interaction between 3d spins and conduction electrons.[41] The anomalous Hall effect is proportional to the sample magnetisation.

5. 2. Experimental Procedure

Electronic transport measurements were carried out on oriented films and pressed powder compacts of CrO_2. The electronic transport measurements included resistivity as a function of temperature, isothermal magnetoresistance and the Hall Effect. Below, the various methods for preparing samples for measurement will be discussed as well as the procedure for carrying out transport experiments.

5. 2. 1. Sample Preparation

Pressed powder compacts were prepared by pressing commercial or reactor produced CrO_2 powder, into pellets using a non-magnetic die and a Buehler hydraulic bench top press. Disks with a diameter of 6.5-9 mm and thickness ~ 0.8 mm were pressed at pressures of 0.4 GPA. Typical densities of 45% were achieved though densities up to 57% could be obtained if the disks were compressed further. Mixed powder composites of CrO_2 and Cr_2O_3 were prepared by mixing a weight fraction x of CrO_2 with a fraction (1-x) of Cr_2O_3 and pressing in the usual manner. The Cr_2O_3 was obtained by reducing the CrO_2 to Cr_2O_3 in vacuum at 500°C. In this way, the Cr_2O_3 powder had the same particle size as the CrO_2. Very often the pressed powder samples were very delicate and difficult to work

with. To overcome this problem, the samples could be mixed with epoxy resin. The pellets were pressed and then heat treated at 100°C. Densities of up to 80% could be achieved using this method.

Amongst the oriented films that were measured were (100), (110) and (001) oriented CrO_2 films grown on the TiO_2 substrates (see Chapter 2). In some cases, transport measurements were carried out on films which had been patterned using photolithography and chemical wet etching techniques (see Section 6.3, Chapter 6, for a description of the patterning process).

Electrical contacts were made using silver paint and silver wire having a diameter of 50 μm. When high-temperature resistivity measurements were to be performed, the sample contacts were baked in air at 570 K for 1-2 hours before measurement in order to avoid oxidation and/or diffusion of the contacts into the sample during measurement. If this procedure was not carried out the data acquired was found to be very noisy and difficult to measure. The standard linear 4-point measuring geometry was the contact configuration adopted for transport measurements, Fig. 5.8.

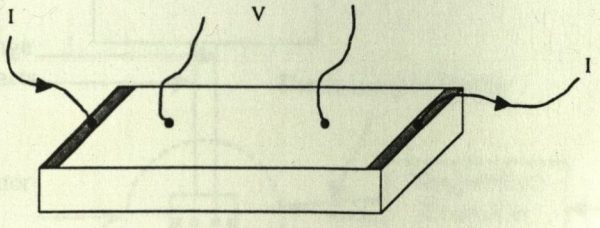

Fig. 5. 8. Linear 4-point geometry for transport measurements

5. 2. 2. Electronic Transport Measurements

Low-temperature resistivity measurements were measured using the experimental set-up shown in Fig. 5.9. Samples were placed in thermal contact with a highly conducting copper block using a thermally conducting, electrically neutral gel. The copper block is attached to the head of a closed-cycle helium refrigerator operating in the temperature

range 10-300 K. A chromel-gold thermocouple located in the copper block just beneath the sample was used to control and measure the temperature. In most cases, a dc method was used and a dc current ranging from 5 nA to 10 mA was supplied to the sample using a Keithley 224 constant current source. The output voltage was measured using a Keithley 195A voltmeter.

High-temperature resistivity measurements were carried out at temperatures ranging between room temperature and 500 K. The set-up is very similar to that described above except in this case, samples were attached, again using the thermally conducting electrically neutral gel, to a ceramic rod encasing copper wires to which the sample contacts were bonded using silver paint. The sample is then placed in a furnace operating from room temperature to 1500 K. The temperature was measured using a K-type (Nickel-Chromium/Nickel-Aluminium) thermocouple from which the voltage is read using a Keithley 197 voltmeter and converted to kelvin using a polynomial conversion. A dc method described was also used for high-temperature measurements.

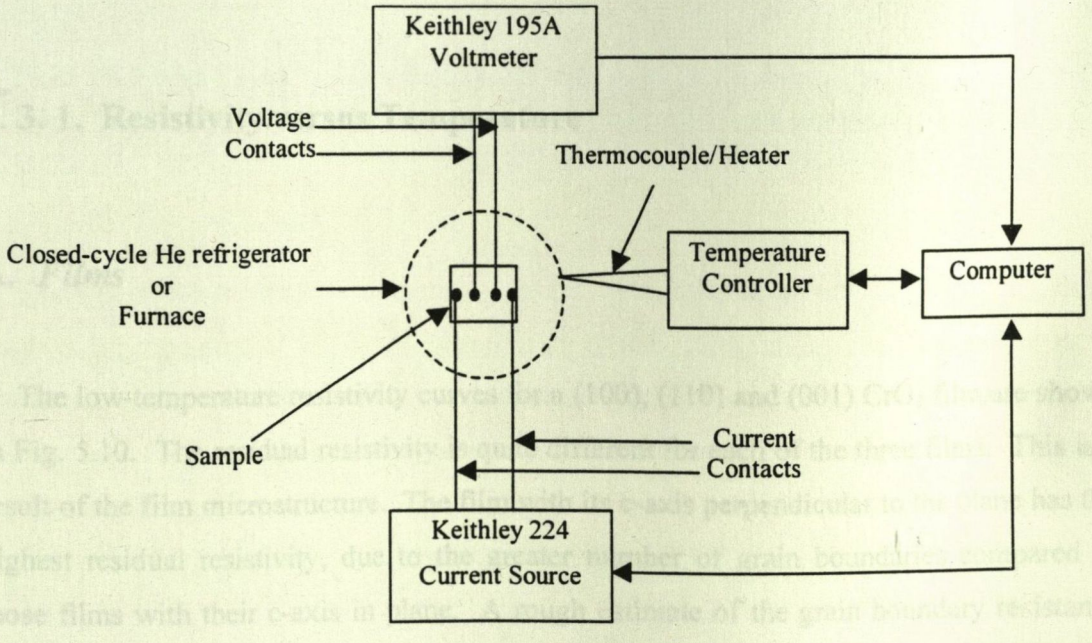

Fig. 5. 9. General schematic diagram of the experimental set-up for low- and high-ρ(T) measurements.

Magnetoresistance measurements were carried out on pressed powders and oriented films in a variable temperature cryostat with a superconducting magnet. Measurements were performed in fields of up to 25 T and at several temperatures ranging from 4.2-300 K at the NHFM and MARTECH laboratory, Tallahasee as well as at UCSD, San Diego. The method used to measure the magnetoresistance was similar to that described above except in this case, the input signal was a low-frequency (30-100 Hz) ac current supplied by the reference input of a lock-in amplifier and the output signal was measured using the lock-in detection.

Hall effect measurements were carried out on patterned CrO_2 films in the same variable temperature cryostat with a superconducting magnet. For Hall measurements, the film plane was oriented perpendicular to the field direction.

5. 3. Results

5. 3. 1. Resistivity versus Temperature

A. *Films*

The low-temperature resistivity curves for a (100), (110) and (001) CrO_2 film are shown in Fig. 5.10. The residual resistivity is quite different for each of the three films. This is a result of the film microstructure. The film with its c-axis perpendicular to the plane has the highest residual resistivity, due to the greater number of grain boundaries compared to those films with their c-axis in plane. A rough estimate of the grain boundary resistance for the (001) film having an average needle diameter of 3 μm is $r_{gb} = R_o \times A \sim 2.0 \times 10^{-11}\ \Omega.m^2$ where R_o is the residual resistance and A is the cross-sectional area of the needle.

At low temperatures it can be seen that the films with few grain boundaries are good metals with residual resistivities of the order of 0.1 $\mu\Omega$ m. The resistivity barely changes up to about 80 K for these films. At temperatures greater than 80 K it increases rapidly.

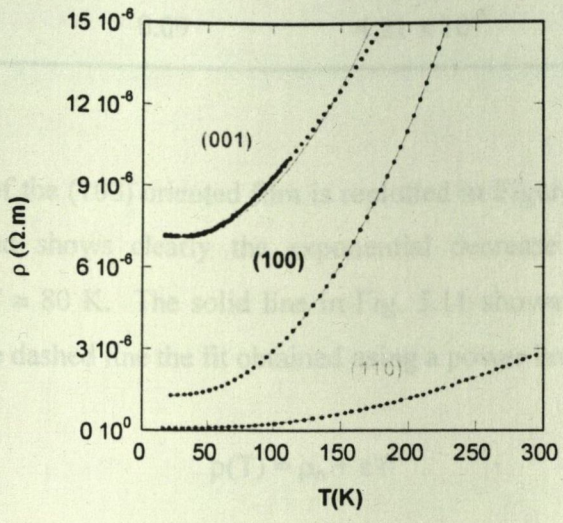

Fig. 5. 10. Resistivity as a function of temperature in the range 10-300 K for a F3-(100), F17-(110) and F15-(001) oriented CrO_2 film. The solid black line shows the fit to the experimental data using equation 5.14.

Consistent fits to the low temperature resistivity could not be obtained using a normal expression in powers of T. These power laws are described in section 5.1.2 and relate to scattering due to electron-phonon interactions, electron-electron interactions, scattering by defects and magnon scattering processes. Instead superior fits were obtained using the expression set out in equation 5.14 i.e:

$$\rho(T) = \alpha T^2 \exp(-\Delta_g / kT)$$

The solid black lines in Fig. 5.10 are the fits to the data using this expression. The parameters ρ_o, α and Δ_g are listed in Table 5.1.

Table 5. 1. Results of the fits to the experimental data in Fig. 5.10 using equation 5.14.

Film Type	ρ_o ($\mu\Omega$ m)	α($\mu\Omega$ m/K^2)	Δ_g (K)
(001)	7.07	4.80×10^{-4}	73
(100)	1.29	3.72×10^{-4}	81
(110)	0.09	4.21×10^{-5}	87

The resistivity data of the (100) oriented film is replotted in Figure 5.11 in the temperature range 20-120 K and shows clearly the exponential decrease of the resistivity with temperature below T ≈ 80 K. The solid line in Fig. 5.11 shows the fit to the data using equation 5.14 and the dashed line the fit obtained using a power law of the type:

$$\rho(T) = \rho_o + cT^n$$

The exponential fit to the resistivity data of the (100) film (equation 5.14) is clearly superior to the power law fit. The same is true for the (110) and the (001) oriented film.

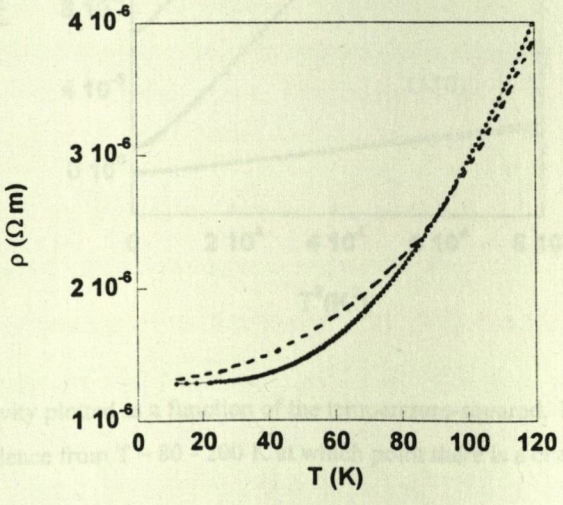

Fig. 5. 11. Resistivity as a function of temperature for the (100) oriented CrO_2 film. The solid line corresponds to the exponential fit to the data (equation 5.14) and the dashed line shows the fit to the data using a power law.

For a metallic ferromagnet at low temperatures, the resistivity is described by: $\rho(T) \sim \rho_o + \alpha' T^2 + ...$ (equation 5.13) and the T^2 dependence arises from electron-magnon scattering.[42, 43, 44] However, as Fig. 5.10 and 5.11 show, the resistivity of CrO_2 shows a significant departure from this behaviour at low temperatures suggesting that magnon scattering is suppressed. Fig. 5.12 shows $\rho(T)$ plotted as a function of the temperature-squared for the (001), (100) and (110) oriented films. From this diagram it can be seen that $\rho(T)$ is linear from approximately 80 K to 200 K. The slopes of the curves in this temperature range correspond to the coefficient α' which ranges between 10^{-4}–10^{-5} $\mu\Omega$ m/K^2, the highest value for α' being obtained for the (001) oriented film. Suzuki and Tedrow found similar deviations from the T^2 dependence at 130 K and 240 K for a (100) oriented CrO_2 film grown on a ZrO_2 substrate and reported comparable values for the α' coefficient.[45]

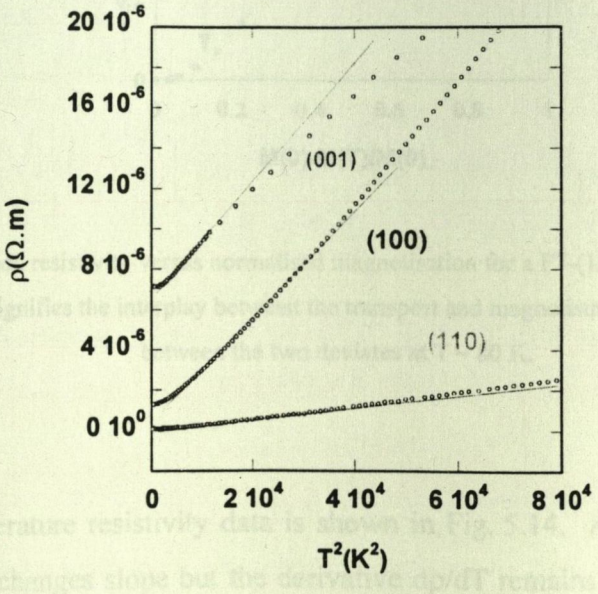

Fig. 5. 12. Resistivity plotted as a function of the temperature-squared. Note that there is a linear dependence from T ~ 80 - 200 K at which point there is a change in slope.

Fig. 5.13 shows that if the low temperature resistivity is plotted as a function of magnetisation, a linear behaviour that deviates strongly at T ~ 80 K is observed.[46] This

linear dependence suggests that the resistivity scales with the magnetic disorder. The deviation at 80 K from a near linear dependence supports the idea that magnon scattering is exponentially suppressed at low temperatures. At 200K there is a small change in slope, similar to that observed in the $\rho(T)$ vs T^2 plot. The significance of this change in slope at 200 K may be interpreted as being due to the onset of other scattering processes such as phonon scattering as well as higher order magnon scattering processes.

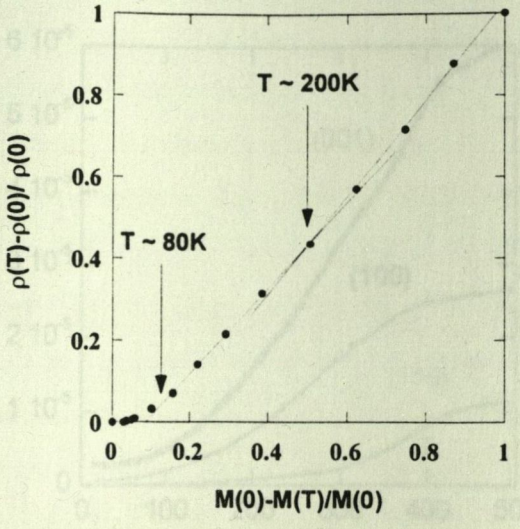

Fig. 5. 13. Normalised resistivity versus normalised magnetisation for a F7-(100) oriented CrO_2 film. The linear dependence signifies the interplay between the transport and magnetism. However the relationship between the two deviates at T ~ 80 K.

The high-temperature resistivity data is shown in Fig. 5.14. At the Curie temperature T_c, the resistivity changes slope but the derivative $d\rho/dT$ remains positive. The transition from the ferromagnetic to the paramagnetic state exhibited in the $\rho(T)$ data is broad. Consequently, T_c is poorly defined by this method. Above the Curie temperature, the resistivity increases almost linearly with temperature. The linear increase appears steeper in the case of the (001) film. In the high temperature limit i.e. the paramagnetic region of resistivity the localised spins fluctuate about their average value and the net magnetisation is zero. Therefore, there is no temperature dependent magnetic contribution to the

resistivity at high temperatures i.e. the magnetic resistivity is constant.[10] The linear increase in resistivity above T_c is likely to be due to phonons. If we extrapolate back to zero temperature it is possible to deduce the temperature independent magnetic resistivity, ρ_M in the paramagnetic state. The slopes of $\rho(T)$ above T_c vary depending on the sample as do the residual resistivities, thus, ρ_M is different for each sample. These values are listed below.

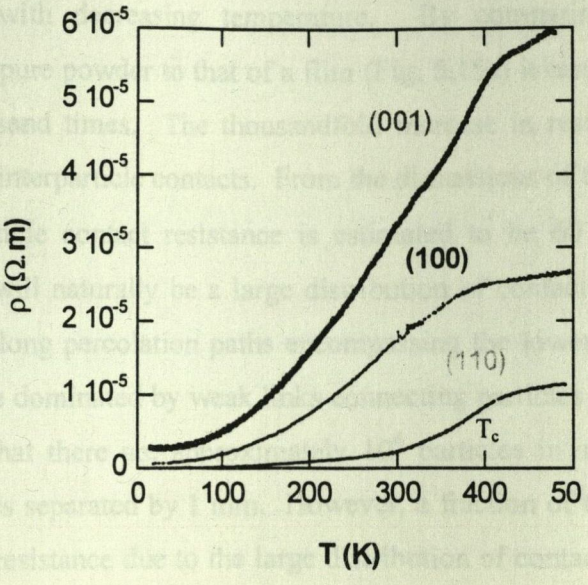

Fig. 5. 14. High-temperature resistivity curves for F62-(100), F61-(110) and F56-(001) oriented films showing a change in slope at $T = T_c$

Table 5. 2. The magnetic resistivity, ρ_M, obtained by extrapolating the high temperature resistivity curves to zero temperature for F62-(100), F61-(110) and f56-(001) oriented CrO_2 films.

Film Type	ρ_M ($\mu\Omega$ m)
(001)	28.5
(100)	17.2
(110)	2.8

B. *Powders*

The low temperature resistivity of a pure and diluted pressed powder compact prepared from commercially produced CrO_2 powder is shown in Fig. 5.15b and c respectively. (This was work carried out at the Centre for Magnetic Recording, University of California, San Diego in collaboration with A. E. Berkowitz, Ll. Balcells and F. F. Putris). The resistivity behaviour of the pressed powders is similar to that of an insulator or semiconductor where $\rho(T)$ increases with decreasing temperature. By comparing the room temperature resistivity of the pure powder to that of a film (Fig. 5.15a) it can be seen that the resistivity increases a thousand times. The thousandfold increase in resistivity is attributed to the resistance of the interparticle contacts. From the dimensions of the particles (~ 300 nm) the average interparticle contact resistance is estimated to be 60 kΩ at room temperature. However, there will naturally be a large distribution of contact resistance and conduction will take place along percolation paths encompassing the lowest resistance contacts. The resistivity will be dominated by weak links connecting particles on these percolation paths. It is estimated that there are approximately 10^4 particles in a conduction path between voltage electrodes separated by 1 mm. However, a fraction of these particles are expected to dominate the resistance due to the large distribution of contact resistances. The number of contacts involved in the transport process is estimated by reconciling the temperature and voltage dependence of the MR ratio as we shall see in section 5.3.3B.

Comparing the contact resistance, R_c, to the quantum limit of resistivity, which is given by $R_Q = h/2e^2 = \sim 13$ kΩ and defines the maximum resistance of a metallic contact, we see that $R_c > R_Q$. Hence, it can be concluded that the interparticle contacts dominate the resistance and they are not metallic. Consequently, it can be further concluded that transport between grains must occur via tunneling.

Diluting CrO_2 in an insulating matrix of Cr_2O_3 so that we have a mixed powder composite of the type, $xCrO_2/(1\text{-}x)Cr_2O_3$ gives rise to higher resistivities as can be seen in Fig. 5.15c. However, for conduction to take place, the dilution factor, x, must be below a certain percolation threshold, x_p. This critical concentration can be determined by fitting the resistivity of cold-pressed $xCrO_2/(1\text{-}x)Cr_2O_3$ composites to the percolation theory expression:[47]

$$\rho(x) = (x - x_p)^{-t} \qquad 5.25$$

with the critical exponent t=2. This yields a percolation threshold $x_p = 0.23$. A dilute composite with x = 0.25 is very near the percolation threshold and shows a resistivity that is a thousand times greater than the undiluted CrO_2 powder with a room-temperature resistivity of 2 Ω m. The temperature dependence of the interparticle resistivity in these powders is given by equation 5.16 and the resistivity of the 25%CrO_2/75%Cr_2O_3 composite in Fig. 5.15c is fitted to this expression with $\rho_\infty = 2.09$ Ω m and $\Delta = 6.0$ K.

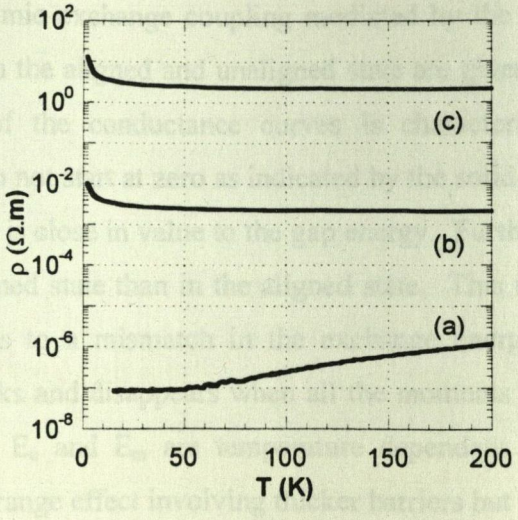

Fig. 5. 15. Temperature dependence of resistivity of (a) a F17-(110) oriented film (b) a pure pressed powder of CrO_2 and (c) a 25%CrO_2/75%Cr_2O_3 mixed powder composite.

In these CrO_2 pressed powders, the particles are small enough and the interparticle contact resistance large enough for single-particle charging to influence the conductivity. As discussed in section 5.1.3.D the charging energy is $E_c \sim e^2/2C$ where $C = 4\pi\varepsilon_o\varepsilon_r r$. If we take an average value for r ~ 125 nm and $\varepsilon_r = 5$ then C is 7×10^{-17} F giving a charging energy of 1.2 meV (13 K). The effect of the single-particle charging is to give rise to a Coulomb gap. The Coulomb gap has a significant influence on the I-V curves at low temperatures and is different for the magnetically unaligned and aligned states. Fig. 5.16

shows the conductance curves derived from the I-V curves measured at 2 K and 5 K in fields of 0.1 T (coercive state) and 2 T (saturated state). The conductance, σ, as a function of voltage can be fitted to the formula:[33]

$$\sigma = \sigma_\infty \exp[-\Delta'/eV] = \sigma_\infty \exp[-(E_c + E_m)/eV] \qquad 5.26$$

Helman and Abeles introduced the extra magnetic energy term, E_m, to account for the difference in exchange energy of contiguous, magnetically misaligned particles with n and n' electrons, and the same two particles with n-1 and n'+1 electrons. This energy is ≈ J/2 where J is the interatomic exchange coupling mediated by the conduction electron. The values for E_c and E_m in the aligned and unaligned state are given in Table 5.3 below. The voltage dependence of the conductance curves is characteristic of a Coulomb gap. However, the curves do not start at zero as indicated by the solid lines in Fig. 5.16 since the measuring temperature is close in value to the gap energy. Furthermore, the gap appears to be larger in the unaligned state than in the aligned state. This is to be expected since the energy E_m corresponds to a mismatch in the exchange energy of neighbouring grains connected by weak links and disappears when all the moments are aligned in a saturating magnetic field. Both E_c and E_m are temperature dependent because tunneling at low temperatures is a long-range effect involving thicker barriers but lower Coulomb gaps.

Table 5. 3. Results of the fits of equation 5.26 to the conductance curves in the aligned and unaligned states at 2 K and 5 K

T (K)	B (T)	E_c (mV)	E_c (K)	E_m (mV)	E_m (K)
2K	0.1T	0.29	3.4	0	-
2K	2.0T	0.29	3.4	0.31	3.6
5K	0.1T	0.34	3.9	0	-
5K	2.0T	0.34	3.9	0.47	5.5

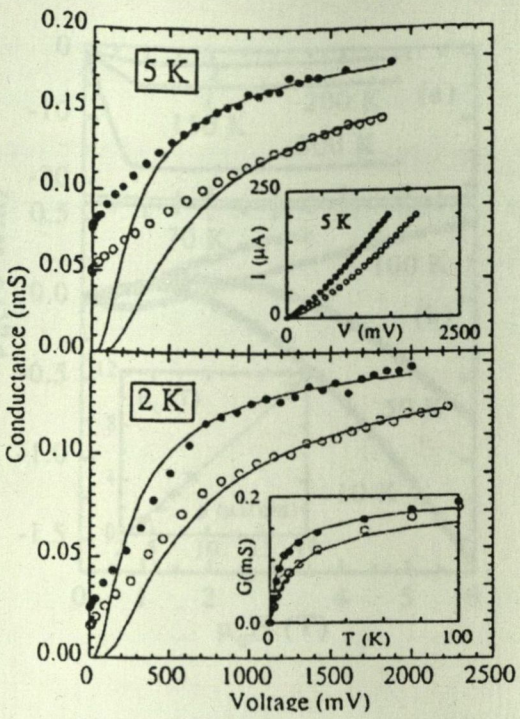

Fig. 5. 16. Conductance curves at 5 K and 2 K for the 25%CrO_2/75%Cr_2O_3 measured in 0.1 T (open circles) and 2T (solid circles). The solid lines in the main frames represent the fits to the conductance curves according to equation 5.26. The insets show the I-V curves at 5 K from which the conductance curves are deduced and the temperature dependence of the conductivity is fitted to equation 5.16.

5. 3. 2. The Hall Effect

The Hall effect was measured on a (110) oriented film that had been etched into a Hall bar having multiple voltage probes. The bar was oriented so that the current flowed parallel to the c-axis. The Hall resistivity, ρ_H, measured at several temperatures ranging from 10 K to 300 K as a function of magnetic field, is shown in Fig. 5.17.

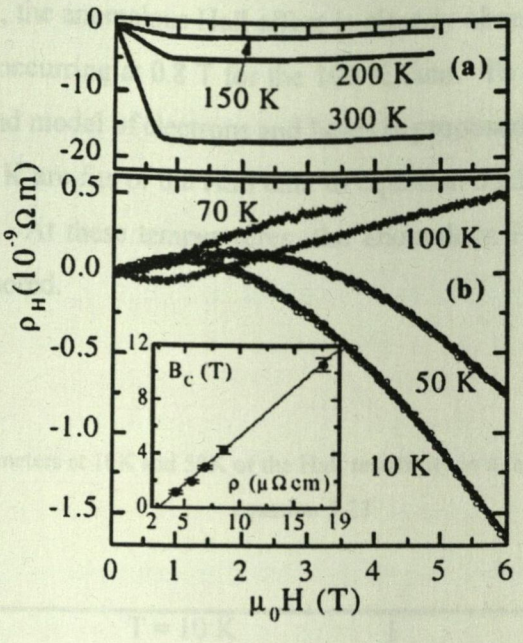

Fig. 5. 17. The Hall resistivity, ρ_H, of a (110)-F49 oriented film versus applied magnetic field, for temperatures ranging from (a) 150 K to 300 K and (b) 10 K to 100 K when the current is applied parallel to the c-axis. For temperatures above 100 K, the anomalous Hall effect dominates the resistivity. At temperatures below 100 K, the normal Hall effect is dominant. In particular, at 50 K and 10 K there is a change in slope of the Hall resistivity from positive to negative. The solid lines are fits to the data at 10 K and 50 K using the two band model described by equation 5.23. The inset shows that B_c scales linearly with the Hall resistivity.[48]

At temperatures above 70 K, there is a contribution to the Hall resistivity from both the normal Hall effect and the anomalous Hall effect. At high temperatures and low fields the Hall resistivity decreases with increasing magnetic field. This is due to the anomalous Hall effect. Beyond a magnetic field of 0.8 T, which corresponds to the magnetisation saturation field, the Hall resistivity is seen to show a linear positive slope characteristic of transport by hole-like charge carriers.

At temperatures below 100 K, the Hall data does not show a simple linear dependence with magnetic field. In particular, curves measured at 10 K and 50 K show a change in slope from positive to a negative at a crossover field, B_c. The value of B_c increases slowly

as the temperature is raised from 10 K to 50 K and then increases rapidly between 50 K and 100 K. Above 70 K, the anomalous Hall effect is already observable and is responsible for the change in slope occurring at 0.8 T for the 100 K data. To explain the low temperature properties, a two-band model of electrons and holes is proposed.[48, 49] The solid lines in Fig. 5.17 at 10 K and 50 K are fits of the Hall data to equation 5.23 and the results of these fits are tabulated below. At these temperatures, the anomalous Hall coefficient is negligible and hence can be ignored.

Table 5. 4. Fit parameters at 10K and 50K of the Hall resistivity to a the two band model defined by equation 5.23

	T = 10 K		T = 50 K	
Parameter	Electron	Hole	Electron	Hole
$\sigma_{e/h}$ ($10^7/\Omega$ m)	2.3	0.13	1.65	0.11
$R_{e/h}$ (m^3/C)	-4.8×10^{-10}	1.8×10^{-7}	-4.7×10^{-10}	1.4×10^{-7}
n/p (m^{-3})	1.3×10^{28}	3.5×10^{25}	1.34×10^{28}	4.6×10^{25}
$\mu_{e/h}$ (m^2/V s)	0.011	0.24	0.0077	0.15

The results of the fits indicate that the positive slope, at fields less than the crossover field, reflect the dominance of highly mobile holes at low temperatures and low fields ($\omega_c\tau << 1$). At fields greater than the crossover field, the holes have moved into the high field limit ($\omega_c\tau >> 1$), and the high density of electrons dominates the Hall resistance.

Using the values given in Table 5.4 the electron and hole mean free paths λ_e and λ_h respectively, are estimated from the free electron theory where:

$$\lambda = v\,\tau$$

and v is the free carrier velocity and is obtained using the equation:

$$v = \frac{\hbar}{m^*}(3\pi^2 n)^{1/3}$$

For electrons, $n = 1.3 \times 10^{28}$ m^{-3} and $m^* = 2m_e$ is the effective mass of the electron as deduced from the specific heat data (Section 4.4.3.2, Chapter 4). The relaxation time $\tau = 6.08 \times 10^{-14}$s is obtained using the equation:

$$\tau = m^*/ne^2\rho$$

where the value $\rho = 0.09$ $\mu\Omega$ m used is the residual resistivity of the (110) film (see Section 5.3.1). Hence λ_e is determined to be ~ 300 Å. Extending this calculation to holes, it is possible to deduce a hole mean free path of the order of 1.3 μm, for a hole concentration of 3.5×10^{25} m^{-3} and an effective mass $m^* = m_e$. Hence, $\lambda_h >> \lambda_e$.

5. 3. 3. Magnetoresistance

A. *Films*

The magnetoresistance has been measured for a (001) and a (110) oriented film for various current-field-c-axis configurations. Some of these measurements were carried out at MARTECH, FSU, Tallahasee, in collaboration with S. Watts. S. Wirth and S. von Molnar.

(001) Oriented Films: Figure 5.18 show the magnetoresistance measurements for a (001) oriented CrO_2 film when the field is applied in the longitudinal (L), transverse (T) and perpendicular (P) geometries respectively. The current in this case can only be oriented perpendicular to the c-axis which is lying out of the film plane. A (001) oriented film only ever shows a negative MR which decreases in magnitude when the temperature is

raised. The MR ratios are summarised in Table 5.5 below for the various geometries at 5 K, 55 K, 100 K, 150 K and 300 K.

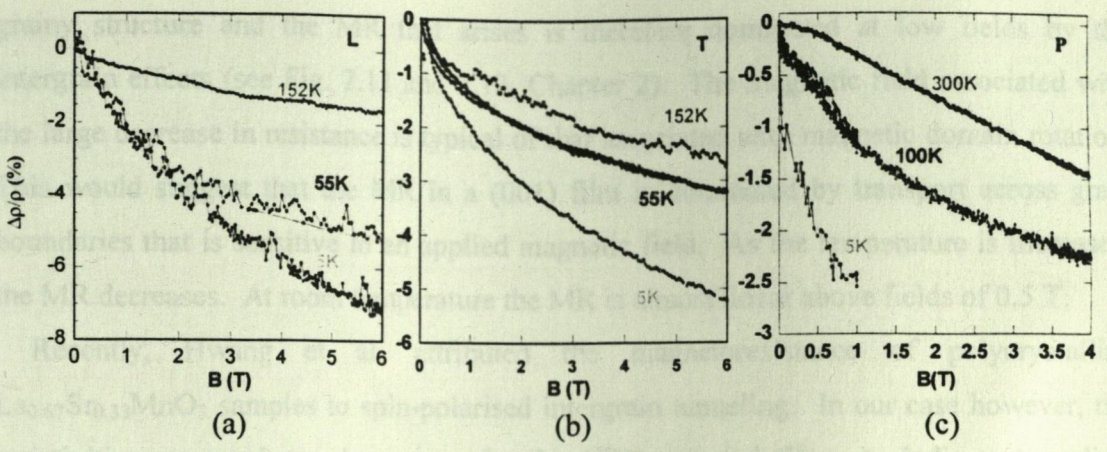

Fig. 5. 18. Longitudinal (L), transverse (T) and perpendicular (P) MR for a (001) (F15 and F55) oriented film.

Table 5. 5. Longitudinal, transverse, perpendicular MR ratios for a (001) oriented film. The data are in 6T unless stated otherwise

	F15-Longitudinal MR (%)	F15-Transverse MR (%)	F55-Perpendicular MR (%)
5K	-7.25	-5.25	-2.6 in 1T
55	-5.00	-3.25	-
100K	-	-	-2.25 in 5T
152K	-1.5	-2.75	-
300K	-	-	-1.75 in 5T

At low temperatures, the longitudinal and transverse data are observed to exhibit a relatively large low field negative MR with a lower high field slope which is typically

observed in polycrystalline or granular ferromagnetic metallic metals.[38] The large negative MR exhibited by (001) films at low temperatures and low fields is attributed to the extrinsic properties of the film. These films have a larger resistance and a particularly grainy structure and the MR that arises is therefore dominated at low fields by the intergrain effects (see Fig. 2.11 and 2.13, Chapter 2). The magnetic field associated with the large decrease in resistance is typical of that associated with magnetic domain rotation. This would suggest that the MR in a (001) film is dominated by transport across grain boundaries that is sensitive to an applied magnetic field. As the temperature is increased, the MR decreases. At room temperature the MR is almost linear above fields of 0.5 T.

Recently, Hwang et al. attributed the magnetoresistance of polycrystalline $La_{0.67}Sr_{0.33}MnO_3$ samples to spin-polarised intergrain tunneling. In our case however, the resistivities are much too low, even for the (001) oriented films, to indicate tunneling between grains. Instead, the low field MR is more likely to be a GMR response where in addition to scattering by a spin-dependent potential, there is also scattering at the grain boundaries. More difficult to explain is the high field slope.

(110) Oriented Films: The perpendicular, transverse and longitudinal magnetoresistances of a (110) oriented film at 10 K and in fields up to 6 T are compared in Fig. 5.19 when the current is applied parallel and perpendicular to the c-axis. A qualitative description of the various MR's measured is be given below.

In the (110) oriented CrO_2 film, a positive MR is observed to be the dominant MR effect present and is due to the curving of the carrier trajectory by the Lorentz force. As expected, the MR ratio is smallest in the longitudinal direction (B || I) for both current parallel and perpendicular to the c-axis configurations. This is due to the fact that the Lorentz force acts on only a small fraction of the carriers in this configuration and these carriers undergo cyclotron motion about the field axis, in a plane perpendicular to the film plane. A small positive MR of ~ 2% is observed at fields greater than ~ 0.8 T in both current configurations. Below 0.8 T the longitudinal MR is negative and measures ~2% when the current is perpendicular to the c-axis and less than 1% when the current is parallel to the c-axis. When the current is parallel to the c-axis, the negative MR may be identified as an intrinsic property of CrO_2. The larger negative MR, in the current perpendicular to c-axis configuration, may be attributed to a combined contribution from both intrinsic

properties and extrinsic properties arising from intergrain transport between progressively aligned ferromagnetic domains.

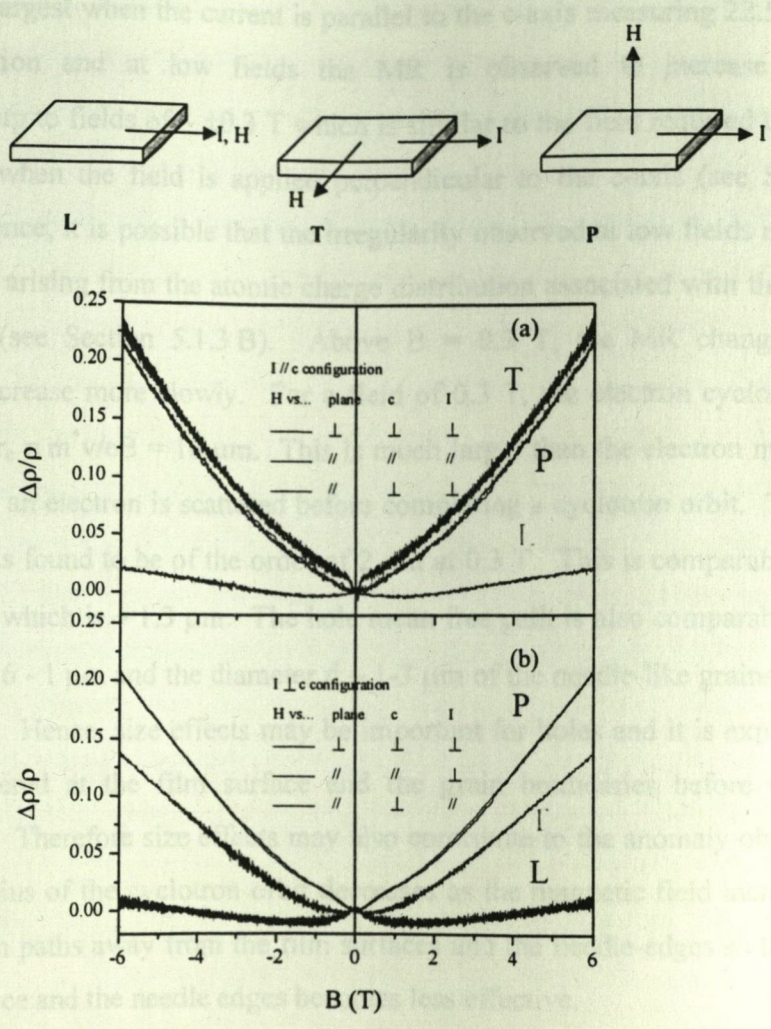

Fig. 5. 19. Longitudinal (L), transverse (T) and perpendicular (P) MR of a (110) oriented CrO_2 film (F49) at 10 K when the current is (a) parallel to the c-axis and (b) perpendicular to the c-axis.

The transverse magnetoresistance (B in plane and ⊥ I) shows a large positive MR for both the current parallel and perpendicular to c arrangements. In this geometry, carriers again move in cyclotron orbits about the field axis, perpendicular to the film plane. The

transverse MR is larger than the longitudinal MR, since all the carriers are in cyclotron motion.

The MR is largest when the current is parallel to the c-axis measuring 22.5% in 6 T. In this configuration and at low fields the MR is observed to increase rapidly and symmetrically up to fields of ~ ±0.3 T which is similar to the field required to saturate the magnetisation when the field is applied perpendicular to the c-axis (see Section 3.3.1, Chapter 3). Hence, it is possible that the irregularity observed at low fields may be due to an AMR effect arising from the atomic charge distribution associated with the direction of magnetisation (see Section 5.1.3 B). Above B = 0.3 T, the MR changes slope and continues to increase more slowly. For a field of 0.3 T, the electron cyclotron radius is approximately $r_c = m^* v/eB = 16$ μm. This is much larger than the electron mean free path of ~ 300 Å and an electron is scattered before completing a cyclotron orbit. The cyclotron orbit for holes is found to be of the order of 2 μm at 0.3 T. This is comparable to the hole mean free path which is ~ 1.3 μm. The hole mean free path is also comparable to the film thickness, t ~ 0.6 - 1 μm and the diameter d ~ 1-3 μm of the needle-like grains of which the film comprises. Hence, size effects may be important for holes and it is expected that the holes are scattered at the film surface and the grain boundaries before completing a cyclotron orbit. Therefore size effects may also contribute to the anomaly observed at low fields. The radius of the cyclotron orbit decreases as the magnetic field increases and the carriers move in paths away from the film surfaces and the needle-edges so that scattering at the film surface and the needle edges becomes less effective.

When the current is perpendicular to the c-axis the MR is positive for fields greater than ~ 0.8T and measures 13.5% in 6 T. In this current configuration, there is extra scattering of the carriers at the grain boundaries and the carrier lifetime is further reduced hence, so is the MR since $\Delta\rho/\rho \propto (\omega_c\tau)^2 = (\mu B)^2$. A very small negative MR up to 0.8 T is observed to dominate the magnetoresistance at low fields in this current arrangement and is thought to result from the transport of electrons across grain boundaries separating ferromagnetically aligned domains.

The perpendicular MR (B out of plane and ⊥ I) also shows a strong positive MR with similar MR ratios (~22% in 6 T) for both current orientations. In this field geometry the cyclotron orbits, are circulating in the plane of the film. The perpendicular MR ratio is

slightly smaller when the current is perpendicular to the c-axis and may be due to the reduction of the carrier lifetime due to scattering at the grain boundaries.

When the current is parallel to the c-axis, the MR is parabolic in low fields tending towards a linear field dependence at higher fields. Its magnitude is comparable to that of the transverse MR in the same current configuration. When the current is perpendicular to the c-axis, the perpendicular MR shows some structure at fields less than 2 T. In fact, the MR looks like it is starting to saturate at approximately 1.5 T before increasing in a linear fashion to 6 T. This may arise as a result of the competition between the negative MR associated with transport between ferromagnetically aligned grains at low fields and the positive OMR effects including size effects. In this configuration, higher fields are required to rotate the moments out of the film plane. The field required to do this is 0.8 T, as is the demagnetising field for a film. Hence, once the moments are aligned in the direction of the magnetic field the normal OMR again dominates the magnetotransport.

The perpendicular magnetoresistance of the same (110) oriented film was measured at different temperatures ranging from 10 K to 300 K for a current parallel to the c-axis. Fig. 5.20 shows this magnetoresistance when the current is parallel to the c-axis. At low temperatures the magnetoresistance is dominated by the ordinary magnetoresistance arising from the action of the Lorentz force on the conduction electrons. At 10 K and in a field of 5 T, the MR ratio is 17%. At 50K the MR is still positive but lower in magnitude at 10% in a 5 T field. At 100 K, the MR is seen to show a small negative MR which becomes positive above ~ 1.2 T indicating the competition between OMR and the onset of spin-fluctuations and a MR that arises from the alignment of ferromagnetic spins. At temperatures above 100 K the MR is negative and is entirely due to the alignment of ferromagnetic spins in a magnetic field. At room temperature, the MR is approximately -2.5% at 5 T.

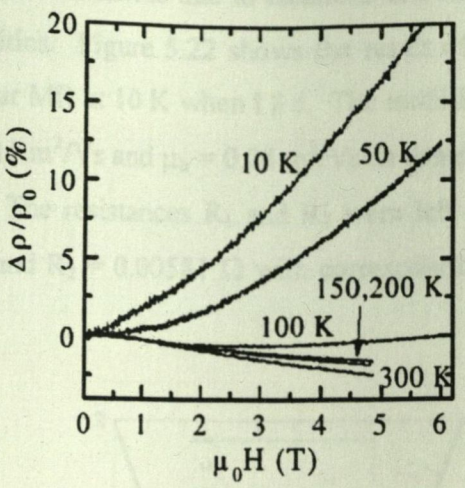

Fig. 5. 20. Perpendicular MR of the F49-(110) film at different temperatures ranging from 10-300 K, I || c.

These measurements were also extended to fields of 25 T at the NHFML, Tallahasee at 4.2 K, 77 K and 300 K and are shown in Fig. 5.21. The positive MR at 4.2 K is observed to increase without saturation up to 25 T giving a MR ratio of 200%. At 77 K, a negative MR at fields below 1.2 T is observed and reflects the onset of spin fluctuations at this temperature. The positive MR sets in at this temperature at 1.2 T, and the OMR again dominates the magnetotransport process. At room temperature, the MR is entirely negative and arises due to the transport between ferromagnetically aligned regions. The negative MR ratio measured at 300 K is -10% at 25 T and shows no sign of saturating. The temperature dependence of the perpendicular magnetoresistance at 5 T is shown in the inset.

We have attempted to fit the high field perpendicular MR at low temperatures using a two term generalisation of the Frank's formula, $\Delta R/R \propto \mu B^2/(1+(\mu B)^2)$ in which electrons and holes are assumed to be present and is written as:[50]

$$\Delta R = R_1 \frac{(\mu_e B)^2}{1+(\mu_e B)^2} + R_2 \frac{(\mu_h B)^2}{1+(\mu_h B)^2} \qquad 5.27$$

where R_1 and R_2 are the resistances due to electrons and holes respectively and μ_e and μ_h their respective mobilities. Figure 5.22 shows the result of these fits (dashed line) to the high field perpendicular MR at 10 K when I || c. The mobilities used to fit the data at 10 K were fixed at $\mu_e = 0.011$ m^2/Vs and $\mu_h = 0.24$ m^2/Vs as these were the values obtained from fitting the Hall data. The resistances R_1 and R_2 were left as variable fittings parameters giving $R_1 = 0.586\ \Omega$ and $R_2 = 0.00581\ \Omega$ with corresponding resitivities $\rho_1 = 0.94\ \mu\Omega$ m and $\rho_2 = 0.01\ \mu\Omega$ m.

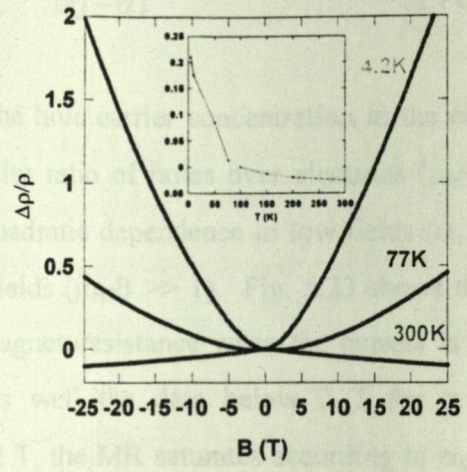

Fig. 5. 21. Perpendicular magnetoresistance of F49-(110) film at 25 T, I || c.

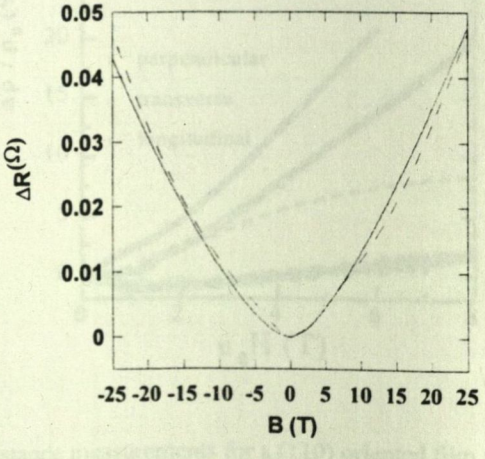

Fig. 5. 22. Fits to the Perpendicular MR (I || c) up to 25 T at 10 K using equation 5.27. The dashed curve is the fit to the data.

Within a two-band model where electrons and holes are present with different mobilities and concentrations, a more general expression for the magnetoresistance has been used to fit the transverse MR when the current is perpendicular to the c-axis. This is given by:[51]

$$\frac{\Delta\rho}{\rho} = \frac{\rho(B)-\rho(0)}{\rho(0)} = \xi \frac{(\mu_{eff}B)^2}{1+(\mu_{eff}B)^2} \qquad 5.28$$

$$\xi = \frac{\alpha(1+\beta)^2}{\beta(1-\alpha)} \qquad \mu_{eff} = \frac{1-\alpha}{1+\alpha\beta}\mu_h$$

where α is the ratio of the hole carrier concentration to the electron carrier concentration (p/n) and β is the mobility ratio of holes over electrons (μ_h/μ_e). The MR described by equation 5.28 shows a quadratic dependence in low fields ($\omega_c\tau = eB\tau/m^* = \mu_{eff}B = << 1$) which saturates at high fields ($\mu_{eff}B >> 1$). Fig. 5.23 shows the results of this fit (dashed line) to the transverse magnetoresistance when the current is perpendicular to the c-axis. The expression 5.28 fits well the data below 2 T for $\alpha = 4 \times 10^{-3}$, $\beta = 25$ and $\mu_h = 0.3\ m^2/Vs$. Above 2 T, the MR saturates according to equation 5.28. Therefore, this equation alone is inadequate for fitting the MR data.

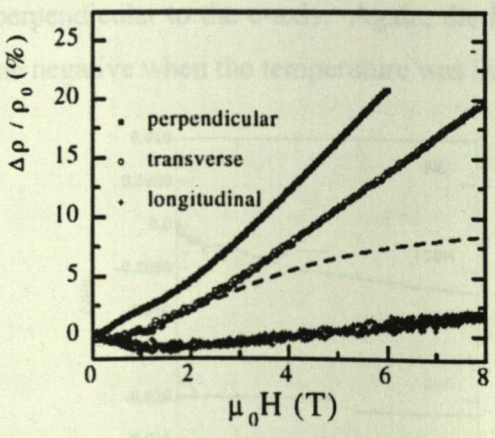

Fig. 5. 23. Magnetoresistance measurements for a (110) oriented film at 10 K for the perpendicular, transverse and longitudinal MR. The dashed line shows the result of the fit of equation 5.28 to the transverse MR. The inset shows the perpendicular MR up to 25 T at 10 K on an etched Hall bar sample used for Hall measurements. $I \perp c$ in all cases.

Suzuki and Tedrow also used a two term single-carrier expression to fit the transverse MR of CrO_2 films grown on ZrO_2 substrates at low temperatures up to 10 T. They interpreted their data as being a combination of the effects of size and cyclotron motion on the MR which they defined as:

$$\frac{\Delta\rho}{\rho} = \frac{\zeta B^2}{1+\gamma B^2} + \varepsilon B^2 \qquad 5.29$$

$$\zeta = \gamma\left(\frac{3(1-P)}{8\delta}\right), \qquad \gamma = \left(\frac{e\tau}{m^*}\right)^2, \qquad \delta = \left(\frac{t}{\lambda}\right) \qquad 5.30$$

ε is a constant coefficient of the cyclotron motion, P is the fraction of electrons impinging on the film surface, t is the thickness of the film, λ is the mean free path of the carriers, e is the electron charge, τ the relaxation time and m* the effective mass. B included a correction due to the demagnetisation field. However, using parameters similar to those obtained by Suzuki and Tedrow for ζ and γ it was not possible to fit the transverse or the perpendicular MR data. It is concluded that the MR at low temperatures arises therefore from the transport of highly mobile holes and less mobile electrons.

The transverse magnetoresistance was also measured in fields of 1 T at 5 K, 100 K and 300 K for the current perpendicular to the c-axis. Again, the MR was observed to show a positive MR that became negative when the temperature was increased, Fig. 5.24.

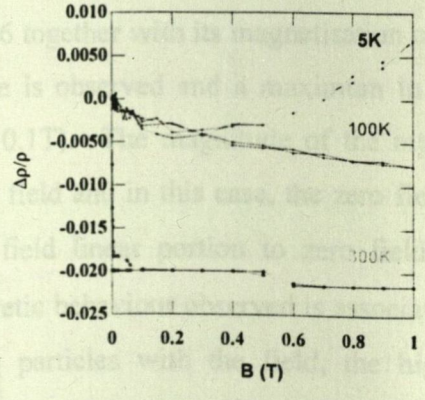

Fig. 5. 24. Transverse magnetoresistance of the (110) film (F49) at 1 T and 5 K, 100 K and 300 K (I ⊥ c-axis)

The longitudinal MR with the current parallel to the c-axis was measured up to 1 T at 5 K, 100 K and 300 K, Fig. 5.24. Only small negative MR ratios which decreased in magnitude with increasing temperature were observed in these fields. This may be attributed to the intrinsic properties of CrO_2 and the scattering of spin-polarised carriers.

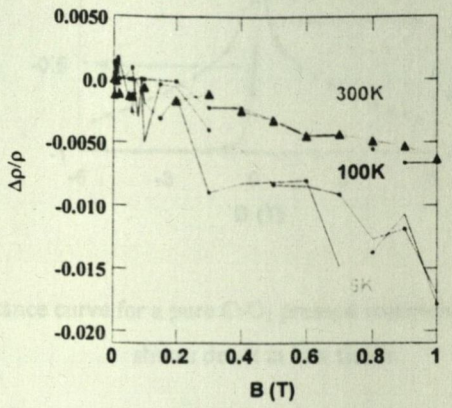

Fig. 5. 25. Longitudinal magnetoresistance of the (110) film (F49) at 1 T and 5 K, 100K and 300 K (I || c-axis).

B. *Powders*

The magnetoresistance at 5K of a pure powder composite prepared from commercial powder is shown in Fig. 5.26 together with its magnetisation curve. A butterfly curve with a reversible high field slope is observed and a maximum in the resistance occurs at the coercive field for CrO_2 (~ 0.1T). The magnitude of the magnetoresistance ratio at this temperature is 29% in a 5T field and in this case, the zero field resistance R(0) is defined by extrapolating the high field linear portion to zero field. $\Delta\rho/\rho$ is then defined as ρ_{max} - $\rho(0)/\rho(0)$. The hysteretic behaviour observed is associated with the alignment of the magnetisation of the CrO_2 particles with the field, the highest resistance state being associated with the coercive state where the resistance is observed to undergo a maximum.

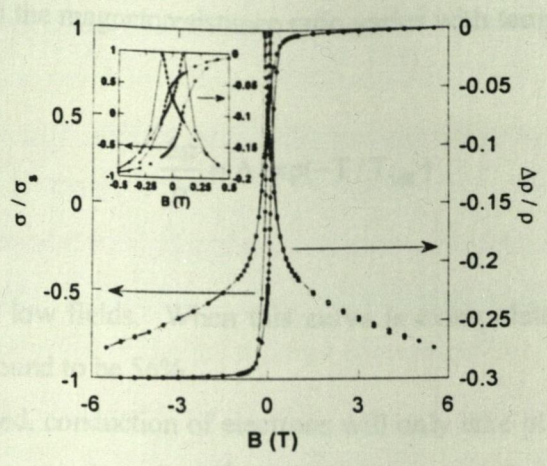

Fig. 5. 26. Magnetoresistance curve for a pure CrO_2 pressed commercial powder compact at 5 K. Inset shows detail at low fields.

The magnetoresistance for the dilute powder at 5 K is shown in Fig. 5.27. Again a hysteretic behaviour with a large drop in resistance at low fields and a linear high field slope is observed. In this sample, the magnetoresistance is seen to show much greater magnetoresistance ratios. At 5 K and in a field of 5 T the MR ratio is measured to be 50%.

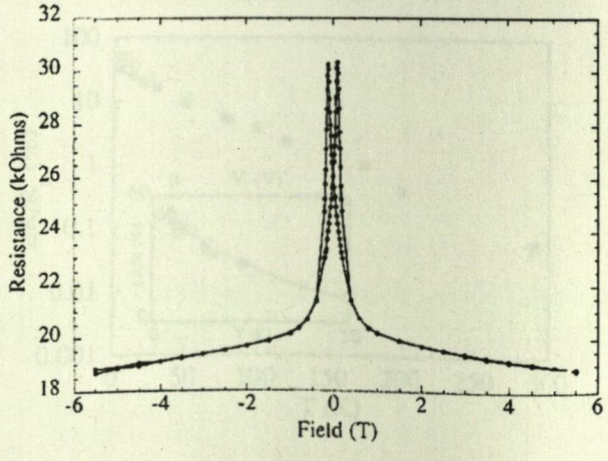

Fig. 5. 27. Magnetoresistance of a 25% CrO_2/75% Cr_2O_3 mixed powder composite at 5 K.

The low field temperature dependence of the MR ratio for the pure and dilute samples is shown in Fig. 5.28 and the magnetoresistance ratio varies with temperature according to:

$$\frac{\Delta\rho}{\rho} = A\exp(-T/T_{MR}) \qquad 5.31$$

where T_{MR} = 46 K at low fields. When this curve is extrapolated back to T = 0 K, the magnetoresistance is found to be 56%.

As already mentioned, conduction of electrons will only take place via lowest resistance contacts. If there are approximately 10^4 particles between voltage contacts separated by 1mm, only a fraction of these will actually offer significant resistance along the conduction path. The number contacts involved in the transport measurements can be estimated by measuring the voltage dependence of the magnetoresistance and comparing it to the temperature dependence, see the inset of Fig. 5.28. This can be measured in the dilute, high resistance samples without any significant heating of the sample (Power (heat) = V^2/R). The magnetoresistance is observed to decrease by a half when V = 4V and T = 25K. Scaling the energy associated with the temperature (k_BT) and the bias voltage across a single junction (eV_b) we obtain 4V = 25K, which indicates that the number of contacts involved in the magnetotransport process is $4e/25k_B \approx 1900$.

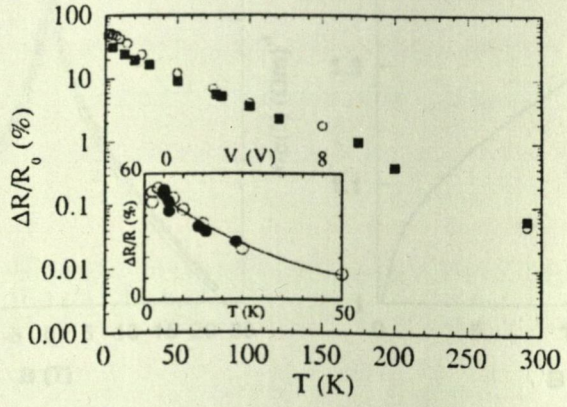

Fig. 5. 28. Log plot of the temperature dependence of the magnetoresistance for a pure CrO_2 powder and a mixed composite 25%CrO_2/75%Cr_2O_3. The inset compares the voltage and temperature dependencies for the mixed composite.

The low-field and high field magnetoresistances have different origins and this is indicated by their different temperature dependencies. The high field slope is only half as sensitive to temperature and falls as $\exp(-T_{HF}/T)$ with T_{HF} = 87 K. Measurements of a CrO_2 powder at 4.2 K up to 20 T show that the conductivity continues to increase linearly with magnetic field with slope ~1%/T.

The magnetoresistance at 4.2 K of a pressed powder compact prepared from pure reactor powder is shown in Fig. 5.29. For these powders there is no large hysteresis effect observed and this is reflective of the larger grain sizes found for these powders ($H_c \propto 1/d$, where d is the grain size). The magnetoresistance shows both the characteristic low field and linear high field effects. The MR ratio is almost 25% at 25 T. At 5 T the MR ratio is approximately 12.5%, half that obtained for the commercial powder at this temperature and field. This therefore indicates the importance of the particle size (single or multi-domain character) and contact resistance to the large magnetoresistance ratios such as those obtained for the commercial powders. As a result of the increased MR ratio when mixed composites are used it is to be expected that, by controlling grain size and shape and barrier thickness the effect may be manipulated. For all magnetoresistance measurements, no AMR was observed.

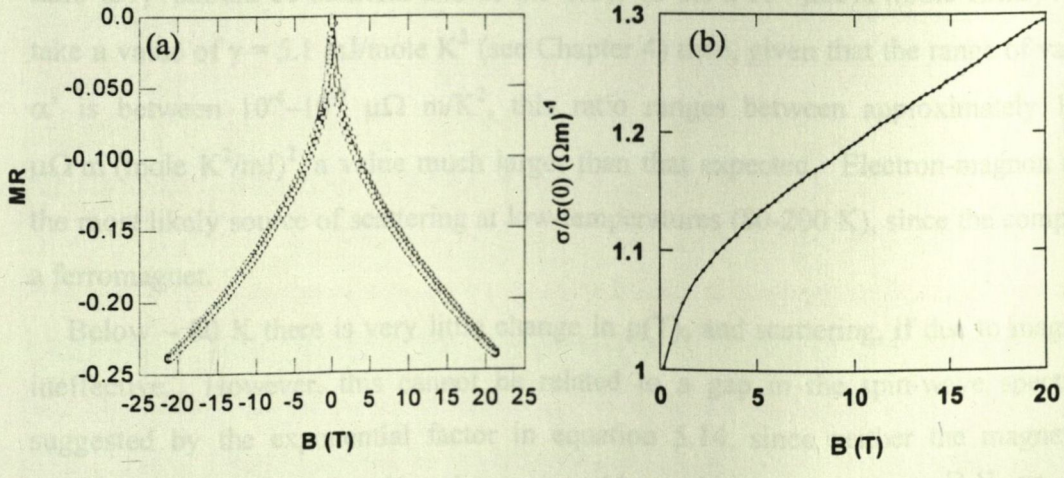

Fig. 5. 29. (a) Magnetoresistance of a pressed powder compact prepared from reactor powder up to 20 T at 4.2 K. The lack of hysteresis is indicative of the larger grains which are found in these powders compared to the commercial powder. (b) Corresponding normalised conductivity curve.

5. 4. Discussion

A. Films

At low temperatures, CrO_2 is intrinsically a fairly good metal, with a residual resistivity in the range 0.1-10 $\mu\Omega$ m. The films in which we measure the lowest resistivity are F3-(100) (1 $\mu\Omega$ m) and F17-(110) (0.1 $\mu\Omega$ m). In general, the (100) films tended to be of slightly poorer quality compared to the (110) films, hence the larger resistivity for these films. The films with a resistivity considerably larger than this are the (001) oriented films, which have a distinct granular structure and show a large low-field magnetoresistance characteristic of its granular nature. The MR of the (001) oriented CrO_2 films is an extrinsic property similar to the GMR observed in ferromagnetic heterostructures and transport across grain boundaries separating randomly aligned ferromagnetic domains dominates the magnetotransport process.

Between approximately 80 K and 200 K the temperature dependence of the resistivity follows a T^2-dependence. There are several possible origins of a T^2-dependence. Electron-electron scattering cannot account for the T^2-dependence since if this were the case, the ratio α'/γ^2 should be constant and of the order of 0.9×10^{-8} $\mu\Omega$ m (mole K/mJ)^2.[9] If we take a value of $\gamma = 5.1$ mJ/mole K^2 (see Chapter 4) then, given that the range of values for α' is between 10^{-4}–10^{-5} $\mu\Omega$ m/K^2, this ratio ranges between approximately 10^{-5}-10^{-6} $\mu\Omega$ m (mole K^2/mJ)^2, a value much larger than that expected. Electron-magnon remains the most likely source of scattering at low-temperatures (80-200 K), since the compound is a ferromagnet.

Below ~ 80 K there is very little change in $\rho(T)$, and scattering, if due to magnons, is ineffective. However, this cannot be related to a gap in the spin-wave spectrum, as suggested by the exponential factor in equation 5.14, since neither the magnetisation, specific heat nor the anisotropy show any evidence for a gap this large.[12, 52] That is, the low temperature magnetisation follows the usual Bloch $T^{3/2}$-law for spin-waves and the low temperature anisotropy is measured to be ~ 6.5×10^4 J/m^3 which is equivalent to a gap of ~

0.27 K which is far too small to account for the gap Δ_g measured (see Table 5.1). The specific heat also has a magnetic component which varies as $T^{3/2}$ with no sign of a gap of the magnitude of Δ_g (see Chapter 4). The scattering mechanism must therefore be associated with the electronic structure of CrO_2. Electron-magnon scattering is a spin-flip process and at low temperatures, spin-flip scattering is impossible in a half-metallic ferromagnet because the nearest available down states to scatter into are well above the Fermi level. The problem is then how to relate the spin-polarised density of states to the electron-magnon scattering. One suggestion is to relate the spin-flip process to the local deviations in the spin-polarisation.[53]

Assuming that only magnons of a certain minimum wavelength λ_T can be excited at a certain temperature T then, the significance of the gap, $\Delta_g \sim 80$ K, may be to define a critical wavelength $\lambda_\Delta = 30$ Å where spin-flip scattering becomes important. λ_T is defined by the relation:

$$kT = Dq^2 = \frac{4\pi^2 D}{\lambda_T^2} \qquad 5.32$$

and $D = zJSa^2/d$, is the spin-wave stiffness constant and is estimated to be of the order of 100 meV Å^2 where z = 8 is the coordinate number, J = 37.5 K is the exchange constant, a = 3.449 Å is the interatomic spacing, S=1 is the total spin on each ion and d = 3 is the dimension of the lattice.[54] An electron which travels the distance λ_Δ finds states of opposite spin on sites where there is locally a maximum spin deviation associated with the spin wave and it can therefore undergo a spin flip scattering process there with the absorption or emission of a magnon. λ_Δ corresponds to a non-spin-flip mean free path. An electron can only undergo a spin-flip process if λ_Δ is greater than the shortest magnon wavelength λ_T. At temperatures where $\lambda_\Delta < \lambda_T$, spin-flip scattering remains ineffective, see Fig. 5.30. It should be noted however that λ_Δ is less than the electron mean free path at 10 K obtained from the Hall data (300 Å).

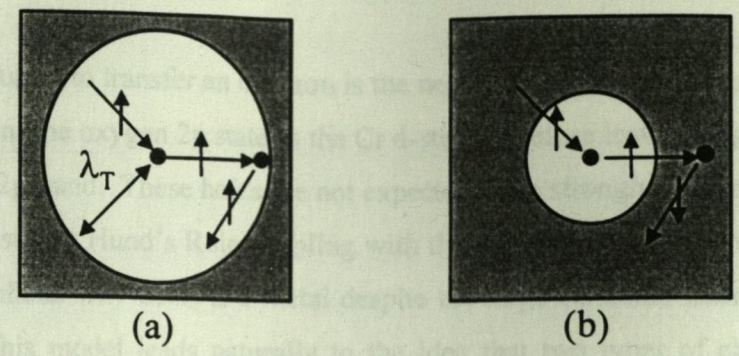

Fig. 5. 30. Spin- flip scattering in half-metallic ferromagnetic CrO_2. (a) At low temperatures, the wavelength of a magnon is long compared to the mean free path of a spin-up electron and spin-flip scattering is ineffective. (b) At higher temperatures, the magnons have short wavelengths compared to the mean free path of the spin-up electron and magnons are able to scatter electrons with spin-flip. The temperature at which spin-flip scattering becomes effective is related to Δ_g.

Jaime et al. find report results for the resistivity of a $La_{0.67}(Pb,Ca)_{0.33}MnO_3$ single crystal.[7] At temperatures below 50 K, the resistivity was also reported to change precipitously from a strong quadratic dependence to essentially a temperature independent behaviour. They attributed the behaviour to one-magnon scattering processes which disappear due to a collapse of the minority band as each local down-spin hole axis aligned with the magnetisation.

Suzuki and Tedrow on the other hand prefer to attribute the low temperature resistivity of CrO_2 to a conduction process involving a parallel combination of metallic majority-spin electrons and semiconducting minority-spin electrons. Their model claims that the Fermi level acts as a donor level to the semiconducting minority-spin electrons and they ascribe the T^2-dependence of resistivity at low temperatures to electron-electron scattering despite their large value of the α/γ^2 ratio.[45]

Korotin et al have classed CrO_2 as a self-doped half-metallic ferromagnet with a negative transfer gap.[55] Basically this means that there is some spontaneous electron transfer out of the oxygen p-states which extend up to the Fermi level in a manner that can be described by:

$$d^n p^6 \rightarrow d^{n+1} p^5$$

The energy required to transfer an electron is the negative charge transfer gap. The transfer of electrons from the oxygen 2p state to the Cr d-state therefore leaves a significant amount of holes in the 2p-band. These holes are not expected to be strongly scattered since they do not experience strong Hund's Rule coupling with the 3d ion cores. Korotin et al. claim that self-doping explains why CrO_2 is a metal despite the large Coulomb interactions between d-electrons. This model leads naturally to the idea that two types of charge carrier are responsible for the transport processes in CrO_2 e.g. 3d electrons and 2p holes. Furthermore, it predicts that the mobility of the holes will be much greater than that of the electrons. Experimental evidence of two-band transport involving electrons and holes is given by our magnetoresistance and Hall data. In particular, fits to the Hall data indicate that a small number of highly mobile holes as well as a large number of less mobile electrons are present in CrO_2. At low fields and at temperatures below 100 K, it was found that the holes dominate the magneto-transport properties. Therefore, the suppression of the T^2 term in the resistivity at 80 K arising from the suppression of scattering by spin-waves of a certain critical wavelength defined by Δ, may further signify the increasing dominance of mobile holes to the conductivity below this temperature.

The presence of holes as well as electrons in CrO_2 is inferred from several other experiments. For example, neutron diffraction experiments show that the moment on the Cr ion in a commercial powder of CrO_2 is larger than the expected moment of 2 μ_B/fu suggesting the presence of holes in the oxygen p-band with an opposite spin angular momentum to compensate (see section 3.3, Chapter 3). Magnetic X-ray dichroism experiments carried out on CrO_2 at the oxygen K-edge revealed a magnetic moment on the oxygen and therefore supported this idea.[56, 57] Both theses results provide evidence for the existence of holes in the oxygen p-band.

In addition, calculations of the Fermi surface indicate the presence of chains of alternating hole and electron pockets along the c-axis.[58, 59] The electron pocket is box-like whilst the hole pockets are like a pseudosphere with tentacles. The Fermi surface of Mazin et al. is shown in Fig. 5.31 below. The flat surfaces of the electron box suggest that electrons at the Fermi surface have a large effective mass ($1/m^* = 1/\hbar^2 \, d^2E/dk^2$) and

therefore a high density of electrons. The pseudospherical hole Fermi surface on the other hand implies a smaller effective mass and therefore a lower density. Whilst the above argument is qualitatively consistent with the findings from the Hall data, a major discrepancy arises since, both calculations of the Fermi surface indicate the presence of equal numbers of electrons and holes, while the Hall and MR data indicate that the mobile holes are much less numerous than the electrons.

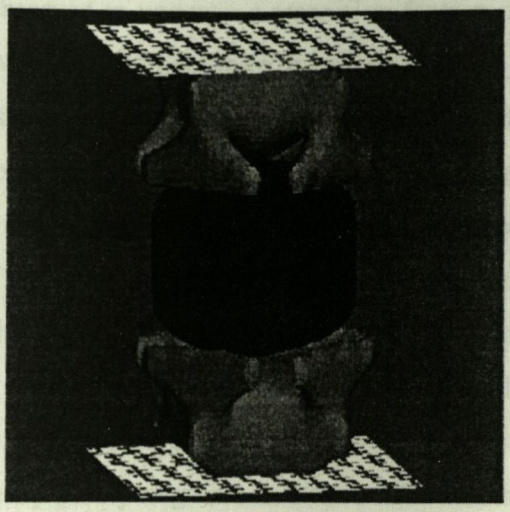

Fig. 5. 31. Fermi surface of CrO_2 calculated by Mazin et al.[58] The electron pseudocube is centred around the Γ point and the hole hammerheads touching the pseudocube point towards the Γ point along the [110] axis. Small pockets along the AM line are not shown.

The large effective mass of the electrons is inferred from the low temperature specific heat measurements which show a larger density of states at the Fermi level than predicted by band structure calculations. The electronic contribution to the specific heat measured in Chapter 4, suggests an effective mass for the electron $m^* = 2.5m_e$ while effective masses between $3\text{-}4m_e$ have been reported by other authors.[60] Since the Hall data reported here indicates that there are significantly more electrons than holes at the Fermi level, the enhanced effective mass can be attributed to the d-band electrons. The electron mobility can be deduced independently of the Hall data by using the scattering rate obtained from

optical conductivity measurements.[60] The extrapolated dc scattering rate at 10 K is $1/\tau$ = 30 cm^{-1} (9×10^{11} Hz) which results in an electron mobility μ_e = 0.012 m^2/Vs, which is in good agreement with the value obtained from the Hall data.

The change in behaviour of the Hall resistivity between 70 K and 100 K from seemingly two-band-like to a behaviour dominated by the anomalous Hall effect at low fields and a single-band hole-like conduction at higher fields is not only mirrored in the resistivity but in the magnetoresistance data as well. Here both the perpendicular and the transverse magnetoresistances are observed to undergo a transition from a positive-like behaviour to negative-like behaviour when the temperature is raised through 80K. In particular, the perpendicular magnetoresistance at 77K shows both a positive and a negative MR. That is, at low fields a negative magnetoresistance dominates the magnetotransport properties whilst at higher fields a positive MR is observed. This could well be interpreted as an indication of the onset of spin-dependent scattering due to the appearance of spin waves at this temperature. As the field is increased, the electron spins are aligned and spin dependent scattering is suppressed so that the holes are again free to dominate the magnetoresistance up to 25 T. At 100 K, for both transverse and perpendicular field geometries the MR is already purely negative in effect. The fact that the magnetoresistance does not saturate in fields as high as 25 T (perpendicular MR) supports the idea of a low concentration of highly mobile holes since $\Delta\rho/\rho \propto (\omega_c\tau)^2 \propto 1/n$ where n is the carrier concentration and the mobility is defined as $\mu = e\tau/m$.[61] Furthermore, it has been possible to fit qualitatively the perpendicular MR at 10 K up to 25 T using a two-band model which separates the hole and electron contributions. Reasonable fits to the MR data were obtained using the parameters obtained by fitting the Hall data again to a two-band model of electron and holes.[48, 50]

Furthermore, the optical conductivity of a (110) oriented CrO_2 film also shows that there is a sharp narrowing of the Drude peak and a collapse of the low frequency scattering rate at temperatures below 150 K in agreement with the collapse of the resistivty, MR and Hall data.[60]

With regards to the high temperature resistivity behaviour of CrO_2, it is observed that on approaching T_c, the good metal changes into a poor one, and the resistivity is observed to exhibit a change in slope at the ferromagnetic to paramagnetic transition temperature. That

is, at room temperature and above CrO_2 becomes a bad metal with a resistivity that exceeds the Ioffe-Regel limit, $k_F\lambda \sim 1$ where k_F is the Fermi wave vector and λ the mean free path.[62] The resistivity in the Ioffe-Regel limit is estimated using the formula:[63]

$$\rho_{IR} = [\frac{e^2 k_F}{3\pi^2 \hbar}]^{-1}$$

and found to be of the order of $\sim 15.0\ \mu\Omega$ m. The Ioffe-Regel limit refers to the deviation from the free electron theory and represents the minimum mean free path required for metallic conduction.[63] At high temperatures the transport is dominated by the magnetic contribution, ρ_M, to the resistivity which varies as: $\alpha T^2 \exp(-\Delta/k_B T)$. For $T > Tc$, ρ_M saturates and it is ρ_M which exceeds the Ioffe-Regel limit making CrO_2 a bad metal. The poor metal at room temperature and above, where the mean free path is comparable to the interatomic spacing is understood in terms of the Mott-Hubbard localisation in a half metallic system. Mott-Hubbard localisation occurs when the bandwidth $W = 2zt \leq U$, where $z = 8$ is the coordination number, t the transfer integral and U the effective on-site Coulomb interaction. At temperatures near and above the Curie temperature, any site will have a fluctuating number z' of neighbours with reversed spin to which transfer is forbidden so the effective bandwidth is reduced by a factor $(z - z')/z$. In a half-metallic system, electron transfer is possible if the nearest neighbour Cr ions have the same spin orientation. That is, conduction is only possible when a local fluctuation of the spins of an atom relative to all parallel neighbours makes the system locally metallic. At any instant, the number of 3d electrons which are delocalised and available to conduct is reduced to a fraction of the number of sites. The resistivity of CrO_2 would become insulating at a certain temperature, T_M say, were it not for spin fluctuations. The spin fluctuations make it possible for the electrons to move some fraction of the time when there is an instantaneous favourable nearest neighbour configuration.

Regarding the magnetoresistance at low temperatures, a comparison of the longitudinal, transverse and perpendicular magnetoresistance of a (110) oriented film at 10 K when the current is parallel and perpendicular to the c-axis reveals the existence of several competing factors to the overall magnetoresistance observed.

The dominant feature in all cases is the positive MR arising from the Lorentz force acting on the charge carriers. As expected, the longitudinal MR is smallest since the Lorentz force in this case is only acting on a very small fraction of the charge carriers. A small negative MR (~ 1%) observed at low fields for the longitudinal geometry when the current is parallel to the c-axis is attributed to an intrinsic property of the material. A slightly larger negative MR (~ 2%) is observed when the current is perpendicular to the c-axis and is attributed to intergrain transport between progressively aligned ferromagnetic domains.

At 10 K, the transverse magnetoresistance is observed to show a small glitch at low fields when the current is parallel to the c-axis, (see Fig. 5.19). The mean free path for both electrons and holes has been estimated from the Hall data to be 300 Å and 1.3 μm respectively. A small electron mean free path would suggest that the magnetoresistance be dominated by electrons. However, as inferred from the Hall data, holes appear to dominate the transport properties at low fields and temperatures. Therefore, a possible explanation for the low field transverse MR behaviour may be that, since in the transverse geometry the cyclotron orbits are moving perpendicular to the film plane and the mean free path of the holes (1.3 μm) is comparable to the film thickness (t ~ 0.6-1 μm) and the diameter of the needle-like gains (d ~ 1-3 μm), scattering of holes at the film surface and needle edges may be significant. In general $t \leq d$, and consequently scattering at the film surface may be more significant than at the needle edges. In the perpendicular geometry, the hole cyclotron orbits are turning in the plane of the film and thus scattering can only occur at the needle edges. The extra scattering at the film surfaces in the transverse geometry, which is absent in the perpendicular geometry, may give rise to the glitch observed at low while the perpendicular MR is seen to show no such anomaly. Size effects are expected to be significant for holes only since the electrons have a mean free path that is much smaller than the dimensions of the film.

Alternatively, the irregularity at low fields for the transverse geometry may be related to an AMR effect. The magnetisation in CrO_2 is parallel to the c-axis. Therefore when the current is parallel to the c-axis, the charge carriers see a larger charge distribution cross section from which they can be scattered than if the current was perpendicular to the magnetisation (see Section 5.1.3B). When a magnetic field is applied perpendicular to the

direction of magnetisation, the magnetisation aligns with the magnetic field. The magnetisation aligns with the applied field at ~ 0.2 T when the field is applied perpendicular to the c-axis and in the film plane (see Section 3.3.1, Chapter 3) which is close to the value at which the glitch in the transverse MR is observed.

At low temperatures, the negative magnetoresistance observed at low fields when the current is perpendicular to the c-axis in the transverse geometry is associated with the dominance of spin-dependent scattering at the grain boundaries. The effect is not as large as for the (001) oriented film for which there are a greater number of grain boundaries. However, the grain boundary scattering is obviously more effective at low fields and low temperatures in this current configuration. The perpendicular MR also shows some structure around 2 T and this again may be attributed to the competition between the negative MR arising from spin-dependent transport across grain boundaries separating ferromagnetically aligned grains and the ordinary MR. At higher fields the MR is observed to show a large a positive MR and is again credited to the Lorentz force acting on charge carriers. The positive transverse MR is much smaller (13.5%) when the current is perpendicular to the c-axis while the magnitude of the perpendicular MR on the other hand remains practically the same. The large reduction in the transverse MR when the current is perpendicular to the c-axis may be due to a large reduction of the carrier lifetime due to collisions of the charge carriers with the films surface (which carriers in the perpendicular geometry do not suffer) as well as additional scattering of carriers on passing through the grain boundaries. As $\Delta\rho/\rho \propto (\omega_c\tau)^2$ it is understood that a reduced carrier lifetime results in a smaller MR ratio.

B. Powders

The resistivity of pure and diluted pressed powder compacts arises exclusively from the interparticle contact and is many orders of magnitude higher than the resistivity of the films. These contacts are not metallic, since $R > R_Q$ and transport of carriers is by tunneling. The temperature dependence of resistivity is characteristic of a granular metal in

the dielectric regime given by equation 5.16. For diluted powders, a percolation threshold of $x_p = 0.23$ exists and conduction takes place via the lowest resistance contacts. Hence, only a fraction of the particle contacts contribute to the transport process.

An important aspect of charge transport in tiny metallic particles imbedded in an insulating matrix is the Coulomb gap, which is also observed in the conductance curves of CrO_2 powder particles at low temperatures. The Coulomb gap in a ferromagnetic metal has two origins, the first is the usual single particle charging energy, E_c, associated with the transfer of charge from one particle to an adjoining particle. The second, is an extra charging term, E_m, of magnetic origin which is defined as the difference in exchange energies between adjoining misaligned particles. Hence the Coulomb gap is spin-dependent. In the saturated state $E_m = 0$. E_c and E_m both depend on temperature and decrease in magnitude with decreasing temperature. This is to be expected since at lower temperatures tunneling is longer range involving thicker barriers but lower gaps (charging energies).

The large magnetoresistance observed in pressed powder compacts of CrO_2 is an extrinsic effect. The main MR effect is the low-field response associated with the alignment of the magnetisation of particles in poor electrical contact with each other. Tunneling of carriers between contiguous ferromagnetic particles depends on the relative orientation of the magnetisation. Neighbouring particles that are magnetically misaligned in zero field prevent spin-polarised carriers from tunneling due to the mismatch in the exchange energies i.e. majority spin-states in one particle correspond to minority spin states in another. Hence, electrons having a majority spin cannot propagate to a particle where minority states exist at the Fermi level, resulting in a high resistance state. A small magnetic field aligns the magnetisation direction in the grains so that the density of states in one grain matches that of another.

By diluting CrO_2 in an insulating matrix of Cr_2O_3, the resistivity is increased by three orders of magnitude and is due to the increased contact resistance. This increased contact resistance leads to larger magnetoresistance ratios. The probability that charge will be transferred into an adjacent particle is given by equation 4.18. In CrO_2, there are two 3d electrons. One is localised in an orbital of xy character and the other is delocalised in a half-filled orbital of $yz \pm zx$ character which forms the conduction band. Hence, S, the core

spin is taken to be a ½ and the probability of electron transfer $f(\theta_{ij})$ into an adjacent grain is 5/8 for random orientation of particle magnetisation resulting in a predicted magnetoresistance ratio is 60%. This is in good agreement with the extrapolated value of 56% at T = 0 K.

The exponential variation of the magnetoresistance with temperature and voltage is a combination of the low temperature effects associated with the spin-dependent Coulomb gap and high temperature spin-flip scattering processes. A possible source of spin-flip scattering at higher temperatures, may involve excitation of antiferromagnetic spin waves in the surface layer of the Cr_2O_3 in the mixed composites. It may also come from the excitation of bulk or surface spin waves arising from the tunneling of carriers into magnetically misaligned particles. Spin-flip scattering may also occur where Cr ions are weakly exchange coupled or misaligned at the interface or surface.

The large increase in the low field magnetoresistance, with decreasing temperature was recently attributed to a transport process across grain boundaries involving two types of electron: those that hop in a succession of steps and a smaller number that tunnel across in one step between the conduction bands of two grains.[64] At low temperatures, the tunneling electrons dominate the magnetotransport while at higher temperatures multistep hopping by electrons which lose their initial spin orientation are said to dominate the conductivity.

The high field slope has been observed in both the pressed powder compacts and the granular CrO_2 films. The origin of the high field slope is not yet fully understood. At high fields, the magnetisation is already saturated and the linear high-field slope is not therefore due to a magnetisation process of the particles. The effect could be intrinsic to CrO_2 and could be associated with small changes in the chemical potential ($g\mu_B SB \sim 0.12$ mV/T) which arise when a magnetic field is applied. Other possible explanations are that an applied field reduces the tunnel barrier height or width between particles by modifying the width of a layer of localised charge at the surface or that it polarises disordered spins which may be present in the interface layer.

References

[1] J. R. Hook and H. E. Hall, *Solid State Physics*, 2nd Edition, J. Wiley and Sons (1994)

[2] J. M. Ziman, *Principles of the Theory of Solids*, Cambridge University Press (1965)

[3] J-Ph Ansermet, J. Phys.: Condens. Matter, **10**, 6027-6050 (1998)

[4] T. van Peski-Tinbergen and A. J. Dekker, Physica, **29**, 917-937 (1963)

[5] M. J. Rice, Phys. rev. Lett., 20(25), 1439-1441 (1968)

[6] A. H. Thompson, Phys. Rev. Lett., **35**, 1786-1789 (1975)

[7] M. Jaime, P. Lin, M. B. Salamon and P. D. Han, Phys. Rev. B, **58**, R5901-5904 (1998)

[8] I. Mannari, Prog. Theor. Phys., **22**, 335-343 (1959)

[9] K. Kadowaki and S. B. Woods, Sol. St. Commun., **58**, 507-509 (1986)

[10] B. Coqblin, *The Electronic Structure of Rare-Earth Metals and Alloys, the Magnetic Heavy Rare-Earths*, 1st Edition, Academic Press Inc. (1977)

[11] K. Nira, Phys. Rev., **117**, 129-133, (1960)

[12] A. R. Mackintosh, Phys. Lett., **4**, 140-142 (1963)

[13] Kubo and Ohata; two magnon process

[14] N. W. Ashcroft and N. D. Mermin, *Solid State Physics*, International Edition, Saunders College Publishing (1976)

[15] A. Ramirez; G. H. Jonker and J. H. van Santen, Physica, **16**, 337 (1950)

[16] J. M. D. Coey, J. Appl. Phys., **85**, 5576-5581 (1999)

[17] S. P. Lewis and P. B. Allen, Phys. Rev. B, **55**, 10253-10260 91997)

[18] A. B. Pippard, *Magnetoresistance in Metals*, Cambridge University Press (1989)

[19] C. Zener, Phys. Rev., **81**, 440 (1951)

[20] A. J. Millis, B. I. Shraiman and R. Mueller, Phys. Rev. Lett. **77**, 175 (1996)

[21] H. Röder, J. Zhang, A. R. Bishop, Phys. Rev. Lett.,**76**, 1356 (1996)

[22] J. R. Fletcher, K. W. H. Stephens, J. Phys. C: Solid State Phys., **2**, 444 (1969)

[23] M. N. Babich et al, Phys. Rev. Lett., **61**, 2472 (1988)

[24] A. E. Berkowitz et al., Phys. Rev. Lett., **68**, 3745 (1992)

[25] N. F. Mott, Adv. Phy **13**, 325 (1964)

[26] J. Q. Wang and G. Xiao, Phys. Rev B, **49** (1994);

[27] T. Valet and A. Fert, Phys. Rev. B, **48**, 7099-7113, (1993)

[28] A. Fert, T. Valet and J. Barnas, J. Appl. Phys., **75**, 6693-6698 (1994)

[29] M. Jullière, Phys. Lett., **54A**, 225 (1975)

[30] S. Maekawa and U. Gäfvert, IEEE Trans. Magn. **18**, 707 (1982)

[31] A. E. Berkowitz, S. Sankar and D. J. Smith, Appl. Phys. Lett., **73**, 535 (1998)

[32] J. M. D. Coey, A. E. Berkowitz, Ll. Balcells, F. Putris and A. Barry, Phys. Rev. Lett., **80**, 3815-3818 (1998)

[33] J. S. Helman and B. Abeles, Phys. Rev. Lett., **37**, 1429-1432 (1976)

[34] Honda, J. Mag. and Mag. Mat., **165**, 153-156, (1997)

[35] B. Geerligs, *Classical and Quantum Charge Dynamics in Small Tunnel Junctions*, Ph. D. Thesis (1990)

[36] F. W. Sears, M. W. Zemansky and H. D. Young, *University Physics*, 7th Edition, Addison-Wesley Publishing Co. (1987)

[37] F. Guinea (unpublished)

[38] H. Y. Hwang, S. –W. Cheong, N. P. Ong and B. Batlogg, Phys. Rev. Lett., **77**, 2041-2044 (1996)

[39] C. Kittel, *Introduction to Solid State Physics*, 7th Edition, John Wiley and Sons (1996)

[40] R. G. Chambers, Proc. Phys. Soc. Lond. A, **65**, 903 (1952)

[41] H. Kamimura and H. Aoki, *The Physics of Interacting Electrons in Disordered Systems*, Oxford Clarendon Press (1989)

[42] F. C. Zumsteg and R. D. Parks, Phys. Rev. Lett., **24**, 520 (1970)

[43] D. S. Simons and M. B. Salamon, Phys. Rev. B, **10**, 4680 (1974)

[44] L. W. Shacklette, Phys. Rev. B, **9**, 3789 (1974)

[45] K. Suzuki and P. M. Tedrow, Phys. Rev. B, **58**, 11957-11602 (1998)

[46] L. Klein, J. S. Dodge, C. H. Ahn, G. J. Snyder, T. H. Geballe, M. R. Beasley and A. Kapitulnik, Phys. Rev. Lett., **77**, 2774-2777 (1996)

[47] K. Stauffer and A. Ahorony, *Introduction to Percolation Theory*, 2nd Edition, Taylor and Francis (1985)

[48] S. Watts, S. Wirth, S. von Molnar, A. Barry and J. M. D. Coey (in press)

[49] J. –P. Jan, N. L. Martin and A. Wenger, Phys. Rev. B, **9**, 1377-1380 (1974)

[50] K. Hong, F. Y. Yang, K. Liu, D. H. Reich, P. C. Searson and C. L. Chien, J. Appl. Phys., **85**, 6184-6186 (1999)

[51] J. M. Ziman, *Principles of the Theory of Solids*, Camridge University press (1965)

[52] K. Niira, Phys. Rev., **117**, 129-132 (1960)

[53] A. Barry, J. M. D. Coey, L. Ranno, K. Ounadjela, J. Appl. Phys., **83**, 7166-7168 (1998)

[54] R. Skomski and J. M. D. Coey, Permanent Magnetism, IoP Publishing Ltd. (1999)

[55] M. A. Korotin, V. I. Anisimov, D. I. Khomskii and G. A. Sawatsky, Phys. Rev. Lett., **80**, 4305-4308 (1998)

[56] L. Ranno, A. Barry, J. M. D. Coey, unpublished data.

[57] K. Attenkofer and G. Schülz, J. Phys. IV France, **7**, C2-459-460, (1997)

[58] I. I. Mazin, D. J. Singh and C. A. Draxl; Phys. Rev. B, **59**, 411-415 (1999)

[59] S. P. Lewis and P. B. Allen (private communication)

[60] D. N. Basov, E. J. Singley, C. P. Weber, A. Barry and J. M. D. Coey, Phys. Rev. B, **60**, 4126-4130 (1999)

[61] K. Liu, C. L. Chien and P.C. Season, Phys. Rev. B, **58**, R14681-14685(1998)

[62] N. F. Mott, *Metal-Insulator Transitions*, Taylor and Francis Ltd. (1990)

[63] P. P. Edwards and C. N. R. Rao, *The Metallic and Non-metallic States of Matter*,Taylor and Francis Ltd. (1985)

[64] S. S. Manoharan, D. Elefant, G. Reiss and J. B. Goodenough, Appl. Phys. Lett., **72**, 984-986 (1998)

Chapter 6

Device Fabrication and Application

"Mistletoe can be deadly if you eat it ..... so can a computer."

James O'Sullivan when writing his thesis one lonely Christmas, 1998.

6. 1. Introduction

There has been a great deal of interest in materials and structures exhibiting large changes in resistance when subjected to a magnetic field.[1, 2, 3] The systems which have attracted most attention fall into three classes: GMR structures, CMR materials and magnetic tunnel junctions. GMR has been observed in heterogeneous ferromagnetic materials such as thin film magnetic multilayers and cluster alloys and is associated with the alignment of randomly oriented ferromagnetic entities or antiferromagnetically coupled layers in a magnetic field. GMR values greater than 70% have been achieved at room temperature.[4] CMR has been observed in the mixed valence manganese perovskites, $Ln^{3+}_{1-x}A^{2+}_{x}MnO_3$ where Ln=Y, La, Pr, Nd, Sm and Gd, R=Ca, Ba, Sr and Pb. CMR is associated with a large decrease in resistivity that occurs at the metal-insulator and ferromagnetic-paramagnetic transitions. A CMR ratio of 20% has been measured at room temperature for single crystalline $La_{1-x}Pb_xMnO_3$.[5] Magnetic tunnel junctions which operate on the basis of spin polarised tunneling and that show large magnetoresistive effects are now being developed.[2, 3, 6] Magnetic tunnel junctions comprise of two ferromagnetic electrodes separated by an insulating layer and are prepared by conventional lithographic techniques (section 6.3).

The reasons for studying and developing the GMR structures, CMR materials and magnetic tunnel junctions are two fold. Firstly, by studying their transport properties it should be possible to gain insight into the physical processes occurring therein. Secondly, these structures and materials show great potential for use in the fabrication of novel electronic devices based on the ability of ferromagnetic metals to conduct spin-polarised currents. The effectiveness of the magnetoelectronics depends largely on the extent to which a current is spin-polarised. All device designs improve their

performance as the spin polarisation, P approaches 100%.[7, 8, 9] Hence materials having a large spin-polarisation at the Fermi surface are desirable from a technological point of view. Ferromagnetic metallic oxides such as $La_{0.7}Sr_{0.3}MnO_3$ and CrO_2 are expected to have such a high degree of spin polarisation at the Fermi surface.[10, 11, 12, 13, 14] The question remains however as to how to measure P.

In this chapter methods used for measuring the spin polarisation of a ferromagnet will be discussed with particular attention being paid to a method which exploits a phenomenon known as Andreev reflection (section 6.2.3) as well as techniques using magnetic tunnel junctions (section 6. 2. 2). The fabrication of a magnetic tunnel junction of the type CrO_2/I/Co will be described and its transport properties elucidated.

6. 2. Spin-Polarised Tunneling and Transport

6.2.1. Background

In a ferromagnetic metal, there exists a splitting between up- and down-spin states called the 'exchange splitting' which acts to lower the overall energy of the system. As a result of this splitting, there is an imbalance in the number of spin-up and spin-down states occurring at the Fermi level as shown in Fig. 6.1. Consequently there exists a predominance of electrons of one spin orientation, spin-up say at the Fermi level which gives rise to a magnetic moment. The magnetic moment, μ, is proportional to the difference between occupations for the spin-up and spin-down states and is a measure of the net polarisation of the electrons:

$$\mu = \frac{N_\uparrow - N_\downarrow}{N_\uparrow + N_\downarrow} = P \qquad 6.1$$

Measuring the spin-polarisation, P, requires a technique that can discriminate between the spin-up and spin-down electrons near ε_F. Spin-polarised photoemission spectroscopy provides the most direct technique for measuring P. Spin resolved

photoemission experiments carried out on CrO_2 indicated the existence of a fully spin polarised d-like band. However, 100% spin polarisation was found to exist 2 eV *below* the Fermi level.[10] This result opposed theoretical calculations which predicted complete spin-polarisation *at* the Fermi level. Alternative methods for measuring the spin polarisation more accurately were therefore required.

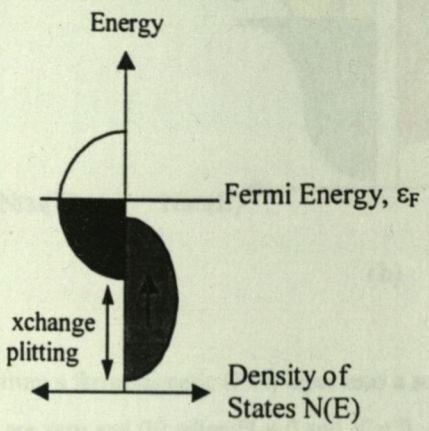

Fig. 6. 1. Typical schematic of the density of states in a ferromagnet showing the splitting of the spin-up and spin-down states due to the exchange field.

Tunnel junctions provide another means for measuring the spin polarisation. Tedrow and Mersevey were the first to investigate the problem of spin-polarised transport and spin-polarised tunneling in a trilayer device.[15] In this seminal work, a ferromagnetic-insulator-superconductor trilayer structure of the type $Ni/Al_2O_3/Al$ was used to show that the current tunneling out of a ferromagnetic electrode was spin-polarised. It was found that when a magnetic field, H, was applied, the superconducting density of states of the Al layer was split into spin-up and spin-down states by an amount μH, μ is the spin magnetic moment of the electron, see Fig. 6.2. The magnetic field also acted to define the orientation of the magnetic moment and therefore the spin direction in the film. In practice, very thin films of Al (~ 4 nm) were used in the tunneling device. Thin films of Al exhibit a critical field that can be much larger than the critical field of bulk Al and the saturation field of the ferromagnetic film.[15, 16, 17] This is due to a small orbital depairing parameter when the field is applied parallel to the film. Consequently, large fields (~ 0.5 T) can be applied without destroying the superconducting state.

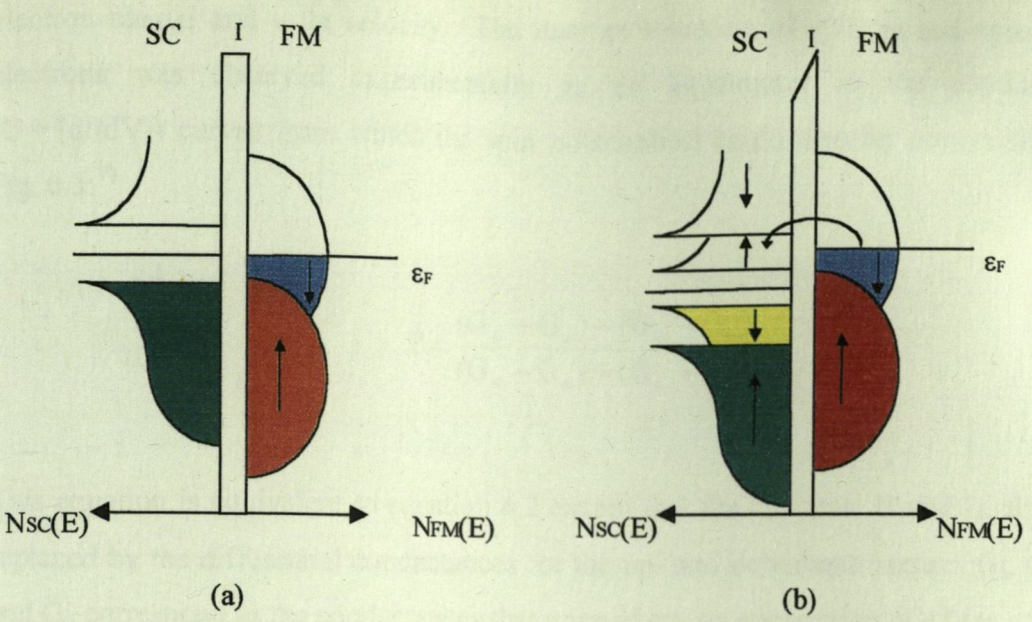

Fig. 6. 2. Tunneling through a barrier from a ferromagnetic (FM) layer into a superconductor (SC) (a) when the field, H, and voltage, V, are zero and (b) when $H \neq 0$ and $V \neq 0$. H acts to split the superconducting density of states into up and down states by μH. V shifts the ferromagnetic density of states with respect to the spin-up and spin-down superconducting density of states so that at some V down ferromagnetic spin states coincide with the down states in the superconductor. Curved arrow shows electron flow.

The Zeeman splitting of the spin states provided the basis for spin-polarised tunneling, since at an energy of Δ-μH the electrons in the tunnel current are almost entirely of one spin direction and at $-\Delta+\mu H$ almost entirely of the opposite spin direction. (Δ is the energy gap of the superconductor). By careful analysis of the currents $I_\uparrow$ and $I_\downarrow$ transmitted through the tunnel barrier into the superconductor's spin states, as a function of voltage and applied magnetic field, the percentage polarisation of current, P, could be determined. This fraction was defined simply as:

$$P = \frac{I_\uparrow - I_\downarrow}{I_\uparrow + I_\downarrow} = \frac{N_\uparrow - N_\downarrow}{N_\uparrow + N_\downarrow} \qquad 6.2$$

As can be seen from equation 6.2, P can also be written in terms of the spin–up and spin-down densities of states, $N_\uparrow$ and $N_\downarrow$, respectively since $I = Nev$, where e is the

electron charge and v its velocity. The distinct selection of spin-up and spin-down electrons was observed experimentally as an asymmetry in the conductance (G = (dI/dV)) curves from which the spin polarisation could also be determined, see Fig. 6.3:[18]

$$P = \frac{(G_d - G_a) - (G_c - G_b)}{(G_d - G_a) + (G_c - G_b)} \qquad 6.3$$

This equation is equivalent to equation 6.2 except that the currents, $I\uparrow$ and $I\downarrow$, are now replaced by the differential conductances for the up- and down-spin states. G_a, G_b, G_c and G_d correspond to the conductances that arise when, on application of a bias voltage, the ferromagnetic density of states coincides with the superconducting density of states of the same spin orientation. The asymmetry in the conductance curve arises as a result of the difference in the spin-up and spin-down density of states in the ferromagnet.

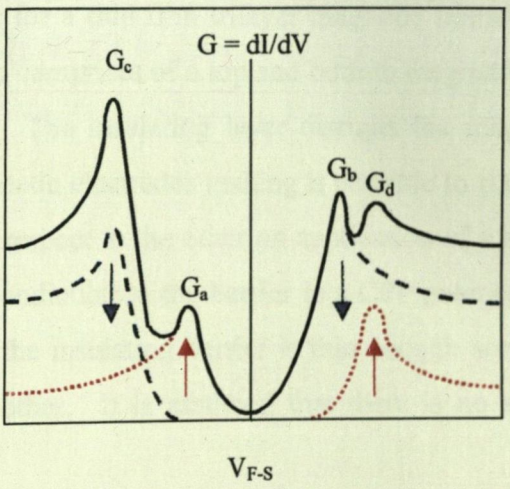

Fig. 6. 3. Ferromagnetic metal - superconductor tunneling. The blue dashed lines represent the conductance, G = dI/dV, for spin-down states, the red dotted line the conductance for spin-up electrons. The solid black line represents the total conductance. Electrons oriented with their spins in the direction of the applied magnetic field predominate in the tunneling current, thus the peak G_b is larger than the corresponding peak G_a at negative voltage. This diagram was taken from R. Mersevey and P. M. Tedrow, Phys. Lett., 238, 173-243 (1994).[19]

Julliere made an important advance that corroborated the above results of spin-polarised tunneling.[8] In this work, the superconducting layer was replaced with another ferromagnetic layer to produce a ferromagnetic-insulator-ferromagnetic system. This type of structure became known as a *magnetic tunnel junction* and shall be discussed below.

An alternative method, which utilises the transport of spin-polarised electrons, was recently developed for measuring the polarisation of CrO_2. It requires no magnetic field and no lithography techniques to fabricate a layered device. This method involves forming a metallic contact between the ferromagnetic CrO_2 sample and a superconducting tip. The electronic transport properties at the point contact measures the conversion of normal current to supercurrent and is called Andreev reflection.[20] This method will also be discussed in detail below (see section 6.2.3).

6. 2. 2. Magnetic Tunnel Junctions

A typical structure for a thin film trilayer magnetic tunnel junction is illustrated in Fig. 6.4. The junction comprises of a top and bottom magnetic electrode separated by a thin insulating layer. The insulating layer disrupts the magnetic exchange-coupling between the ferromagnetic electrodes making it possible to rotate the magnetic moment in one electrode with respect to the other on application of a magnetic field. A current is forced to flow perpendicular to the barrier in a CPP geometry (current perpendicular to plane). Providing the insulating barrier is thin enough some current will pass from one electrode to the other. It is assumed that there is no spin-flip scattering in the barrier layer.[21]

The tunneling of a spin-polarised current between the two magnetic layers depends on the relative orientation of the magnetic moments in these layers. In other words, electrons originating from one spin state at the Fermi level of the first ferromagnetic layer will be accepted by unfilled states of the same spin in the second ferromagnetic layer. If, however, the two ferromagnetic layers are magnetised antiparallel to each other, then majority electrons from the first ferromagnetic layer have no states available to them since states of opposite spin now exist at the Fermi level in the second ferromagnetic electrode. The tunneling of the spin polarised current is forbidden. In

the antiparallel arrangement the junction is found to be in a high resistance state. The resistance of the junction decreases dramatically when a spin-polarised current is passed through the two ferromagnetic electrodes in the parallel configuration.

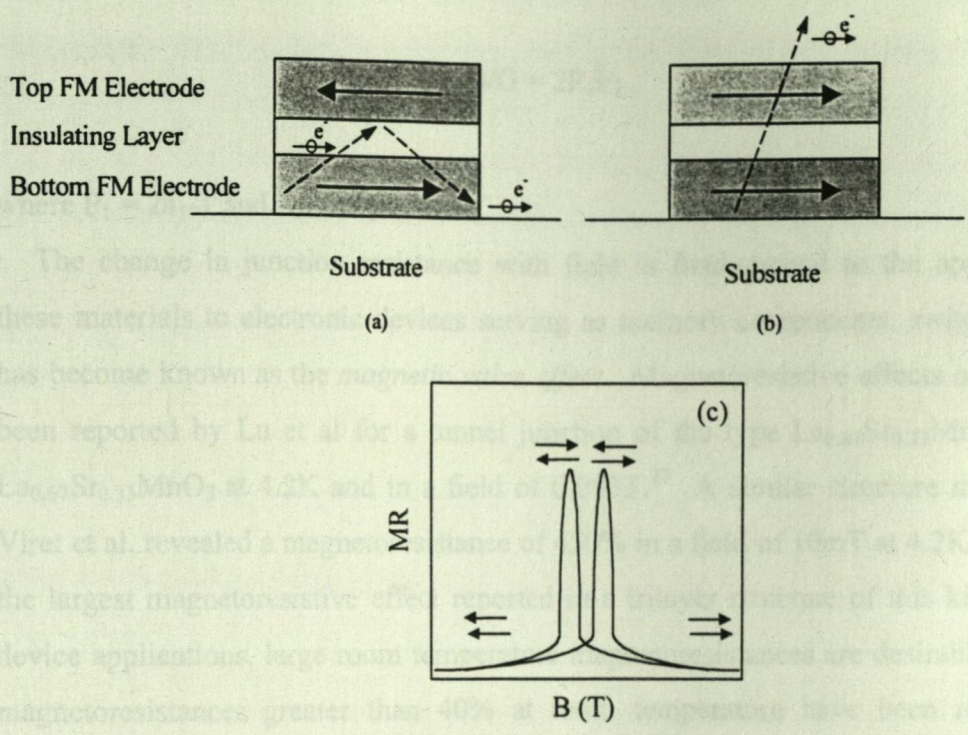

Fig. 6. 4. Schematic of a magnetic tunnel junction in (a) the high resistance antiparallel configuration and (b) the low resistance parallel configuration. The direction of the moments in the ferromagnetic layers are given by the solid arrows and the passage of the spin-polarised tunnel current is given by the dashed arrows. Diagram (c) shows how the resistance changes abruptly with field at the coercive fields of the two FM layers. The arrows represent s the direction of magnetisation of the top and bottom FM layers.

By measuring the I-V characteristics of the junction, the conductivities for the parallel (G_p) and antiparallel (G_{ap}) arrangements can be deduced. These are given by:[19]

$$G_p = a_1a_2 + (1-a_1)(1-a_2) \qquad 6.4$$

$$G_{ap} = a_1(1-a_2) + (1-a_1)a_2 \qquad 6.5$$

where $a_1 = N_{1\uparrow}/N_{1\uparrow}+N_{1\downarrow}$ and $a_2 = N_{2\uparrow}/N_{2\uparrow}+N_{2\downarrow}$ are the fractions of the majority spin electrons in the density of states in the two ferromagnets. The fractional difference in the conductivities can be written in terms of the polarisations of the two ferromagnetic metal electrodes, P_1 and P_2:[22]

$$\Delta G/G = 2P_1P_2 \qquad 6.6$$

where $P_1 = 2a_1\text{-}1$ and $P_2 = 2a_2\text{-}1$.

The change in junction resistance with field is fundamental to the application of these materials to electronic devices serving as memory components, switches etc. It has become known as the *magnetic valve effect*. Magnetoresistive effects of 83% have been reported by Lu et al for a tunnel junction of the type $La_{0.67}Sr_{0.33}MnO_3/SrTiO_3/La_{0.67}Sr_{0.33}MnO_3$ at 4.2K and in a field of 0.003T.[23] A similar structure measured by Viret et al. revealed a magnetoresistance of 450% in a field of 10mT at 4.2K. [24] This is the largest magnetoresistive effect reported in a trilayer structure of this kind. But for device applications, large room temperature magnetoresistances are desirable. To date magnetoresistances greater than 40% at room temperature have been reported for magnetic tunnel junctions of the type Co /Al_2O_3/Fe.[25, 26]

The tunnel magnetoresistance measured is basically the difference of resistance in the parallel and antiparallel states divided by their sum. This in turn can be written in terms of the polarisation of the two ferromagnetic layers:[8]

$$MR(\%) = \frac{R_{\uparrow\uparrow} - R_{\uparrow\downarrow}}{R_{\uparrow\uparrow} + R_{\uparrow\downarrow}} = \frac{2P_1P_2}{1 - P_1P_2} \qquad 6.7$$

From this expression it can be seen that as the polarisation of the ferromagnetic layer approaches 100%, the magnetoresistance ratio increases indefinitely. The criterion of 100% spin-polarisation is met by half-metallic ferromagnets, exhibiting a gap in the density of minority states, such as CrO_2. Measuring the I-V characteristics and magnetoresistance of a junction provides therefore a means for determining the polarisation of a material whilst the use of half-metallic ferromagnets like CrO_2 in these junctions provide potential for high magnetoresponsive devices. The transport

measurements are carried out using the DC technique described in Section 5.2.2, Chapter 5.

Theoretically large MR ratios are expected for half-metallic ferromagnets. But in reality this has yet to be achieved. The models used thus far in describing the magnetoresistance arising from the tunneling of electrons from one ferromagnetic electrode to another, assume that the transmitted electron has a well defined spin throughout the tunneling process. However, several processes can occur which flip the spin of the tunneling electron in a junction causing spin depolarisation and limiting the size of the magnetoresistance ratio. Among the processes which can cause spin flipping are scattering by magnetic impurities in the barrier layer, scattering by bulk magnons in the ferromagnetic electrodes, scattering by magnons at the interface and Coulomb blocade effects.[27]

6. 2. 3. Andreev Reflection

Electrons in a metal cannot penetrate into a superconductor if their excitation energy with respect to the Fermi level is below the superconducting gap, Δ. Still, a current may flow through a normal metal-superconductor junction in response to a small applied voltage $eV < \Delta$ by means of a scattering process known as Andreev reflection.[28] The process of Andreev reflection, which involves the conversion of normal current to supercurrent at a metallic interface, is illustrated in Fig. 6. 5. Diagram (a) shows a spin-up electron propagating from a normal metal with no net polarisation ($P = 0$) toward the interface. It is converted to a supercurrent by extracting another electron of opposite spin and momentum from the metal to form a Cooper pair. As a result a spin-up hole is left behind at the interface. The hole has a momentum opposite to that of the incident spin-up electron and propagates away from the interface. This is an Andreev reflected hole and it occupies the opposite spin band to the incident electron. The Andreev reflected holes act as a parallel conduction channel to the initial electron current with the result that the normal-state conductance of the point contact is doubled since 2e is transferred at each Andreev reflection. In an I-V measurement the conversion to supercurrent appears as an excess current added to the ohmic response at the interface.

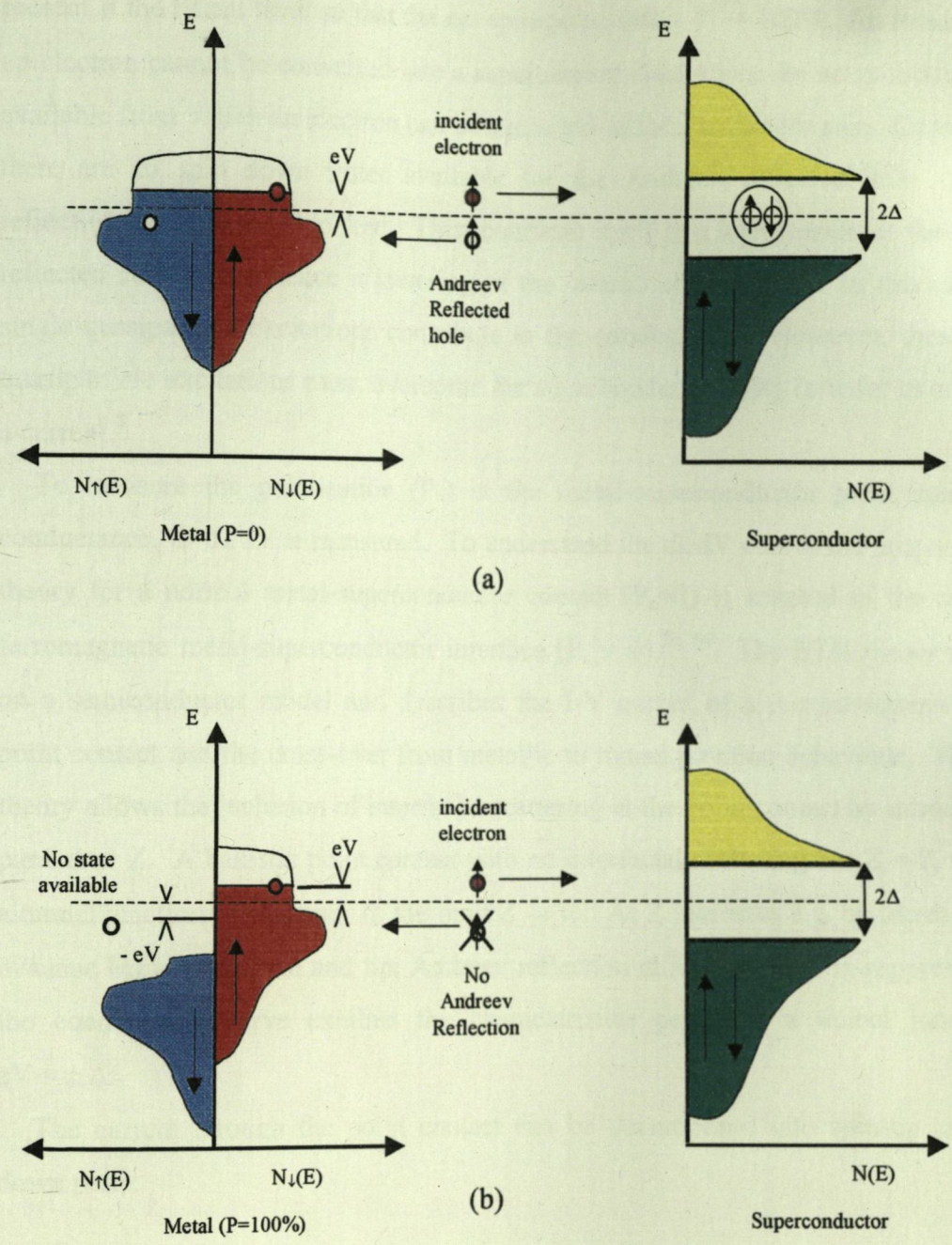

Fig. 6. 5. Supercurrent conversion at a superconductor-metal interface for spin-polarisations (a) P = 0 and (b) P = 100%. In the first case, the Andreev reflection is unhindered by a spin minority population at ε_f. For P=100%, Andreev reflection is suppressed due to the lack of minority spin states at the ε_f.

The diagram (b) of Fig. 6.5 shows what happens when the metal used is a ferromagnetic metal and the spin-up and spin-down states are split by an amount equal

to the exchange splitting. In this case, electrons of only one spin state i.e. spin-up are present at the Fermi level so that the net spin-polarisation P → 100%. An incident spin-up electron cannot be converted into a supercurrent since there are no spin-down states available from which an electron can be extracted to form a Cooper pair. Consequently there are no spin down states available for the Andreev reflected hole. Andreev reflection is effectively blocked. This manifests itself in a suppression of the Andreev reflected current and hence a lowering of the overall conductance. In this case, only single-quasiparticle excitations contribute to the conductance. However, these single-quasiparticle excitations must overcome the superconducting gap in order to contribute a current.[7]

To measure the polarisation (P_c) at the metal-superconductor point contact the conductance, G=dI/dV is measured. To understand the dI/dV curves the proposed BTK theory for a normal metal-superconductor contact (P_c=0) is adapted to the case of a ferromagnetic metal-superconductor interface ($P_c \neq 0$).[29, 30] The BTK theory is based on a semiconductor model and describes the I-V curves of a normal-superconductor point contact and the cross-over from metallic to tunnel junction behaviour. The BTK theory allows the inclusion of interfacial scattering at the point contact by introducing a parameter Z. A ballistic point contact with no interfacial scattering has Z = 0, whereas a tunnel junction corresponds to the limit $Z \rightarrow \infty$. As Z increases e.g. by increasing the distance between sample and tip, Andreev reflection at low voltages is suppressed and the conductance curve exhibits the characteristics peaks of a tunnel junction at $eV = \pm \Delta$.

The current through the point contact can be decomposed into spin-up and spin-down parts:

$$I = I_{\uparrow} + I_{\downarrow} = 2I_{\downarrow} + (I_{\uparrow} - I_{\downarrow}) \qquad 6.8$$

$$= I_{unpol} + I_{pol}$$

The unpolarised current, I_{unpol}, has equal numbers of up- and down-spins and therefore carries no net polarisation, while I_{pol} is entirely composed of the spin majority carrier and carries all of the polarisation. But, I_{pol} cannot undergo Andreev reflection due to a lack of minority spin states at ε_F for the Andreev reflected hole.

The total conductance curve dI/dV can then be written as:

$$\frac{d}{dV}I(V,T;P_c,Z) = (1-P_c)\frac{d}{dV}I_{unpol}(V,T;Z) + P_c\frac{d}{dV}I_{pol}(V,T;Z) \qquad 6.9$$

where V is the voltage and T the temperature. Hence, while P_c is a measure of the spin polarisation of the ferromagnetic layer it is also a measure of the fraction of current not undergoing Andreev reflection and $(1-P_c)$ is the fraction of current undergoing normal Andreev reflection. For minimum interfacial scattering ($Z \approx 0$), low voltages ($eV << \Delta$) and low temperatures $R_N dI_{unpol}/dV=2$ where R_N ($=1/G_N$, the normal state conductance of the point contact) is the contact resistance and $dI_{pol}/dV = 0$ giving:[31]

$$R_N\frac{dI}{dV}(eV \to 0, T \to 0; Z = 0) = 2(1-P_c) \qquad 6.10$$

from which the spin-polarisation P_c can be extracted.

6. 3. Experimental Procedure

The patterning of films into simple structures for transport measurements and/or for use in the fabrication of devices involves several stages. Below I shall briefly outline the procedure involved for patterning and etching CrO_2 films as well as the procedure for constructing a simple ferromagnetic trilayer device of the type CrO_2/barrier layer/Co. It should be noted that in the case of CrO_2, it is not necessary to deposit a barrier layer for the device to operate as a tunnel junction.

The I-V measurements of a tunnel junction will be discussed briefly as well as the procedure used for measuring the spin polarisation of a CrO_2 film using a superconducting point contact.

6. 3. 1. Device Fabrication

Stage 1: Sample Preparation

Deposition of the CrO_2 film (see Section 2.2 and 2.3, Chapter 2). (110) oriented films with thicknesses of the order of 0.8 μm were used in the fabrication of tunnel junctions.

Stage 2: Photolithography

Optical lithography is commonly used for defining small structures (typically of the order of 200 nm to 5 mm) in thin films. For our purposes the method of contact printing was used to pattern structures onto CrO_2 thin films. The first step in the photolithographic process involves spinning a thin layer of photoresistive material onto a thin film sample.[♦] This is done by securing the sample onto a jig (either by mechanical means or by suction using a rotary pump) and placing a drop of the photoresist in the centre of the sample. The sample is then spun at a particular angular velocity depending on the type of photoresist used and the thickness of photoresist required. For the patterning of CrO_2 films several photoresists e.g. S1400, S1600, S1818 and AZ 5214 can be used. Initially the photoresist S1400 (ethyglycol acetate) was used. However, it was recently reported that this compound is dangerous by inhalation and has subsequently been banned from use.[†] For this reason the photoresist AZ 5214 is used instead and the procedure described below applies to this photoresist. The sample is spun at a speed of 4000 revolutions per minute (r.p.m) for 30-40 seconds and then at 6000 r.p.m for 4 seconds. Using these spinning parameters it is possible to

---

♦ A photoresistive material is one which becomes resistant to chemical attack once it has been exposed to light.

† For the photoresist S1400 the soft bake was carried out at 90 °C for 10-15 minutes, exposed to UV radiation for 36 seconds and hard baked at 150°C for a further 15 minutes. Developing was as for AZ 5214. The photoresists were supplied by SOTRACHEM, St. Denis, France.

obtain a layer of photoresist approximately 1.5 μm in thickness. Once the photoresist has been deposited, the sample is "soft baked" on a hot plate at a temperature of 105 °C for 30-60 seconds to allow the solvents in the resist to evaporate. A Karl Suss MJB3 mask aligner equipped with a 4 inch photomask having the desired structure is then used to pattern the photoresistive layer. The mask, viewed through an optical microscope, can be positioned anywhere over the sample. The sample stage is mechanically raised and brought into contact with the mask. The unmasked regions are exposed to UV light for 17 s. The UV light is created by a mercury lamp of wavelength 310-420 nm. The exposed photoresist is dissolved or "developed" in an alkaline solution (developer no. AZ 351) that is prepared by mixing with distilled water in the ratio 5:1. (The developer solution is usually NaOH based). Developing takes approximately 30 seconds. The sample is rinsed in distilled water and dried using an air gun. Providing the sample has not been over exposed to UV radiation and/or over developed, the photoresist remaining visibly defines the structure to be etched. However, to ensure that the photoresist remains hard and impenetrable during the etching process, the resist is further "hard baked" in an oven pre-set to 150 °C for 30 minutes. Typical working structures are shown in Fig. 6. 6.

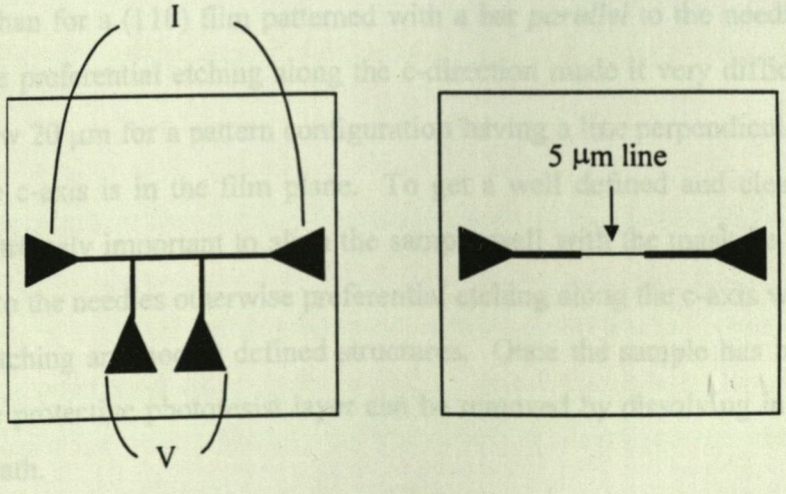

Fig. 6. 6. (a) Hall bar for measuring normal resistivity and (b) 5 μm line for tunnel junction

Stage 3: Wet Etching

The simplest and the fastest way to complete a pattern transfer is wet etching. Lines wider than 1 μm can be obtained by this technique which involves immersing the sample in an acidic or basic solution. The photoresist pattern protects the sample beneath it from chemical attack by the acid (or base) whilst regions of the sample where there is no photoresist are effectively etched and removed. To etch CrO_2 an industrial Chrome etch is used.* This consists of a solution of ammonium ceric nitrate ($(NH_4)_2[Ce(NO_3)_6]$) and Nitric acid (HNO_3). For CrO_2 films, the etch rates depended on the sample quality, the sample orientation and the pattern configuration. The etch rate of a (001) oriented film, 0.6-0.8 μm in thickness and oriented with its needle/c-axis lying out of the film plane, is between 45 and 75 seconds/μm (depending on sample quality). On the other hand, a (110) oriented film comprising of needles lying in the plane of the film and having a similar thickness has an etch rate between 90 and 120 seconds/μm (again the difference arising from sample quality i.e. slower etch rates correspond to poorer quality films). The more rapid etching of the (001) oriented film is due to the preferential etching along the c-axis. As a consequence of this anisotropic etching, the etch rate was also found to depend on the pattern configuration. For example, the etch rate for a (110) film patterned with a bar *perpendicular* to the needle axis is lower than for a (110) film patterned with a bar *parallel* to the needle axis. In many cases the preferential etching along the c-direction made it very difficult to etch structures below 20 μm for a pattern configuration having a line perpendicular to the c-axis where the c-axis is in the film plane. To get a well defined and cleanly etched pattern it is extremely important to align the sample well with the mask i.e. parallel or perpendicular to the needles otherwise preferential etching along the c-axis will result in non-uniform etching and poorly defined structures. Once the sample has been etched completely the protective photoresist layer can be removed by dissolving in acetone in an ultrasonic bath.

The etching process was found to be highly sample dependent and anisotropic along the c-direction. For this reason it was difficult to make definite estimates of the etch rates for the various samples. The range of etch rates are summarised in Table 6.1.

---

* The chrome etch is supplied by Transene Co. Inc., Danvers, Maryland, USA.

Table 6. 1. Etching rates for oriented CrO_2 films using industrial chrome etch

Sample	Etch Rate (μm/s)
(001)	0.0130 - 0.022
(110)	0.008-0.011

Stage 4: Deposition of the Insulating Layer

An insulating layer between the top and bottom ferromagnetic electrodes is the next step in the fabrication of a simple ferromagnetic tunnel junction. As already mentioned, where CrO_2 films are concerned it is not necessary to deposit a separate insulating layer for the device to operate as a tunnel junction since it would appear that a native insulating layer aready exists. This most likely a thin layer of Cr_2O_3.

Stage 5: Deposition of the Top Ferromagnetic Electrode: Co

RF sputtering was used to deposit the Co layer. RF sputtering involves bombarding a target with a beam of high energy ions, usually Ar^+ ions, which extract atoms from the target. The Ar^+ ions are produced by applying a RF signal to argon gas. The plasma is collimated by a magnetic field which focusses the beam onto a target, in this case a Co target. Co atoms are extracted from the target and deposited onto the sample.

The thickness of the layer being deposited can be monitored using a vibrating quartz crystal which is positioned close to the sample. As the material is deposited on the sample (and hence the quartz crystal) the frequency of the vibrations changes. The relationship between the frequency of the vibrations and the thickness, t, of the deposit is given in its simplest form by:

$$t = \left(\frac{N_q d_q}{d_f f_q^2} \right) (f_q - f_c) \qquad 6.11$$

and d_q is the density of quartz (2.60 g/cm^3), d_f is the density of the film (g/cm^3), N_q is the frequency constant for AT-cut quartz crystal (=1664 x 10^4 Hz/cm), f_q is the resonance frequency of the unplated crystal (=6.05 x 10^6 Hz) and f_c is the resonant frequency of the loaded crystal. The deposition rate was 3.3 Å/s for an Ar pressure of mbar and a RF power output of 150W. Using these parameters a Co layer approximately 150 nm in thickness was deposited.

The Co layer could then be patterned as outlined in stage 2 of the device fabrication process. Etching of the Co layer was carried out by ion beam milling. The etching parameters for Co are listed in Table 6.2. and figure 6.7 shows a simple diagram of the ion beam milling set up.

Table 6. 2. Ion beam milling parameters for the deposition of an Al and etching of a Co layer

	Co etching
Argon pressure (mbar)	$8x10^{-4}$
Cathode current (A)	7.8
Discharge voltage (V)	40
Discharge current (A)	0.2
Accelerating voltage (V)	200
Beam voltage (V)	500
Beam current density (mA/cm^2)	1.2
Sample ion-gun distance (cm)	10
Deposition/Etch rate (nm/s)	0.3

Ion beam milling is similar in effect to RF sputtering. In this case, the ion beam is produced by the collision of electrons emitted from a cathode with Ar atoms. The argon ions are collimated by magnets positioned either side of the cathode ionising chamber and accelerated through a potential toward the target. A neutraliser cathode in front of the target prevents the build up of too much positive charge on the target which would otherwise hinder the ion beam from reaching the sample.

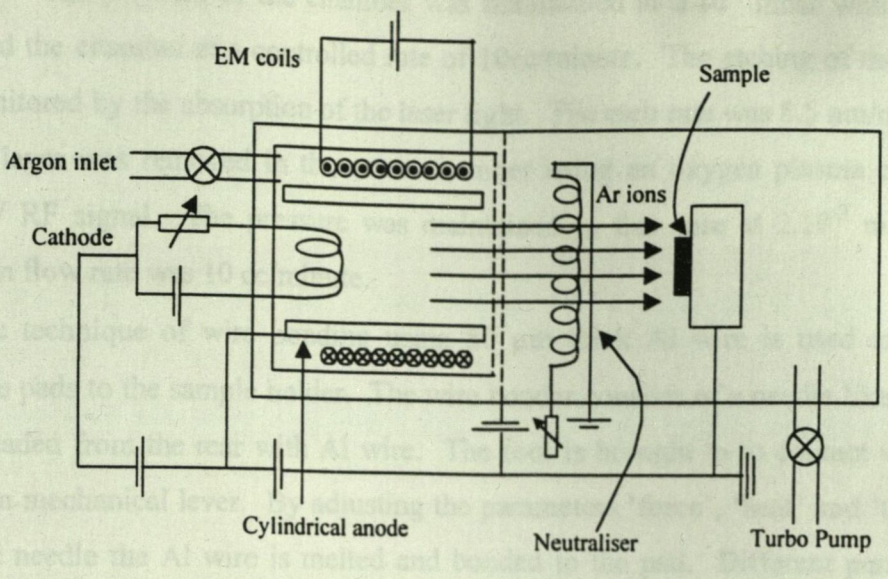

Fig. 6. 7. Ion beam milling set-up

Stage 6: Contacts

The final and probably the most critical stage in the fabrication process is applying the 'contacts' since this enables the samples to be measured. In this work, contacts were made by depositing a layer of gold by electron beam evaporation. The electron beam, which is produced by a cathode, collimated and accelerated through a potential in a manner similar to that for ion beam milling and RF sputtering, heats the gold locally causing it to melt and then evaporate. The gold layer was then patterned using UV lithography and etched. For the patterning of gold however, the hard bake stage can be excluded. Where contacts to very small structures are concerned high resolution techniques such as electron beam lithography are required to pattern the contacts otherwise the usual photolithographic process of contact printing is used. The rate of Au deposition in vacuum was and the thickness of the Au layer deposited was 200 nm. The gold layer was etched using reactive ion etching. Again this technique is similar to ion beam milling and RF sputtering in that a plasma is created and used to bombard a target where it acts to extract atoms from the target. In the case of reactive ion etching however, particular gases are used for etching certain substances. For example, to etch the gold layer CHF_3 was used. The plasma was created by applying a RF signal of

150 W. The pressure in the chamber was maintained at 5.10^{-3} mbar while the CHF_3 entered the chamber at a controlled rate of 10cc/minute. The etching of the gold layer is monitored by the absorption of the laser light. The etch rate was 8.5 nm/minute. The resist layer was removed in the same chamber using an oxygen plasma created by a 100 W RF signal. The pressure was maintained in this case at 2.10^{-3} mbar and the oxygen flow rate was 10 cc/minute.

The technique of wire bonding using 50 μm thick Al wire is used to attach the sample pads to the sample holder. The wire bonder consists of a needle like foot which is threaded from the rear with Al wire. The foot is brought in to contact with sample using a mechanical lever. By adjusting the parameters 'force', 'heat' and 'time' acting on the needle the Al wire is melted and bonded to the pad. Different parameters are required when bonding to different metals. Table lists the parameters for bonding Al wire to gold, Co and the Cu pads on the sample holder. Fig. 6.8 shows a typical trilayer structure

Table 6. 3. Parameters for wire bonding Al to Au, Co and Cu

	Au	Co	Cu
Force (a.u.)	2.00	1.20	4.00
Heat (a.u.)	2.75	2.00	5.50
Time(a.u.)	2.50	1.70	4.90

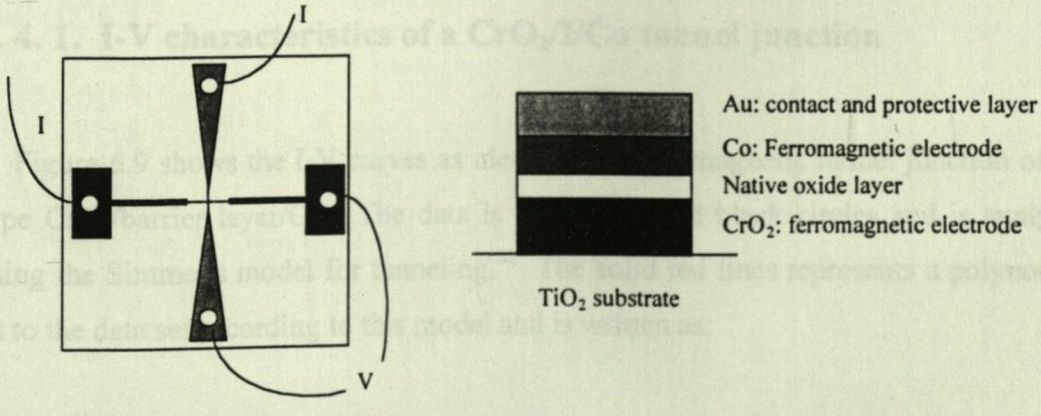

Fig. 6. 8. Ferromagnetic Tunnel Junction: CrO_2/I/Co in the cross-stripe geometry with the current perpendicular to plane (CPP).

6. 3. 2. Transport measurements

The resistivity as a function of temperature was carried out on etched structures of CrO_2 in a manner identical to that used in chapter 5, section 5.2.2. The I-V characteristics of the magnetic tunnel junctionCrO_2/I/Co were measured for the CPP geometry, Fig. 6.8 using again the typical DC 4-point probe technique. The experimental set-up was again the same as that used for $\rho(T)$ measurements.

To measure the spin polarisation of CrO_2 a metallic point contact was formed between a CrO_2 film and a Nb superconducting tip. The tip was prepared by mechanically polishing a rod of superconducting material to a sharp point using progressively finer sandpaper. The superconducting tip was attached to a drive shaft above the sample. The tip height could be adjusted using a micrometer capable of moving the point linearly by amounts as small as 100 μm per revolution. Transport measurements were carried out using the typical 4-point probe technique and ac lock-in detection at a frequency of 2 kHz. The point contact and sample were immersed in a liquid He bath at 1.6 K during measurement. The measurement of the spin-polarisation of CrO_2 was carried out in collaboration R. J. Soulen and coworkers at the Naval Research Laboratories, Washington.

6. 4. Results and Discussion

6. 4. 1. I-V characteristics of a CrO_2/I/Co tunnel junction

Figure 6.9 shows the I-V curves as measured on the magnetic tunnel junction of the type CrO_2/barrier layer/Co. The data is given by solid black circles and is analysed using the Simmons model for tunneling.[32] The solid red lines represents a polynomial fit to the data set according to this model and is written as:

$$I/A = \beta(V + \gamma V^3) \qquad 6.12$$

where I is the tunneling current, A is the area of the tunnel junction (25 μm^2), V is the voltage, β is a parameter depending on the barrier height, φ (eV) and width, s (Å) and given by the following expression:

$$\beta = \frac{3}{2s}\left(\frac{e}{\hbar}\right)^2 (2m\varphi)^{1/2} \exp\left[-\left(\frac{4\pi s}{\hbar}\right)(2m\varphi)^{1/2}\right] \qquad 6.13$$

here e and m are the charge and the mass of the electron respectively, $\hbar$ is Planck's constant. γ is also a parameter depending on the barrier height and width and is defined as:

$$\gamma = \left(\frac{\pi m}{3\varphi}\right)\left(\frac{es}{\hbar}\right)^2 \qquad 6.14$$

The parameter β can be determined graphically by noting that at very low voltages equation 6.10 reduces to $I/A = \beta V$. Hence, plotting the linear low-voltage J-V characteristics (J=I/A is the current density) and finding the slope determines β. The parameter γ can be determined by plotting $J-\beta V$ against V^3 in the region of higher voltages. Again, according to the equation 6.10 a straight line should be obtained. The slope of this line is then equal to $\beta\gamma$. Since β is known γ can be obtained. The barrier height in electron volts is given by:

$$\varphi = \left(\frac{0.266}{\gamma^{1/2}}\right)L \qquad 6.15$$

The barrier width, s, can be defined as:

$$s = 4.94\gamma^{1/4}L^{1/2} \qquad 6.16$$

and L in both cases is given by:

$$L = \log\left(\frac{4.87x10^{13}}{\beta\gamma^{1/2}}\right) \qquad 6.17$$

We can see clearly from the I-V curve in Fig. 6.9 that the junction shows a non-linear, non-ohmic behaviour at 13 K suggesting that electrons are tunneling between the two ferromagnetic electrodes despite no barrier layer being deposited. From this it can be concluded that a native barrier layer exists on top of the CrO_2. It is not known what this layer is but it is believed to be a thin layer of Cr_2O_3. The conductance curve can be obtained from this data by taking the derivative of the current with respect to voltage (dI/dV). This curve is plotted in Fig. 6.9(b) and shows the parabolic behaviour typical of tunneling of electrons through a barrier. Table 6.4 lists the results of the fits to the I-V data at low and high voltage. From these fits we can see that the barrier width, s, is of the order of 20 Å. The capacitance of the junction can be determined by using the following equation:

$$C = \varepsilon_o \varepsilon_r A/s \qquad 6.18$$

where ε_o is the permittivity of vacuum, ε_r is the relative permittivity and A the area of the junction. Using an average value for s of 20 Å and a relative permittivity of 5.6 the capacitance C ~ 6.2 x 10^-13 F and hence the charging energy $E_c = e^2/2C \sim 1.3 \times 10^{-7}$ meV.

Table 6. 4. Results at 13 K of the fits in the linear low voltage region and the linear high voltage regions giving rise to values for the barrier height, φ and width, s.

	β (A/V.m^2)	γ (A/V^3.m^2)	L	φ (eV)	s (Å)
Positive I-V	8.94e5	6.3	7.34	0.78	21(1)
Negative I-V	6.21e5	5.4	6.50	0.74	19(1)

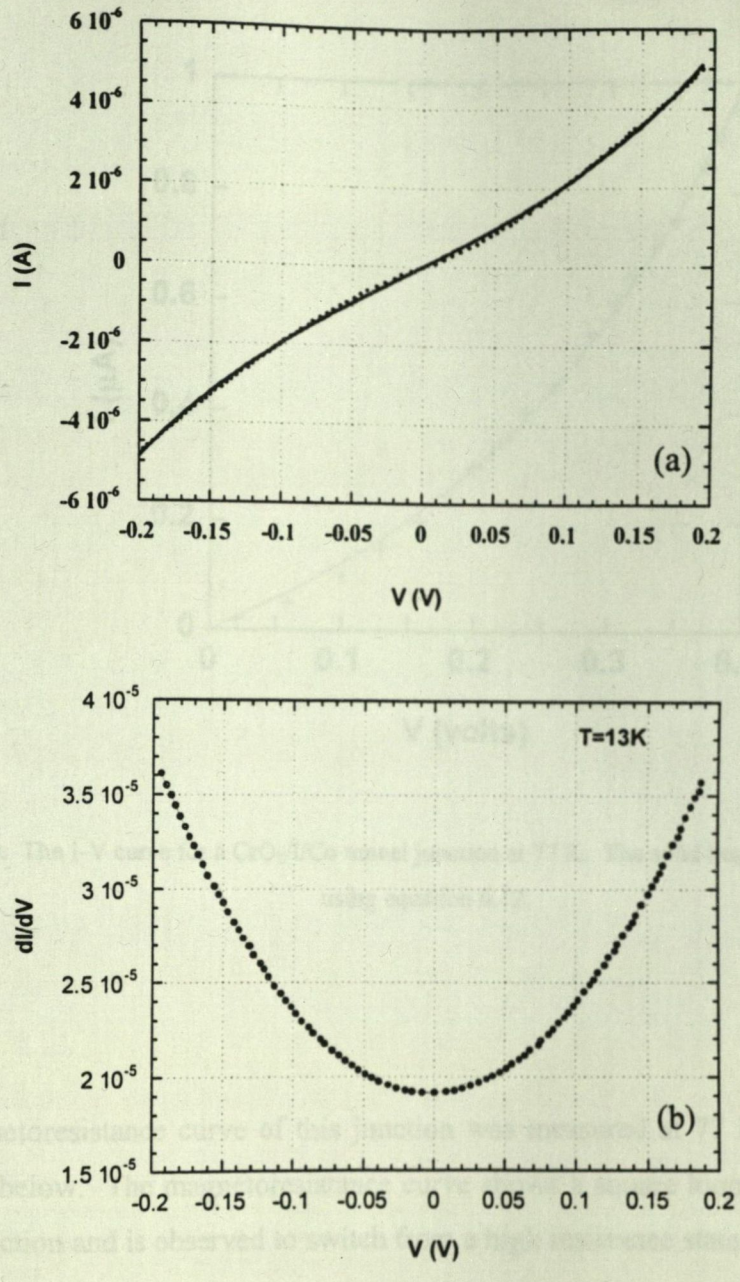

Fig. 6. 9. (a) I-V characteristics at T=13 K for a tunnel junction of the type CrO_2/barrier layer/Co and (b) dI/dV curve of the above I-V curve showing the parabola shaped conductance as a function of applied voltage.

Figure 6.10 shows the I-V curve at 77 K of a junction similar to that measured above (CrO_2/I/Co). The Simmons' model was again used to analyse the data and the following parameters obtained: $\beta = 0.4 \times 10^5$ A/V m^2, $\gamma = 8.3$, $L = 8.6$, $\phi = 0.79$ eV and $s = 24.6$ Å. These values are in fairly good agreement with the values obtained at 13 K.

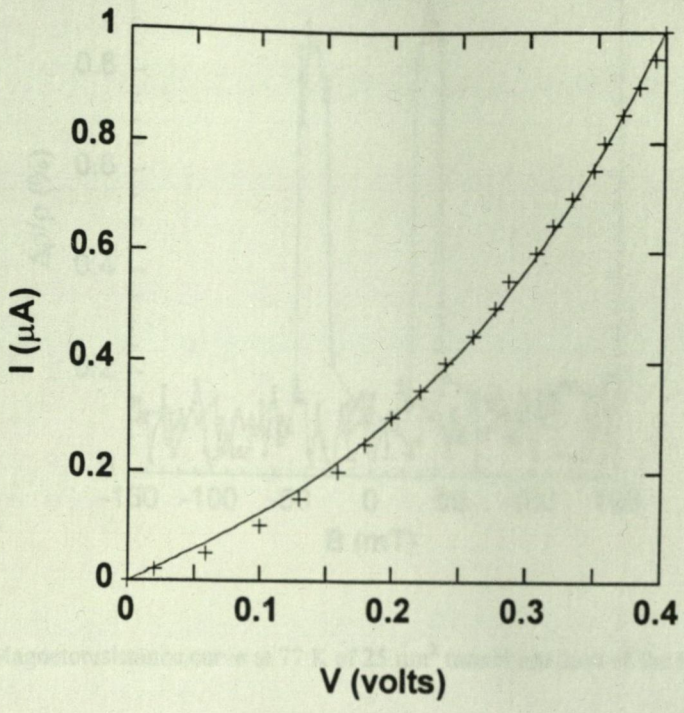

Fig. 6. 10. The I-V curve for a CrO_2/I/Co tunnel junction at 77 K. The solid line is the fit to the data using equation 6.12.

The magnetoresistance curve of this junction was measured at 77 K and is shown in Fig. 6.11 below. The magnetoresistance curve shows a square loop characteristic of a tunnel junction and is observed to switch from a high resistance state to a low resistance state at a coercive field of approximately ± 25 mT. However, the magnetoresistance ratio measured is only 1% at this temperature. For a tunnel junction of the type CrO_2/I/Co a magnetoresistance of 25% is expected if the spin polarisation of the CrO_2 and Co ferromagnetic layers is $P(CrO_2) = 100\%$ and $P(Co) = 34\%$ respectively. Subsequent measurements at higher temperatures were unsuccessful due to a progressively worsening signal-to-noise ratio.

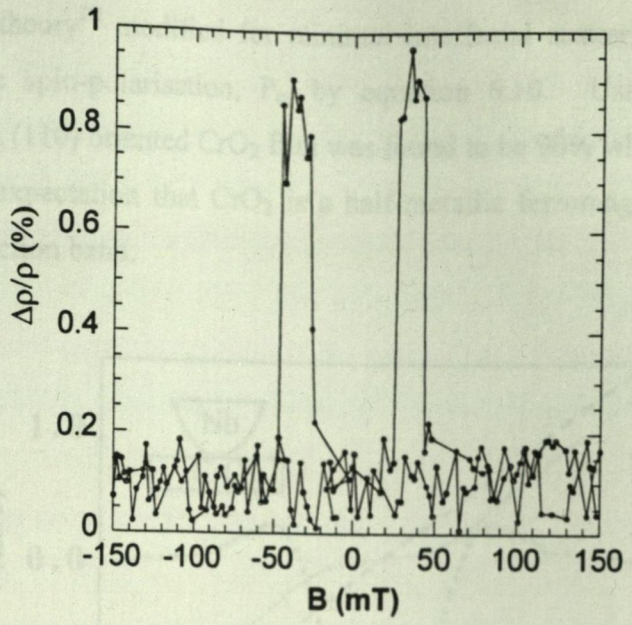

Fig. 6. 11. Magnetoresistance curve at 77 K of 25 μm^2 tunnel junction of the type CrO_2/I/Co.

6. 4. 2. Spin Polarisation by Andreev reflection

Figure 6.12 shows the I-V curve and conductance curve for a Nb superconducting point contact on a (110) oriented CrO_2 film at T = 1.6 K. At low voltages, the conductance is reduced almost to zero indicating that nearly all the Andreev reflection has been suppressed due to a lack of minority spin states at the Fermi level. This in turn, is direct evidence for a fully spin polarised conduction band at the Fermi level. The vertical lines at ± 1.5 mV denote the bulk gap, Δ, for Nb. The peaks occurring at these positions are characteristic of the singularities occurring in the superconducting density of states at $E = \pm \Delta$. At higher voltages the conductance $dI/dV \rightarrow 1$ indicating a return of the superconductor to its normal state. In the I-V curve this is witnessed as a return to a linear dependence on V. In this case, the linear I-V dependence arises due to the conductance between two closely spaced metals with a potential difference.

The spin polarisation, P_c, is obtained by numerically fitting the conductance curve with the BTK theory[29] modified for minimal interfacial scattering allowing a direct estimate of the spin-polarisation, P_c, by equation 6.10. Using this method, the polarisation of a (110) oriented CrO_2 film was found to be 90% which is consistent with the theoretical expectation that CrO_2 is a half-metallic ferromagnet with a fully spin polarised conduction band.

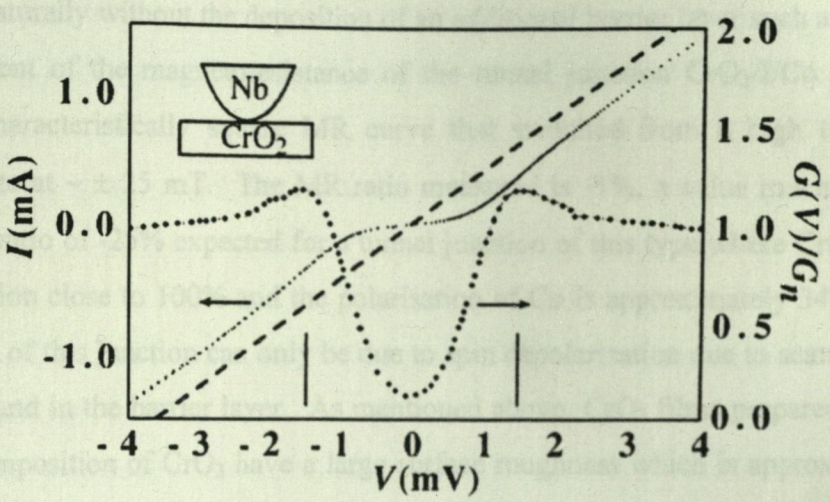

Fig. 6. 12. The heavy dotted line shows the I-V characteristics of the CrO_2 ferromagnetic metal-Nb superconducting point contact at T = 1.6K. The light dotted line shows the corresponding dI/dV curve. The dashed line shows the I-V characteristics when the superconductor is in the normal state from which the conductance $G_n = 0.417\ \Omega^{-1}$.

6.5. Discussion

The spin polarisation, P, of CrO_2 has been measured using a technique which measures the conversion between supercurrent and normal current when a Nb superconducting tip is placed in point contact with a (110) oriented CrO_2 film. Measurement shows that P = 90% at 1.6 K for CrO_2 which is close to the 100% spin polarisation predicted for half-metallic ferromagnet CrO_2.[10] Consequently, it was expected that magnetic tunnel junctions into which CrO_2 had been incorporated would show large magnetoresistance ratios.

The I-V characteristics of a tunnel junction of the type CrO_2/I/Co having an area of 25 μm^2 has been measured at 13 K and 77 K. The I-V curves show the non-linear behaviour characteristic of transport by tunneling. Fits to the data using the Simmons' model resulted in reasonable values for the barrier thickness and the barrier height of approximately 20 Å and 0.8 eV respectively. However, since the precise nature of the barrier layer is not known and the surface roughness of the (110) CrO_2 films is large (~ 10%), these values can be viewed only as an estimate and an indication that a barrier layer exists naturally without the deposition of an additional barrier layer such as Al_2O_3.

Measurement of the magnetoresistance of the tunnel junction CrO_2/I/Co at 77 K revealed a characteristically square MR curve that switched from a high to a low resistance state at ~ ± 25 mT. The MR ratio measured is -1%, a value much smaller than the MR ratio of -25% expected for a tunnel junction of this type where CrO_2 has a spin polarisation close to 100% and the polarisation of Co is approximately 34%. The low MR ratio of this junction can only be due to spin depolarisation due to scattering at the interface and in the barrier layer. As mentioned above, CrO_2 films prepared by the thermal decomposition of CrO_3 have a large surface roughness which is approximately 10% in the (110) oriented films (see Chapter 2) and diffusive scattering at the surface is expected to contribute significantly to spin depolarisation. Furthermore, whilst the junction unambiguously shows properties characteristic of a tunnel junction (non-linear I-V curves, square switching of the magnetoresistance) it is not known exactly what the barrier layer is. It is assumed that a native oxide layer of Cr_2O_3 provides the barrier layer. Cr_2O_3 is antiferromagnetic and therefore, spin flip scattering resulting in spin depolarisation may arise due to antiferromagnons at the interface. Furthermore, it is possible that the barrier layer is not homogeneous and that there is a mixture of Cr^{3+} and Cr^{4+} magnetic ions. The direction of the magnetic impurity spin can be random and consequently, electrons hopping between the two ferromagnetic electrodes in a tunnel junction can again suffer spin flip scattering leading to a reduction in the magnetoresistance.

References

[1] A. P. Ramirez, J. Phys.: Condens. Matter (review article), **9**, 8171-8199 (1997)

[2] Y. Lu, X. W. Li, G. Q. Gong, Gang Xiao, A. Gupta, P. Lecoeur, J. Z. Sun, Y. Y. wang and V. P. David, Phys. Rev. B, **54**, R8357-R8360 (1996)

[3] J. S. Moodera, L. R. Kindler, T. M. Wong and R. Mersevey, Phys. Rev. Lett., **74**, 3273-3276 (1995)

[4] S. S. P. Parkin, R. Bhadra and K. P. Roche, Phys. Rev. Lett., **66**, 2152-2155 (1991)

[5] C. W. Searle and S. T. Wang, Can. J. Phys., **48**, 2023-2025 (1970)

[6] J. M. de Theresa, A. Barthélémy, A. Fert, J. P. Contour, R. lyonnet, F. Montaigne, P. Seneor and V. Vaurès, Phys. Rev. Lett., **82**, 4288-4291 (1999)

[7] R. Mersevey and P. M. Tedrow, Phys. Rep., **238**, 175-243, (1994)

[8] M. Julliere, Phys. Lett., **54A**, 225 (1975)

[9] A. M. Bratkovsky, Phys. Rev. B, **56**(5), 2344-2347 (1997)

[10] K. Schwarz, J. Phys. F: Met. Phys., **16**, L211-L215 (1986)

[11] M. A. Korotin, V. I. Anisimov, D. I. Khomski and G. A. Sawatsky, Phys. Rev. Lett., **80**, 4305-4308 (1998)

[12] S. Matar, G. Demazeau, J. Sticht, V. Eyert and J. K übler, J. Phys. I France, **2**, 315-328 (1992)

[13] A. V. Nikolaev and B. V. Andreev, Phys. Sol. St., **35**, 603-605 (1993)

[14] S. P. Lewis, P. B. Allen and T. Sasaki, Phys. Rev. B, **59**, 411-418 (1999)

[15] P. M. Tedrow and R. Mersevey, Phys. Rev. Lett., **26**, 192-195 (1971)

[16] P. M. Tedrow and R. Mersevey, Phys. Rev. B, **7**, 318-326 (1973)

[17] P. M. Tedrow and R. Mersevey, Phys. Rev. B, **8**, 5098 (1973)

[18] R. Wiesendanger, D. Bürgler, G. Tarrach, H. -J. Güntherodt and G. Güntherodt, AIP Conference Proceedings, **241**, 504-510 (1991)

[19] R. Mersevey and P. M. Tedrow, Phys. Lett., **238**, 173-243 (1994)

[20] R. J. Soulen, J. M. Byers, M. S. Osofsky, B. Nadgorny, T. Ambrose, S. F. Cheng, P. R. Broussard, C. T. Tanaka, J. Nowak, J. S. Moodera, A. Barry and J. M. D. Coey, Science, **282**, 85-88 (1998)

[21] M. Johnson and R. H. Silsbee, Phys. Rev. Lett., **55**(17), 1790-1793 (1985)

[22] S. Maekawa and U. Gäfvert, IEEE Trans. Magn., **18**, 707-708(1982)

[23] Y. Lu, X. W. Li, G. Q. Gong, G. Xiao, A. Gupta, P. Lecoeur, J. Z. Sun, Y. Y. Wang and V. P. Dravid, Phys. Rev. B, **54**, R8357-8360 (1996)

[24] M. Viret, M. Druet, J. Nassar, J. P. Contour, C. Fermon and A. Fert, Europhys. Lett., **39**, 545 (1997)

[25] S. S. P. Parkin, K. P. Roche, M. G. Samant, P. M. Rice, R. B. Beyers, R. E. Scheuerlein, E. J. O'Sullivan, S. L. Brown, J. Bucchigano, D. W. Abraham, Y. Lu, M. Rooks, P. L. Trouilloud, R. A. Wanner, W. J. Gallagher, J. Appl. Phys., **85**, 5828-5833 (1999)

[26] T. Miyazaki and N. Tezuka, J. Magn. And Magn. Mat., **139**, L231-L234 (1995)

[27] F. Guinea, Phys. Rev. B, **58**, 9212-9216 (1998)

[28] M. J. M. Jong and C. W. J. Beenaker, Phys. Rev. Lett., **74**, 1657-1660 (1995)

[29] G. E. Blonder, M. Tinkham, T. M. Klapwijk, Phys. Rev. B, **25**, 4515-4532 (1982)

[30] G. E. Blonder and M. Tinkham, Phys. Rev. B, **27**, 112-118 (1983)

[31] Yu. V. Sharvin, Sov. Phys.-J. Exp. and Theor. Phys., **21**, 655-656 (1965)

[32] J. G. Simmons and G. J. Unterkofler, J. Appl. Phys., **34**, 1793-1803 (1963)

Chapter 7

Conclusions

"What doesn't kill you, makes you stronger.

Chanted by Nora Dempsey when completing her thesis in the summer of 1998.

7. 1. Conclusions

Thin films and powders of CrO_2 have been prepared and their transport, magnetic and thermal properties studied. A magnetic tunnel junction has been fabricated and preliminary transport measurements performed.

Chromium dioxide was prepared in thin film and powder form by the thermal decomposition of the precursor CrO_3 in a closed reactor vessel under high oxygen pressure. Films were grown on oriented TiO_2 substrates and X-ray diffraction showed that the films were pure, highly textured and had the same orientation as the substrate. Powders on the other hand were found to contain a substantial amount of the intermediate oxide Cr_2O_3. Microscopy showed that the films had a granular nature and comprised long acicular needles up to 50 μm in length and 1-3 μm in diameter. Powders were also found to comprise needle shape particles up to 20 μm in length and 1 μm in diameter. The needle-axis was found by X-ray diffraction to correspond to the c-axis. The films showed a large surface roughness, which was larger when the orientation of the film was such that the c-axis was out of the film plane. In this case, films had a texture similar to the New York skyline. The granular nature of the films was found to influence significantly the magnetic and transport properties.

CrO_2 films show properties characteristic of a half-metallic ferromagnet. At 1.6 K the spin-polarisation of an (110) oriented CrO_2 film was found to be close to 100%. Films and powders of CrO_2 were ferromagnetic with a Curie temperature of 400 K and magnetisation measurements of (001) and (110) oriented thin films showed a low temperature saturation

magnetisation close to the value of 133 J/T kg (= $2\mu_B/CrO_2$) expected for half-metallic ferromagnetic CrO_2. The residual resistivity was reflective of a good metal with values lying in the range 0.1-10 $\mu\Omega$ m.

Thin films show a temperature dependence of resistivity that follows a T^2-law characteristic of electron-magnon scattering at intermediate temperatures. At temperatures below 80 K the transport properties of oriented CrO_2 films show behaviour indicative of two-band transport: a sign reversal with field that indicated the presence of highly mobile holes as well as a much larger number of less mobile electrons, and a large positive magnetoresistance that could be interpreted qualitatively in terms of the two-band model. The two-band model is supported by low temperature neutron diffraction measurements where a moment of 2.11 μ_B/Cr^{4+} is interpreted as a sign of holes in the O 2p band. All of the magnetotransport properties show dramatic changes in behaviour on passing through T = 80 K and this can be correlated to the exponential decrease in the resistivity behaviour and the Hall data.

The transport properties of pressed powder compacts was governed by the tunneling of electrons between contiguous ferromagnetic particles along a critical path with a spin-dependent Coulomb gap. The magnetoresistance increased from 29% to 50% at 5 K when the powder was diluted to within its percolation limit. It is concluded that it should be possible to control the PMR by controlling the particle size, orientation and surface state.

A magnetic tunnel junction of the type CrO_2/I/Co was fabricated using photolithography techniques. It was found that in order to observe tunneling between the two ferromagnetic layers it was not necessary to deposit an insulating layer. Instead, a native insulating layer, most likely Cr_2O_3, formed the barrier layer. A preliminary study of the I-V characteristics at 13 K and 77 K revealed a barrier width in the region of 20 Å and a height of nearly 0.8 eV. The magnetoresistance measured at 77 K revealed a surprisingly low MR ratio of -1% for a tunnel junction comprising a half-metallic ferromagnet as one of the electrodes. However, it is expected that improving the interface and barrier regions should enhance the MR ratio by reducing any spin-depolarisation that may occur from spin-flip scattering due to the surface roughness, surface magnons and magnetic impurities in the barrier layer.

7. 2. Suggestions for Future Work

Due to the granular nature of the films prepared by the thermal decomposition of CrO_3 under high oxygen pressure, it should be possible to measure the transport characteristics along a single needle and across a grain boundary. This should enable a more precise extraction of the intrinsic and extrinsic properties of CrO_2, particularly those arising from grain boundary scattering.

To improve the surface quality of films for use in magnetic tunnel junctions, it is suggested that alternative preparation techniques in which the thickness and surface roughness can be controlled be developed.

CrO_2 does show potential for use as a spin electronic device. However, magnetic tunnel junctions with a well characterised interface and barrier layer is required if the performance of the tunnel junction is to be improved.

Appendix 1

The Rietveld algorithm fits the observed diffraction pattern using as variables the instrumental characteristics and the approximate structural parameters of the sample. The refinement is based on a method of least squares and involves minimising the function:

$$M = \sum_i w_i (y_i - y_{ic})^2$$

where $w_i = 1/y_{io}$ is the weight assigned to each experimental value, y_{io} and y_{ci} are the observed and calculated intensities at each step i respectively.

Residual factors are introduced as a means of estimating the agreement between the calculated profile and the diagram observed. The residual factors are given by:

$$R_p = \left[\frac{\sum_i |y_{io} - y_{ic}|^2}{\sum_i w_i y_{io}^2} \right]^{1/2}$$

$$R_{wp} = \left[\frac{\sum_i w_i |y_{io} - y_{ic}|^2}{\sum_i w_i y_{io}^2} \right]^{1/2}$$

where R_{wp} and R_p are the agreement factors of the weighted profile and the profile respectively. The profile residual factors are dominated by the success or inadequacy of the profile function in describing the peak shape but are rather insensitive to the structural parameters. The Bragg residual factor compares the calculated intensity to the observed intensity and is given by:

$$R_{Bragg} = \frac{\sum_k |I_k - I_k^c|}{\sum_k I_k}$$

where I_k is the observed integrated intensity of the kth reflection at the end of the refinement after apportioning each individual intensity y_i between the contributing Bragg peaks to the calculated intensities I^c. The magnetic residual factor R_{mag} is given by:

$$R_{mag} = \frac{\sum_i | J_{io}^2 - J_{ic}^2 |}{\sum_i J_{io}^2}$$

where J_{io} and J_{ic} are the observed and calculated magnetic scattering cross-sections respectively. R_{mag} expresses the agreement between the experimental data and the magnetic structure model used during refinement.

A measure of the 'goodness of fit' of the calculated pattern to the observed pattern is given by the statistical parameter χ^2:

$$\chi^2 = \left[\frac{M}{N - P + C} \right]$$

where N, P and C are successively, the total number of steps, the total number of parameters and the number of constraints. χ^2 is expected to converge to 1 for a successful refinement, however much larger values are commonly observed.

The Bragg- and the magnetic R-factor as well as the value of χ^2 are the best criterion to assess the agreement between the experimental data and the structural model used during the refinement process.